Université de Liège

Faculté des Sciences

Modelling Glacial-Interglacial Atmospheric CO$_2$ Variations: The Role of Continental Weathering

Modélisation des variations glaciaires-interglaciaires du CO$_2$ atmosphérique : Rôle de l'érosion continentale

Dissertation présentée par

Guy Munhoven

en vue de l'obtention
du grade de Docteur en Sciences

1997

Foreword — Avant-propos

Je tiens à remercier Jean-Claude Gérard et Louis François de m'avoir accueilli dans leur groupe de recherche, et à leur exprimer ma gratitude pour la patience qu'ils ont eue avec mon travail tout au long des années passées. Je remercie aussi Jean-Luc Probst et ses collègues du Centre de Géochimie de la Surface (C.N.R.S.) à Strasbourg pour l'hospitalité dont j'ai pu profiter au cours de l'année que j'ai eu le bonheur de passer chez eux.

Il y a un bon nombre de personnes qui m'ont fourni des données et les résultats de leurs recherches, sans lesquels je n'aurais pas pu mener à terme ce travail. Ernst Maier-Reimer et Katharina Six du Max-Planck-Institut für Meteorologie de Hambourg m'ont fourni les champs de circulation océanique de leur modèle de circulation générale des océans. Gilles Ramstein et Sylvie Joussaume m'ont de même rendu accessibles des simulations glaciaires qu'ils ont effectuées avec les modèles atmosphériques du Laboratoire de Météorologie Dynamique de Paris. Frank Millero a bien voulu me fournir des détails sur le calcul des constantes thermodynamiques qui régissent l'équilibre des carbonates en milieu marin. A eux tous, un grand merci. Il faudrait enfin aussi penser à tous ceux qui ont rendu accessibles sur le réseau mondial Internet les fruits de leur recherche, que ce soient des bases de données ou des résultats de modèles. Sans leur générosite, ma tâche aurait certainement été beaucoup plus difficile, sinon impossible à accomplir.

Des grands mercis aussi à mes collègues de LaPlage : Anne, avec qui j'ai partagé le bureau ces dernières années, et qui m'a donné quelques coups de main plus que bienvenus dans la phase terminale de la rédaction de cette thèse; Pierre, Bernard, Benoît, puis Vincent et Denis (travaillant plus loin dans l'espace, mais moins loin dans le temps), et sans oublier Claude et Angela bien sûr. Enfin les ex-LaPlage, qui deviennent de plus en plus nombreux : Yves, Christine, Bernard, Frédéric, Nadine, Gilles, Thierry et Saïd. Votre compagnie joyeuse a toujours garanti une ambiance de travail digne de ce nom. Un merci tout spécial aussi à Carlo Denis, qui n'a cessé de m'encourager au fil des années, et sur qui j'ai toujours pu compter.

A Strasbourg, j'ai apprécié la collaboration avec Philippe et Wolfgang.

Mais sans la présence de Marie-Claire, Jean-Pierre, Pascal, Khadija et bien d'autres encore, mes souvenirs de Strasbourg seraient certainement plus pauvres.

Quittant le cercle plus restreint du milieu du travail, je pense à mes parents qui ont aussi attendu que ce travail touche à sa fin, et que je n'ai plus vus depuis très longtemps. Serge, mon frère, a relu ce manuscrit en profondeur et m'a apporté son aide pour sa mise en forme finale (dommage qu'il ne me reste plus qu'une seule Trappiste pour clôturer).

Il va sans dire que c'est grâce à Françoise que ce travail a pu voir le jour. C'est elle qui m'a fait garder la route au fil des derniers mois.

Enfin, mes remerciements vont à Bach, Schütz, Monteverdi et Händel, dont les oeuvres m'ont accompagné et réconforté pendant bien des heures. Il me semble d'ailleurs que personne de mieux que Schütz ne pouvait convenir pour l'Ouverture de ce travail.

La défense publique de cette thèse a eu lieu le 25 novembre 1997 à l'Institut d'Astrophysique et de Géophysique de l'Université de Liège, devant le jury composé de MM. les Professeurs Jean-Clair Duchesne (président), Jean-Claude Gérard et Albert Pissart (tous de l'Université de Liège) et de MM. les Docteurs James Orr (L.M.C.E.-C.E.A., Saclay), Jean-Luc Probst (C.G.S.-C.N.R.S., Strasbourg), Louis François et Michel Frankignoulle (Université de Liège).

J'ai profité de ce deuxième tirage pour corriger des fautes d'anglais, réécrire certains passages du texte et réarranger quelques tableaux et figures afin de rendre la présentation plus claire. Je remercie James Orr pour ses nombreux commentaires qui m'ont aidé à mener cette réédition à bien.

The heavens tell the glory of God
and the firmament states the work of His Hands

*Les cieux racontent la gloire de Dieu
et le firmament annonce l'œuvre de Ses Mains*

Heinrich Schütz — Geistliche Chormusik 1648

Summary

An eleven-box model of the ocean-atmosphere subsystem of the global carbon cycle is developed to study the potential contribution of continental rock weathering and of oceanic sedimentation to variations of atmospheric CO_2 pressure over glacial-interglacial time scales. The model is capable of reproducing the present-day distributions of total dissolved inorganic carbon, total alkalinity, phosphate, $\delta^{13}C$, and $\Delta^{14}C$ between the various ocean basins, as well as the partial pressure of atmospheric CO_2. A simple sedimentation scheme drives carbonate deposition and dissolution at the sea-floor as a function of the depths of carbonate and aragonite lysoclines in each ocean basin considered (Atlantic, Antarctic and Indo-Pacific). Carbonate accumulation on the shelf is also taken into account

Three different methods are used to calculate histories for the evolution of CO_2 consumption by continental rock weathering processes, with special emphasis on silicate weathering. The first method relies on the marine $^{87}Sr/^{86}Sr$ isotopic record. We find that this record does not represent a very strong constraint, due to the large spread of the $^{87}Sr/^{86}Sr$ ratios of waters draining silicate terrains. It is possible to construct a silicate weathering history that reproduces both the strontium isotopic record and the glacial-interglacial CO_2 signal. This weathering history implies that CO_2 consumption by silicate rock weathering was about 120% higher during glacial than during interglacial time.

The second approach is based upon the marine Ge/Si record. Taking the major uncertainties in the knowledge of the Ge and Si cycles into account, several histories for the evolution of the riverine dissolved silica fluxes are calculated from this record. The investigation of the systematics between riverine dissolved silica and bicarbonate fluxes under different weathering regimes leads us to the tentative conclusion that, although there is no correlation between dissolved silica and total bicarbonate concentrations in the major rivers, there may exist a negative correlation between weathering intensity and the ratio of bicarbonate derived from silicate weathering alone to dissolved silica. With this correlation as a working hypothesis, it is possible

to interpret the dissolved silica fluxes in terms of equivalent CO_2 consumption rates. The calculated histories indicate that glacial rates of CO_2 consumption by chemical silicate rock weathering could have been twice, and possibly up to three times and a half, as high as they are today. When used to force the carbon cycle model, they are responsible for glacial-interglacial p_{CO_2} variations in the atmosphere of typically 50–60 ppm and up to 95–110 ppm. These variations are superimposed to a basic oscillation of 60 ppm generated by the model, mainly in response to coral reef buildup and erosion processes. The total p_{CO_2} signal has an amplitude of about 80–90 ppm and up to 125–135 ppm. Although these large amplitudes indicate that silicate weathering processes should be taken into account when studying glacial-interglacial changes of CO_2 in the atmosphere, it also raises new problems, such as too high CO_2 levels during the period from 110–70 kyr B.P.

In the third approach, the glacial-interglacial histories for the consumption of CO_2 and the resulting transfer of bicarbonate to the ocean are calculated from the erosion model GEM-CO_2. The required variations of the continental runoff are derived from four different GCM climatologies. We find that the CO_2 consumption and river bicarbonate fluxes were about 20% higher at the last glacial maximum than at present. The exposed shelf accounts for a large fraction of the calculated LGM flux, overcompensating the 20% decrease of the two fluxes over the continent. The constructed weathering scenarios still produce p_{CO_2} variations of about 60 ppm between glacial and interglacial times, but the contribution from variable silicate weathering to this signal is now reduced to only 12 ± 5 ppm.

Résumé

Un modèle du cycle du carbone dans le système océan-atmosphère a été développé afin d'étudier la contribution potentielle de l'érosion des roches continentales ainsi que de la sédimentation océanique aux fluctuations du CO_2 atmosphérique lors des transitions climatiques glaciaires-interglaciaires. Ce modèle, contenant 11 compartiments, reproduit les distributions actuellement observées entre les différents bassins, du carbone inorganique dissous, de l'alcalinité, des phosphates, du $\delta^{13}C$ et du $\Delta^{14}C$ ainsi que de la pression atmosphérique en CO_2 . Un schéma de sédimentation simplifié détermine l'accumulation et la dissolution de $CaCO_3$ sur les fonds marins en fonction des profondeurs respectives des lysoclines pour la calcite et l'aragonite dans chaque bassin océanique (atlantique, antarctique et indo-pacifique). Le dépôt de carbonate sur les marges continentales est aussi considéré.

Trois méthodes sont utilisées pour calculer l'historique de l'évolution de la consommation de CO_2 dans les processus d'érosion des roches continentales avec une attention spéciale apportée au rôle des roches silicatées.

La première méthode se base sur l'enregistrement du rapport isotopique $^{87}Sr/^{86}Sr$ en milieu marin. Nous concluons que ce traceur n'apporte pas assez de contraintes suite à la large gamme de valeurs du rapport $^{87}Sr/^{86}Sr$ observées dans les eaux drainant des terrains silicieux. Il est cependant possible de construire une histoire de l'érosion des silicates qui reproduise à la fois l'évolution observée du rapport des isotopes du strontium ainsi que le signal glaciaire-interglaciaire du CO_2 atmosphérique. Cette reconstruction implique que la consommation de CO_2 par l'érosion des roches silicatées serait d'environ 120% plus élevée pendant l'époque glaciaire qu'à présent.

La deuxième approche utilise les données du rapport Ge/Si dans l'océan. En tenant compte des incertitudes dans la connaissance actuelle des cycles respectifs du Ge et du Si, plusieurs scénarios d'évolution des flux fluviaux de silicates dissous sont déduits de ces données. L'étude des interrelations entre le contenu en silice dissoute des fleuves et les flux de bicarbonate pour différents régimes d'érosion nous conduit à la conclusion provisoire que, bien qu'il n'existe aucune corrélation entre la teneur en silice dissoute et la concen-

tration totale en bicarbonate dans les eaux des principales rivières, il pourrait
y avoir une corrélation négative entre l'intensité de l'érosion et le rapport
entre la quantité de bicarbonates obtenus lors de l'érosion des roches sili-
catées seules et celle de silice mise en solution. En prenant cette corrélation
comme hypothèse de travail, il est alors possible d'interpréter les flux de
silice comme des taux de consommation équivalents de CO_2. Les recon-
structions effectuées dans ce travail indiquent que les taux d'utilisation du
CO_2 lors de l'érosion des roches silicatées pourraient avoir été deux fois, et
même jusqu'à trois fois et demi, aussi importants pendant l'époque glaciaire
qu'ils ne le sont actuellement. Ces flux, utilisés pour forcer le modèle du
cycle du carbone, produisent des variations de la pression atmosphérique de
CO_2 au cours des cycles glaciaires-interglaciaires de l'ordre de 50–60 ppm,
pouvant aussi atteindre 95–110 ppm. Ces fluctuations sont superposées à
un signal d'une amplitude de 60 ppm produit par la construction et la
désagrégation des récifs coralliens, processus inclus dans le modèle. Le signal
atmosphérique total a une amplitude d'environ 80–90 ppm, cette dernière
pouvant augmenter jusqu'à 125–135 ppm. Ces amplitudes élevées montrent
la nécessité d'inclure les processus d'érosion des roches silicatées dans l'étude
des variations glaciaires-interglaciaires du CO_2 atmosphérique. De nouveaux
problèmes découlent cependant de cette hypothèse. Ainsi, par exemple, la
pression atmosphérique du dioxyde de carbone est trop élevée dans les simu-
lations précédentes pour la période s'étendant de 110.000 à 70.000 ans avant
l'ère actuelle.

Dans une troisième approche, l'évolution glaciaire-interglaciaire de la con-
sommation de CO_2 et le transport de bicarbonate vers l'océan qui en résulte
sont calculés à l'aide du modèle global d'érosion GEM-CO_2. Les clima-
tologies produites par quatre modèles de circulation générale atmosphérique
différents sont utilisées pour déduire les fluctuations du ruissellement conti-
nental nécessaires au calcul. Il en résulte que la consommation de CO_2 et
les flux fluviaux de bicarbonate lors du dernier maximum glaciaire étaient
d'environ 20% supérieurs à leur valeur actuelle. Une grande partie des flux
obtenus pour le dernier maximum glaciaire provient des marges continentales
exposées suite au retrait du niveau des mers, contribution qui compense am-
plement une diminution d'environ 20% de ces flux sur les continents. Les
scénarios d'érosion obtenus par cette approche produisent des fluctuations
de la pression atmosphérique en CO_2 d'environ 60 ppm entre les époques
glaciaires et interglaciaires, mais la contribution de l'érosion des roches sili-
catées à ce signal n'est plus que de 12 ± 5 ppm environ.

Contents

Introduction

Almost exactly ten years have elapsed since J.-M. BARNOLA together with French and Russian colleagues published the first paleo-CO_2 record spanning the whole last glacial-interglacial cycle (BARNOLA et al., 1987). It was derived from the analyses of air extracted from an ice-core recovered by the Soviet Antarctic expeditions at the Vostok station in East Antarctica. At that time, it was already known that the atmosphere of the Last Glacial Maximum (18–21 kyr BP) had only about 200 ppm of CO_2, instead of 280 at the pre-industrial time (DELMAS et al., 1980; NEFTEL et al., 1982). But the Vostok record clearly established a firm correlation between atmospheric CO_2 and climate, with low levels during peak glacial, and high levels during peak interglacial times.

Although a large number of hypotheses have been proposed over the past decade to explain the observed oscillation, the causes of these are still not exactly known. Most authors have focused on an oceanic cause, invoking changes in the dynamics, the chemistry or the biology of the World ocean. The oceanic circulation has a characteristic time of about 1000 years and it involves rather large carbon and alkalinity fluxes. Changes in the rates of dynamical and chemical oceanic processes have thus the ability to substantially modify the atmospheric CO_2 content over time scales of several thousand years.

In this study, we propose to analyse the potential effects on atmospheric CO_2 levels of changing continental chemical weathering. In most of the previous studies, the global ocean as a closed system, and the long-term cycle of rock weathering on the continents followed by sedimentary deposition on the sea-floor neglected.

In the first two chapters we present a literature review of different aspects of the carbon cycle that are important for this study. In chapter 1, the global carbon cycle is described in its present-day state, and, where possible, changes since the pre-industrial are evaluated. We describe the various reservoirs and processes by which carbon gets transferred between and within them. The chapter closes with a short presentation of a few important records

1

of glacial-interglacial changes. Chapter 2 deals with the thermodynamics of the marine carbonate system. Different concepts, such as total dissolved carbon and total alkalinity are defined and discussed. We give a complete list of the thermodynamical constants that are required to determine the speciation of dissolved carbon.

In chapter 3, the role of the weathering processes in the carbon cycle is analysed. The differences between carbonate and silicate weathering are emphasized and their respective impact on atmospheric CO_2 levels over glacial-interglacial times are compared.

In chapter 4, we give a complete description of the carbon cycle model developed for this study. The different components are described in full detail. We complete the presentation by a thorough sensitivity analysis.

In the remaining three chapters, we describe the different methods used to reconstruct the histories for the consumption of atmospheric CO_2 by weathering processes over the last glacial-interglacial period. In chapters 5 and 6, two marine records are used for this purpose : the marine strontium isotope record and the Ge/Si record. In chapter 7, these histories are calculated from a global erosion model. Each of the histories obtained is in turn used as a forcing scenario in the carbon cycle model, which calculates the corresponding evolution of atmospheric p_{CO_2}.

We will close our study with a short summary and discussion of the results, completed by a general conclusion concerning future research.

Chapter 1

The Global Carbon Cycle

The global carbon cycle consists of the geochemical reservoirs that store carbon, and the pathways that transport carbon between them. Figure 1.1 presents a schematic overview of the generally obvious partitioning of the global environment into reservoirs which make up the carbon cycle. Boundaries between these are nevertheless not always as sharp as it is the case between the atmosphere and the oceans or the terrestrial biosphere. Oceanic sediments are an example of a sub-reservoir at the transition between two major reservoirs (ocean and lithosphere in this case), staying in exchange with the oceans on short time scales and, at the same time, supplying parts of its content to the lithosphere on longer time scales.

Figure 1.1 also identifies relevant processes by which carbon is exchanged among them. Time scales span many orders of magnitude, ranging from months (e.g., assimilation/respiration of carbon by marine biota and by the continental vegetation) to hundreds of millennia and more (e.g., volcanism, sea-floor weathering). Both natural and perturbation fluxes due to human activity have been considered. Although the latter are not of prime interest for the present study, they need to be quantified in order to reconstruct the state of the carbon cycle before the large-scale onset of human activity. In the first four sections of this chapter, we will review the different reservoirs one by one. In the last section, we will then present the most important changes in the carbon cycle related to the glacial-interglacial climatic cycles, with emphasis on the Vostok ice-core record of atmospheric CO_2.

In this review chapter, special attention will be given to the oceanic part of the cycle. Ultimately, this is the actor which determines CO_2 levels in the atmosphere. If we are to explain the important atmospheric CO_2 variations during the Late Pleistocene, we need to understand the interplay of the important factors. We also need to quantify the sensitivity of the whole oceanic carbonate system to internal perturbations and reorganizations (cir-
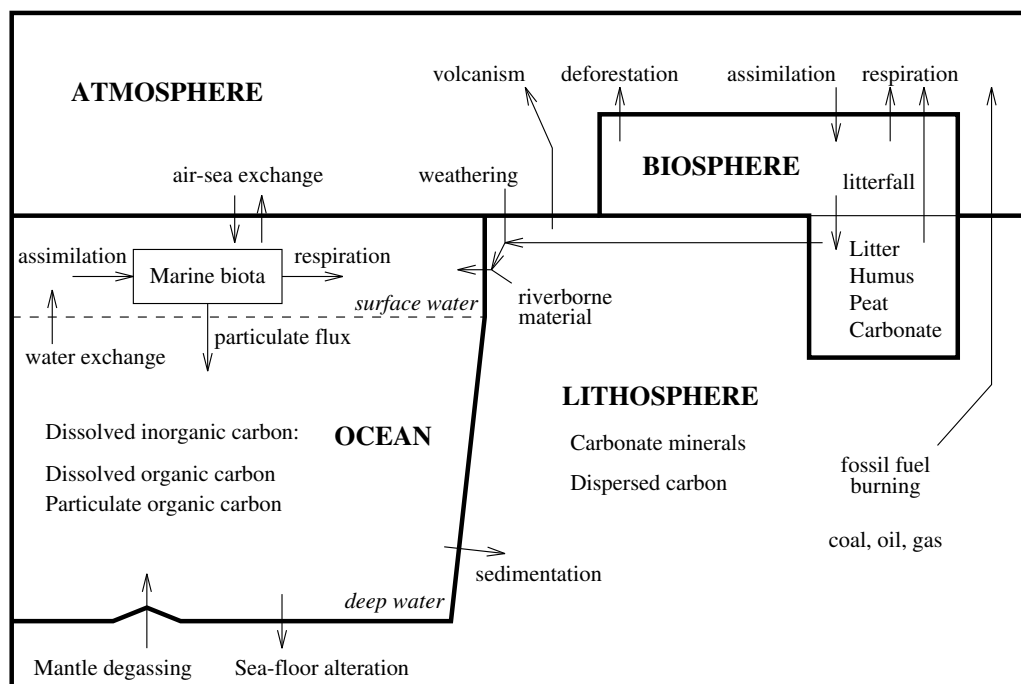
Figure 1.1: The global cycle of carbon: reservoirs and processes (modified from HOLMÉN 1992).

culation changes, productivity changes, etc.) and to external perturbations (such as varying air-sea exchange or changing supply of bicarbonate by rivers, e.g., due to altered continental weathering, etc.). Even if perturbations of the global carbon cycle directly act upon the atmospheric reservoir, as it has been the case for the huge anthropogenic input of CO_2 from fossil fuel burning for more than 150 years now, CO_2 levels in the atmosphere will ultimately equilibrate with the surface oceans which, on longer time scales, will themselves tend towards an overall equilibrium with the deep waters.

A great deal of information on the global carbon cycle has been derived from carbon isotopic information. There are three isotopes of carbon that are of interest for carbon cycle studies: ^{12}C, ^{13}C and ^{14}C. Only the first two of these are stable. ^{14}C is radioactive (and therefore generally called *radiocarbon*), with a half-time of decay currently estimated at 5730 ± 40 years (GODWIN, 1962). There are small but significant differences in the isotopic composition of carbon in the different reservoirs of the carbon cycle. The differences arise from fractionation effects related to the processes which cycle carbon between and within the reservoirs, and of course from radioactive decay in the case of ^{14}C. Processes where diffusion plays an important role can lead to isotopic fractionation, heavy isotopes being discriminated against light ones.

In natural environments, the relative abundances of ^{12}C and ^{13}C are respectively 98.9% and 1.1% on average while radiocarbon is only present in traces. In the atmosphere, for example, atomic $^{14}C/C$ ratios are of the order of 10^{-12} (BROECKER and PENG, 1982). ^{14}C is nevertheless very valuable for estimating overturning rates of different reservoirs, especially of the ocean, residence times of carbon within reservoirs, and exchange fluxes. Its only source is in the upper atmosphere where it originates from the reaction of cosmic ray-produced neutrons with ^{14}N nuclei: $^{1}_{0}n + ^{14}_{7}N \longrightarrow ^{14}_{6}C + ^{1}_{1}p$. The only sink on Earth for the so-produced ^{14}C is through radioactive decay back into ^{14}N by emission of a β^- particle. The half-time of decay for radiocarbon is long enough to allow it to enter carbon reservoirs that react directly or indirectly with the atmosphere. It is also short enough to allow for measurable gradients to establish along the pathways that a given carbon sample follows after becoming isolated from the atmosphere and which can be related to the time elapsed since then. After oxidation to $^{14}CO_2$, it gets rapidly mixed throughout the atmosphere and enters the global cycle through the processes that involve CO_2. Carbon from geologically important reservoirs, like old carbonate rocks, or coal and fossil fuels, will be devoid of radiocarbon, due to the characteristic turnover times of these reservoirs which largely exceed the half-time of ^{14}C.

Because isotopic ratios in nature are generally small (of the order of 0.01

in the case of $^{13}C/^{12}C$) and because their relative variations seldom exceed a few percent, they are typically reported as deviations relative to the isotopic ratio of a standard. For ^{13}C, this so-called δ value is noted $\delta\,^{13}C$ and it is defined by

$$\delta\,^{13}C = \frac{\left(^{13}C/^{12}C\right)_{\text{sample}} - \left(^{13}C/^{12}C\right)_{\text{standard}}}{\left(^{13}C/^{12}C\right)_{\text{standard}}} \tag{1.1}$$

Most often, this $\delta\,^{13}C$ is multiplied by 1,000 in order to express it in permil. The internationally accepted standard for ^{13}C is PDB, (from *PeeDee Belemnite*) named after the Cretaceous belemnite from the Peedee formation in South Carolina, which was used to prepare the first reference CO_2 gas.

The definition of $\delta\,^{14}C$ differs somewhat from that of $\delta\,^{13}C$. Radiocarbon data are typically expressed as $^{14}C/C$ rather than $^{14}C/^{12}C$ ratios because, historically, they have been derived from sample activities, measured by β-decay counting, while ^{13}C data come from mass-spectrometric measurements. Recently developed methods for ^{14}C now also use mass spectrometry (Accelerator Mass Spectrometry, AMS). $\delta\,^{14}C$ is defined by

$$\delta\,^{14}C = \frac{\left(^{14}C/C\right)_{\text{sample}} - \left(^{14}C/C\right)_{\text{standard}}}{\left(^{14}C/C\right)_{\text{standard}}} \tag{1.2}$$

The international reference $(^{14}C/C)_{\text{standard}}$ is derived from the activity of an oxalic acid preparation of the U.S. National Bureau of Standards, after correction for fractionation and radioactive decay since the reference date of January 1, 1950. In the literature, ^{14}C data are usually given as $\Delta^{14}C$ values, obtained after normalization to a reference $\delta\,^{13}C$ value of -0.025 ($= -25\,^0\!/\!_{00}$) typical of average terrestrial wood, in order to eliminate variations that are due to fractionation:

$$\Delta^{14}C = \delta\,^{14}C - 2(\delta\,^{13}C + 0.025)(\delta\,^{14}C + 1) \tag{1.3}$$

An in-depth discussion of this normalization can be found in STUIVER and POLACH (1977).

1.1   Atmosphere

Of all the carbon reservoirs considered in figure 1.1, the atmosphere is the smallest and also the best known. On the time scale of a few years, it can be considered that it is homogeneous: if only the troposphere is considered, its mixing time is of the order of 1–2 years. The atmospheric carbon is mostly present as CO_2. Other carbon compounds, including CH_4 and CO make up

Monthly Mean CO$_2$ in the Atmosphere

Annual Mean CO$_2$ in the Atmosphere
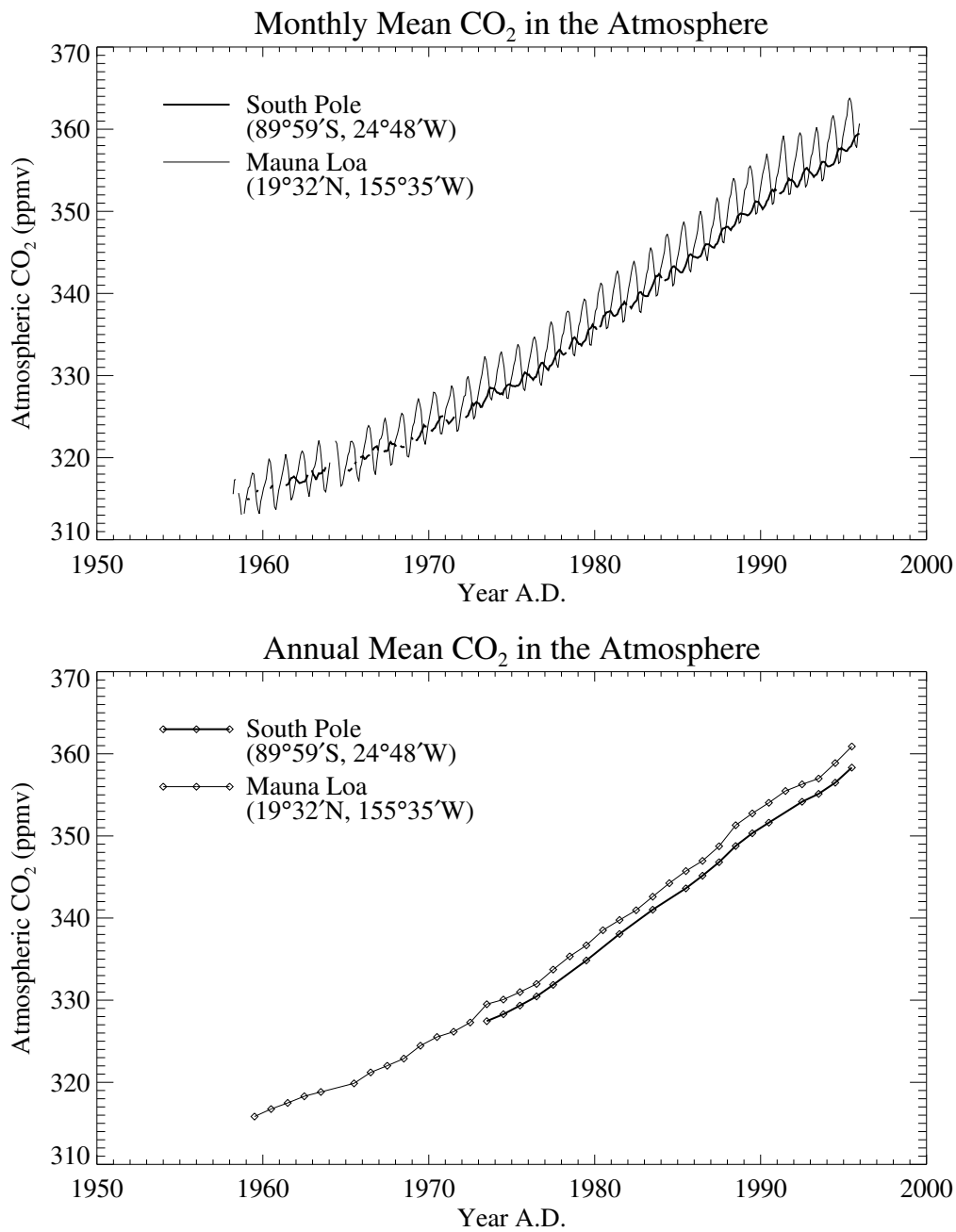
Figure 1.2: Evolution of the monthly (top) and annual (bottom) mean atmospheric CO$_2$ abundances at the South Pole and Mauna Loa Observatories. On the time axis, ticks mark the date of January 1st for each year. In the lower panel, diamonds indicate the years for which data were available. Plotted from data of KEELING and WHORF (1996).

less than 1% of the total mass of carbon in the atmosphere. Direct and precise monitoring of atmospheric CO_2 is performed since 1957 at the South Pole and since 1958 at Mauna Loa, Hawaii. The evolutions of monthly and annual mean concentrations at these two sites are shown in figure 1.2. The values obtained at Mauna Loa are very close to global average. In the late 50s, annual average concentrations in dry air were about 315 ppmv. Using a conversion factor of 176.73×10^{12} mol C/ppmv (SUNDQUIST, 1985), we find that this corresponds to a total of $55,670 \times 10^{12}$ moles of carbon or 55,670 Tmol C. At that time, the annual growth rate was already 0.6 ppmv/yr. It has been continuously increasing, reaching decadal averages of 0.83, 1.28 and 1.53 ppmv/yr over the 60s, 70s and 80s respectively (SCHIMEL et al., 1996). In 1995, the annual average concentration at Mauna Loa was 360.9 ppmv, representing an increase by 14.6% in less than 40 years. This was the first year to present an average value in excess of 360 ppmv. The documented increase is without any doubt due to human activity, and stems mainly from the burning of fossil fuels, but also from changing land use. After removal of the seasonal and short-term trends, it can be calculated that the annual increase corresponds to only about half of the total anthropogenic emissions (KEELING et al., 1989, 1995). The remainder is taken up by the ocean and the continental biosphere. The inter-hemispheric difference has been increasing in parallel with emissions from fossil fuel burning (KEELING et al., 1989; SIEGENTHALER and SARMIENTO, 1993), which can be related to the fact that 95% of these emissions originate in the Northern Hemisphere. The most striking evidence for the anthropogenic origin of the observed increase however comes from the ^{14}C record. ^{14}C concentrations recorded in tree rings decreased by 2% between 1800 and 1950 (SUESS, 1955). This isotopic decrease, called *Suess effect* can easily be related to the burning of fossil fuels, which gives rise to a ^{14}C-free source to the atmosphere. After 1950, the interpretation in terms of fossil fuel dilution is impossible due to the contamination by ^{14}C produced from thermonuclear weapon testing in the atmosphere. A similar dilution effect exists for ^{13}C. The $\delta^{13}C$ values of fossil fuels are well below that of the atmosphere, which has decreased from about $-6.4\,^0\!/_{00}$ during pre-industrial times to $-7.8\,^0\!/_{00}$ in the early 1990s (see below). TANS (1981) calculates that the average $\delta^{13}C$ values of the CO_2 released by the burning of fossil fuels has varied from about $-24\,^0\!/_{00}$ in 1850 to less than $-27\,^0\!/_{00}$ in the late 1970s. However, the observed decrease of atmospheric $\delta^{13}C$ cannot only be ascribed to the release of CO_2 from fossil fuel burning. A non-negligible part of this decrease is due to the transfer of carbon from the terrestrial biosphere as CO_2 to the atmosphere as a result of deforestation and soil manipulation (see, e.g., PENG, 1985). As mentioned before, the average $\delta^{13}C$ of terrestrial organic material is about $-25\,^0\!/_{00}$, very close to that of fossil fuel CO_2.
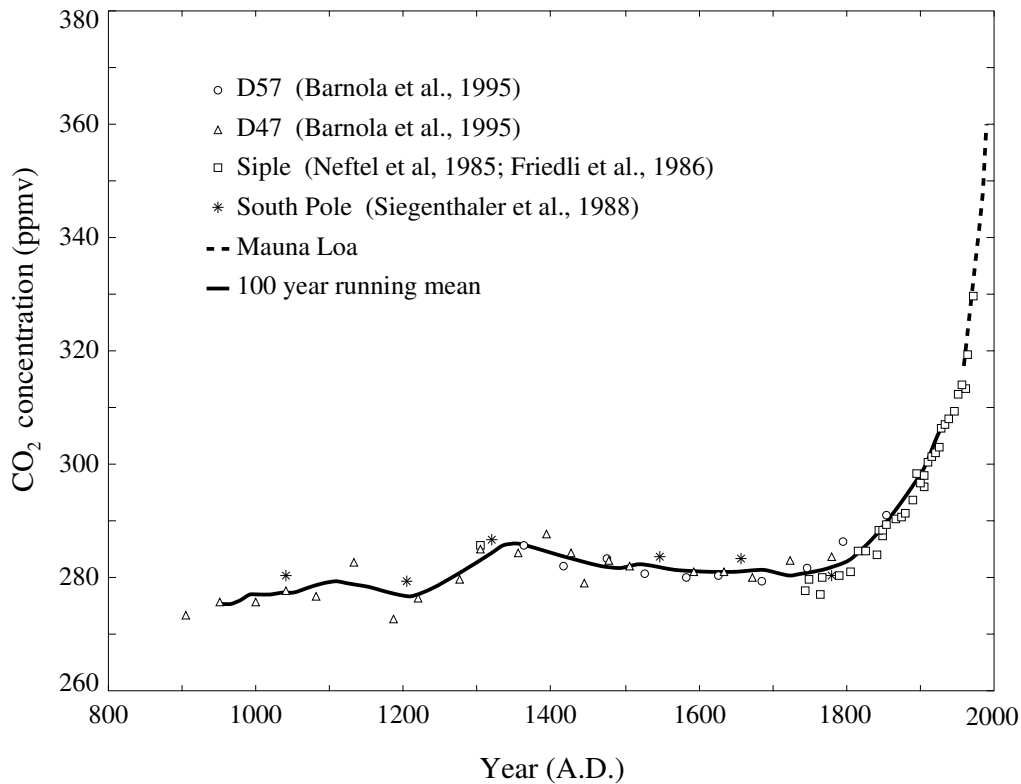
Figure 1.3: Composite record of atmospheric CO_2 concentrations over the past 1000 years, derived from direct atmospheric measurements at Mauna Loa and from Antarctic ice-cores (figure simplified from SCHIMEL et al. (1995)).

Prior to 1957, atmospheric CO_2 levels can only be indirectly obtained. The most reliable pre-1958 data stem from the measurement of the CO_2 content of air bubbles occluded in ice from Antarctica. Greenland ice is contaminated, which makes its measured CO_2 content difficult to interpret (DELMAS, 1993). The best ice-core CO_2 records available today for the millennium before 1800 witness of pre-industrial CO_2 levels fluctuating within a narrow band of ± 10 ppmv around an average value of 280 ppmv (see figure 1.3). The largest pre-industrial variation during the covered period is observed between AD 1200 and 1350. Compared to the 80 ppmv increase between AD 1800 and today, it remains however very small. The most recent global scale variation of similar magnitude in Earth history dates back to the close of the last glaciation.

Before the availability of reliable data from ice-cores, various other meth-

ods had been used to reconstruct pre-industrial CO_2 levels. By studying the carbonate chemistry of supposedly uncontaminated deep seawater samples, BREWER (1978) estimated an increase of 50 ± 20 ppmv from pre-industrial times to 1972 when annual average concentrations had risen to 325 ppmv. Using a similar method, CHEN and MILLERO (1979) found a 65 ± 30 ppmv variation. Accordingly, pre-industrial levels of 275 ± 20 ppmv and 260 ± 30 ppmv can be calculated. By deconvolution of different tree-ring $\delta^{13}C$ records, PENG (1985) arrived at estimates ranging from 266 to 283 ppmv.

We adopt here the ice-core derived value of 280 ± 10 ppmv as the best available pre-industrial datum.

Monitoring of atmospheric $\delta^{13}C$ began only in the mid-70s. At that time, the annual average value was close to $-7.5\,^0\!/_{00}$, and it has since then decreased to less than $-7.8\,^0\!/_{00}$, again due to industrial activity (KEELING, 1993). For the pre-industrial atmosphere, ice-core measurements have revealed levels of $-6.4 \pm 0.1\,^0\!/_{00}$ (FRIEDLI et al., 1986).

1.2 Continental Biosphere

The terrestrial biosphere forms a carbon reservoir with a highly complex dynamics. It can readily be subdivided into two major sub-reservoirs: on one hand the *biota*, comprising life vegetation, and on the other hand the *soils*, consisting of decomposing plant matter (mostly humus and peat), but also including litter. Most of the carbon in these reservoirs is organic, but a non-negligible amount of mineral carbon forms within the soil horizons affected by biotic processes. Estimates for the present-day terrestrial biomass range from 421 to 1,000 Pg C (HOUGHTON et al., 1985; SUNDQUIST, 1985). Most of the uncertainty is due to the poor data available on tropical forest systems. Following HOUGHTON et al. (1985), the probable range is about 420–570 Pg C (100–200 Pg C from tropical forests and 319–368 Pg C for the rest). In more recent evaluations of the global carbon budget, preferred values are at the upper end of this range. SARMIENTO and SIEGENTHALER (1992) (and also SIEGENTHALER and SARMIENTO, 1993) whose work served as a basis for the latest IPCC assessments (SCHIMEL et al., 1995, 1996) adopt 550 Pg C.

For soil carbon, figures are even less certain. Estimates for the pool of soil organic carbon cover the range from 700 to 3,450 Pg C, most of them falling however between 1,200 and 2,200 Pg C (HOUGHTON et al., 1985; SUNDQUIST, 1985). HOUGHTON et al. (1985) think that the best value is probably 1500 Pg C, with an uncertainty of 20%. Taking more recent estimates into account (e.g., PRENTICE and FUNG, 1990) an uncertainty of 30% seems to be more realistic. Soils in arid and semiarid regions also contain

carbon as carbonate, in calcic and calcrete horizons. Following HOUGHTON et al. (1985), this represents a carbon stock of 550 to 1,800 Pg C. OLSON et al. (1985) estimate it at 1,000–1,200 Pg C.

OLSON et al. (1985) add a further and quite large sub-reservoir of organic carbon to the terrestrial biosphere carbon reservoir. With an estimated 1,000–3,000 Pg C, so-called *subfossil carbon*, it is of the same order of magnitude as the biota and the soil reservoirs together. It lies at the transition between the terrestrial biosphere and the lithosphere. It it is fed by the soil reservoir (from peatlands) and by shallow aquatic systems. The carbon stored there is slowly incorporated into geologic formations.

Just like the atmosphere, the biospheric carbon reservoir has been affected by human activities. Estimates of the anthropogenic changes are again highly variable, ranging from a 54 Pg C increase to a 60 Pg C decrease for the biomass sub-reservoir and a 22–300 Pg C (and higher) decrease for the soil sub-reservoir since the pre-industrial time (SUNDQUIST, 1985). The overall trend of these studies points towards a net loss of 38–274 Pg C to the atmosphere, well below the current uncertainty on the global reservoir size. SIEGENTHALER and SARMIENTO (1993) and SARMIENTO and SIEGENTHALER (1992) adopt pre-industrial values of 610 and of 1,560 Pg C for the biomass and the soil sub-reservoirs respectively, assuming a net loss of about 120 Pg C. This loss is the same as that of SOLOMON et al. (1985) who estimate it at 120 Pg C, with an uncertainty range of 90–180 Pg C.

As witnessed by the well-pronounced seasonal cycle in the atmospheric CO_2 signal (figure 1.2), the terrestrial biosphere is characterized by large exchange fluxes with the atmosphere. The global Gross Primary Productivity (GPP), i.e., the rate at which photosynthesizing plants are able to assimilate CO_2 into their organic tissues is estimated at 90–120 Pg C/yr. It is however possible that only 60–70% of the involved CO_2 stems from the atmosphere, the rest being recycled from within the plant canopy (HOUGHTON et al., 1985). These authors therefore propose an overall annual exchange of 60–120 Pg C between the biosphere and the atmosphere. Net Primary Productivity (NPP) is the rate of fixation less the autotrophic respiration of plants. Carbon from NPP gets either transferred to soils, is temporarily stocked in the long-lived parts of vegetation (e.g., wood) before getting transferred, or returns to the atmosphere through fires. From the soils, it is released to the atmosphere through heterotrophic respiration on more or less longer time scales, going from a few years for the litter to hundreds of years for humus (OLSON et al., 1985). In steady-state conditions, NPP should nearly balance the soil's loss of carbon to the atmosphere. Following HOUGHTON et al. (1985), annual NPP is of the order of 55 Pg C/yr, with an uncertainty of perhaps 15–35%. The mean residence time of organic carbon in the soil

reservoir should be of the order of 20–40 years.

Carbonate precipitation rates in the calcic soil horizons are very poorly known, but seem to be several orders of magnitude smaller than NPP. Following HOUGHTON et al. (1985) and OLSON et al. (1985), they should be of the order of 0.01 to 0.03 Pg C/yr. The turnover time of this carbon stock can hence be estimated at 55,000–75,000 years (average pool size divided by the average production, and average of extreme values for the residence times). For the subfossil carbon reservoir, OLSON et al. (1985) estimate a residence time between 1000 and 10,000 years. They furthermore indicate that this reservoir may at present be accumulating carbon at a rate of 0.024–0.030 Pg C/yr.

To close this section, we must say some words about the role of vegetation on carbon isotope distribution. The average $\delta^{13}C$ of terrestrial organic material is close to $-25\,^0\!/_{00}$, about $18\,^0\!/_{00}$ less than atmospheric CO_2 (TANS et al., 1993). This difference varies as a function of the photosynthetical pathway: for C-3 plants, it is of 19–$22\,^0\!/_{00}$, for C-4 plants, it is only of $4\,^0\!/_{00}$ (CIAIS et al., 1995). Due to normalization, the $\Delta^{14}C$ of newly formed plant material is close to $0\,^0\!/_{00}$. Humus has typical $\Delta^{14}C$ values of $-50\,^0\!/_{00}$, reflecting the prolonged residence time of that kind of organic carbon in the soil reservoir (HOLMÉN, 1992).

1.3   Ocean

The oceanic reservoir plays a key role within the global carbon cycle. It is by far the largest of the three active reservoirs, i.e., the atmosphere, the biosphere and the ocean, which make up the exospheric cycle. The ocean's global carbon content is about an order of magnitude larger than that of the atmosphere and the terrestrial biosphere taken together. Only the lithosphere is larger. Nearly all of the carbon on its way through the lithosphere-exosphere-lithosphere cycle transits through it.

Before getting onto describing the oceanic reservoir of carbon, a short description of the oceanic environment itself is of need. Many features of the distribution and cycling of carbon compounds in the ocean are strongly dependent, for example, on the ocean circulation patterns.

1.3.1   Physical Characteristics of the Oceanic Environment

Vertical Stratification

The average oceanic water column is characterized by a well-pronounced vertical stratification, strongly inhibiting vertical water movements. It can be readily divided into three zones, primarily based on the density distribution, itself governed by the temperature and salinity distributions: the surface ocean, the pycnocline and the deep ocean (GROSS, 1982).

- The *surface ocean*, averaging about 100 m in thickness, contains the least dense water. It is well mixed by the action of winds and waves. Furthermore, the surface ocean is relatively warm, except at high latitudes (the average surface ocean temperature is close to 17°C).

- The *pycnocline* lays beneath the surface zone. It extends to a typical depth of about 1,000 m. Water density rapidly increases with depth throughout it. This density increase is most often associated with temperature decrease, and the pycnocline often coincides with the *thermocline*, the zone where temperature quickly declines from the surface values to the top temperature of the underlying deep-water zone. At latitudes higher than 60°, the thermocline is generally absent or it forms only during the summer season. Here, the pycnocline results from the presence of a *halocline*, a pronounced salinity gradient, due to important precipitation at the surface, which lowers the surface salinity. Thermocline and halocline may also work together and lead to a particularly stable stratification.

- The *deep ocean*, which contains the most dense water, extends from a depth of 1,000 m to the bottom. Temperatures gently decline from about 4–5°C at the top to 0–3°C at the bottom. Neither temperature nor salinity are affected by seasonal variations in this zone.

Global Overturning

The large-scale overturning of the oceans is driven by the *thermohaline* circulation, the density-driven ventilation of the deep waters. An idealized overview of the water movement by the thermohaline circulation in the oceans is presented in figure 1.4 (after JR, 1995), a modification of BROECKER's (1991) *Great Ocean Conveyor Belt*.

   Water that is dense enough to sink from the surface to the bottom of the ocean forms at present only in the cold high-latitude regions of the North
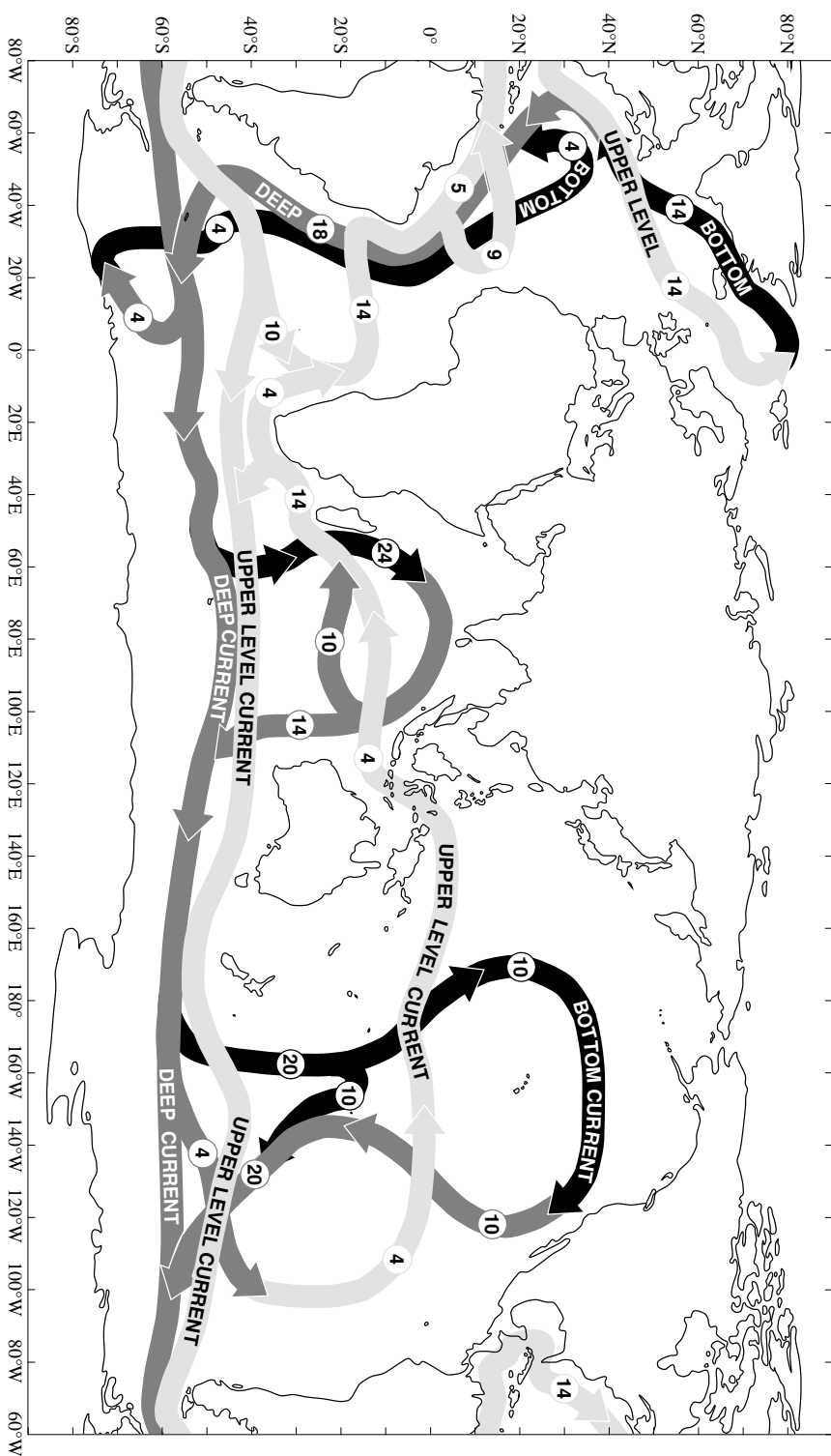
Figure 1.4: Three-layer thermohaline conveyor belt circulation (adapted by the author from Jr, 1995). The grey arrows represent the flow pathways of water near the bottom (black), in the deep (dark grey) and in the upper water column (light grey). Changing grey tones along pathways indicate water mass conversion. The circled numbers are estimates for the water transport in sverdrups (1 sverdrup = 1 Sv = 10^6 m^3/s).

Atlantic and around the Antarctic continent (BROECKER and PENG, 1982; BROECKER, 1991). The mechanisms for the required densification are cooling by winds and salinity increases due to sea-ice formation (this latter being however of secondary importance) during the winter season.

Around the perimeter of the Antarctic continent (particularly in the Weddell and Ross Seas), water that has upwelled from the deep circumpolar current densifies during winter time at the surface, due to strong cooling and sea-ice formation. It sinks down the continental slope to the bottom into the less dense deep water, entraining some of this, and mixing with it. At the bottom, the newly formed Antarctic Bottom Water (AABW) joins the deep Antarctic Circumpolar Current. While circulating eastwards with this deep current, it mixes upward into it. The resulting water mass spreads northwards, feeding the near bottom regions of all the major ocean basins (BROECKER and PENG, 1982).

In the North Atlantic (more precisely, in the Labrador, Greenland and Norwegian Seas), cooling of the already very salty surface water during winter time leads to the formation of North Atlantic Deep Water (NADW). This deep water mass flows to the south through the western basin of the Atlantic Ocean to the tip of Africa. As it reaches the southern part of the North Atlantic, it begins to overlie the denser AABW. Somewhat further south, it gets itself overlaid by Antarctic Intermediate Water (AAIW). AAIW forms all along the Antarctic Polar Frontal Zone from upwelling deep circumpolar water that reaches this zone from the south. It sinks only to a depth of 500–1,500 m and spreads northwards throughout the whole Southern Hemisphere oceans, generally at sub-thermocline depths. While flowing to the south, at a depth of 2–4 km, NADW progressively mixes with AAIW above and the AABW below, contributing this way to recirculate them back to their circumpolar source region. When reaching the tip of Africa, NADW gets entrained by the strong, eastward flowing deep Antarctic Circumpolar Current. It finally enters the deep Indian and Pacific basins only after intense mixing with water from the circumpolar current.

In the different basins, water flowing in along the bottom eventually combines with the overlying deep and intermediate waters to return to the circumpolar region.

The formation of bottom and deep waters is compensated by a return flow of water to the surface. This return flow is not confined to restricted areas as is the deep water formation. It is rather of diffusive nature throughout the World oceans, although large parts of it must take place in the circumpolar region (BROECKER, 1991). There is furthermore a net southward export of water from the Atlantic and a net import into the Indian and Pacific ocean below a depth of about 1,500 m (BROECKER, 1979; BROECKER and PENG,

1982; BROECKER, 1991). The corresponding return flow in the upper water (above 1,500 m) from the Indian and Pacific Oceans to the source region of NADW in the North Atlantic is thought to follow pathways through the Antarctic into the South Atlantic via the Drake Passage, and around the tip of Africa via the Indonesian Archipelago as shown in figure 1.4 (BROECKER, 1991; JR, 1995). From a quantitative point of view, the transport rates indicated in figure 1.4, which derive from observational constraints, still remain subject to debate. The least well established feature of the conveyor belt circulation scheme of figure 1.4 are associated with the processes that drive the vertical exchange in the Indian and Pacific Oceans (JR, 1995).

For the calibration of our carbon cycle model, we rely on constraints from both observations and numerical simulations. The water exchange of our model ocean is first of all based upon the velocity field from the 11-layer version of the Hamburg Large-Scale Geostrophic Oceanic General Circulation Model (LSG-OGCM, MAIER-REIMER et al., 1993). This model produces a net transfer of 16 Sv to the deep sea across the 1,500 m depth horizon in the North Atlantic. In the Antarctic Circumpolar Ocean, it presents a net upwelling of 16 Sv in the Atlantic sector, and net deep water formation rates of 11 and 23 Sv respectively in the Indian and Pacific sectors (each time across the 1,500 m depth horizon). At depth, there is a net transfer of 16 Sv from the Atlantic to the Circumpolar, and of 15, resp. 19 Sv, from the Circumpolar to the Indian and Pacific. The upper ocean return flow to the North Atlantic is almost completely via the Drake Passage (MAIER-REIMER et al., 1993).

In addition, the distribution of $\Delta^{14}C$ in the oceans serves as a calibration means to upscale the circulation field from the three-dimensional grid of the OGCM (with a horizontal resolution of 3.5° and a vertical resolution of 50 m at the surface and 1000 m at depth) to the several orders of magnitude coarser representation of the ocean in our model. Figures 1.5 (from STUIVER et al., 1983) and 1.6 (after BROECKER and PENG, 1982) show the latitudinal distributions of $\Delta^{14}C$ in the deep and the surface waters of the three major ocean basins. The distributions shown in these figures have been corrected for the effects from anthropogenic perturbations to the carbon cycle. For ^{14}C, the most important correction is due to contamination by ^{14}C produced during the thermonuclear weapon tests in the atmosphere in the late 50s and early 60s. At the time of the GEOSECS survey, this so-called bomb-^{14}C had not yet penetrated waters deeper than 1,500 m, except for the North Atlantic (STUIVER et al., 1983). In the surface waters, the values measured during GEOSECS were on global average $160 \pm 15\,^0\!/\!_{00}$ higher than those shown in figure 1.6, which represents a reconstruction for the state prior to the testing of nuclear weapons (BROECKER and PENG, 1982). Although this prenuclear
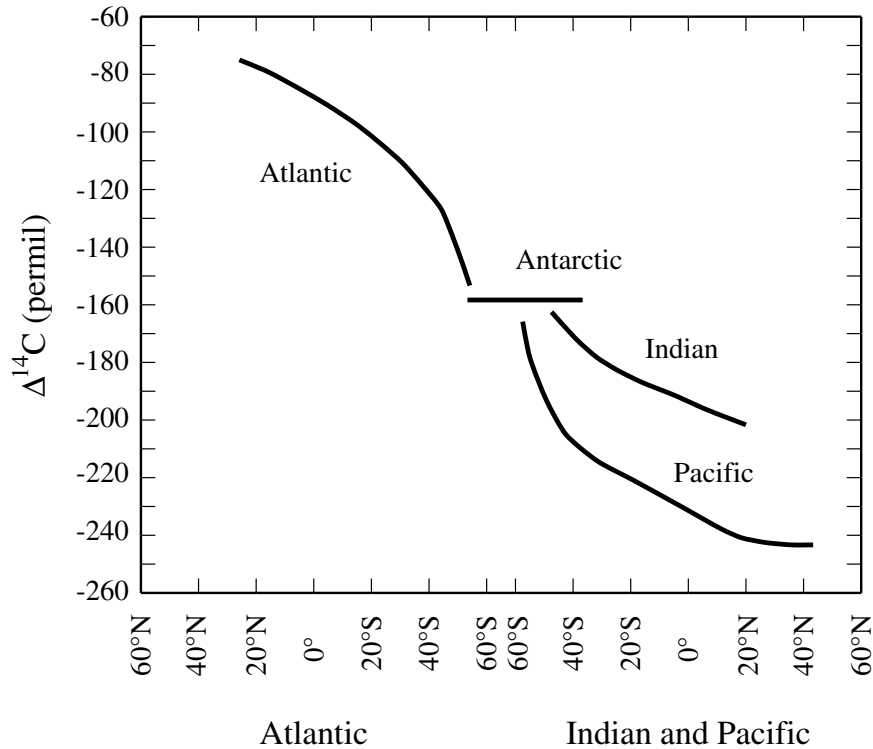
Figure 1.5: Distribution of $\Delta^{14}C$ in the deep waters below 1,500 m of the World Ocean (from Stuiver et al., 1983).

distribution is not exactly the same as the pre-industrial or natural one, it is nevertheless sufficiently close to it for our purposes. Broecker and Peng (1982) estimate that the magnitude of the Suess effect in the surface ocean is less than $10\,{}^0\!/_{00}$ between 1800 and 1950; in the deep sea, it is lower than the accuracy of ^{14}C measurements. The deep-sea distribution of $\Delta^{14}C$ has been widely used to estimate the global overturning rates of the World oceans. The global mean residence time of water in the ocean below 1,500 m depth has this way been estimated at about 500–600 yr (Broecker, 1979; Broecker and Peng, 1982; Stuiver et al., 1983). For individual ocean basins, the respective residence times are shorter, ranging from about 200–300 yr for the Atlantic and the Indian Oceans to 500–600 yr for the Pacific Ocean (Broecker, 1979; Stuiver et al., 1983; Broecker et al., 1991a).

According to Broecker and Peng (1982), biological carbon fluxes affect $\Delta^{14}C$ *values* in the deep ocean by less than 10%. The distribution of $\Delta^{14}C$ thus depends mostly on air-sea exchange, and once a water sample has been isolated from the zone of CO_2 exchange with the atmosphere, on radiodecay
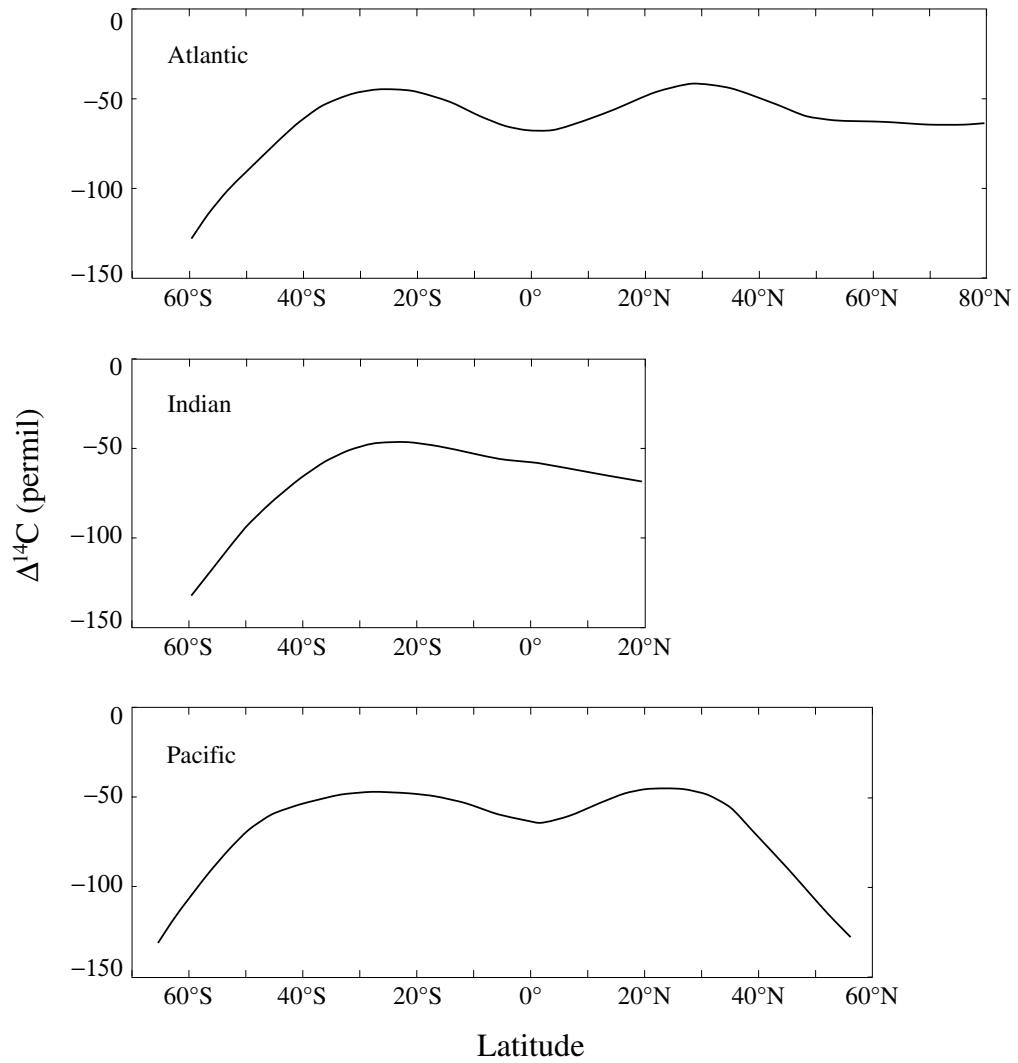
Figure 1.6: Surface water $\Delta^{14}C$ as a function of latitude in the Atlantic, Indian and Pacific Oceans prior to the onset of nuclear weapon testing in the atmosphere. The curves indicate only average latitudinal distributions. The real data present substantially more scatter (of the order of about $\pm(15-20)\,^0\!/_{00}$) (after BROECKER and PENG, 1982).

and mixing with water of different composition. This is well reflected in the distributions of deep-sea Δ^{14}C in figure 1.5. The highest Δ^{14}C are found in the deep Atlantic, the lowest in the northernmost parts of the Indian and Pacific Oceans.

1.3.2 Carbon in the Oceans

Four major pools of carbon can be distinguished in the ocean. These are, by decreasing size, the dissolved inorganic carbon (DIC), the dissolved and the particulate organic carbon (DOC and POC) and the living biomass pools. Within the atmosphere, CO_2 is chemically rather inert and its budget is controlled by surface sources and sinks. In aqueous media, the situation is very different. Upon dissolution, CO_2 is hydrated to H_2CO_3, leading to the formation of bicarbonate and carbonate ions. The *dissolved inorganic carbon*, or *total carbonate* concentration, C_T, is defined as

$$C_T = [CO_{2(aq)}] + [HCO_3^-] + [CO_3^{2-}].$$

H_2CO_3 only exists in trace amounts and is conveniently included with CO_2 as $[CO_{2(aq)}]$ (see page 48). The relative amounts of these three different species depend on the pH buffer capacity of the ocean. This buffer capacity is generally expressed in terms of *total* or *titration alkalinity*, A_T, which is a measure of the acid neutralization capacity of a solution. It is expressed in proton equivalents per unit mass. Both A_T and C_T are directly measured. Taking the average composition of natural seawater into account, one can generally reduce A_T with good precision to

$$A_T = [HCO_3^-] + 2\,[CO_3^{2-}] + [B(OH)_4^-] + [OH^-] - [H_3O^+],$$

although the contributions from OH^- and H_3O^+ can most often be neglected. If the relevant thermodynamic equilibrium constants for carbonate and borate equilibria (and the dissociation constant for water in seawater) are known, one can then calculate the individual concentrations of $CO_{2(aq)}$, HCO_3^- and CO_3^{2-} from C_T and A_T. A more comprehensive presentation of carbonate chemistry, with discussion of selected topics of importance for the understanding and modelling of the oceanic carbon cycle is given in chapter 2.

The distributions of C_T and A_T in the world oceans are known with a good precision since the GEOSECS expeditions from 1972 to 1977. Figure 1.7 shows average distributions of both quantities throughout different water masses. Using the available profiles, TAKAHASHI et al. (1981a) derive a total DIC pool of 3.16×10^{18} mol C or 37,920 Pg C and a total alkalinity pool of 3.33×10^{18} eq. Other authors give quite similar figures, between 36,600 and
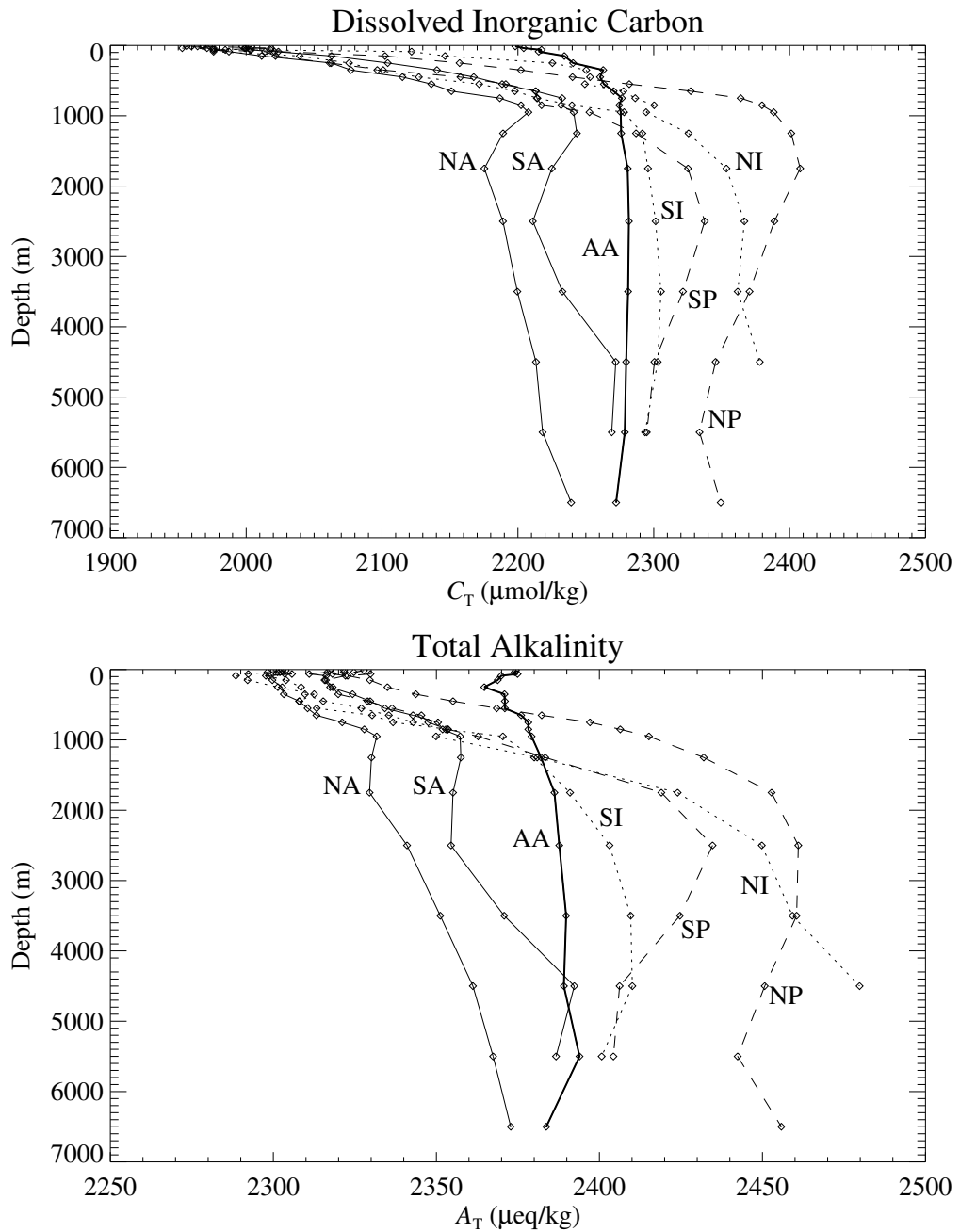
Figure 1.7: Average distributions of C_T and A_T for different water masses. Shown are the North and South Atlantic (NA, SA), the Antarctic (AA), the North and South Indian (NI, SI) and the North and South Pacific (NP, SP) (drawn from data of TAKAHASHI et al., 1981b).

39,600 Pg C for DIC and close to 3.205×10^{18} eq for total alkalinity (GIESKES, 1974; BOLIN et al., 1981; SUNDQUIST, 1985).

For the organic pools, SUNDQUIST (1985) lists estimates of 480–1,100 Pg C (DOC), 6.5–9 Pg C (POC) and 1–5 Pg C (living biomass). OLSON et al. (1985) estimate the DOC stock at 725 Pg C, with an uncertainty range of 600–2,200 Pg C. The most recent figures for DOC, of the order of 700 Pg C (SIEGENTHALER and SARMIENTO, 1993), are at the lower end of this range. According to the latest IPCC report, this value of 700 Pg C should even be considered as an upper limit (SCHIMEL et al., 1996). SUNDQUIST's (1985) estimate for POC on the other hand might be somewhat low. Other authors generally prefer larger values, of up to 60 Pg C (MACKENZIE et al., 1993). For the carbon stocked in living biomass, there is better agreement in the literature. In all of the recent carbon cycle budgets, they account for 3 Pg C (WATSON et al., 1990; SARMIENTO and SIEGENTHALER, 1992; SIEGENTHALER and SARMIENTO, 1993; MACKENZIE et al., 1993; SCHIMEL et al., 1995, 1996), which is well within the range of SUNDQUIST (1985). This range is probably still representative for the uncertainty on this figure. Probable ranges for the different pools are hence 33,600–39,600 Pg C (DIC), 500–700 Pg C (DOC), 10–60 Pg C (POC) and 1–5 Pg C (living biomass). Total alkalinity is estimated at 3.14–3.40×10^{18} eq, applying the same relative uncertainty as for DIC ($\pm 4\%$) to the average of the two values cited above.

Two large-scale gradients can be distinguished for both C_T and A_T in figure 1.7:

- an overall surface-to-deep sea gradient;

- within the deep sea, another one along the pathway of net water transport depicted in the previous section, from the North through the South Atlantic to the Antarctic Circumpolar waters, and from there, continuing through the South to the North Indian ocean on one hand, and through the South to the North Pacific ocean on the other hand.

Both are maintained by the interplay between the large-scale water circulation in the World oceans, biologically mediated fluxes from the surface to the deep waters and the air-sea exchange of CO_2. Carbon and alkalinity taken up by marine organisms at the surface get released to solution at depth during remineralization. Here they get collected all along the pathway of water transport between the deep parts of the ocean basins, leading to the observed gradual enrichment.

Air-Sea Exchange of Carbon Dioxide

Gas transfer between the ocean and the atmosphere is controlled by molecular diffusion across a very thin liquid boundary layer in the surface water, which has a thickness of the order of tens of microns (Watson, 1993). At its top surface, this thin layer is in equilibrium with the overlying atmosphere and at its base, with the underlying seawater. The net ocean-to-atmosphere CO_2 flux F_{net} is related to the concentration gradient of gaseous dissolved CO_2 across the boundary layer through the *transfer velocity K*, defined by (Watson, 1993)

$$F_{net} = K \left([CO_2]_w - [CO_2]_{sat} \right). \tag{1.4}$$

Here, $[CO_2]_w$ is the actual concentration of dissolved gaseous CO_2 in the bulk water below the boundary layer, while $[CO_2]_{sat}$ is the concentration of gaseous dissolved CO_2 to be expected for water in equilibrium with the overlying air. This latter is related to the partial pressure of CO_2, p_{CO_2}, in the atmosphere by Henry's law stating that

$$[CO_{2(aq)}] = K_0 \, p_{CO_2}.$$

Using this law to define p_{CO_2} in seawater, we can rewrite the definition (1.4) in the more usual form

$$F_{net} = K' \left(p_{CO_2(w)} - p_{CO_2(atm)} \right), \tag{1.5}$$

where $K' = K \, K_0$. The gross exchange flux of CO_2 between the atmosphere and the ocean is currently estimated at $9\text{–}18 \text{ mol m}^2 \text{ yr}^{-1}$, for an atmospheric p_{CO_2} of 280 ppm. Methods based upon natural or bomb-produced ^{14}C systematically lead to higher results than other methods ($15\text{–}18 \text{ mol m}^2 \text{ yr}^{-1}$ compared to $9\text{–}11 \text{ mol m}^2 \text{ yr}^{-1}$, following Siegenthaler (1993)). The reasons for this discrepancy still remain unknown, but for global studies, the ^{14}C-based results seem to be preferable (Siegenthaler, 1993; Watson, 1993). Accordingly, $K' = 0.059 \pm 0.005 \text{ mol m}^2 \text{ yr}^{-1} \text{ ppm}^{-1}$, and the pre-industrial gross CO_2 exchange flux must be of the order of 5,900 Tmol C or 71 Pg C per year, with an uncertainty of $\pm 10\%$. With an atmospheric CO_2 content of 350 ppm, this flux can then be estimated at 7,375 Tmol C/yr or 88.5 Pg C/yr. Figure 1.8 shows the seasonal variations of the global distribution of the $p_{CO_2(w)} - p_{CO_2(atm)}$ difference. It can be seen that the equatorial regions represent a net source of CO_2 to the atmosphere throughout the year. Seasonal changes are most pronounced in the north Pacific, where large areas act as a net sink during the Northern Hemisphere winter time, and become a net source during summer time, when the equatorial source belt spreads to the north.
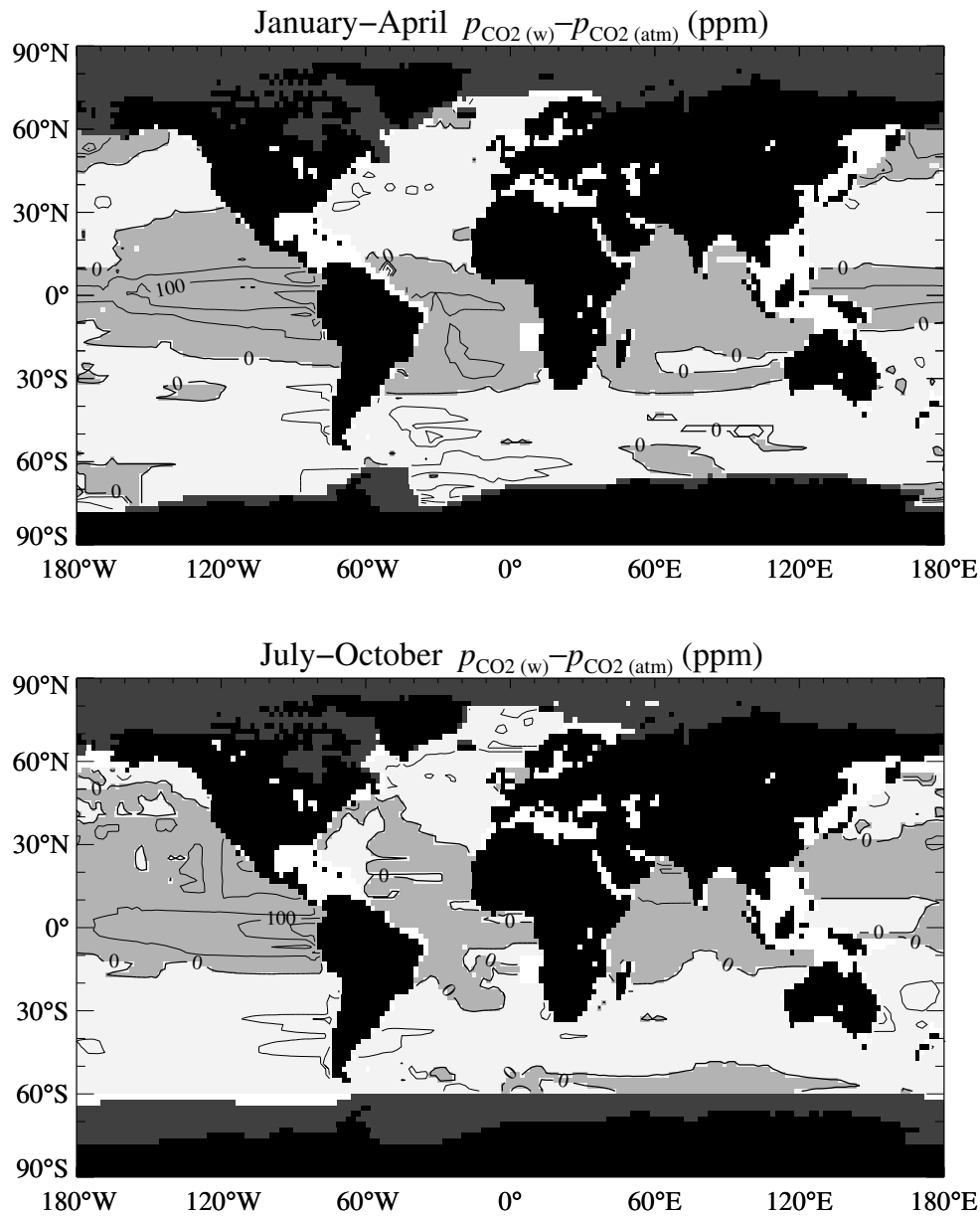
Figure 1.8: Seasonal variation of the difference between surface water and atmospheric p_{CO_2} (TANS et al., 1990). The different grey shades are used to identify the following regions: white – no data; lightest grey – net transfer from the atmosphere to the ocean ($p_{CO_2(w)} < p_{CO_2(atm)}$); medium grey – net transfer from the ocean to the atmosphere ($p_{CO_2(w)} > p_{CO_2(atm)}$); darkest grey – ice-covered; black – land. Data (data set version 5E) courtesy of I. FUNG and T. TAKAHASHI.

Since the air-sea exchange of carbon dioxide is essentially a diffusion process, one must expect that it leads to some fractionation of the carbon isotope ratios. By analogy with (1.4) above, the net flux of $^{13}CO_2$, $^{13}F_{net}$ is given by

$$^{13}F_{net} = {}^{13}K \left([^{13}CO_2]_w - [^{13}CO_2]_{sat} \right). \tag{1.6}$$

SIEGENTHALER and MÜNNICH (1981) have related the $^{13}F_{net}$ from equation (1.6) to the total CO_2 concentrations used in (1.4), and to the carbon isotope ratios actually measured in the two phases (i.e. $^{13}R_{atm}$, that of CO_2 in the atmosphere and $^{13}R_{DIC}$, that of DIC in seawater) by two one-way fractionation factors α_{as} and α_{sa}, writing

$$^{13}F_{net} = K \left(\alpha_{sa}\,{}^{13}R_{DIC}\,[CO_2]_w - \alpha_{as}\,{}^{13}R_{atm}\,[CO_2]_{sat} \right). \tag{1.7}$$

They estimate that $\alpha_{as} = 1 - 0.0018$ to $1 - 0.0023$ and that $\alpha_{sa} = 1 - 0.0097$ to $1 - 0.0107$ at 20°C. For $^{14}C/C$, the two respective fractionation factors are simply the squares of α_{as} and α_{sa}.

Biogenic Carbon Fluxes

The pathways of biogenic carbon cycling in the oceans are schematically represented in figure 1.9, separately for organic (SMITH and HOLLIBAUGH, 1993) and inorganic matter (after SMITH and HOLLIBAUGH, 1993; MILLIMAN and DROXLER, 1996). For the organic part of this figure, the fluvial input of organic matter from land has also been taken into account. With a total amount of 380–450 Tg C/yr, or 31.7–37.5 Tmol C/yr to use the same units as in the figure (MEYBECK, 1982, 1993; LUDWIG et al., 1997), it exceeds the overall net burial rate of 126 ± 63 Tg C/yr (BERNER, 1982), adopted for the figure, by a factor of 3. The recent reevaluation of this burial rate at 160 Tg C/yr by HEDGES and KEIL (1995) does not significantly alter this observation. The isotopic and chemical compositions of organic matter in marine sediments (and even generally that of organic materials in seawater) furthermore indicate that most of the buried organic matter has an oceanic rather than a continental origin (JØRGENSEN, 1983; HEDGES and KEIL, 1995). River-borne organic material entering the oceans hence undergoes intense degradation there, together with organic carbon from marine primary productivity, and it represents a major participant in the ocean's organic carbon balance.

For inorganic carbon, the situation is somewhat different. The bulk of the fluvial particulate carbonate load, which represents an annual input of 170 Tg C or 14 Tmol C (MEYBECK, 1993), gets deposited and buried in deltas, estuaries and on the continental shelves. It does not reach great
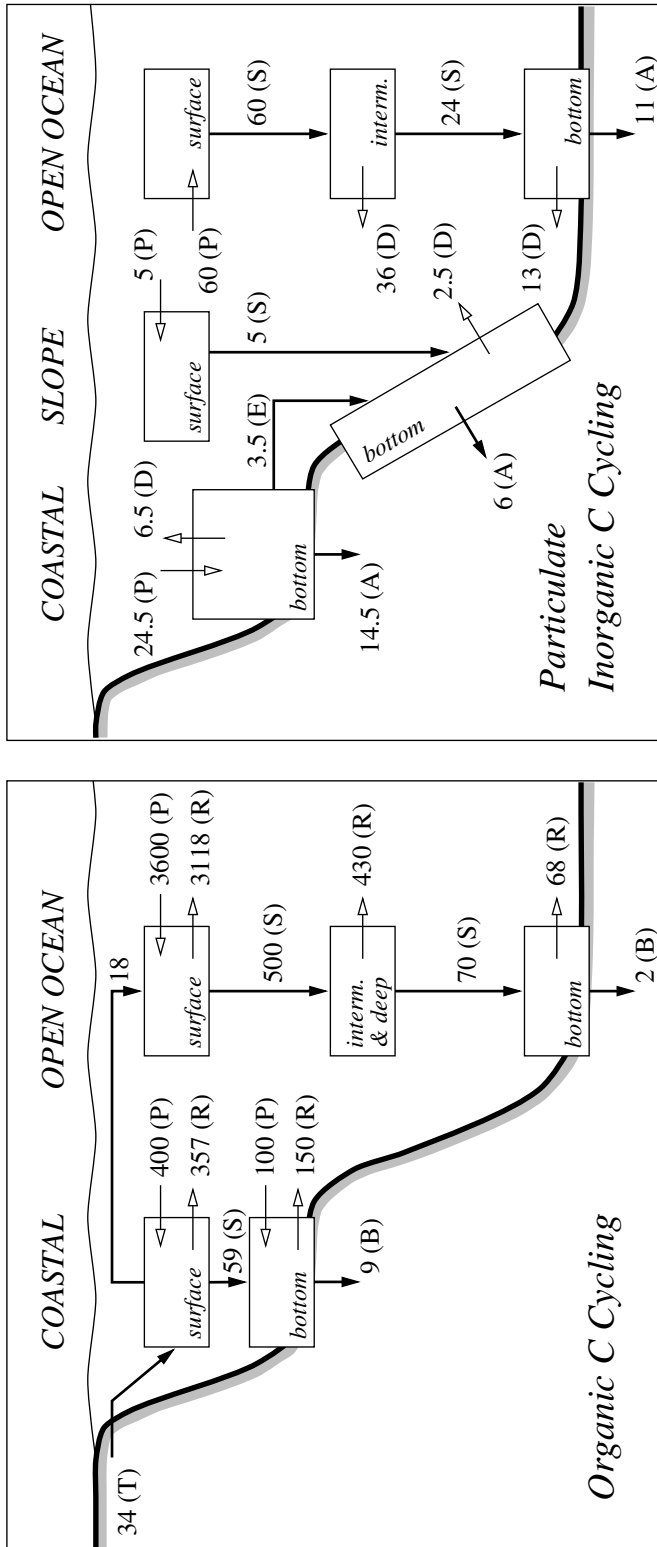
Figure 1.9: "Best Estimates" for the present-day cycling of organic carbon (DOC and POC) and of carbonate particles in the ocean (Smith and Hollibaugh, 1993; Milliman and Droxler, 1996). Thick black-headed arrows represent fluxes of organic and of carbonate material; thin open-headed arrows represent exchange fluxes with the oceanic DIC pool. The budget of this latter has not been equilibrated. The uppercase letters denote the relevant processes: (A) – Accumulation of $CaCO_3$ in the sediments; (B) – Burial of organic carbon in the sediments; (D) – Dissolution of $CaCO_3$; (E) – Export of $CaCO_3$; (P) – Production of organic matter and of $CaCO_3$; (R) – Respiration/Remineralization of organic carbon; (S) – Sedimentation/Settling; (T) – Terrigeneous input of organic carbon by rivers. All fluxes are in 10^{12} mol C/yr.

enough water depths where conditions for dissolution are given (MILLIMAN, 1993). As a consequence, its influence on the global oceanic carbonate budget is negligible. This is of course only true as long as the shelves are flooded. During the low sea stands typical of glacial periods, it can be expected that up to 90% of the riverine suspended load gets transferred to the deep sea (HAY and SOUTHAM, 1977).

The budget of dissolved inorganic carbon in the oceans has deliberately not been balanced in figure 1.9. It will be discussed in a later section of this chapter.

Organic Matter Production and Remineralization. In the euphotic zone, which is restricted to the uppermost 100–200 m, sunlit layers of the ocean, organic matter is produced by phytoplankton during photosynthesis, taking up dissolved CO_2 and inorganic nutrients (essentially phosphate and nitrate), and releasing oxygen. This process can be described by the following idealized chemical equation, called *RKR-equation* (REDFIELD, KETCHUM, and RICHARDS, 1963):

$$106\,CO_2 + 16\,NO_3^- + H_2PO_4^- + 17\,H_3O^+ + 105\,H_2O$$
$$\longrightarrow (CH_2O)_{106}(NH_3)_{16}(H_3PO_4) + 138\,O_2 \qquad (1.8)$$
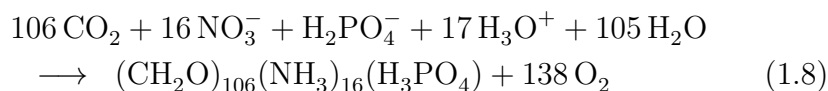
The characteristic $C:N:P:O_2$ ratios of $106:16:1:-138$ in this equation are known as *Redfield ratios*. Their exact values are still subject to debate. TAKAHASHI et al. (1985) find slightly different values of $122(\pm18):16:1:-172$. SHAFFER (1993, 1996) has shown that the high C:P ratio around 122:1 suggested by TAKAHASHI et al. (1985) is inconsistent with ocean chemistry, in contrast to the classical one of 106:1. This latter is of course still within the range of uncertainty indicated by TAKAHASHI et al. (1985), but it ranges nevertheless at the very lower end. SHAFFER furthermore finds that P and N are returned to solution at shallower depths than C. This in turn is contradicted by the study of ANDERSON and SARMIENTO (1994) who find that the nutrient regeneration proceeds with $C:N:P:O_2$ ratios approximatively constant with depth and basins between 400 and 4,000 m of depth. With ratios of $117(\pm14):16(\pm1):1:-170(\pm10)$, they furthermore confirm the results of TAKAHASHI et al. (1985).

The most recent evaluations for the overall marine primary productivity that we have found in the literature are in the range of 36.5–50 Pg C/yr (NELSON et al., 1995; ANTOINE et al., 1996). NELSON et al. (1995) give a maximum upper limit of 60 Pg C/yr. This is in good agreement with the total organic production of 4,100 Tmol C/yr or 49.2 Pg C/yr from figure 1.9, obtained by SMITH and HOLLIBAUGH (1993), who indicate relative

uncertainties of about $\pm 25\%$ for their production rates and of $\pm 50\%$ for their production−respiration differences. Most of the primary production gets recycled within the euphotic zone, and only of the order of 10–20% get exported out of the euphotic layer, either as DOC with the oceanic circulation or as POC in sinking particles (EPPLEY and PETERSON, 1979; SUESS, 1980; BERGER and WEFER, 1990; SMITH and HOLLIBAUGH, 1993). The DOC:POC ratio of this export flux is only poorly known. SIEGENTHALER and SARMIENTO (1993) fix it at 6:4, which is also used by SCHIMEL et al. (1996).

In the intermediate and deep waters below, the exported matter gets rapidly oxidized through microbial activity and by the organic metabolism of bathypelagic fauna. In the open ocean, about 80% of the exported POC gets remineralized or decomposes to DOC (and gets oxidized on longer time scales) before reaching a depth of 1,000 m (SUESS, 1980; BERGER and WEFER, 1990). This intense recycling within the water column is also reflected in the distributions of nutrients (e.g., phosphate) and of dissolved oxygen (figure 1.10). During remineralization in the water column, oxygen is taken up, while the carbon and the nutrients fixed in the course of photosynthesis are released to their dissolved inorganic form at depth from where they may return to the euphotic layer through upwelling and diffusion. As a consequence, only a very small fraction of the exported POC reaches the sediments at the sea-floor where oxidation continues at a significant rate. According to JAHNKE (1996), 72 Tmol C/yr (or 0.86 Pg C/yr) in POC fall below a depth of 1,000 m, 45% of which reaches the sea-floor where it gets almost entirely remineralized. In the water column, for remineralization, the direction of the equation (1.8) is reversed; O_2 is consumed. At the sea-floor, where oxygen may become depleted, remineralization of freshly deposited organic material may follow different pathways, involving sulphate and nitrate instead of oxygen (see, e.g., BERNER (1980) or JØRGENSEN (1983) for details). This is especially true for the coastal regions where large amounts of organic matter reach the sea-floor. There, up to 50% of organic matter degradation is due to sulphate reduction (JØRGENSEN, 1983).

Carbonate Production, Dissolution and Preservation. Besides organic matter, marine organisms also produce carbonate material for their skeletons and shells. Most of this is calcium carbonate as calcite (coccolithophorids and foraminifera) and aragonite (pteropods). Additionally there is also some precipitation of magnesian calcite: the average abundances of $MgCO_3$ are 5 mole-% in the shelf and 0.5 mole-% in deep-sea carbonates (MORSE and MACKENZIE, 1990).
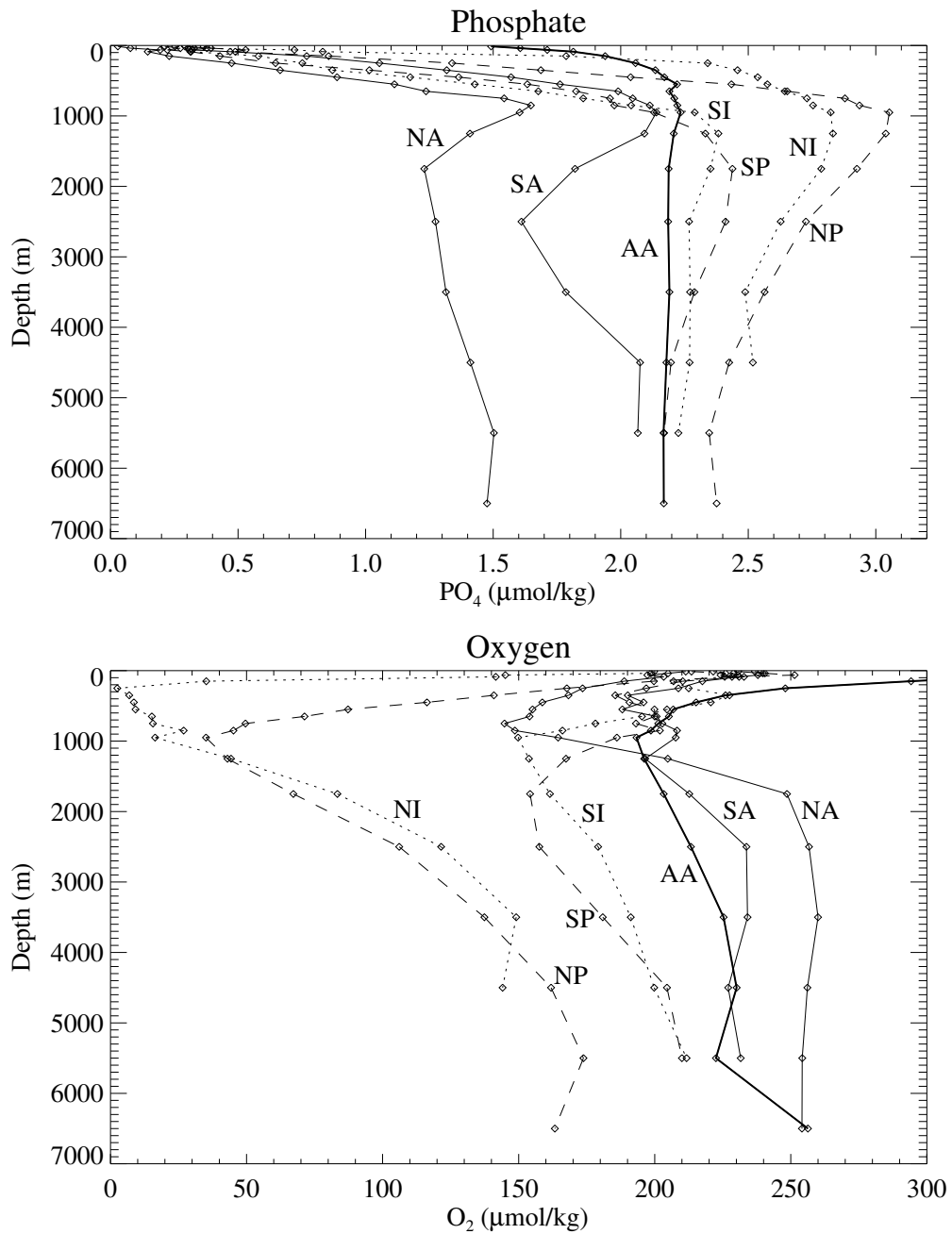
Phosphate

Oxygen

Figure 1.10: Average distributions of phosphate and dissolved oxygen for different water masses. Shown are the North and South Atlantic (NA, SA), the Antarctic (AA), the North and South Indian (NI, SI) and the North and South Pacific (NP, SP) (drawn from data of TAKAHASHI et al., 1981b).

The CaCO$_3$-C/Organic-C ratio, called *rain ratio*, is not uniform throughout the oceans. In high-productivity areas, diatoms, which produce opaline shells, tend to dominate carbonate-walled organisms, thus leading to reduced rain ratios. Estimates for the global average CaCO$_3$-C/Organic-C ratio are commonly within 1:3.5–7.5 (SHAFFER, 1993).

Upon death, the hard remains of these organisms sink out of the euphotic zone, together with the organic export production. While the fate of organic export production largely depends on microbial activity in the water column, that of carbonate depends on the saturation state of seawater with respect to carbonate minerals. The *degree of saturation* of seawater with respect to calcite (Ω_{Calc}) and that with respect to aragonite (Ω_{Arag}) are defined by

$$\Omega_{\text{Calc}} = \frac{[\text{Ca}^{2+}]\,[\text{CO}_3^{2-}]}{K_{\text{Calc}}} \quad \text{and} \quad \Omega_{\text{Arag}} = \frac{[\text{Ca}^{2+}]\,[\text{CO}_3^{2-}]}{K_{\text{Arag}}}$$

respectively, where K_{Calc} and K_{Arag} are the solubility products of calcite and aragonite in seawater. *Aragonite* and *Calcite Saturation Depths* (ASD and CSD) are defined as the depths where the respective degree of saturation equals unity. Such a depth, sometimes also called *horizon*, is not necessarily defined everywhere (see, e.g., the case of ASD in the North Pacific in figure 1.11). Waters where $\Omega_{\text{Calc}} < 1$ are undersaturated with respect to calcite, those where $\Omega_{\text{Calc}} > 1$ are supersaturated (*idem* for Ω_{Arag} and aragonite). In the oceans, the concentration of Ca^{2+} is only very weakly affected by the precipitation and dissolution of of carbonate minerals, and it can be considered as quasi-conservative (deviations from strict conservation are less than 0.5%). Variations of Ω_{Calc} and Ω_{Arag} are thus related to deviations of [CO$_3^{2-}$] from the respective carbonate ion concentrations at saturation defined by

$$[\text{CO}_3^{2-}]_{\text{Calc sat}} = \frac{K_{\text{Calc}}}{[\text{Ca}^{2+}]} \quad \text{and} \quad [\text{CO}_3^{2-}]_{\text{Arag sat}} = \frac{K_{\text{Arag}}}{[\text{Ca}^{2+}]}$$

The top panel of figure 1.11 shows the distributions of [CO$_3^{2-}$] throughout the oceans that we have calculated from the C_{T} and A_{T} distributions of figure 1.7, using the thermodynamic constants presented and discussed in section 2.3 of the next chapter. The profiles of [CO$_3^{2-}$]$_{\text{Arag sat}}$ and [CO$_3^{2-}$]$_{\text{Calc sat}}$ have been added for comparison. The bottom panel of the figure shows the degree of saturation with respect to calcite and aragonite throughout the oceans. For Ω_{Arag}, the indicated scale is only approximate, based upon the assumption that $\Omega_{\text{Calc}}/\Omega_{\text{Arag}} = 1.52$. In fact, this ratio increases from 1.46 at the surface to 1.59 at 7,000 m depth, according to the thermodynamic constants used.

Solubilities of both aragonite and calcite increase with depth: surface waters are supersaturated with respect to these minerals, the deeper parts

Carbonate Ion Concentration and Saturation Levels
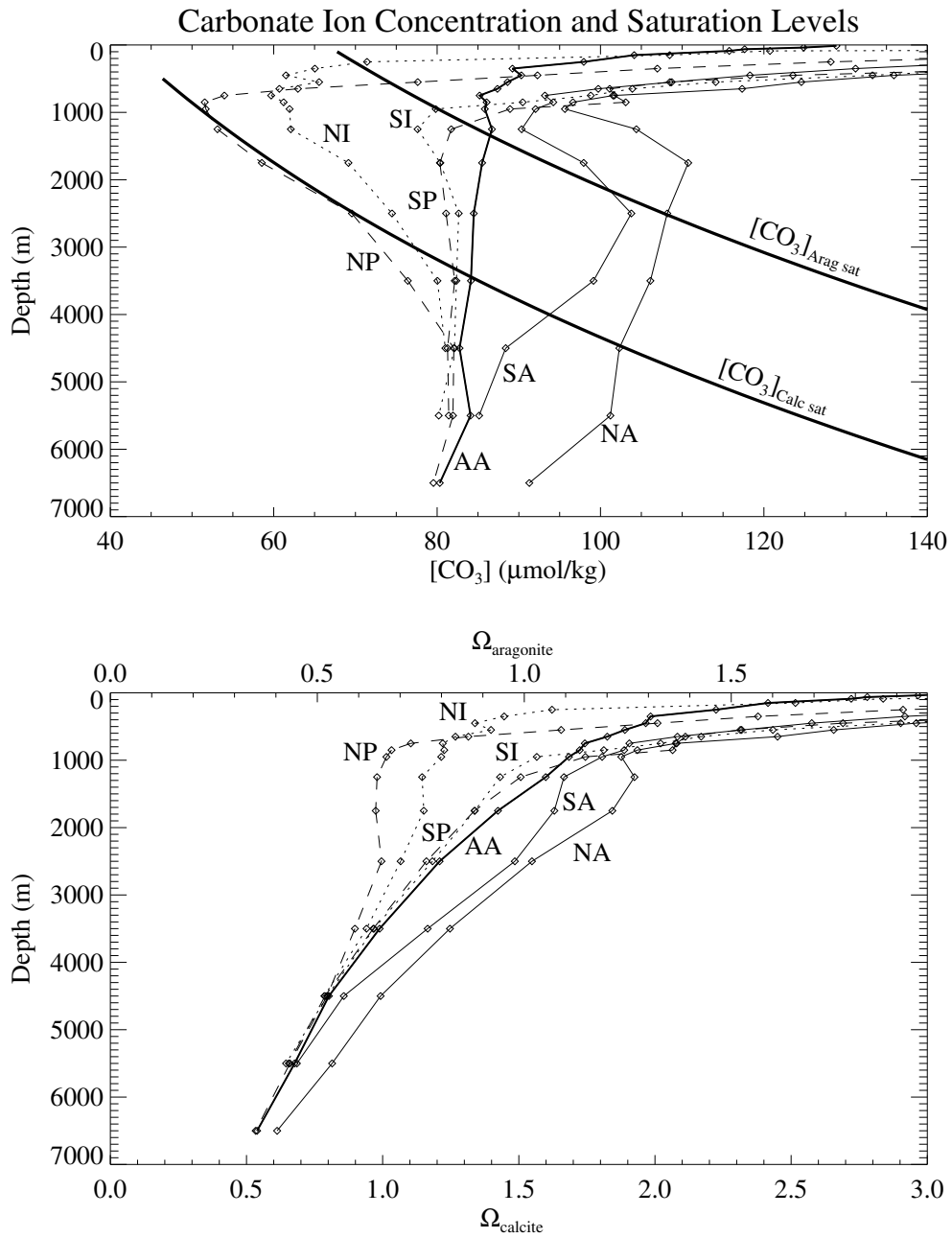
Figure 1.11: Average distributions of carbonate ion concentrations and of saturation degrees with respect to calcite and aragonite (assuming here that $\Omega_{Calc}/\Omega_{Arag} \equiv 1.52$ — see text) for different water masses. Also shown are the profiles of carbonate ion concentrations at saturation with respect to calcite and aragonite. Calculated by the author from data of figure 1.7. The identification of the water masses is the same as in the previous figures.

of the oceans are undersaturated. When settling down the water-column, the inorganic detritus will dissolve as they reach undersaturated waters, first aragonite, then calcite. Different characteristic depth horizons can be identified in the sediments.

- *Lysocline.* At this depth, dissolution effects on carbonate shells are first seen in the sediments. Different lysoclines can be defined, depending on whether particular microfossils are used as indicators (e.g., pteropod lysocline, foraminiferal lysocline, . . .), or particular minerals (aragonite lysocline, calcite lysocline). In this study, we will deal only with the latter two, which have been linked to the ASD and the CSD respectively (BROECKER and TAKAHASHI, 1978).

- *Compensation Depth.* This is the depth where sedimentation and dissolution fluxes balance each other. We again distinguish *Aragonite* and *Calcite Compensation Depths*, ACD and CCD. The CCD is often identified with the depth where the fraction of $CaCO_3$ in the surface sediment has fallen to a given threshold value, typically 0–20%, depending on the authors (BROECKER and PENG, 1982; MORSE and MACKENZIE, 1990). Such identifications are however somewhat problematic on time scales as short as those of the glacial-interglacial climate variations, where the inherent steady state assumption of the oceanic carbon and alkalinity cycles is most probably not justified.

Figure 1.12 shows how the $CaCO_3$ content in the surface sediments at the seafloor decreases with increasing water depth, for different regions of the ocean. This figure illustrates that the transition from carbonate-rich and carbonate-poor sediments takes several hundred meters to more than a kilometer. The primary control of the thickness of this transition zone appears to be of the dissolution kinetics of carbonate material.

As MORSE and MACKENZIE (1990) emphasize, carbonate dissolution in sediments can only be detected once it has proceeded to a large extent. As a consequence, the relationship between lysocline depth and saturation state is not as direct as the results of BROECKER and TAKAHASHI (1978) might suggest. A non negligible part of carbonate dissolution has been shown to take place above the lysocline and even above the saturation depths, due to the presence of respiration-derived CO_2 in the sediment that can neutralize CO_3^{2-} in the pore water. Pore water eventually becomes undersaturated and carbonate material may dissolve, even if the overlying water is supersaturated (ARCHER, 1996, and references therein).

The production-dissolution/accumulation patterns of the marine $CaCO_3$ cycle have recently been reviewed and discussed in a series of papers (MIL-
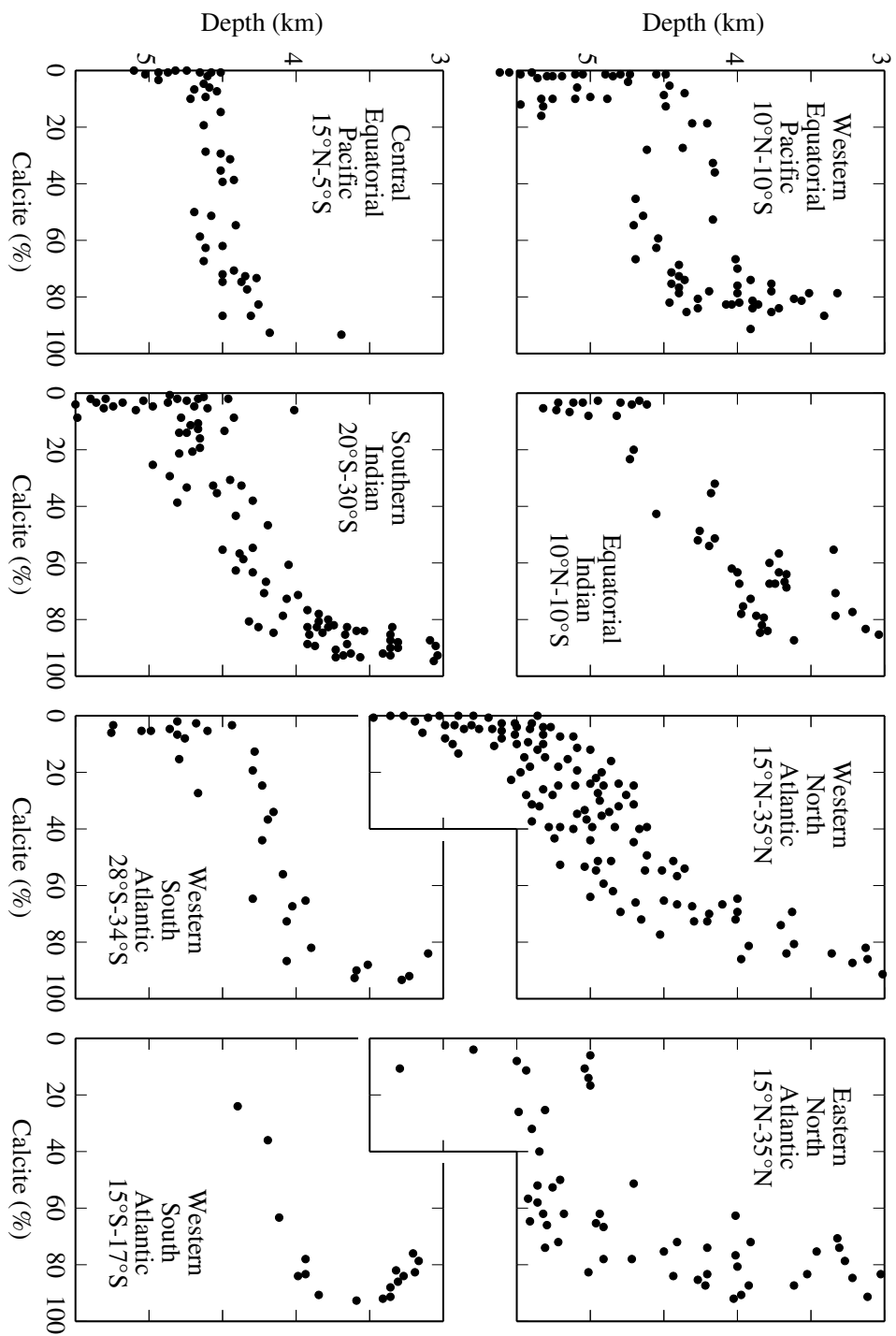
Figure 1.12: Fraction of CaCO₃ in the surface sediments as a function of water depth for various ocean regions. (BROECKER and PENG, 1982).

Table 1.1: Estimates (and quality indices) for present-day carbonate production and accumulation rates (excerpt from a table by MILLIMAN and DROXLER, 1996).

Habitat	CaCO$_3$ Production (10^{12} mol/yr)		CaCO$_3$ Accumulation (10^{12} mol/yr)	
Neritic environments				
Coral reef complex	9	(G)	7	(G)
Banks/bays	4	(F)	2	(F)
Non carbonate shelves	4 ?	(P)	1	(G)
Carbonate shelves	6 ?	(P)	3 ?	(P)
Halimeda bioherms	1.5 ?	(P)	1.5 ?	(P)
Slopes				
Production	5	(F)	4	(F)
Imported	3.5	(F)	2	(F)
Deep Sea				
Surface Production	60 ?	(F)		
Flux at 1000 m	24	(F)	11	(G)
Total	$\gg$ 57		32	(?)

Uppercase letters are indices for the accuracy of the estimates: (G) – good, probably better than a factor 0.5; (F) – fair, probably better than a factor 1; (P) – poor, possibly worse than a factor 1.

LIMAN, 1993; WOLLAST, 1994; ARCHER, 1996; MILLIMAN and DROXLER, 1996). The inorganic part of figure 1.9 represents a summary of the results of MILLIMAN and DROXLER (1996). Here, uncertainties on the flux rates are even larger than for the organic fluxes. According to MILLIMAN (1993), they are of 20–50% at least. This pessimism is still shared by the recent update of MILLIMAN's work by MILLIMAN and DROXLER (1996). They think that, except for the production and accumulation by coral reefs as well as for the accumulation on non-carbonate shelves and in the deep-sea sediments, uncertainties are larger than 50% (see table 1.1).

Similar uncertainties affect the knowledge of water column dissolution. Figure 1.9 suggests that 60% of the carbonate raining down to the deep sea in the open ocean dissolves within the water column. According to ARCHER (1996), this fraction is currently not constrained to any better than 5–65%. A large part of the uncertainty related to this fraction is due to the poorly known fraction of the more soluble aragonite in the carbonate rain. BETZER et al. (1984) have shown that about 90% of the aragonite is dissolved within

the upper 2.2 km of the water column during sinking. Published estimates for the average fraction of aragonite in the carbonate rain are 10–50% (BERNER, 1977; BERNER and HONJO, 1981; FABRY, 1989), but we cannot exclude the possibility that it is larger than 50%. BETZER et al. (1984) measured an average pteropod:foraminifera ratio of 5:1 in the carbonate settling down to the deep sea along a transect in the North Pacific. When the calculations of BERNER (1977) are repeated with this ratio of 5:1, instead of his 1:1, we find that 75% of the carbonate sinks from the surface ocean as aragonite.

Figure 1.9 also makes the fundamental differences between the two pathways of biologically controlled carbon fluxes obvious. Although organic carbon production is about 50 times larger than carbonate production, the latter dominates the carbon input to the sea-floor sediments. The preservation efficiency is indeed more than 100 times higher for carbonate than for organic carbon. For both organic and inorganic carbon cycling, the coastal region plays a relatively important role. From the flux magnitudes given in the figure, we calculate that it accounts for 12% of the global primary organic matter production, and for 81% of its preservation. For carbonate, the figures are less contrasted: 28% of the total carbonate production and 45% of the overall preservation take place in the shallow water regions.

The vertical distribution of alkalinity in the oceans is dominated by carbonate production-dissolution cycle. For DIC, both organic and inorganic cycling work together. The influence of organic matter production on the alkalinity distribution is much smaller, although non negligible. Due to the uptake of nitrate and phosphate, it can be calculated from the RKR-equation that surface water alkalinity increases by $17/106 = 0.16$ eq for each mole of carbon that gets exported from the surface ocean as organic matter (assuming classical C:N:P Redfield ratios of 106:16:1). For each mole of carbon that gets exported as carbonate, alkalinity decreases by 2 eq. Assuming a global average Organic-C:CaCO$_3$-C ratio of 5:1, we may calculate that biological activity leads to a net decrease of C_T and A_T in surface waters in a ratio of about 5:1 too. The net effect of this is a drawdown of surface water p_{CO_2}, the p_{CO_2}-increasing effect from the alkalinity drawdown being largely outpaced by the p_{CO_2}-decreasing effect from the drawdown of dissolved inorganic carbon.

Carbon-13 in the Ocean

Earlier in this chapter, we have already seen that the distribution of ^{14}C in the oceans represents a major constraint on the global circulation pattern. To be complete, we still have to say a few words on ^{13}C in the marine environment. The distribution of δ^{13}C is strongly influenced by the cycling of organic

matter. Just as in the terrestrial environment, ^{13}C is discriminated against ^{12}C during photosynthesis. According to TANS et al. (1993), the $\delta\,^{13}C$ of marine organic matter is on average about $20\,^0\!/_{00}$ lower than that of the bulk dissolved inorganic carbon from which it has been produced. The results of SMITH and KROOPNICK (1981) and KROOPNICK (1985) indicate similar global average values for this fractionation of 18.6 and $21.6\,^0\!/_{00}$ respectively. As a consequence of the surface production/deep-sea remineralization cycle, $\delta\,^{13}C$ values are lower at depth than at the surface. Profiles of $\delta\,^{13}C$ in the ocean actually mirror those of phosphate. Based upon analyses of water samples from the GEOSECS expeditions, KROOPNICK (1985) has established that there is a well pronounced negative correlation between the $\delta\,^{13}C$ of DIC and the concentration of phosphate in the present-day ocean:

$$\delta\,^{13}C = (1.92 \pm 0.01) - (0.70 \pm 0.008) \times [PO_4], \quad R^2 = 0.79 \qquad (1.9)$$

where the phosphate concentration $[PO_4]$ is expressed in μmol/kg-SW. If only deep-sea water samples are taken into account for this linear regression, an intercept of 1.89 and a slope of -0.71 are obtained, while R^2 improves to 0.88. $\delta\,^{13}C$ hence exhibits gradients opposite to those of phosphate between the surface and the deep sea, and also along the Atlantic-Antarctic-Pacific pathway of the deep thermohaline circulation. Warm surface waters typically have $\delta\,^{13}C$ values around $1.5\,^0\!/_{00}$ (KROOPNICK, 1985). For the deep Atlantic, Antarctic and Pacific Oceans, the above relationship yields values of 0.75, 0.40 and $0.15\,^0\!/_{00}$ respectively.

The Oceanic Carbon Budget

So far, we have mostly dealt with carbon *sinks* in the ocean: at present, 9 Tmol leave it in organic and 32 Tmol in inorganic particles each year. The 25 Tmol C/yr difference between the terrigeneous input (34 Tmol C/yr — see figure 1.9) and the burial of organic carbon gets remineralized within the ocean and returns to the atmosphere as CO_2. This is ultimately also where it comes from: riverine organic matter is in fact generally too young to have a fossil origin and it hence must come from terrestrial vegetation, most of it probably from soils (LUDWIG, 1996).

In addition to the 34 Tmol of organic carbon (dissolved + particulate), and the 14 Tmol in particulate inorganic matter mentioned in the previous section, rivers also carry each year 32 Tmol of dissolved inorganic carbon as bicarbonate to the oceans (MEYBECK, 1979). The uncertainty on this flux is difficult to estimate. It should be mentioned that if a global water discharge of 45,000 km^3/yr (KORZOUN et al., 1977) is used instead of 37,400 km^3/yr (MEYBECK, 1979), it would increase to 38.5 Tmol/yr. This

flux is the main driving force for the average positioning of the CCD (and ACD) since it represents the major source of alkalinity to the oceans. It is estimated that about two thirds of the riverine bicarbonate flux stem from the soil CO_2 (MEYBECK, 1987; BERNER and BERNER, 1987). This CO_2, which ultimately comes from the atmosphere, is released in the soils by oxidation of organic matter. Upon dissolution in the soil water, it actively participates in the dissolution of rock minerals. Carbonate minerals provide the remaining third of riverine bicarbonate. $\delta^{13}C$ of this supply hence results from the mixing of CO_2 with a $\delta^{13}C$ value close to that of terrestrial organic matter ($-25\,^0\!/_{00}$) and of carbonate rock carbon. DERRY and FRANCE-LANORD (1996) estimate that this latter source has a typical $\delta^{13}C$ of $(1.8 \pm 0.2)\,^0\!/_{00}$.

We also have to take into account exchange fluxes at the sea-floor. Mantle degassing at the mid-ocean ridges represents a first source of CO_2 there. This flux is currently estimated at 1–8 Tmol C/yr by DES MARAIS (1985). The large range of uncertainty evidences the difficulty of the assessment of this flux. A similar, if not larger uncertainty affects the carbon consumption by sea-floor weathering. GODDÉRIS (1997) estimates that it represents a sink of 1.5 Tmol C/yr, but he also points out that there is almost no constraint on this figure.

The last process to consider in the oceanic carbon budget is the exchange of CO_2 with the atmosphere. Its net effect is impossible to calculate since it results from the difference between two gross fluxes of the order of 5,900 Tmol C/yr (value estimated for pre-industrial time).

1.3.3   Related Elements: Ca, Mg, P

As seen before, the dynamics of the carbon cycle in the ocean is closely related to the cycling of other elements, such as Ca, Mg, N and P. Of these, P is the most important for our study. Production of organic carbon is currently not limited by carbon availability, but rather by nutrient availability. We have chosen phosphate as the key nutrient because its geochemistry in the oceans is less complex than that of nitrogen. For global scale studies such as ours, this choice is also justified by the well-pronounced correlation between their overall distributions in the oceans (BROECKER and PENG, 1982).

Compared to phosphorus, calcium and magnesium play only secondary roles on time scales of hundreds of thousands of years, although their link with inorganic carbon fluxes is quantitatively much better constrained. With residence times of the order of 10^6 yr for Ca and of 10^7 yr for Mg (BROECKER and PENG, 1982; BERNER and BERNER, 1987), even large variations of their sources and sinks will only have a minor influence on their concentration in seawater: doubling the input of an element for a period equivalent to 10% of

its residence time will only lead to a 10% increase of its concentration, if the output stays constant.

1.4 Lithosphere

The lithosphere is by far the largest of the four carbon reservoirs under consideration. AMIOTTE SUCHET (1995) has calculated that the Earth's crust contains 120×10^{21} g C as inorganic and 23×10^{21} g C as organic carbon, with an uncertainty of $\pm 20\%$. Far more than half of both seems to be stocked in continental sedimentary rocks and in marine sediments: 80.4×10^{21} g C of the inorganic and 14.7×10^{21} g C of the organic. The rest is locked up in igneous and metamorphic rocks. These figures for the sedimentary rocks compare well with those of other authors, although their estimates for the inorganic carbon tend to be somewhat lower than AMIOTTE SUCHET's range. According to OLSON et al. (1985), sedimentary rocks contain 62.2×10^{21} g of inorganic and 10.3–15.6×10^{21} g of organic carbon.

For the mantle reservoir, which exchanges some carbon with the oceans through mid-ocean ridge degassing, there are only very few estimates. JAVOY et al. (1982) estimate its carbon content at $4,000 \times 10^{21}$ g C. This is also the value adopted by AMIOTTE SUCHET (1995).

We have already mentioned that mantle degassing at mid-ocean ridges is currently estimated to supply between 1–8 Tmol C/yr (DES MARAIS, 1985). To this, we must add an emission of nearly 1.5 ± 1.0 Tmol C/yr by subaerial volcanic activity (WILLIAMS et al., 1992).

The carbon fluxes out of and into the lithospheric reservoir are orders of magnitude lower than those between the three other reservoirs. They are nevertheless of primary importance because they set the background level around which the other carbon reservoirs may fluctuate.

1.5 Glacial-Interglacial Variations of the Carbon Cycle

About 18–21 kyr ago, the Earth was at the Last Glacial Maximum (LGM), the peak of the latest of a number of glaciations that took place over the past million years, alternating with much shorter warm periods (interglacials) at intervals of about 100 kyr. The Earth's surface conditions at LGM were considerably different from today's. Huge ice-sheets, possibly up to several kilometers thick, covered large parts of the Northern Hemisphere continents (CLIMAP PROJECT MEMBERS, 1981). As a consequence, sea level

stood 120–130 m lower than now (CHAPPELL and SHACKLETON, 1986; FAIR-BANKS, 1989). Sea surface temperatures were nevertheless on average only about 2°C lower than today, with little or no change in the tropics (CLIMAP PROJECT MEMBERS, 1981). There is a wealth of data available in records both from the continents and in the oceans. Even a summary description of the observed changes between that glacial period and the present interglacial would go beyond the scope of this study. For a comprehensive review on these changes, we refer to the work of CROWLEY and NORTH (1991), who spend more than 100 pages on the Quaternary climates. Here, we will only focus on a few selected topics, directly related to the carbon cycle. These include the CO_2 variations documented by the ice-core records, fluctuations of the carbonate content of deep-sea sediments and pH reconstructions in the oceans.

1.5.1   Ice-Core Records

As for the pre-industrial times, the analyses of air trapped in the ice from ice-cores are the most reliable source of information on the evolution of the atmospheric CO_2 content over the glacial-interglacial cycles. The Vostok ice-core provided the first record of the atmospheric CO_2 content over a whole glacial-interglacial climate oscillation (BARNOLA et al., 1987). It was already known from previous ice-core studies that CO_2 was 25–30% less abundant in the LGM than in the Holocene atmosphere (DELMAS et al., 1980; NEFTEL et al., 1982). The Vostok CO_2 record was nevertheless the first to unveil the close relationship between atmospheric CO_2 levels and climate, indicated by the correlation to the temperature evolution reconstructed from the deuterium profile along the same core (JOUZEL et al., 1987). These observations have not been altered by the later extension of the records back to 240 kyr BP (JOUZEL et al., 1993). Both records are represented in figure 1.13 together with that of CH_4 (CHAPPELLAZ et al., 1990). Atmospheric CO_2 oscillates between extreme levels of 290 ppmv (full interglacials) and 190 ppmv (glacials).

1.5.2   Carbonate Content in Deep-Sea Sediments

Carbonate cycles in the Pleistocene record from the equatorial Pacific were first described by Arrhenius in 1952 (see, e.g., ARRHENIUS, 1988), even before EMILIANI (1955) published his pioneering work on oxygen isotopes. The reconstruction of the carbonate content of sediments from the equatorial Pacific between 4,000 and 5,000 m depth for the last 800 kyr by FARRELL and PRELL (1989) evidences that the locus of the 80% $CaCO_3$ content level has undergone cyclic shifts of the order of 600 m (see figure 1.14). This indi-
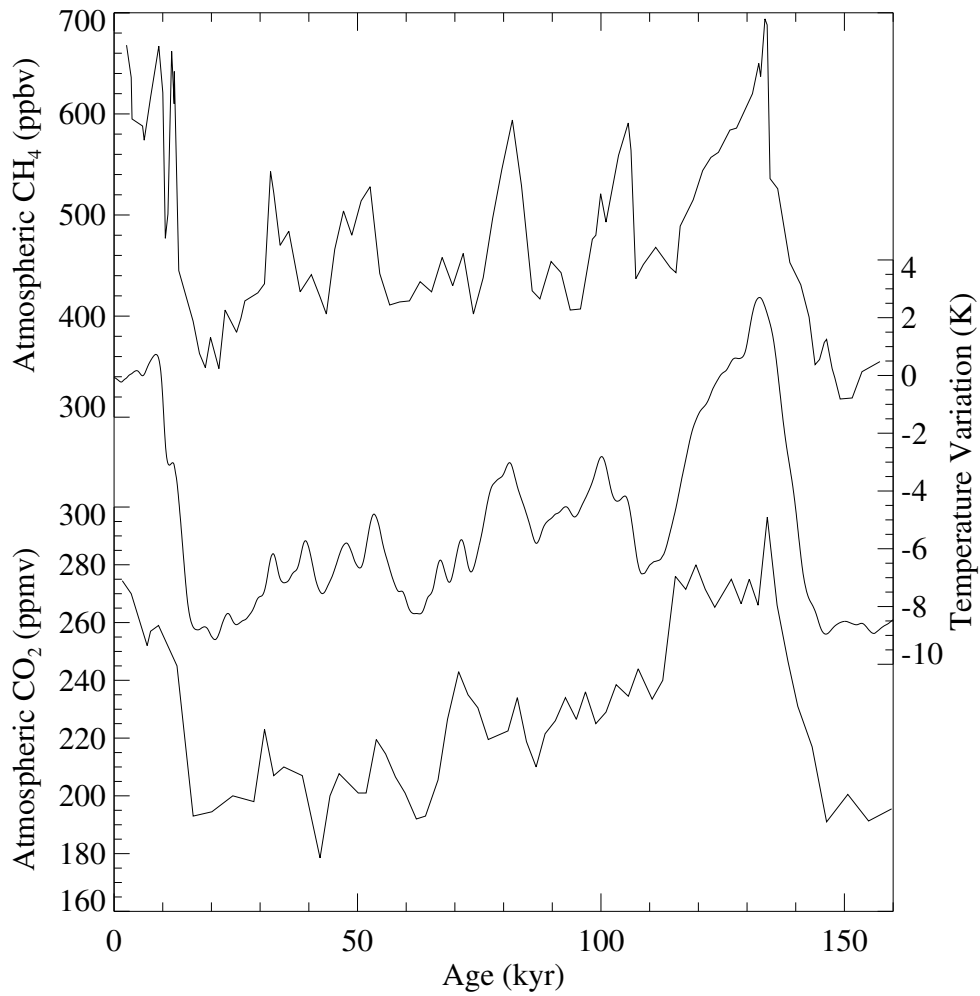
Figure 1.13: Vostok ice-core records of CH_4 (top – Chappellaz et al., 1990), temperature (middle – Jouzel et al., 1987) and CO_2 (bottom – Barnola et al., 1987) for the past 160,000 years.
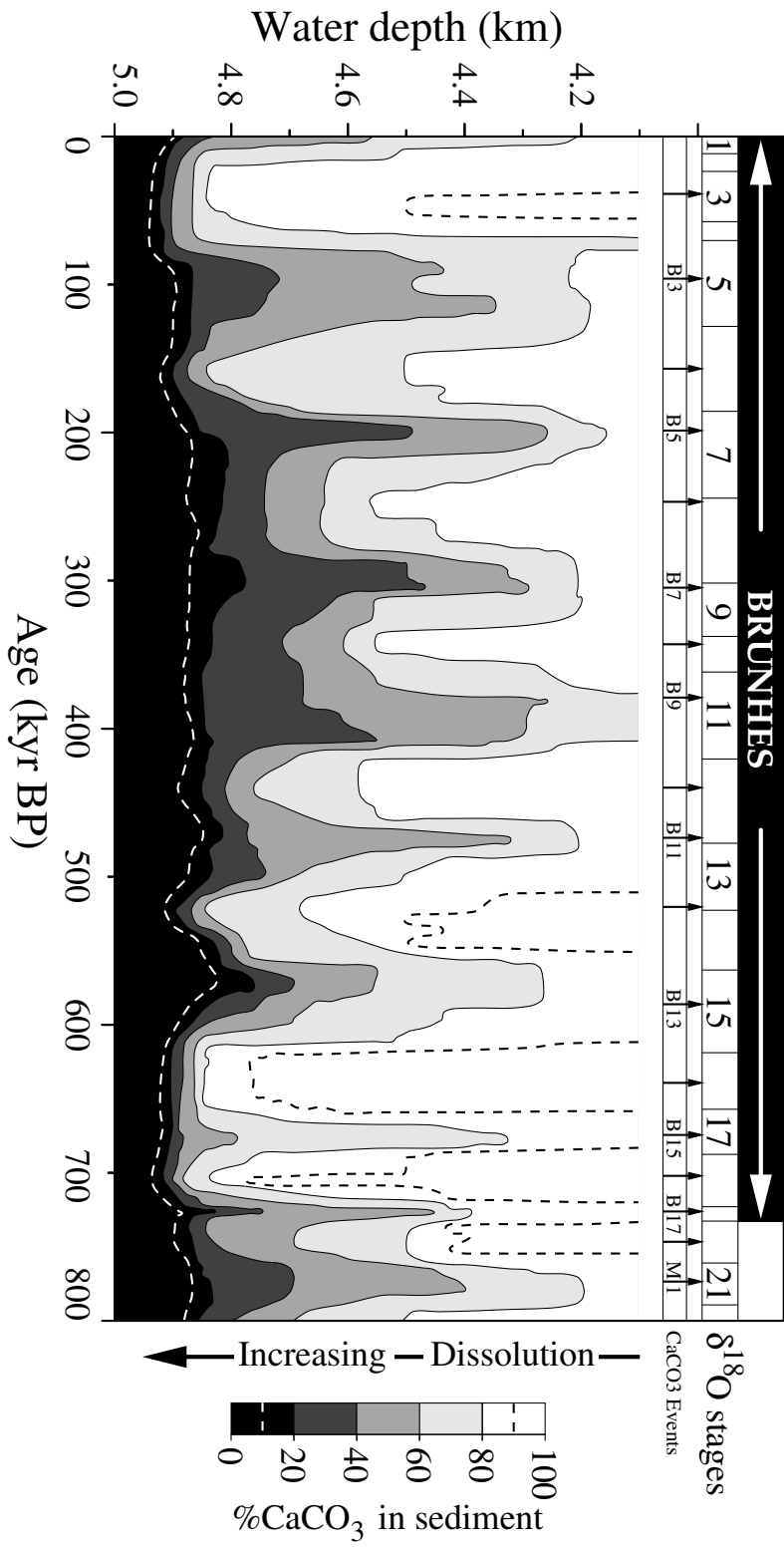
Figure 1.14: Variations of the CaCO₃ content in sediments in the equatorial Pacific, as a function of water depth, for the past 800,000 years (FARRELL and PRELL, 1989).

cates a deepening of the calcite saturation horizon by a similar amount, and thus an increase of the deep-sea CO_3^{2-} concentrations during glacials, compared to interglacials. The less pronounced fluctuation of the 10–20% lines (isopleths) is probably due to post-depositional chemical erosion during the interglacial lysocline high-stand, when deeper water became more corrosive again (BROECKER et al., 1991b). Similar cycles have been observed in the Atlantic, but they are much weaker and opposite to those in the Pacific (CROWLEY, 1983). These out-of-phase responses of the Atlantic and Pacific are probably the result of circulation changes (CROWLEY, 1985). BROECKER and PENG (1993) indicate a net global average deepening of about 500 m during glacial times. The reasons for the observed fluctuations are not fully understood. One possible explanation is an enhanced carbonate accumulation rate on the shelves during interglacials, when sea level is high. If the riverine supply of carbon and alkalinity were to remain constant during glacial times, the process of carbonate compensation would then require this accumulation to take place in the deep sea. Another possibility, discussed in this study, is that the supply of carbon and alkalinity was higher during glacial than during interglacial times, thus depressing the lysocline during glacials.

1.5.3 Boron Isotopes and Paleo-pH

As we will show in the next chapter, seawater pH is a key parameter of the carbonate chemistry. Paleo-pH records should provide very useful constraints on the evolution of carbonate chemistry with time. One potential tracer of seawater pH is the boron isotopic composition of marine carbonate. Calcareous organisms indeed incorporate trace amounts of boron when building up their shells. There are two stable isotopes of boron, ^{10}B and ^{11}B, which respectively make up about 20% and 80% of the total boron in seawater (HEMMING and HANSON, 1992). There are also two dominant species of boron in seawater: $B(OH)_3$ and $B(OH)_4^-$. The partitioning between them is pH-dependent, according to

$$B(OH)_3 + 2\,H_2O \rightleftharpoons B(OH)_4^- + H_3O^+. \tag{1.10}$$
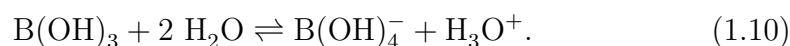
This equilibrium, which also plays a non-negligible role in the speciation of the carbonate system in seawater, is discussed in more details in section 2.3.3 of the next chapter. KAKIHANA et al. (1977) have shown that $B(OH)_3$ is enriched in ^{11}B with respect to $B(OH)_4^-$ by about $20\,^0/_{00}$. The isotopic composition of the two species thus also depends on pH. HEMMING and HANSON (1992) find that modern marine carbonates have a boron isotopic composition very close to that of $B(OH)_4^-$ in seawater.

SANYAL et al. (1995) have analysed glacial-age foraminifera from the tropical Atlantic and Pacific sediments for their boron isotopic composition. They observe that in both oceans, the pH of surface and deep waters was higher during LGM by about 0.2 ± 0.1 and 0.3 ± 0.1 respectively. They calculate that this variation of pH in the deep sea corresponds to an increase of the CO_3^{2-} ion concentration of the order of $100\ \mu mol/kg$-SW. This would be equivalent to a deepening of the calcite saturation horizon of several kilometers, in strong disagreement with the sedimentary carbonate record of FARRELL and PRELL (1989), represented in figure 1.14. To our knowledge there is as yet no satisfactory explanation for this discrepancy.

1.5.4   Other Changes: Oceanic $\delta^{13}C$, Terrestrial Vegetation

The average $\delta^{13}C$ in the oceans has increased by 0.3–$0.4\,^0/_{00}$ since the last glacial to interglacial transition (CURRY et al., 1988; DUPLESSY et al., 1988). A recent revision by CROWLEY (1995) tends to favour the upper limit of $0.4\,^0/_{00}$. The lower value observed during LGM is most probably to be attributed to the transfer of isotopically light carbon from the land to the ocean. ADAMS et al. (1990) estimated from continental data that the terrestrial biospheric carbon reservoir (i.e., soils + biomass) was 1,351 Pg C smaller at the LGM than during the Holocene. More recent studies (CROWLEY, 1991; FRIEDLINGSTEIN et al., 1992; VAN CAMPO et al., 1993; CROWLEY, 1995; FRANÇOIS et al., 1997) come up with much smaller estimates (generally half as large). FRANCOIS ET AL. (1997), using the CARAIB model of the terrestrial biosphere (WARNANT et al., 1994) have shown that a transfer of 606 Pg C from the oceanic to the terrestrial biosphere reservoir during deglaciation would lead to a $0.41\,^0/_{00}$ increase in the oceanic $\delta^{13}C$, in excellent agreement with the observations.

1.5.5   Glacial-Interglacial Variations of Carbon Dioxide in the Atmosphere: Proposed Scenarios

Of all the available records on glacial-interglacial changes of the carbon cycle, the atmospheric CO_2 signal represents the strongest constraint, because of its significance at the global scale. Numerous mechanisms have been proposed to explain the documented variations. There is agreement that the ocean plays a major role, because it represents by far the largest reservoir that can exchange large amounts of CO_2 with the atmosphere on time scales of less than 10,000 years. The ocean contains about 60 times more carbon than the

atmosphere, and the residence time of CO_2 in the atmosphere with respect to air-sea exchange is close to 10 years, as can be calculated from the flux estimates given earlier in this chapter.

Most proposed mechanisms call upon changes of the dynamics, the chemistry or the biology of the World oceans. As there are a number of review papers on this subject in the literature (e.g., SARMIENTO and BENDER, 1994; BROECKER and PENG, 1993, 1989, 1987; BROECKER, 1992; CROWLEY and NORTH, 1991; KEIR, 1988; BOYLE, 1988a,b; BERGER and KEIR, 1984), we will give only a short outline of the most important ideas forwarded. The following summary is largely based upon the work of BROECKER and PENG (1993).

BROECKER (1992) calculates that the combination of the average sea-surface temperature decrease of 2°C with the salinity increase from about 35 to 36, due to the 120 m less deeper ocean, only accounts for about 12 μatm of the observed CO_2 fluctuation of 90 μatm. BROECKER and PENG (1993) calculate furthermore that the glacial-interglacial variation of the terrestrial biomass, as deduced from the 0.4 $^0\!/_{00}$ lower global average $\delta\,^{13}$C during glacial time corresponds to a p_{CO_2} variation of 25 μatm, which goes in the direction opposite to the Vostok signal. There must hence have been a major decrease of the dissolved inorganic carbon content in the surface ocean or an increase of its alkalinity to drive p_{CO_2} to the observed glacial values.

A first class of mechanisms concentrates on changes of the biological pump (VOLK and HOFFERT, 1985). They are based upon the observation that the present-day atmosphere would exhibit atmospheric CO_2 levels of about 470 μatm if there were not the permanent transfer of carbon from the surface to the deep sea by organic matter production and remineralization. If all the available nutrients were used up by marine organism on the other hand, it would drop to 150 μatm (BROECKER and PENG, 1993). A stronger biological pump during glacial times could hence efficiently reduce atmospheric CO_2 levels. Different possibilities leading to a more intense cycling have been explored and have given rise to several hypotheses.

- *The Phosphate Extraction Hypothesis* assumes that a larger amount of nutrients (usually phosphate) was present in the glacial than in the interglacial ocean, leading to a larger overall production. It was proposed by BROECKER (1982), who estimated that the extraction of 30% of the total phosphate in the ocean by deposition of organic matter (with a Redfield C/P/N composition) during the marine transgression of the shelves at the deglaciation could lead to the productivity changes required for an 80 μatm increase of CO_2 in the atmosphere.

- *The Denitrification Model* is a variant of the previous, where nitrate

instead of phosphate is chosen as a limiting factor. BROECKER (1982) and KEIR and BERGER (1983) have shown that the phosphate extraction model looses 40% of its efficiency because the organic matter deposition also subtracts carbon from the ocean. BERGER and KEIR (1984) propose that nitrate as the limiting nutrient can efficiently be subtracted from the oceans by denitrification.

- *The C/P Model* was proposed as an alternate scenario to the phosphate extraction hypothesis by BROECKER (1982). He indicated that a 30% higher glacial C/P ratio of organic matter would have the same effect as the extraction of 30% of the oceans phosphate during the deglaciation.

- *The Polar Nutrient Hypothesis* does not assume a larger content of nutrients, but either calls upon a better utilization of available nutrients in the high-latitude oceans, or on a constant production and a reduced mixing between the surface and the deep ocean in polar regions (KNOX and MCELROY, 1984; KNOX-ENNEVER and MCELROY, 1985; SARMIENTO and TOGGWEILER, 1984; TOGGWEILER and SARMIENTO, 1985; SIEGENTHALER and WENK, 1984; WENK and SIEGENTHALER, 1985). In these regions, upwelled nutrients presently return largely unused by biological production to the deep ocean.

- *The Iron Hypothesis*, proposed by MARTIN (1990), is in fact a special case of the polar nutrient hypothesis. It assumes that biological production in the southern ocean is currently limited by the availability of dissolved iron. The larger supply of Fe by atmospheric dust during the last glacial period would then stimulate the utilization of the upwelled nutrients, increasing the biological productivity.

All of these mechanisms initially rely upon changes of the concentration of dissolved inorganic carbon in the surface water. They generally also have to take a contribution from alkalinity into account, because the increased DIC concentrations of the deep ocean that result from the more intense organic production-oxidation cycle tends to perturb the carbonate compensation mechanism. Dissolution of a sufficient amount of carbonate then occurs in order to restore the deep-sea CO_3^{2-} concentration required for carbonate deposition at the sea-floor to compensate for the river input of carbon and alkalinity (which is generally assumed to remain constant). The resulting global increase of alkalinity helps to draw down the atmospheric CO_2.

A second group of mechanisms intend to directly produce alkalinity variations.

- *The Rain-Ratio Hypothesis* was first discussed by BERGER and KEIR (1984), as a complement for the nutrient hypotheses. In the present-day ocean, carbonate-C/organic-C ratios in the biogenic particulate rain are generally larger in low-fertility than in high-fertility areas. Hence, if this ratio decreases as productivity increases, there will be a much stronger response of the atmospheric p_{CO_2}, than if it is taken as constant. In fact, the additional downward flux of alkalinity due to the also increased carbonate productivity will be less important, thus reducing the compensating effect that one always has to take into account. DYMOND and LYLE (1985) suggest that the glacial-interglacial CO_2 changes were due in part to global increases in the total oceanic productivity, together with a higher productivity by organisms that secrete opaline silica shells at the expense of those that secrete carbonate shells, leading to lower glacial carbonate-C/organic-C ratios.

  The rain ratio hypothesis has recently been reconsidered by ARCHER and MAIER-REIMER (1994). Having coupled the sediment calcite dissolution model of ARCHER (1991) to the three-dimensional carbon cycle model of MAIER-REIMER (1993), they show that a 40% decrease of this ratio can drive p_{CO_2} to typical glacial values.

- *The Polar Alkalinity Hypothesis* of BROECKER and PENG (1989) ascribes the lower atmospheric p_{CO_2} to increased alkalinity in the Antarctic surface waters. The postulated alkalinity increase is supposed to be the result of a reduced input of low-alkalinity NADW into the Antarctic during glacial times.

- *The Coral Reef Hypothesis* was initially proposed by BERGER (1982) (see also BERGER, 1985; BERGER and KEIR, 1984; KEIR and BERGER, 1985). It assumes that there is a massive basin-to-shelf transfer of the locus of carbonate deposition at the sea-floor during the marine transgression of the shelf at the deglaciation. As a consequence, surface water alkalinity would rapidly decrease during deglaciation, and atmospheric p_{CO_2} would rise. The resulting net imbalance between carbonate deposition in shelf and in deep-sea environments is accommodated for by enhanced dissolution at the sea-floor, after a mixing lag of 1–2 kyr. The amplitude of the response is strongly dependent on the length of this mixing lag. The longer it takes, the larger the drop of alkalinity, and the larger the resulting p_{CO_2} rise. This hypothesis was later reconsidered by OPDYKE and WALKER (1992b) and WALKER and OPDYKE (1995) who included also a varying riverine input of carbonate from the weathering of the exposed shelf, improving its efficiency.

- *The Vertical Nutrient Fractionation Hypothesis* (BOYLE, 1988a,b) is based upon the observation that, in the glacial ocean, nutrients and metabolic CO_2 were concentrated in deep rather than in intermediate waters (BOYLE and KEIGWIN, 1982). This redistribution can be ascribed to a weaker glacial NADW source, relative to Antarctic deep water sources. During the outset of this redistribution, deep waters get enriched in DIC relative to the upper ocean. This leads to the same perturbation of the carbonate compensation mechanism as that mentioned above for the nutrient scenarios. Carbonate dissolution temporarily increases to drive back the deep water carbonate ion concentration to its steady-state value. Atmospheric p_{CO_2} then decreases as a result of the increased alkalinity. The reverse is expected to happen during deglaciation.

Chapter 2

Carbonate Chemistry in the Oceans

In this chapter we want to give a sufficiently comprehensive outline of basical carbonate chemistry in the oceans. After a presentation of the chemical equilibria between the important carbonate species, we will give rigorous definitions of concepts like C_T or A_T already introduced in the previous chapter. The different pH scales used in seawater media are rapidly presented, in order to arrive at a coherent set of parameterizations for thermodynamic equilibrium constants required for our carbon cycle model. Finally, the impact of approximate expressions of A_T will be discussed in detail, both regarding the absolute equilibrium and sensitivity of the carbonate system.

2.1 Chemical Equilibria and Basic Concepts

When CO_2 gas gets dissolved in seawater, a whole series of chemical equilibria establish, which can be represented by the following equations:

$$
\begin{align}
CO_{2(gas)} &\rightleftharpoons CO_{2(aq)} \tag{2.1} \\
CO_{2(aq)} + H_2O &\rightleftharpoons H_2CO_3 \tag{2.2} \\
H_2CO_3 + H_2O &\rightleftharpoons HCO_3^- + H_3O^+ \tag{2.3} \\
HCO_3^- + H_2O &\rightleftharpoons CO_3^{2-} + H_3O^+ \tag{2.4}
\end{align}
$$
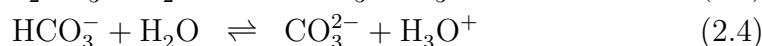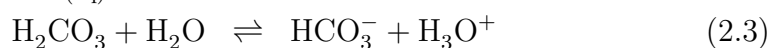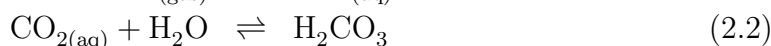
These equations are written in terms of H_3O^+ rather than H^+ to reflect the fact that *free* H^+ ions *sensu stricto* do only exist in insignificantly small amounts in aqueous solutions. Each proton is rather bound to a water molecule to form an H_3O^+ ion[†] (DICKSON, 1984). Equilibria (2.1) – (2.4) are

---

[†]Each of these in turn is furthermore generally hydrogen bonded to three other H_2O molecules to form an $H_9O_4^+$ ion.

of prime importance for the oceanic carbon cycle. The CO_2 flux across the air-sea interface is controlled by the difference between the partial pressure of CO_2 in the atmosphere and in the surface waters (more precisely its fugacity in the surface waters). The carbonate ion concentration is known to control the precipitation and dissolution rates of calcite and aragonite. The overall preservation of carbonate minerals in sea-floor sediments is also controlled by the distribution of carbonate ion concentration in the ocean because it sets the lysocline and, more indirectly, the carbonate compensation depths.

The dissolved CO_2 gas gets only very weakly hydrated (equation (2.2)): the $CO_{2(aq)}/H_2CO_3$ molar ratio is close to 650 (STUMM and MORGAN, 1981). Most of the undissociated dissolved CO_2 is hence in the $CO_{2(aq)}$ form. In practice, it is therefore usual to combine the two species by defining

$$CO_{2(aq)}^* = H_2CO_3 + CO_{2(aq)}. \tag{2.5}$$
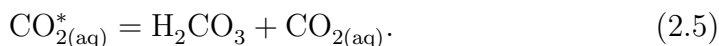
Equilibria (2.1) to (2.3) are then reformulated in terms of $CO_{2(aq)}^*$, becoming

$$CO_{2(gas)} \rightleftharpoons CO_{2(aq)}^* \tag{2.6}$$

$$CO_{2(aq)}^* + 2\,H_2O \rightleftharpoons HCO_3^- + H_3O^+ \tag{2.7}$$
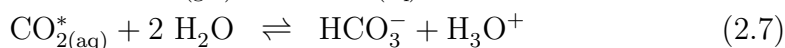
Among the different species that take part in this system, concentrations can be experimentally determined only for H_3O^+ and $CO_{2(gas)}$. None of the others is directly accessible and their concentrations are rather calculated from combinations that can be estimated experimentally, in conjunction with thermodynamic relations. The first of these combinations is the *Dissolved Inorganic Carbon* C_T, also sometimes called *Total Carbonate* or *Total CO_2*, which is defined by

$$C_T = [CO_{2(aq)}^*] + [HCO_3^-] + [CO_3^{2-}]. \tag{2.8}$$

The other one is the *Total Alkalinity* A_T, also called *Titration Alkalinity*, which reflects the excess of chemical bases of the solution relative to an arbitrary specified zero level of protons, or equivalence point. Ideally, A_T represents the amount of bases contained in a sample of seawater that will accept a proton when the sample is titrated with hydrochloric acid to the carbonic acid endpoint. That endpoint is located at the pH below which H_3O^+ ions get more abundant in solution than HCO_3^- ions. Its value is close to 4.5. H_3O^+ added to water at this pH by adding strong acid will remain as such in solution. Rigorously speaking, A_T is defined as the number of moles of H^+ ions equivalent to the excess of "proton acceptors", i.e. bases formed from acids characterized by a $pK_A \geq 4.5$ in a solution of zero ionic strength at 25°C, over "proton donors", i.e. acids with $pK_A < 4.5$ under the

Table 2.1: Contributors to A_T.

Acid	pK_A	Type provided	Species	H$^+$ eq/mol
H_2O	14.0	proton acceptor	OH^-	1
H_2CO_3	6.3	proton acceptor	HCO_3^-	1
HCO_3^-	10.3	proton acceptor	CO_3^{2-}	2
$B(OH)_3$	9.2	proton acceptor	$B(OH)_4^-$	1
HSO_4^-	2.0	proton donor	HSO_4^-	1
HF	3.2	proton donor	HF	1
H_3O^+	—	proton donor	H_3O^+	1
H_3PO_4	2.1	proton donor	H_3PO_4	1
$H_2PO_4^-$	7.2	proton acceptor	HPO_4^{2-}	1
HPO_4^{2-}	12.7	proton acceptor	PO_4^{3-}	2
H_4SiO_4	9.7	proton acceptor	$H_3SiO_4^-$	1
H_2S	7.0	proton acceptor	HS^-	1
HS^-	12.0	proton acceptor	S^{2-}	1
NH_4^+	9.3	proton acceptor	NH_3	1

Compiled from data reported by DICKSON (1981)

same conditions, per kilogram of sample (DICKSON, 1981). Figure 2.1 (see also figure 1.7 where emphasis is put on the vertical dimension) shows the distributions of A_T and C_T in the modern oceans (TAKAHASHI et al., 1981a).

With emphasis on its most important contributors, A_T in natural seawater can generally be reduced to

$$A_\mathrm{T} = [HCO_3^-] + 2\,[CO_3^{2-}] + [B(OH)_4^-] + [OH^-] + \sum [B_\mathrm{minor}]$$
$$- [H_3O^+] - \sum [A_\mathrm{minor}] \tag{2.9}$$

where $\sum [B_\mathrm{minor}]$ and $\sum [A_\mathrm{minor}]$ represent minor concentrations of other bases and acids that can usually be neglected, but which it might be necessary to take into account under some circumstances (e.g., in phosphate- or silicate-rich waters from the deep sea, or in anoxic environments). A more extensive list of potential contributors is given in table 2.1. It is nevertheless far from exhaustive.

STUMM and MORGAN (1981) indicate that total concentrations, including both free (or hydrated) and complex-bound species, are to be considered for the A_T contributors, and also for C_T. As said before, A_T should represent the concentration of all bases that can accept protons when a sample is titrated
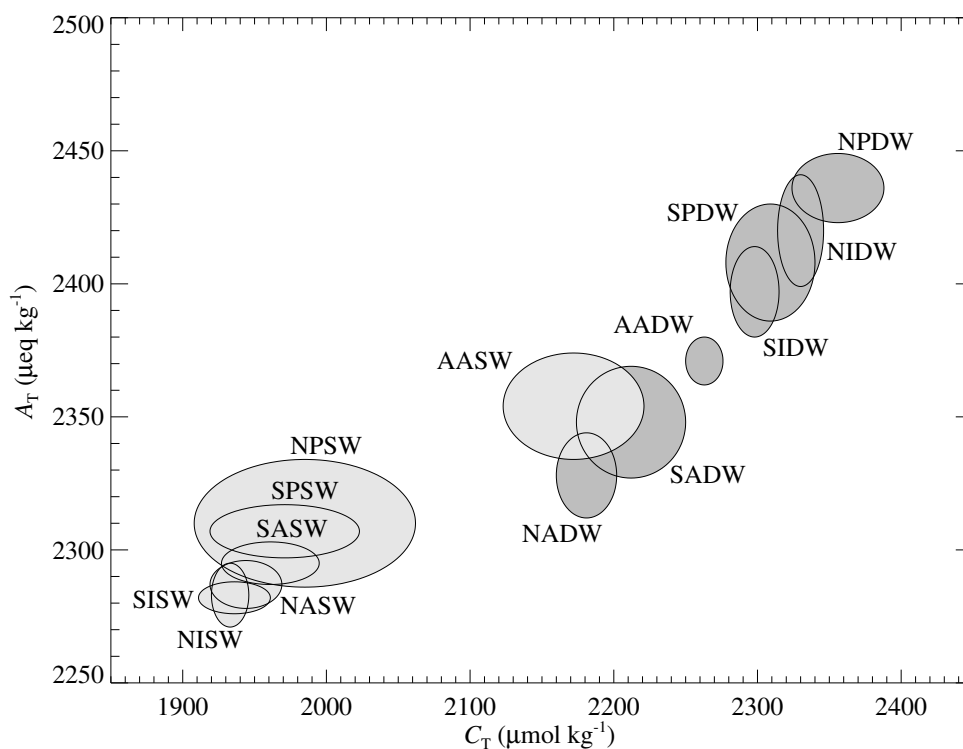
Figure 2.1: Distributions of A_T and C_T in the modern oceans, normalized to the mean ocean salinity of 34.78 (TAKAHASHI et al., 1981a). In the identifications of the different subdivisions, AA stands for Antarctic, NA and SA stand for North and South Atlantic, NI and SI for North and South Indian, and NP and SP for North and South Pacific respectively. SW and DW distinguish surface and deep waters. Figure adapted from an original graph courtesy of ANNE MOUCHET.

with a strong acid (HCl) to the carbonic acid end-point. We can expect that strong acid acts on both free and complexed forms. Total concentrations therefore seem to be much more appropriate. However, DICKSON's (1981) definition does not state this explicitly and among the contributors, he lists HSO_4^- and HF, which are usually considered to be complexed froms of H^+ in natural seawater (see section 2.2 below). If DICKSON would really have intended to include only free species in his definition, we can expect that the complexed ones are taken into account by $\sum [B_{minor}]$ and $\sum [A_{minor}]$, the minor bases and acids. As already mentioned, he indicates that HSO_4^- and HF figure within $\sum [A_{minor}]$. Unfortunately, DICKSON (1981) only considers Mg- and Ca-free waters in his examples, but it can be shown that $Mg(OH)^+$, the major complexed form of $(OH)^-$ in seawater representing more than 70% of the total $(OH)^-$, is part of $\sum [B_{minor}]$, together with $Ca(OH)^+$ and $Na(OH)$. From thermodynamic data given by FAURE (1991), we calculate a pK of 11.4 at 25°C for the hydrolysis of Mg^{2+}, described by $Mg^{2+} + 2\,H_2O \rightleftharpoons Mg(OH)^+ + H_3O^+$. The p$K$s for the hydrolysis of Ca^{2+} and Na^+ are respectively 12.7 and 14.2. Accordingly, $Mg(OH)^+$, $Ca(OH)^+$ and $Na(OH)$ would be included in DICKSON's $\sum [B_{minor}]$.

In agreement with STUMM and MORGAN (1981), we will assume in this study that all concentrations are total concentrations. One exception to this will be $[H_3O^+]$, which will always stand for the only concentration of hydrated H^+ ions. $[H^+]$ on the other hand will always refer to the total concentration of H^+. But this and other possible exceptions will be clearly identified in the text which we have tried to make as consistent as possible. Our exact working definition of A_T will be given in section 2.4, once the concepts of total H^+ concentrations have been clarified.

To determine the concentrations of the different carbon species of the system from C_T and A_T, we need to determine the part of A_T which is due to bicarbonate and carbonate ions alone. This part is referred to as *Carbonate Alkalinity*, A_C, and it is of course defined by

$$A_C = [HCO_3^-] + 2\,[CO_3^{2-}] \tag{2.10}$$

Whereas A_T is a measurable quantity, A_C is not. It must be calculated from A_T by subtracting the contributions of the other contributors. To evaluate these contributions, we need to know equilibrium constants for the appropriate chemical equilibria (e.g., the dissociation constants of the relevant acids). We will show below that, for our purposes, A_T can be reasonably well approximated by the so-called *Borate Alkalinity*, A_{CB}, which is defined by

$$A_{CB} = [HCO_3^-] + 2\,[CO_3^{2-}] + [B(OH)_4^-] \tag{2.11}$$

This approximation will already simplify the calculations to a large extent.

Unfortunately, there remain several difficulties to perform this calculation. The use of *thermodynamic* constants requires us to employ activities and not concentrations. For a given species X, the activity a_X is related to the concentration [X] by an activity coefficient γ_X: $a_X = \gamma_X$ [X]. Thermodynamic equilibrium constants can be calculated from purely theoretical considerations (see, e.g., FAURE, 1991, chapters 11–13). The difficulty in resolving our problem is thus shifted towards the determination of the appropriate activity coefficients, which provide the link between the thermodynamic theory and the measurable composition of seawater. Unfortunately, this is not straightforward because it involves complicated models for ion interactions in solutions. This is especially true for seawater which is too strong an electrolytic solution for the simple DEBYE-HÜCKEL model to be applicable. This model is valid only for ionic strengths of less than 0.01, more than an order of magnitude less than the ionic strength of seawater, which is of about 0.7 according to relationship (2.20).

To circumvent these problems, "*apparent*" and *stoichiometric* constants, which depend only on observable quantities, have been determined from laboratory experiments. For example, the two constants for the dissociation of the bicarbonate ion (equation (2.4)) are respectively defined as

$$K' = \frac{a_{H_3O^+} \, [CO_3^{2-}]}{[HCO_3^-]} \qquad (\text{``apparent'' constant})$$

and

$$K^* = \frac{[H^+] \, [CO_3^{2-}]}{[HCO_3^-]} \qquad (\text{stoichiometric constant})$$

The most important of these observable quantities is salinity, S, used to parameterize the ionic interaction strength and also the major composition of seawater. Apparent constants are hybrid empirical constructs involving total concentrations and some kind of activity of H_3O^+, called *apparent* because it derives from a pH scale that does not reflect the true activity of the hydrogen ion. They are about to disappear since stoichiometric constants became available. These relate only concentrations to each other and are thermodynamically more consistent.

Concentrations are generally taken as total concentrations (free and hydrated + complexed forms of the ions). They are expressed either in molal (moles per kg of solvent, i.e. pure water, which we will note mol/kg-H_2O) or gravimetric (moles per kg of solution, i.e. of seawater, which we will note mol/kg-SW) units. Besides these two, concentrations are also sometimes found expressed per unit volume, in mol/m^3 or mol/l. While the former is directly related to gravimetric units by density, the latter is more prob-

lematic due to the definition of the liter which includes some temperature dependency.

In this chapter, we will use gravimetric units for the thermodynamic constants, which are the most common in oceanography. Molal units are often used for laboratory experiments. To avoid any possible confusion, we will reserve the $[\cdot]$ notation for concentrations in gravimetric units; molal concentrations will be written as $m(\cdot)$. The constants taken from the literature will be converted to the mol/kg-SW scale when necessary. This conversion is based upon the observation that 1 kg of average seawater at a salinity of 35 contains 35.1709 g of solutes (see table A.3 in the appendix). Seawater of salinity S is supposed to contain $(35.1709 \times S/35)$ g of solutes and hence $(1000 - 35.1709 \times S/35)$ g, or $(1 - 0.0010049S)$ kg of pure water per kg. It follows that

$$[\text{mol/kg-SW}] = m(\text{mol/kg-H}_2\text{O}) \times (1 - 0.0010049\,S) \qquad (2.12)$$

When reporting equilibrium constants from the literature, we will, as far as possible, use lower-case letters for those that are based upon molal and upper-case letters for those that are based upon gravimetric concentration units.

2.2   pH Scales for Seawater Media

Besides different concentration scales used in the literature, further complications arise because of the different pH scales used in the course of establishing parameterizations for the equilibrium constant required for carbonate system speciation. The reasons for the use of different such scales are mainly historical. To quote DICKSON (1984):

> "*They reflect the gradual refinement of the experimentally convenient potentiometric determination of acidity in order that the numbers obtained might be usefully interpreted as a property of hydrogen ion in solution.*"

For the sake of completeness, we will rapidly outline the differences among the three pH scales used for the determination of the equilibrium constants. The first one, which leads to the "apparent" equilibrium constants, is the N.B.S. scale:

$$\text{pH}_{\text{NBS}} = -\log a_{\text{H}_3\text{O}^+}$$

As stated before, $a_{\text{H}_3\text{O}^+}$ is not the true proton activity, but rather a conventual definition of it (DICKSON, 1984). Because it is based upon dilute

buffers, the N.B.S. scale is useful only in dilute natural waters (e.g. rivers, lakes). It is recommended not to use it for seawater anymore (DICKSON, 1984; MILLERO, 1995). The other two scales (HANSSON, 1973b; DICKSON and RILEY, 1979) represent an attempt to take into account the fact that the H^+ ions do not only occur as free or hydrated ions in seawater but get complexed by other medium ions such as SO_4^{2-} and F^-:

$$H_3O^+ + SO_4^{2-} \ \rightleftharpoons \ HSO_4^- + H_2O \tag{2.13}$$

$$H_3O^+ + F^- \ \rightleftharpoons \ HF + H_2O \tag{2.14}$$
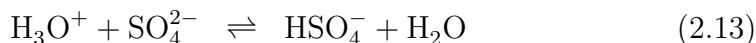
These two scales are the *total proton scale* defined as

$$pH_T = -\log([H^+]_T),$$

where

$$[H^+]_T = [H_3O^+](1 + \beta_{HSO_4} S_T), \tag{2.15}$$

and the *seawater scale*, defined as

$$pH_{SWS} = -\log([H^+]_{SWS}),$$

where

$$[H^+]_{SWS} = [H_3O^+](1 + \beta_{HSO_4} S_T + \beta_{HF} F_T). \tag{2.16}$$

In these definitions, $[H_3O^+]$ takes only free and hydrated hydrogen ions into account. S_T and F_T are respectively the *Total Sulphate* (comprising both the HSO_4^- and the SO_4^{2-} ions) and the *Total Fluoride* (comprising HF as well as F^-) contents in the seawater. The distributions of these two quantities in the modern ocean are conservative, i.e., the ratios of their concentrations to salinity are constant throughout the oceans. We can hence estimate their respective concentrations directly from salinity, using

$$S_T = 0.028234 \frac{S}{35} \quad \text{and} \quad F_T = 0.000068 \frac{S}{35}, \tag{2.17}$$

which directly relate S_T and F_T in mol/kg-SW to salinity S (MILLERO, 1982b, 1995; MILLERO and SOHN, 1992). β_{HSO_4} and β_{HF} are the association constants for the formation of HSO_4^- (equation (2.13)) and of HF (equation (2.14)) respectively:

$$\beta_{HSO_4} = \frac{[HSO_4^-]}{[H_3O^+][SO_4^{2-}]} \quad \text{and} \quad \beta_{HF} = \frac{[HF]}{[H_3O^+][F^-]}. \tag{2.18}$$

These two pH scales are often qualified as *total hydrogen ion concentration scales*. HANSSON (1973b) considered them both as seawater scales, (2.15)

being the special case for fluoride-free water. We should mention that HANS-SON's (1973) original definitions of $[H^+]_T$ and of $[H^+]_{SWS}$ for seawater containing fluoride were based upon the total *analytical* concentration of the hydrogen ion in solution:

$$[H^+]_{SWS(Hansson)} = [H_3O^+] + [HSO_4^-] + [HF].$$

Taking advantage of (2.18) and using $S_T = [HSO_4^-] + [SO_4^{2-}]$ and $F_T = [HF] + [F^-]$, this can be rewritten

$$\begin{aligned}
[H^+]_{SWS(Hansson)} &= [H_3O^+](1 + \beta_{HSO_4}[SO_4^{2-}] + \beta_{HF}[F^-]) \\
&= [H_3O^+](1 + \frac{\beta_{HSO_4} S_T}{1 + \beta_{HSO_4}[H_3O^+]} + \frac{\beta_{HF} F_T}{1 + \beta_{HF}[H_3O^+]}).
\end{aligned}$$

These original definitions were later modified by DICKSON and RILEY (1979) to those given above (equations (2.15) and (2.16)) in order to make $[H^+]_T$ and $[H^+]_{SWS}$ strictly proportional to $[H_3O^+]$, with a proportionality factor that is itself independent of $[H_3O^+]$. The main purpose of this redefinition was to avoid systematic errors in $[H_3O^+]$ calculated from measured pH_T or pH_{SWS} values, due to the lack of accurate estimates for β_{HSO_4} and β_{HF} at that time. Fortunately, the differences are negligible for the common seawater. Using numerical values for β_{HSO_4} and β_{HF} obtained from parameterizations below, we find that both $[SO_4^{2-}]/S_T$ and $[F^-]/F_T$ are greater than 0.99 mol/mol when $[H_3O^+] < 10^{-5}$ mol/kg-SW, and that $[SO_4^{2-}]/S_T > 0.99999$ mol/mol and $[F^-]/F_T > 0.9999$ mol/mol in case $[H_3O^+] < 10^{-7}$ mol/kg-SW. In seawater, it is hence safe to assume that $[H^+]_{SWS} = [H^+]_{SWS(Hansson)}$, but during a titration down to pH < 4 for example, this will not remain true.

DICKSON (1990a) has determined the dissociation constant k_{HSO_4} of HSO_4^- as a function of temperature and salinity, but on a molal concentration scale, i.e.,

$$k_{HSO_4} = \frac{m(H_3O^+) \, m(SO_4^{2-})}{m(HSO_4^-)}.$$

It is given by

$$\begin{aligned}
\ln k_{HSO_4} &= -4276.1/T + 141.328 - 23.093 \ln T \\
&\quad + (-13856/T + 324.57 - 47.986 \ln T) \, I_m^{1/2} \\
&\quad + (35474/T - 771.54 + 114.723 \ln T) \, I_m \\
&\quad - (2698/T) I_m^{3/2} + (1776/T) I_m^2
\end{aligned} \tag{2.19}$$

In this expression, the temperature T must be given in K and I_m, the molal ionic strength of the seawater medium, in mol/kg-H_2O. According to

MILLERO (1982b, 1995) and MILLERO and SOHN (1992), this latter is related to salinity (S) by

$$I_m = \frac{0.019920S}{1 - 0.0010049S}. \tag{2.20}$$

β_{HSO_4}, whose units are $(\text{mol/kg-SW})^{-1}$, is then obtained from

$$\ln \beta_{HSO_4} = -\ln k_{HSO_4} - \ln(1 - 0.0010049S).$$

The variation of β_{HF} as a function of temperature and molal ionic strength has been determined by DICKSON and RILEY (1979) on a molal concentration scale. Following their results, values for β_{HF} in $(\text{mol/kg-SW})^{-1}$, can be calculated from

$$\ln \beta_{HF} = -1590.2/T + 12.641 - 1.525 I_m^{1/2} - \ln(1 - 0.0010049S). \tag{2.21}$$

In this equation, T must again be expressed in K and I_m in $\text{mol/kg-H}_2\text{O}$ (related to salinity by equation (2.20)).

Conversion between the pH_T and pH_{SWS} scales can easily be done using

$$\frac{[\text{H}^+]_{SWS}}{[\text{H}^+]_T} = \frac{1 + \beta_{HSO_4}S_T + \beta_{HF}F_T}{1 + \beta_{HSO_4}S_T} \tag{2.22}$$

It should now be clear that the right-hand side of the previous equation depends only on temperature and salinity. Finally, it should be noticed that both molal and gravimetric units are used in the literature to express the different hydrogen ion concentrations and pH values. We have chosen to base our definition upon the gravimetric concentration scale. The molal concentrations could have been used as well, with $m_T(\text{H}^+)$ and $m_{SWS}(\text{H}^+)$ definitions strictly analogous to (2.15) and (2.16).

2.3 Equilibrium Constants for Carbonate Chemistry in the Oceans

The equilibrium constants reported in this section are all expressed in terms of total analytical concentrations of the respective species (HANSSON, 1973a; WIGLEY and PLUMMER, 1976; GOYET and POISSON, 1989; MILLERO and SOHN, 1992).

2.3.1 Solubility of Carbon Dioxide in Seawater

We will use the solubility coefficient K_0 determined by WEISS (1974) to describe the solubility of CO_2 in seawater (equation (2.6)). It is defined by Henry's law

$$f_{CO_2} = \frac{[CO^*_{2(aq)}]}{K_0},\qquad(2.23)$$

where f_{CO_2} is the fugacity of CO_2 in the atmosphere and $[CO^*_{2(aq)}]$ is the sum of the concentrations of dissolved CO_2 and undissociated hydrated CO_2, as previously defined (equation (2.5)). Under the typical conditions prevailing at the air-sea interface, the difference between the fugacity and the partial pressure of CO_2 is less than 0.5% (UNESCO, 1991). We will therefore take the fugacity in (2.23) equal to the partial pressure p_{CO_2} and use

$$p_{CO_2} = \frac{[CO^*_{2(aq)}]}{K_0}.\qquad(2.24)$$

WEISS (1974) gives the following equation to calculate K_0 in units of mol (kg-SW)$^{-1}$ atm^{-1}, as a function of temperature (T, in K) and salinity (S):

$$
\begin{aligned}
\ln K_0 \;=\;& -60.2409 + 93.4517(100/T) + 23.3585\ln(T/100) \\
& + (0.023517 - 0.023656(T/100) + 0.0047036(T/100)^2)S
\end{aligned}
$$
$$(2.25)$$

2.3.2 Dissociation of Carbonic Acid in Seawater

We will use the SWS pH scale as a common base for the different equilibrium constants required for our study. We therefore define the first dissociation constant for carbonic acid in seawater (equilibrium (2.7)) by

$$K_1 = \frac{[H^+]_{SWS}\,[HCO_3^-]}{[CO^*_{2(aq)}]}\qquad(2.26)$$

and the second dissociation constant (equilibrium (2.4)) by

$$K_2 = \frac{[H^+]_{SWS}\,[CO_3^{2-}]}{[HCO_3^-]}\qquad(2.27)$$

To describe the variations of K_1 and K_2, we use the most recent parameterizations established by MILLERO (1995), which are based upon data and

results originally published by ROY et al. (1993) and by GOYET and POIS-SON (1989). As defined above (i.e. on the SWS pH scale and in mol/kg-SW), both can be calculated from

$$
\begin{aligned}
\ln K_1 \;=\; & 2.18867 - 2275.0360/T - 1.468591 \ln T \\
& + (-0.138681 - 9.33291/T)S^{1/2} \\
& + 0.0726483S - 0.00574938S^{3/2}
\end{aligned} \tag{2.28}
$$

and

$$
\begin{aligned}
\ln K_2 \;=\; & -0.84226 - 3741.1288/T - 1.437139 \ln T \\
& + (-0.128417 - 24.41239/T)S^{1/2} \\
& + 0.1195308S - 0.00912840S^{3/2}.
\end{aligned} \tag{2.29}
$$

2.3.3 Dissociation of Boric Acid and of Water in Seawater

After bicarbonate and carbonate, the orthoborate ion $B(OH)_4^-$ is the most important contributor to A_T in natural seawater. We have therefore to consider the dissociation of boric acid which regulates the concentration of this ion:

$$
B(OH)_3 + 2\,H_2O \rightleftharpoons B(OH)_4^- + H_3O^+ \tag{2.30}
$$
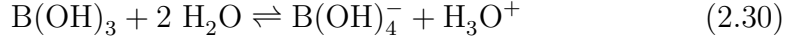
DICKSON (1990b) has determined the dissociation constant of boric acid, on a molal concentration and on the pH_T scale:

$$
k_B = \frac{m_T(H^+)\,m(B(OH)_4^-)}{m(B(OH)_3)} \tag{2.31}
$$

He has fitted the variation of k_B with temperature (T, in K) and salinity (S) to the function

$$
\begin{aligned}
\ln k_B \;=\; & (-8966.90 - 2890.51S^{1/2} - 77.942S + 1.726S^{3/2} - 0.0993S^2)/T \\
& + (148.0248 + 137.194S^{1/2} + 1.62247S) \\
& + (-24.4344 - 25.085S^{1/2} - 0.2474S)\ln T \\
& + (0.053105S^{1/2})T
\end{aligned} \tag{2.32}
$$

In our preferred units of mol/kg-SW and on the pH_{SWS} scale, the dissociation constant of boric acid is defined as

$$
K_B = \frac{[H^+]_{SWS}\,[B(OH)_4^-]}{[B(OH)_3]} \tag{2.33}
$$

and it is related to k_B above by

$$\ln K_B = \ln k_B + \ln(\frac{[H^+]_{SWS}}{[H^+]_T}) + \ln(1 - 0.0010049S). \qquad (2.34)$$

The concentration of $B(OH)_4^-$ is then calculated from

$$[B(OH)_4^-] = \frac{K_B B_T}{K_B + [H^+]_{SWS}}, \qquad (2.35)$$

where B_T is the *Total Boron* content of seawater

$$B_T = [B(OH)_3] + [B(OH)_4^-]. \qquad (2.36)$$

The value of B_T in mol/kg-SW can be calculated from salinity (S) by

$$B_T = 0.0004125\frac{S}{35} \qquad (2.37)$$

because boron exhibits a conservative behaviour in seawater.

Although its contribution is an order of magnitude lower than that of $B(OH)_4^-$, OH^- is often taken into consideration for calculations of the carbonate system species distribution (see, e.g., MAIER-REIMER and BACASTOW, 1990). In order to estimate the influence of $[OH^-]$, we have to consider the dissociation of water in seawater:

$$2\,H_2O \rightleftharpoons OH^- + H_3O^+. \qquad (2.38)$$
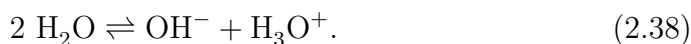
OH^- is even much more subject to ion-pairing by medium ions than H^+. About 70% of them are bound to other ions (CULBERSON and PYTKOWICZ, 1973), most of them to Mg^{2+}. For H^+, this fraction is only around 25%. The stoichiometric dissociation constant of water in seawater defined by DICKSON and RILEY (1979) as

$$K_W = [H^+]_{SWS}\,[OH^-]_{SWS} \qquad (2.39)$$

takes this complexation into account. In this definition, $[OH^-]_{SWS}$ includes the free OH^- and its complexed species, of which $MgOH^+$ is by far the most abundant. In units of $(mol/kg\text{-}SW)^2$, values for K_W as defined by equation (2.39) can be calculated as a function of temperature (T, in K) and salinity (S) from the expression (MILLERO, 1995; MILLERO, pers. comm.)

$$\begin{aligned}
\ln K_W \;=\;& 148.9802 - 13847.26/T - 23.6521\ln T \\
& + (-5.977 + 118.67/T + 1.0495\ln T)S^{1/2} \\
& - 0.01615S
\end{aligned} \qquad (2.40)$$

2.3.4 Solubility of Calcite and Aragonite in Seawater

The formation of $CaCO_3$ minerals by organisms in the surface waters and the subsequent dissolution in the deep-sea must also be considered when studying the global budget of inorganic carbon in the oceans. For calcite, the stoichiometric solubility product

$$K_{Calc} = [Ca^{2+}] [CO_3^{2-}] \tag{2.41}$$

can be calculated in $(mol/kg\text{-}SW)^2$ from (MUCCI, 1983)

$$\begin{aligned} \log K_{Calc} = \ & -171.9065 - 0.077993T + 2839.319/T + 71.595 \log T \\ & + (-0.77712 + 0.0028426T + 178.34/T)S^{1/2} \\ & - 0.07711S + 0.0041249S^{3/2} \end{aligned} \tag{2.42}$$

For aragonite, this solubility product is also

$$K_{Arag} = [Ca^{2+}] [CO_3^{2-}] \tag{2.43}$$

and its value in $(mol/kg\text{-}SW)^2$ is obtained from (MUCCI, 1983)

$$\begin{aligned} \log K_{Arag} = \ & -171.9450 - 0.077993T + 2903.293/T + 71.595 \log T \\ & + (-0.068393 + 0.0017276T + 88.135/T)S^{1/2} \\ & - 0.10018S + 0.0059415S^{3/2} \end{aligned} \tag{2.44}$$

As usual, the temperature T must be expressed in K and the practical salinity scale is used for S. Although Ca is not a truly conservative element in seawater, it is sufficiently abundant that biological cycling does not affect its concentration by more than 0.5% in the water column, when normalized to salinity. It can be considered as approximately conservative (CULKIN, 1965) and we may reasonably well calculate $[Ca^{2+}]$ (in mol/kg-SW) from salinity (S) by

$$[Ca^{2+}] = 0.010282 \frac{S}{35} \tag{2.45}$$

2.3.5 Pressure Effect on Chemical Equilibria

The effect of pressure on the equilibrium constants is usually estimated from (MILLERO, 1982a)

$$\ln K_i^P = \ln K_i^0 - (\Delta V_i/RT)P + (\tfrac{1}{2}\Delta \kappa_i/RT)P^2. \tag{2.46}$$

In this equation, P is the applied pressure (in bar) and T the temperature (in K). ΔV_i and $\Delta \kappa_i$ are respectively the molal volume change in $cm^3\,mol^{-1}$

Table 2.2: Pressure dependence coefficients.

Constant	a_0	a_1	a_2	a_3
K_1	-25.50	-0.151	0.1271	—
K_2	-15.82	0.321	-0.0219	—
K_B	-29.48	0.295	0.1622	-0.002608
K_W	-20.02	—	0.1119	-0.001409
K_{Calc}	-48.76	—	0.5304	—
K_{Arag}	-45.96	—	0.5304	—

Constant	b_0	b_1	b_2
K_1	-0.00308	-0.000578	0.0000877
K_2	0.00113	-0.000314	-0.0001475
K_B	-0.00284	0.000354	—
K_W	-0.00513	—	0.0000794
K_{Calc}	-0.01176	—	0.0003692
K_{Arag}	-0.01176	—	0.0003692

All from MILLERO (1979), except K_W (MILLERO, pers. comm.).

and the molal compressibility change in $\text{cm}^3\,\text{mol}^{-1}\,\text{bar}^{-1}$ for the reaction described by K_i. $R = 8.314510\,\text{J}\,\text{mol}^{-1}\,\text{K}^{-1} = 83.14510\,\text{bar}\,\text{cm}^3\,\text{mol}^{-1}\,\text{K}^{-1}$ is the molar gas constant. MILLERO (1979) has fitted the values of ΔV_i and $\Delta\kappa_i$ to equations of the form

$$\Delta V_i = a_0 + a_1(S - 34.8) + a_2 t^\circ + a_3 t^{\circ\,2} \qquad (2.47)$$
$$\Delta\kappa_i = b_0 + b_1(S - 34.8) + b_2 t^\circ \qquad (2.48)$$

where S is the salinity on the practical salinity scale and t° the temperature in °C. The coefficients of these equations for the different equilibrium constants considered in this study are given in table 2.2.

2.4 Speciation of the Carbonate System from Total Alkalinity and Total Inorganic Carbon

Using the concepts defined and discussed in the previous sections, we will slightly adapt the definition of A_T for our study, in order to get a completely coherent system of chemical constants and of measurables. As a working

Table 2.3: Typical numerical values of the thermodynamic constants.

	$S = 35$ $T = 274.16$ K $P = 0$ bar	$S = 35$ $T = 293.16$ K $P = 0$ bar	$S = 35$ $T = 274.16$ K $P = 3,000$ bar
K_0	6.0460×10^{-2}	3.2398×10^{-2}	6.0460×10^{-2}
pK_0	1.219	1.490	1.219
K_1	8.1228×10^{-7}	1.2771×10^{-6}	1.1278×10^{-6}
pK_1	6.090	5.894	5.948
K_2	4.3799×10^{-10}	9.9669×10^{-10}	5.4005×10^{-10}
pK_2	9.359	9.001	9.268
K_B	1.2995×10^{-9}	2.2800×10^{-9}	1.8996×10^{-9}
pK_B	8.886	8.642	8.721
K_W	5.6135×10^{-15}	3.9012×10^{-14}	7.2228×10^{-14}
pK_W	14.251	13.409	14.141
K_{Calc}	4.2952×10^{-7}	4.3000×10^{-7}	7.9227×10^{-7}
pK_{Calc}	6.367	6.367	6.101
K_{Arag}	6.8298×10^{-7}	6.3665×10^{-7}	1.2142×10^{-6}
pK_{Arag}	6.166	6.179	5.916

Units are $\mathrm{mol\,(kg\text{-}SW)^{-1}\,atm^{-1}}$ for K_0, mol/kg-SW for K_1, K_2 and K_B, (mol/kg-SW)^2 for K_W, K_{Calc} and K_{Arag}.

definition, we will use

$$A_\text{T} = [\text{HCO}_3^-] + 2\,[\text{CO}_3^{2-}] + [\text{B(OH)}_4^-] + [\text{OH}^-]_\text{SWS} - [\text{H}^+]_\text{SWS}, \qquad (2.49)$$

where $[\text{HCO}_3^-]$, $[\text{CO}_3^{2-}]$ and $[\text{B(OH)}_4^-]$ are taken as total analytical concentrations, in agreement with the definitions of the various equilibrium constants, and where $[\text{H}^+]_\text{SWS}$ and $[\text{OH}^-]_\text{SWS}$ are as previously defined (section 2.2).

Rearranging the definitions of K_1 and K_2 (equations (2.26) and (2.27)), we obtain

$$[\text{CO}_{2(\text{aq})}^*] = [\text{HCO}_3^-]\,\frac{[\text{H}^+]_\text{SWS}}{K_1} \qquad (2.50)$$

$$[\text{CO}_3^{2-}] = [\text{HCO}_3^-]\,\frac{K_2}{[\text{H}^+]_\text{SWS}} \qquad (2.51)$$

C_T can then be rewritten as

$$\begin{aligned}
C_\text{T} &= [\text{CO}_{2(\text{aq})}^*] + [\text{HCO}_3^-] + [\text{CO}_3^{2-}] \\
&= [\text{HCO}_3^-]\left(\frac{[\text{H}^+]_\text{SWS}}{K_1} + 1 + \frac{K_2}{[\text{H}^+]_\text{SWS}}\right) \qquad (2.52)
\end{aligned}$$

In the same way, but furthermore taking (2.35) and the definition of K_W into account, we find that

$$\begin{aligned}
A_\text{CB} &= [\text{HCO}_3^-] + 2\,[\text{CO}_3^{2-}] + [\text{B(OH)}_4^-] \\
&= [\text{HCO}_3^-]\left(1 + \frac{2K_2}{[\text{H}^+]_\text{SWS}}\right) + \frac{K_\text{B}\,B_\text{T}}{K_\text{B} + [\text{H}^+]_\text{SWS}} \qquad (2.53)
\end{aligned}$$

and

$$A_\text{T} = A_\text{CB} + \frac{K_\text{W}}{[\text{H}^+]_\text{SWS}} - [\text{H}^+]_\text{SWS} \qquad (2.54)$$

By eliminating $[\text{HCO}_3^-]$ between (2.52) and (2.53), we arrive, after some straightforward algebraic transformations and regroupings of the differents terms, at the following cubic equation

$$\begin{aligned}
A_\text{CB}H^3 &+ \big(K_\text{B}(A_\text{CB} - B_\text{T}) + K_1(A_\text{CB} - C_\text{T})\big)H^2 \\
&+ K_1\big(K_\text{B}(A_\text{CB} - B_\text{T} - C_\text{T}) + K_2(A_\text{CB} - 2C_\text{T})\big)H \\
&+ K_1 K_2 K_\text{B}\big(A_\text{CB} - B_\text{T} - 2C_\text{T}\big) = 0 \qquad (2.55)
\end{aligned}$$

where H stands as a shorthand for $[\text{H}^+]_\text{SWS}$. The speciation of a given sample, of known temperature T, salinity S and submitted to a pressure P, can now be iteratively calculated from its total alkalinity A_T and its dissolved inorganic carbon C_T using equations (2.54) and (2.55).

To start, (2.55) is solved for H ($= [H^+]_{SWS}$) with $A_{CB} = A_T$. This initial value of H is used to calculate a new A_{CB} from (2.54). This estimate of A_{CB} is then used to recalculate H from (2.55), which again serves to refine the value of A_{CB} using equation (2.54). This iteration is continued until the desired precision on H is reached. In section 4.5.2, we present a somewhat different procedure where we resolve the two equations simultaneously using the Newton-Kantorovich method. In most cases, that method requires three iterations to reach a precision of 10^{-13} mol/kg-SW for H.

Once the value of H corresponding to the given C_T and A_T is determined, the complete speciation derives from

$$\frac{[CO_{2(aq)}^*]}{C_T} = \frac{H^2}{H^2 + K_1 H + K_1 K_2} \qquad (2.56)$$

$$\frac{[HCO_3^-]}{C_T} = \frac{K_1 H}{H^2 + K_1 H + K_1 K_2} \qquad (2.57)$$

$$\frac{[CO_3^{2-}]}{C_T} = \frac{K_1 K_2}{H^2 + K_1 H + K_1 K_2} \qquad (2.58)$$

obtained by rearranging (2.52) and by combining (2.52) with (2.50) and (2.51) respectively. p_{CO_2} can then be calculated from (2.24).

2.5 Impact of Total Alkalinity Approximations on Carbonate System Speciation

The complete speciation of the carbonate system as outlined in the previous section rests upon the resolution of the combined equations (2.54) and (2.55), which can be merged into a single polynomial equation of fifth degree. In order to trim the cost of numerical calculations for long-term simulations that rely on frequent recalculations of this speciation, it is useful to examine how well A_T can be approximated by A_{CB}, or even by A_C, without altering the behaviour of the whole system too much. With $A_T \simeq A_{CB}$, the third degree equation (2.55) would be sufficient to determine the distributions of the individual species. If on the other hand $A_T \simeq A_C$ is justified, we may replace (2.55) by the second degree equation

$$A_C H^2 + K_1 (A_C - C_T) H + K_1 K_2 (A_C - 2C_T) = 0. \qquad (2.59)$$

2.5.1 Effects on Absolute Speciation

In order to examine the quality of A_C and A_{CB} as approximations for A_T, we have solved the combined equations (2.54) and (2.55) for alkalinity val-

ues between 2.2 and 2.7 meq/kg-SW, and for C_T values between 1.9 and 2.5 mmol/kg-SW, using the two proposed approximations. The calculations were performed with the second order method described in section 4.5.2. The iterative procedure was stopped once the relative difference between two consecutive values of H fell below 10^{-8}. This is much better than the accuracy which is generally required. Contour plots for p_{CO_2} are reported in figures 2.2, corresponding to $S = 35$ and $T = 293.16$ K, or 20 °C, and 2.3, where $S = 35$ and $T = 274.16$ K, or 1 °C. In both figures, the results for the parts (a) are based upon the assumption that $A_T \simeq A_C$. For the parts (b), we use $A_T \simeq A_{CB}$, and for parts (c), the complete definition from equation (2.49). From parts (d) and (e), which show respectively the differences (b) − (a) and (c) − (b), it clearly appears that the addition of $B(OH)_4^-$ as a contributor leads to very important changes of p_{CO_2} (d). This means that A_C should not be used as an approximation for A_T, and that $B(OH)_4^-$ must be taken into account unless the expected results are only used for purely qualitative purposes. At first sight, it would seem that $[OH^-]_{SWS} − [H^+]_{SWS}$ should also be included, at least in warm waters. Fortunately, temperate and warm surface waters are characterized by C_T and A_T values of about 1.95 ± 0.05 mmol/kg-SW and 2.30 ± 0.05 meq/kg-SW respectively (see figure 2.1). In that region, the effect on p_{CO_2} due to the inclusion of $[OH^-]_{SWS} − [H^+]_{SWS}$ is only of the order of 5 μatm, as can be seen in figure 2.2-e. Such a small difference can fairly well be neglected for our study. In cold surface waters, the effect of taking $[OH^-]_{SWS} − [H^+]_{SWS}$ into account is anyway in all cases less than 2 μatm for p_{CO_2}. A figure corresponding to the typical deep water salinity, temperature and pressure conditions at a depth of 3,000 m would be essentially indistinguishable from 2.3. In deep-sea environments, $[CO_3^{2-}]$ is anyway more important to study than p_{CO_2} because of its determining role in the preservation and dissolution cycles of carbonate minerals raining down from the surface. In figure 2.4, we have therefore preferred to represent contour lines for the carbonate ion concentration under the typical pressure conditions at a depth of 3,000 m, for $S = 35$ and $T = 274.16$ K, i.e. 1 °C. With regard to the various approximations adopted for A_T, the different parts of this figure are again calculated under the same assumptions as their counterparts from figures 2.2 and 2.3. $[CO_3^{2-}]$ decreases as more contributors are taken into account when estimating A_T. The inclusion of $B(OH)_4^-$ again leads to the most significant changes. To emphasize the significance of these differences, we should mention that increasing $[CO_3^{2-}]$ by 20 μmol/kg-SW in the deep sea shifts the carbonate saturation depths down by about 1.5 km. Hence, even if a study requires only moderate accuracy on p_{CO_2} and $[CO_3^{2-}]$, it is not reasonable to use A_C as an approximation to A_T.
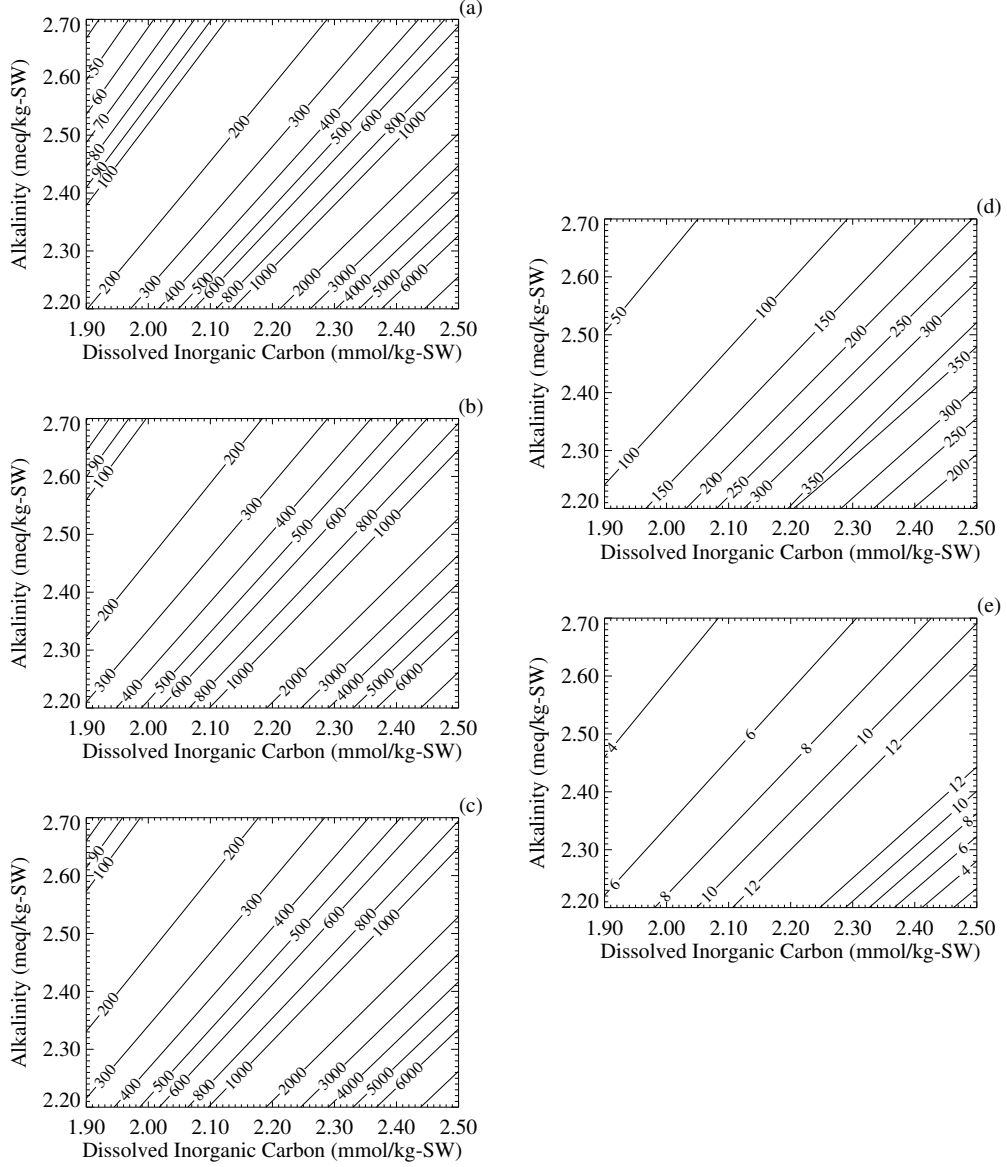
Figure 2.2: Variations of p_{CO_2} (contours in μatm) in warm surface waters ($T = 293.16$ K and $S = 35$) as a function of dissolved inorganic carbon and alkalinity, calculated by adopting different approximations for A_T: (a) — using $A_T \simeq A_C$, i.e., neglecting the contributions from $B(OH)_4^-$, OH^-_{SWS} and H^+_{SWS} to A_T, defined by (2.49); (b) — using $A_T \simeq A_{CB}$, i.e., neglecting only the contributions from OH^-_{SWS} and H^+_{SWS}; (c) — using the complete definition (2.49); (d) = (b) − (a); (e) = (c) − (b).
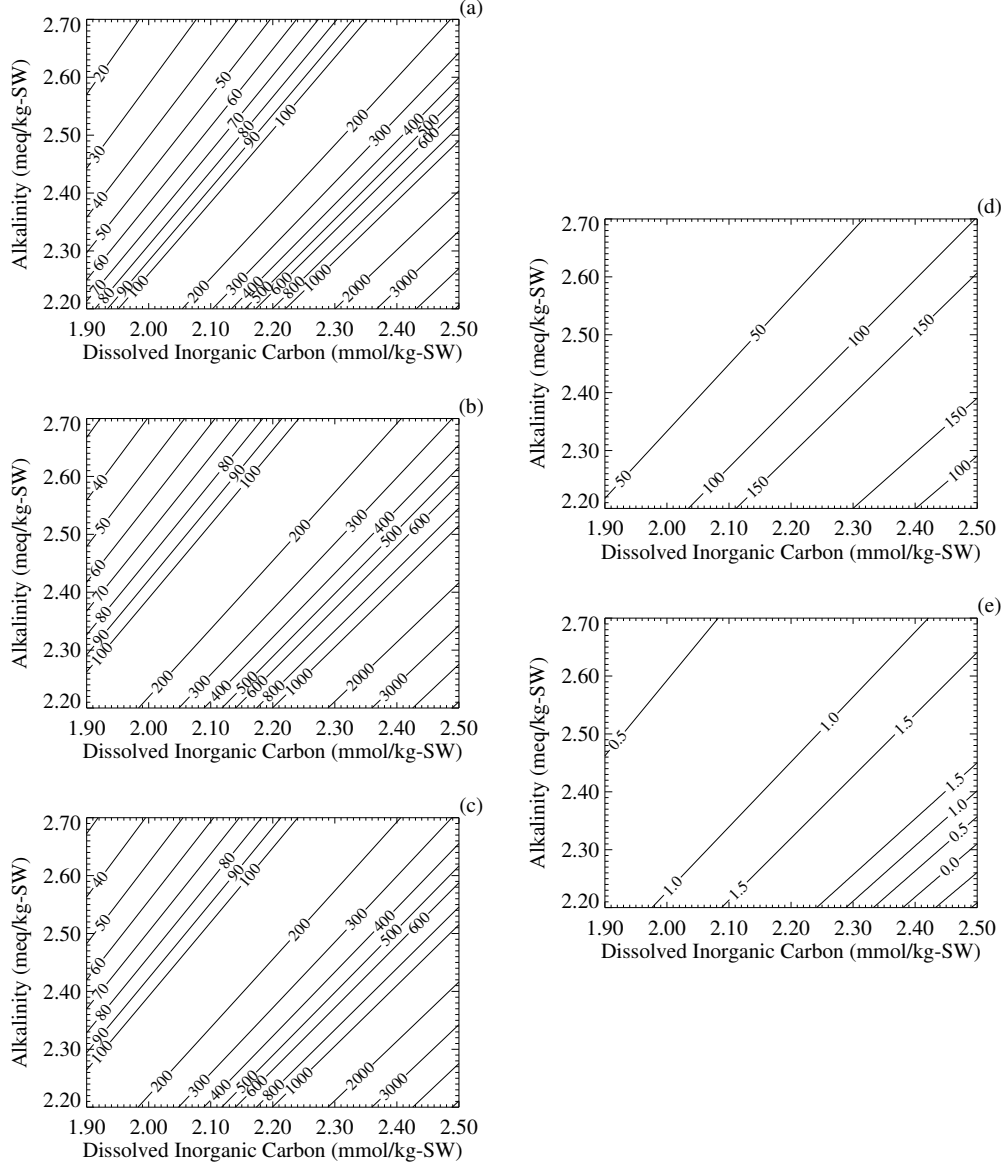
Figure 2.3: Variations of p_{CO_2} (contours in μatm) in cold surface waters ($T = 274.16$ K and $S = 35$) as a function of dissolved inorganic carbon and alkalinity, calculated by adopting different approximations for A_T: (a) — using $A_T \simeq A_C$, i.e., neglecting the contributions from $B(OH)_4^-$, OH^-_{SWS} and H^+_{SWS} to A_T, defined by (2.49); (b) — using $A_T \simeq A_{CB}$, i.e., neglecting only the contributions from OH^-_{SWS} and H^+_{SWS}; (c) — using the complete definition (2.49); (d) = (b) − (a); (e) = (c) − (b).
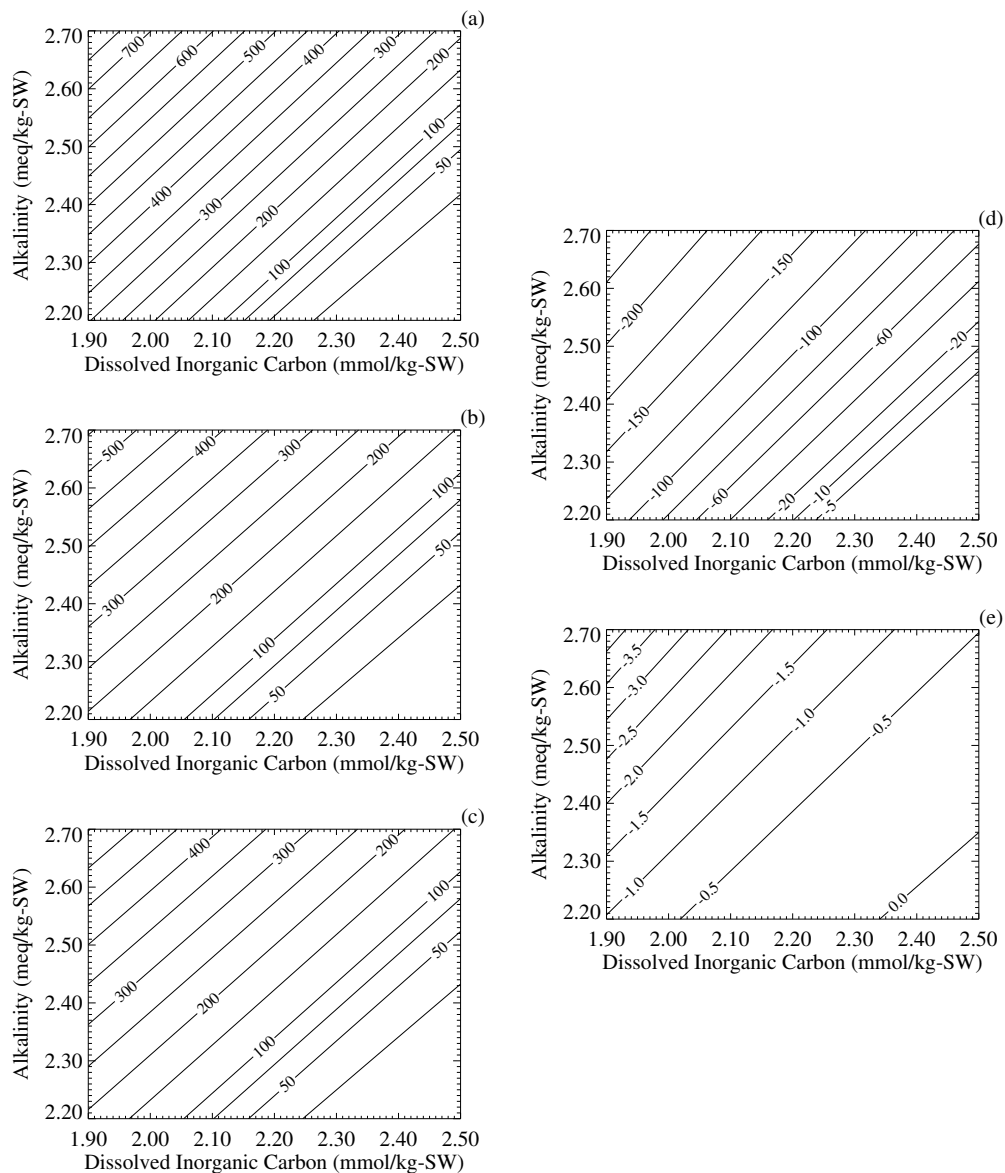
Figure 2.4: Variations of $[CO_3^{2-}]$ (contours in μmol/kg-SW) as a function of dissolved inorganic carbon and alkalinity in waters at a depth of 3,000 m ($T = 274.16$ K and $S = 35$), calculated by adopting different approximations for A_T: (a) — using $A_T \simeq A_C$, i.e., neglecting the contributions from $B(OH)_4^-$, OH^-_{SWS} and H^+_{SWS} to A_T, defined by (2.49); (b) — using $A_T \simeq A_{CB}$, i.e., neglecting only the contributions from OH^-_{SWS} and H^+_{SWS}; (c) — using the complete definition (2.49); (d) = (b) − (a); (e) = (c) − (b).

2.5.2 Effect on Sensitivity to Perturbations

It could now still be argued that A_C may nevertheless be used as a relevant capacity factor to model the evolution of the carbonate system in time. Before comparing with real-ocean A_T data, the calculated A_C could be corrected to yield A_T values by adding

$$[\text{B(OH)}_4^-] + [\text{OH}^-]_{\text{sws}} - [\text{H}^+]_{\text{sws}} = \frac{K_B\, B_T}{K_B + [\text{H}^+]_{\text{sws}}} + \frac{K_W}{[\text{H}^+]_{\text{sws}}} - [\text{H}^+]_{\text{sws}}$$

using the $\text{H}^+{}_{\text{sws}}$-values calculated from (2.59). Unfortunately, the sensitivity of the system changes when it is described in terms of the A_C-C_T pair rather than A_T-C_T. To illustrate this, we will start from one of the hypotheses related to the glacial-interglacial CO_2 variations in the atmosphere. Broecker and Peng (1989) proposed that the observed increase of atmospheric CO_2 levels at the close of the last glacial period were caused by a decrease of alkalinity in Antarctic surface waters. In figure 2.5, we have represented the response of p_{CO_2} in a typical present-day Antarctic surface water sample, where $C_T = 2.170$ mmol/kg-SW and $A_T = 2.350$ meq/kg-SW, and correspondingly, $A_C = 2.283$ meq/kg-SW and $A_{CB} = 2.349$ meq/kg-SW, to hypothetical alkalinity and total dissolved inorganic carbon changes. Parts (a), (b) and (c) show the p_{CO_2} variations resulting from these changes in case the system is described in terms of A_C, A_{CB} and A_T respectively. It can be seen that, at constant C_T, a p_{CO_2} decrease of 100 μatm requires an alkalinity increase of only 0.065 meq/kg-SW when A_C is used, compared to 0.093 meq/kg-SW with A_{CB} and 0.094 meq/kg-SW with A_T. For identical alkalinity changes (which could be due to varying riverine bicarbonate input rates for example, which only indirectly influence B(OH)_4^- concentrations), a system described by A_C and C_T is of the order of 20% more sensitive with respect to p_{CO_2} than if it is described by A_T and C_T. The sensitivities of A_{CB}-C_T and A_T-C_T on the other hand differ by less than 1%.
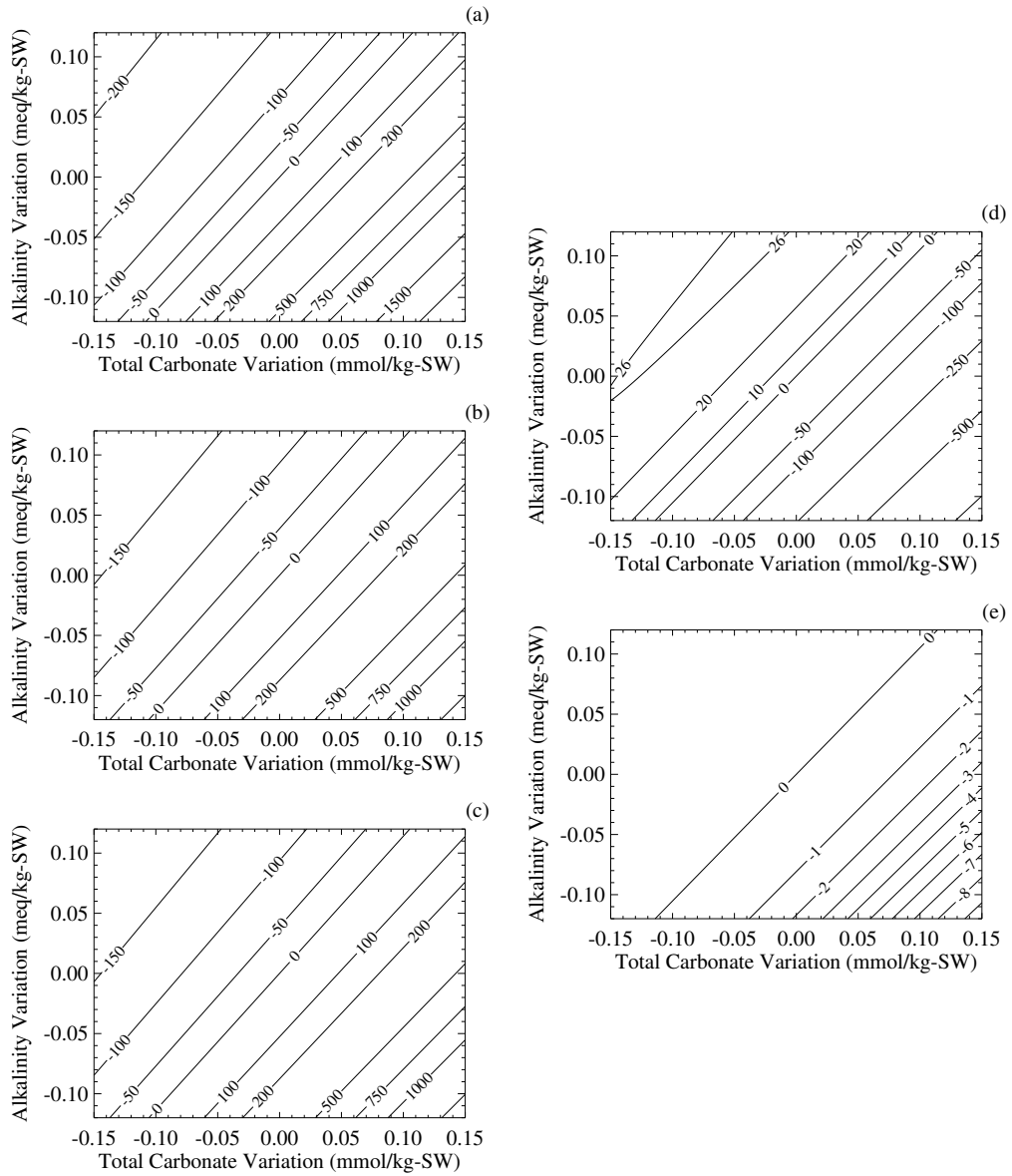
Figure 2.5: Changes of p_{CO_2} (contours in μatm) produced by alkalinity and total carbonate variations applied to a typical Antarctic surface water sample ($T = 274.16$ K, $S = 35$, $C_T = 2.170$ mmol/kg-SW and $A_T = 2.350$ meq/kg-SW, leading to $p_{CO_2} = 281$ μatm). The different parts represent the response of the system described in terms of the A_C-C_T pair (a), of A_{CB}-C_T (b) or of A_T-C_T; (d) = (b) − (a) and (e) = (c) − (b) reflect the sensitivity differences among these pairs. The reference points in part (a), $A_C = 2.283$ meq/kg-SW, and in part (b), $A_{CB} = 2.349_2$ meq/kg-SW, correspond to the A_T value mentioned above.
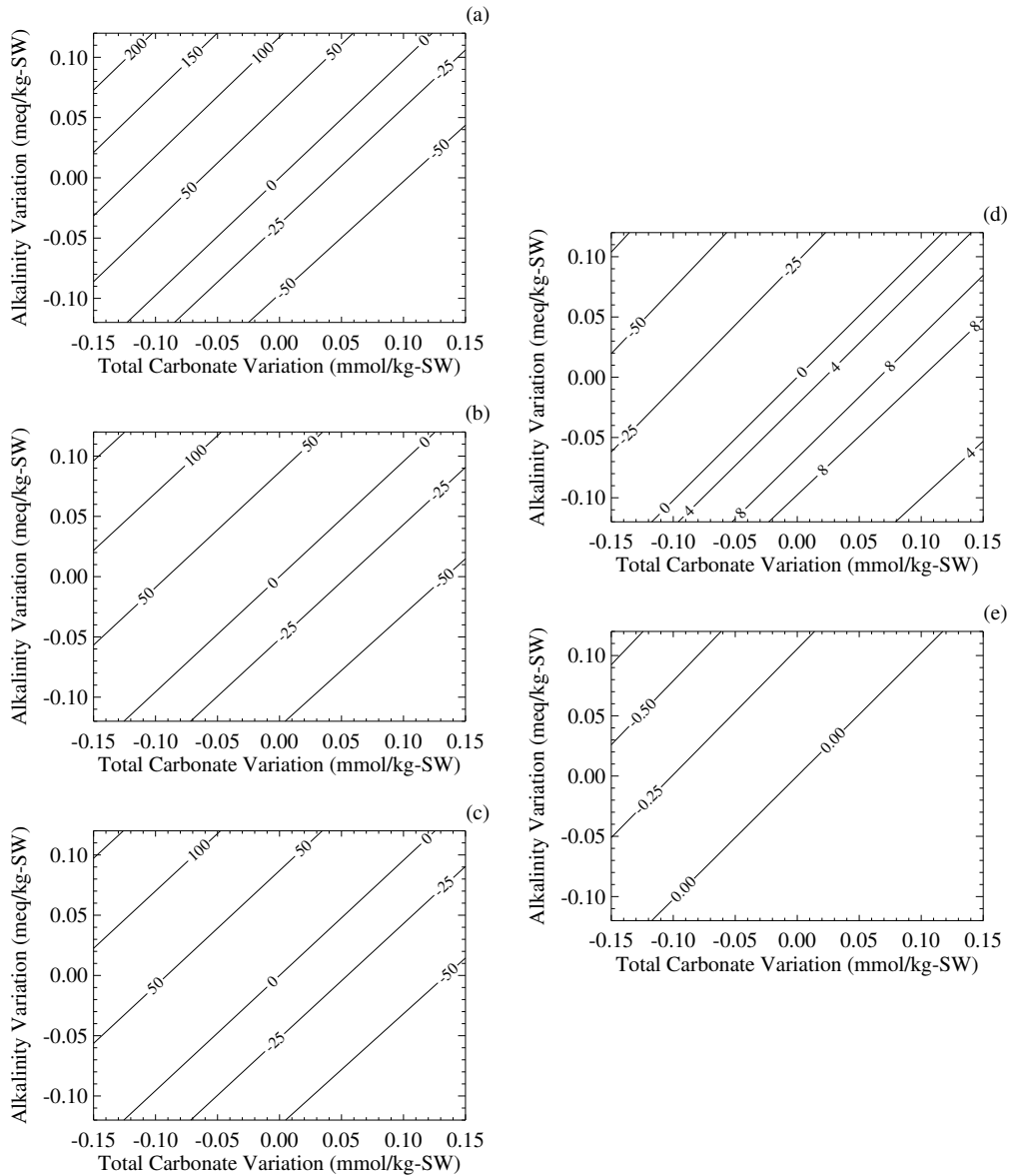
Figure 2.6: Changes of $[CO_3^{2-}]$ (contours in μmol/kg-SW) produced by alkalinity and total carbonate variations applied to a sample of average Pacific deep water (at a depth of 3,000 m, with $T = 274.16$ K, $S = 35$, $C_T = 2.320$ mmol/kg-SW and $A_T = 2.420$ meq/kg-SW, leading to $[CO_3^{2-}] = 81$ μmol/kg). Parts (a), (b) and (c) represent the response depending on whether the A_C-C_T, the A_{CB}-C_T or the A_T-C_T pair is used to trace the system. As previously, (d) = (b) $-$ (a) and (e) = (c) $-$ (b). The reference points in part (a), $A_C = 2.372$ meq/kg-SW, and in part (b), $A_{CB} = 2.419_5$ meq/kg-SW, correspond to the A_T value mentioned above.

Chapter 3

Weathering and the Carbon Cycle: The Silicate Weathering Hypothesis

Atmospheric CO_2 levels are driven by the dissolved inorganic carbon C_T and the total alkalinity A_T concentrations in the surface ocean. Figure 3.1 gives a schematic overview of the sources and sinks of these two quantities. On 100 kyr and longer time scales, their evolution is determined by the interaction of the ocean (and the atmosphere) with the lithospheric crust. We focus here on the *inorganic* exchanges of carbon between these two reservoirs. Rigorously speaking, we may of course not neglect *organic* carbon exchanges. As seen in chapter 1, the organic matter transferred from the surface to the deep ocean is almost entirely recycled. Less than 1% of the export production survives and gets buried into the sediments. The deposition of organic matter on the continental shelf areas is, however, by no means negligible. But we assume here that this deposition is balanced by the riverine input of "elemental" carbon or kerogen from continental shale erosion. We thus disregard the organic exchanges between the lithosphere and the ocean-atmosphere system and assume that input to and output from the oceans constantly balance each other. The organic cycle is of course only disregarded for the global budget. It must still be considered within the ocean in order to obtain realistic CO_2 partial pressures in the surface ocean, and hence in the atmosphere.
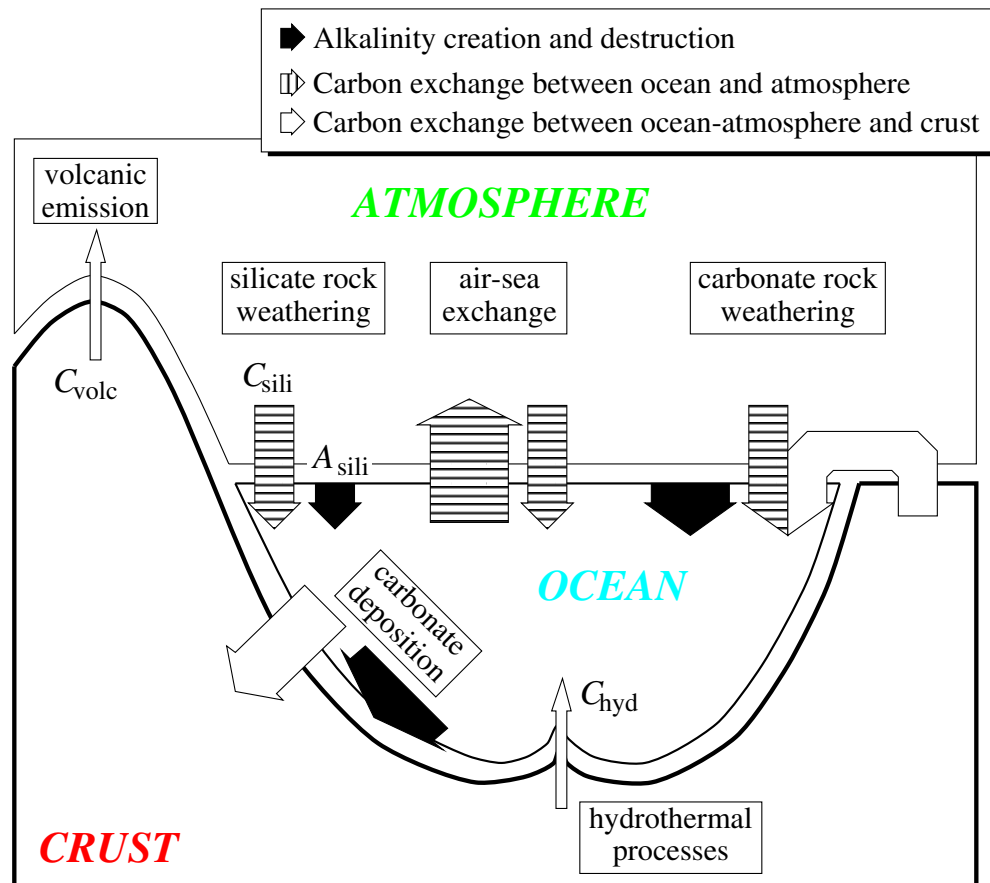
Figure 3.1: Schematic view of the global carbon cycle on geological time scales. White arrows represent carbon fluxes (plain — between the lithospheric crust and the ocean-atmosphere, hatched — internal to the ocean-atmosphere system) and black ones represent the corresponding creation and destruction of alkalinity. The indicated flux names are those used for the calculations of section 3.2.

3.1 Carbon-Alkalinity Systematics Related to Carbon Cycling

3.1.1 Sinks of Carbon and Alkalinity in the Ocean

When neglecting carbon exchange by organic fluxes, the only sink of carbon and alkalinity out of the ocean — and also out of the combined ocean-atmosphere reservoir — is then the deposition of biogenic $CaCO_3$ (including coral reef production). This loss can be written as

$$Ca^{2+} + CO_3^{2-} \longrightarrow CaCO_3 \tag{3.1}$$

or equivalently by

$$Ca^{2+} + 2\,HCO_3^- \longrightarrow CaCO_3 + CO_2 + H_2O, \tag{3.2}$$
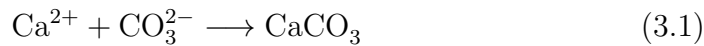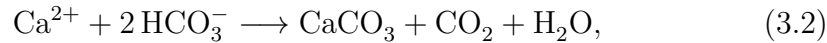
to emphasize the fact that HCO_3^-, and not CO_3^{2-}, is the major component of C_T. This precipitation is obviously characterized by a $\Delta C_T : \Delta A_T$ ratio of 1:2.

3.1.2 Sources of Carbon and Alkalinity to the Ocean

The source for the oceans, i.e., the riverine input of weathering products coming from the continental surface is more complex due to the different contributors that must be considered: carbonate and silicate rocks. The primary minerals of these rocks get dissolved when they come into contact with water in the soils. For a few rare minerals, such as gypsum ($CaSO_4$) or halite ($NaCl$) for example, dissolution results from the contact with the water itself. Generally, dissolution takes place by the action of an acid, mainly *carbonic* and *sulphuric acid* formed through microbiological activity in the soils.

Carbonic acid gets produced from CO_2 deriving from the oxidation of organic matter in the soils:

$$CO_2 + H_2O \longrightarrow H_2CO_3 \longrightarrow HCO_3^- + H^+. \tag{3.3}$$
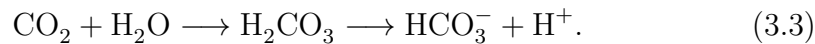
Sulphuric acid stems from the oxidation of sulphide minerals, which is almost always microbially catalyzed (BERNER and BERNER, 1987). The most widespread sulphide mineral is pyrite (FeS_2) which gets oxidized to ferric hydroxide and sulphuric acid according to

$$4\,FeS_2 + 15\,O_2 + 14\,H_2O \longrightarrow 4\,Fe(OH)_3 + 8\,H_2SO_4 \tag{3.4}$$

$$8\,H_2SO_4 \longrightarrow 8\,SO_4^{2-} + 16\,H^+. \tag{3.5}$$
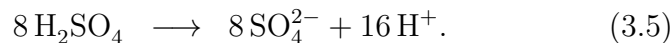
The dissolution of the primary minerals is then initiated by the produced hydrogen ions which can replace cations at the mineral surface.

According to HOLLAND (1978), about 30% of the river-borne SO_4^{2-} originates from the weathering of sulphides. A similar figure is used by MEYBECK (1979) who estimates this amount at about 23 out of 81.5 μmol of SO_4^{2-} dissolved in a liter of average river water. BERNER and BERNER (1987) calculate that pyrite-derived sulphate represents 11% of the total sulphate in present-day average river water. If we correct this fraction for the anthropogenic pollution, which they estimate at 43% of the total, we find that pyrite oxidation contributes about 20% of the sulphate from natural sources. Average river water thus contains about 20 μmol/l of sulphate coming from pyrite. In terms of hydrogen ion yield, this is equivalent to 40 μmol/l of bicarbonate. The actual bicarbonate concentration in average river water is 846 μmol/l (MEYBECK, 1979). It is generally estimated that close to 65% of this (550 μmol/l) derive from soil CO_2, due to organic matter oxidation (MEYBECK, 1986; BERNER and BERNER, 1987). Carbonic acid is thus more than 10 times as important as sulphuric acid in providing hydrogen ions to attack the rock minerals. In this study we will therefore neglect the role of pyrite oxidation, and assume that carbonic acid derived from soil organic matter oxidation is the only acid agent in the weathering processes. Since the carbon of the organic matter that gets oxidized in the soils ultimately comes from the atmosphere, we will furthermore not distinguish between soil and atmospheric CO_2. Figure 3.1 is already based upon these simplifications.

In the following, we will thus quantify the erosional fluxes in terms of atmospheric CO_2 consumed, as we are mainly interested in atmospheric CO_2 levels.

Carbonate Dissolution

Carbonate minerals weather *congruently*, i.e., by simple dissolution under the action of acid, deriving here from soil/atmospheric CO_2:

$$CaCO_3 + CO_2 + H_2O \longrightarrow Ca^{2+} + 2\,HCO_3^- \qquad (3.6)$$
$$CaMg(CO_3)_2 + 2\,CO_2 + 2\,H_2O \longrightarrow Ca^{2+} + Mg^{2+} + 4\,HCO_3^-. \quad (3.7)$$
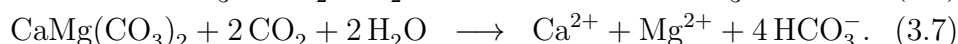
For each mole of atmospheric CO_2 so consumed, two equivalents of alkalinity are delivered to the oceans together with another mole of carbon, originating from the rock.

Silicate Dissolution

Unlike carbonate rocks, silicate rocks do not supply any carbon by themselves. The whole carbon involved in silicate rock weathering is taken from the atmosphere. Silicate mineral dissolution is furthermore generally *incongruent*, with reprecipitation of secondary minerals (BERNER and BERNER, 1987). Both of these characteristics are well illustrated by a few typical weathering reactions (GARRELS, 1967; GARRELS and MACKENZIE, 1971; BERNER and BERNER, 1987; MORSE and MACKENZIE, 1990; FAURE, 1991):

- weathering of albite (Na-plagioclase feldspar) with precipitation of kaolinite

$$2\,NaAlSi_3O_8 + 2\,CO_2 + 11\,H_2O \longrightarrow$$
$$Al_2Si_2O_5(OH)_4 + 2\,Na^+ + 2\,HCO_3^- + 4\,H_4SiO_4, \qquad (3.8)$$
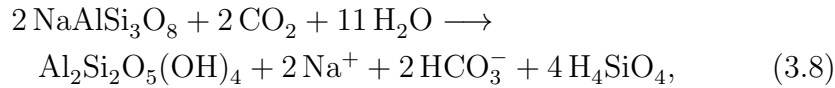
- weathering of anorthite (Ca-plagioclase feldspar) with precipitation of kaolinite

$$CaAl_2Si_2O_8 + 2\,CO_2 + 3\,H_2O \longrightarrow$$
$$Al_2Si_2O_5(OH)_4 + Ca^{2+} + 2\,HCO_3^- \qquad (3.9)$$
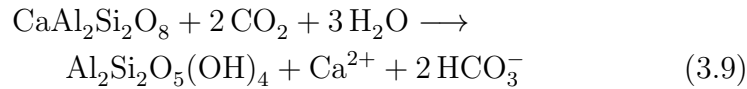
- weathering of microcline (K-feldspar) with precipitation of a mineral similar to montmorillonite (pyrophillite, the prototype three-layer clay)

$$2\,KAlSi_3O_8 + 2\,CO_2 + 6\,H_2O \longrightarrow$$
$$Al_2Si_4O_{10}(OH)_2 + 2\,K^+ + 2\,HCO_3^- + 2\,H_4SiO_4, \qquad (3.10)$$
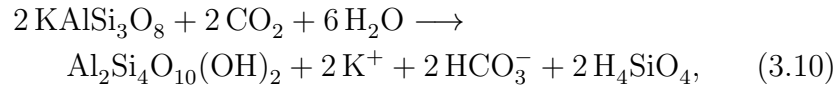
- weathering of chlorite with precipitation of kaolinite

$$Mg_5Al_2Si_3O_{10} + 10\,CO_2 + 5\,H_2O \longrightarrow$$
$$Al_2Si_2O_5(OH)_4 + 5\,Mg^{2+} + 10\,HCO_3^- + H_4SiO_4 \qquad (3.11)$$
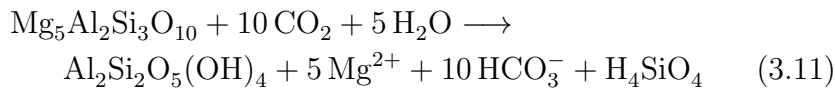
- weathering of microcline with precipitation of gibbsite (aluminium hydroxide, insoluble under common pH conditions)

$$KAlSi_3O_8 + CO_2 + 4\,H_2O \longrightarrow$$
$$Al(OH)_3 + K^+ + HCO_3^- + H_4SiO_4, \qquad (3.12)$$
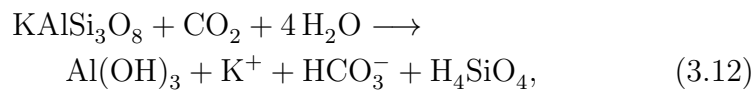
It would be possible to list several pages of such dissolution reactions. All of these examples fit to the following general expression of chemical silicate mineral breakdown:

$$\text{silicate mineral } + \underbrace{n_{\text{bic}} \, CO_2}_{\text{soil/atm}} + \text{ water } \longrightarrow \text{ secondary minerals } +$$

$$n_{\text{bic}} \text{ cation equivalents } + n_{\text{bic}} \, HCO_3^- + n_{\text{sil}} \, H_4SiO_4,$$
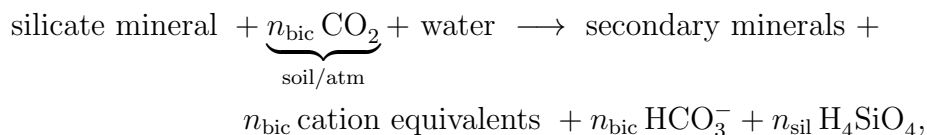
where the "secondary minerals" include all kinds of newly formed minerals (clays, oxides etc.). The type of mineral formed from the dissolution of a given silicate mineral assemblage depends on the environmental conditions, i.e., the pH of the soil solution, the drainage and flushing, and thus removal of the dissolved weathering products.

 For our study, only two points concerning the geochemistry of silicate weathering are important:

1. As can be seen from the examples given above, n_{bic} and n_{sil} depend on the type of silicate material weathered and on the type of secondary minerals produced. The most important of the quoted reactions are probably (3.8) and (3.9), the dissolution of albite and anorthite. Plagioclase feldspar, which is a solid solution of these two minerals in continuous proportions, represents the most abundant silicate mineral in the Earth's crust that also undergoes weathering (GARRELS and MACKENZIE, 1971; BERNER and BERNER, 1987; MORSE and MACKENZIE, 1990). The stoichiometries of the two reactions should however not be taken at face value to calculate the global $n_{\text{bic}}/n_{\text{sil}}$ ratio, since kaolinite is not necessarily the final weathering product. MORSE and MACKENZIE (1990), basing themselves essentially on the works of GARRELS and MACKENZIE (1971), HOLLAND (1978) and MEYBECK (1979), called upon the four silicate minerals albite, microcline, anorthite and chlorite as the sources of Na^+, K^+, Ca^{2+} and Mg^{2+} respectively for the part of the riverine load that they attribute to silicate weathering. They find that $n_{\text{bic}}/n_{\text{sil}} = 1.75$ mol/mol in their global-scale balance.

2. For each mole of atmospheric CO_2 consumed by silicate rock weathering, only one equivalent of alkalinity gets supplied to the oceans.

We will come back to the first point later in this study: in chapter 6 we discuss the global-scale characteristics of the $n_{\text{bic}}/n_{\text{sil}}$ ratio, and show that it can be interpreted as a weathering intensity index.

For the moment, let us focus on the last of these two points, which has quite far-reaching consequences for the long-term global budgets of carbon and alkalinity in the ocean-atmosphere systems. It is indeed at the origin of a constraint upon the weathering rate of silicate rocks. In the next section, we show how to derive this constraint from the above observations.

3.2   Long-Term Carbon-Alkalinity Coupling

The residence times of carbon and alkalinity in the ocean-atmosphere system (the continental biosphere could also be included) are key parameters for studying the carbon balance of the ocean-atmosphere system. The pre-industrial contents of carbon and alkalinity in this system can be estimated at 3.1×10^{18} mol C and 3.3×10^{18} eq, their total outputs at 42.5×10^{12} mol C/yr (11×10^{12} mol C/yr in organic form and 31.5×10^{12} mol C/yr as carbonate) and 63×10^{12} eq/yr (represented by the carbonate deposition of 31.5×10^{12} mol CaCO$_3$/yr — see chapter 1 for details on these figures). We can thus calculate residence times of 73,000 years for carbon and of 52,000 years for alkalinity. These figures are about a factor of two smaller than those generally given in the literature, often based on river inputs or on estimates of the long-term outputs, or neglecting the organic carbon deposition (see, e.g., FRANÇOIS and GODDÉRIS, 1997). If we neglect organic deposition, the residence time of carbon comes close to 100,000 years.

When dealing with the evolution of the carbon cycle on time scales of a million years and longer, where fluctuations such as the glacial-interglacial ones are not of interest, the budgets of carbon and alkalinity in the combined ocean-atmosphere reservoirs can then be considered to be close to steady-state. In studies of the Phanerozoic and Cenozoic[†] carbon cycle (e.g., WALKER et al., 1981; BERNER et al., 1983; BERNER, 1990, 1991; FRANÇOIS and WALKER, 1992; FRANÇOIS et al., 1993) it has been shown that the simultaneous balance of these two budgets requires an additional carbon flux from the crust to the ocean-atmosphere system, besides the weathering and sediment accumulation fluxes already mentioned before. This flux, which has to supply half of the CO$_2$ consumed by silicate weathering is represented by the outgassing of CO$_2$ through volcanic processes (hydrothermal and metamorphic).

This constraint on the CO$_2$ consumption rate by silicate rock weathering can easily be derived from the relationships between the carbon and alkalinity fluxes under steady state conditions. These relationships can be formulated

---

[†]The Phanerozoic covers the past 570 million years, the Cenozoic the past 65 million years.

as a small system of linear equations. To establish this system, we use the following notations for the different fluxes (see also figure 3.1):

$C_{\text{volc}}^{\text{crust}}$ volcanic input of CO_2 into the atmosphere

$C_{\text{hyd}}^{\text{crust}}$ input of CO_2 into the ocean by hydrothermal activity

$C_{\text{sili}}^{\text{atm}}$ atmospheric CO_2 consumed for silicate weathering

$C_{\text{carb}}^{\text{atm}}$ atmospheric CO_2 consumed for carbonate weathering

$C_{\text{carb}}^{\text{crust}}$ carbon liberated during carbonate rock weathering

$C_{\text{sed}}^{\text{oce}}$ carbon deposited on the ocean floor as $CaCO_3$

$C_{\text{a-s}}^{\text{oce}}$ CO_2 transferred from the sea to the atmosphere[‡]

$C_{\text{a-s}}^{\text{atm}}$ CO_2 transferred from the atmosphere to the sea[‡]

A_{sili} alkalinity formed by silicate rock weathering

A_{carb} alkalinity formed by carbonate rock weathering

A_{sed} alkalinity lost by $CaCO_3$ deposition

The different fluxes in this list are labeled as follows:

- C and A are respectively carbon and alkalinity fluxes;

- subscripts denote the processes: 'volc' for volcanic, 'hyd' for hydrothermal, 'sili' for silicate rock weathering, 'carb' for carbonate rock weathering, 'sed' for $CaCO_3$ deposition in the sediments and 'a-s' for air-sea CO_2 transfer;

- for carbon fluxes, superscripts denote the respective origin: 'crust' for crustal, 'atm' for atmospheric and 'oce' for oceanic.

The total contents of carbon in the combined oceanic and atmospheric reservoirs and of alkalinity in the ocean are denoted $\widehat{C}$ and $\widehat{A}$.

The intrinsic characteristics of carbonate and silicate dissolution reactions, that we have emphasized in the previous section, immediately lead to the following relationships, where carbon fluxes must be expressed in moles and alkalinity fluxes in equivalents per unit time:

$$C_{\text{carb}}^{\text{crust}} = C_{\text{carb}}^{\text{atm}} \tag{3.13}$$

$$A_{\text{sili}} = C_{\text{sili}}^{\text{atm}} \tag{3.14}$$

$$A_{\text{carb}} = C_{\text{carb}}^{\text{atm}} + C_{\text{carb}}^{\text{crust}} \tag{3.15}$$

$$A_{\text{sed}} = 2\, C_{\text{sed}}^{\text{oce}} \tag{3.16}$$

[‡]$C_{\text{a-s}}^{\text{oce}}$ and $C_{\text{a-s}}^{\text{atm}}$ are in fact not necessary for the total budget calculations made here. They are only included for completeness.

The steady-state assumption for the carbon and alkalinity budgets in the combined ocean-atmosphere reservoirs translates to

$$\frac{d\widehat{C}}{dt} \;=\; C_{\text{volc}}^{\text{crust}} + C_{\text{hyd}}^{\text{crust}} + C_{\text{carb}}^{\text{crust}} - C_{\text{sed}}^{\text{oce}} \;=\; 0 \tag{3.17}$$

$$\frac{d\widehat{A}}{dt} \;=\; A_{\text{sili}} + A_{\text{carb}} - A_{\text{sed}} \;=\; 0 \tag{3.18}$$

Introducing (3.14), (3.15) and (3.16) into (3.18) and taking (3.13) into account, we find that

$$C_{\text{sed}}^{\text{oce}} = \tfrac{1}{2} C_{\text{sili}}^{\text{atm}} + C_{\text{carb}}^{\text{crust}} \tag{3.19}$$

This means that on time scales of 100 kyr and more, the oceanic sediments take up half of the carbon brought into the oceans as bicarbonate by rivers. By introducing (3.19) into (3.17), we obtain the following identity:

$$\tfrac{1}{2} C_{\text{sili}}^{\text{atm}} = C_{\text{volc}}^{\text{crust}} + C_{\text{hyd}}^{\text{crust}} \tag{3.20}$$

This is a fundamental relationship relating the long-term average consumption of atmospheric CO_2 by silicate rock weathering to the volcanic and hydrothermal outputs.

3.3 Carbon-Alkalinity Coupling over Glacial-Interglacial Time Scales: The Silicate Weathering Hypothesis

The time window of interest in our study is nevertheless considerably shorter than the million year scale characterizing the studies on the Phanerozoic and Cenozoic carbon cycle previously mentioned. The typical duration of a glacial-interglacial climate oscillation is 100,000 years, comparable to the residence times of carbon and alkalinity in the ocean-atmosphere system. Important fluctuations took place on much shorter time scales than this. The CO_2 increase from the glacial to the interglacial level essentially completes in about 10,000 years. The assumption of permanent steady-state behaviour of the carbon and alkalinity cycles adopted in the studies on the Phanerozoic and Cenozoic may not necessarily hold over a whole glacial-interglacial cycle. Although it cannot be excluded that the observed CO_2 variations are only due to redistributions among the sub-reservoirs of the ocean-atmosphere (-biosphere) system — in which case the steady-state assumption for the global carbon and alkalinity budgets would possibly be correct — we think that, in

general, a steady-state hypothesis represents a rather strong constraint that should be considered only very carefully.

With the same notation as above for the different fluxes, the two budgets can then be written in their general form, as

$$\frac{d\widehat{C}}{dt} = C_{\text{volc}}^{\text{crust}} + C_{\text{hyd}}^{\text{crust}} + C_{\text{carb}}^{\text{crust}} - C_{\text{sed}}^{\text{oce}} \qquad (3.21)$$

$$\frac{d\widehat{A}}{dt} = A_{\text{sili}} + A_{\text{carb}} - A_{\text{sed}} \qquad (3.22)$$

where fluxes no longer represent 10^6 yr averages, but rather 10^2–10^3 yr ones.

No significant accumulation of CO_2 in the atmosphere has been observed over the last several hundred thousands of years, as documented by the CO_2 measurements made on the Vostok ice-core (BARNOLA et al., 1987; JOUZEL et al., 1993), as well as by reconstructions of the surface-water p_{CO_2} in the eastern equatorial Atlantic for the last 330 kyr based upon the δ^{13}C of sedimentary organic carbon (WESTERNHAUSEN et al., 1994). As atmospheric p_{CO_2} is very sensitive to even small perturbations of the ocean's carbon and alkalinity contents, we may safely assume that the budgets of these two are near equilibrium, when averaged over hundreds of kiloyears or more. As a consequence, (3.20) above also holds for the glacial-interglacial average carbon fluxes:

$$\tfrac{1}{2}\overline{C_{\text{sili}}^{\text{atm}}} = \overline{(C_{\text{volc}}^{\text{crust}} + C_{\text{hyd}}^{\text{crust}})}. \qquad (3.23)$$

The CO_2 consumption by silicate rock weathering is likely to exhibit a much higher variability than volcanic or hydrothermal activity on the timespan of interest for us: the former is in fact mostly climate-controlled whereas the latter is more dependent on global tectonic activity. Volcanic eruptions are without any doubt at the origin of detectable climate perturbations. This is clearly documented in the historical climate record (JONES et al., 1986). But this same record also shows that the effects of the observed perturbations generally vanish after two years. No correlation between climate and volcanism has been observed on the 100 kyr time scale: ice-core proxies of volcanic activity (such as the abundance of volcanic ashes) show only very little variability over the last glacial-interglacial cycle (JOUZEL, personal communication; DUPLESSY and MOREL, 1990). We will hence consider that, when averaged over 100–1,000 years, the CO_2 release from volcanic and hydrothermal activity has remained constant throughout the whole last glacial-interglacial climate oscillation. Hence,

$$C_{\text{volc}}^{\text{crust}} + C_{\text{hyd}}^{\text{crust}} \equiv \overline{(C_{\text{volc}}^{\text{crust}} + C_{\text{hyd}}^{\text{crust}})}. \qquad (3.24)$$

Equation (3.23) of course only sets the average CO_2 consumption rate by silicate rock weathering for glacial-interglacial. It is perfectly possible that silicate rock weathering temporarily consumes more or less than average. As a consequence, the riverine bicarbonate input may vary in time, which may influence atmospheric CO_2 levels, as shown below.

Since the atmospheric CO_2 consumed by weathering processes gets transported as bicarbonate (i.e., alkalinity) to the ocean, the following discussion principally focuses on alkalinity changes. Replacing $C_{\text{volc}}^{\text{crust}} + C_{\text{hyd}}^{\text{crust}}$ by $\frac{1}{2}\overline{C_{\text{sili}}^{\text{atm}}}$ (obtained by combining (3.23) and (3.24)) and taking advantage of the relationships (3.13)–(3.16), which hold regardless of the time scale of interest, we can rewrite equation (3.21) in terms of alkalinity fluxes only:

$$\frac{d\widehat{C}}{dt} = \frac{1}{2}(\overline{A_{\text{sili}}} + A_{\text{carb}} - A_{\text{sed}}). \tag{3.25}$$

By combining this equation with (3.22), we find that

$$\frac{d\widehat{A}}{dt} - 2\,\frac{d\widehat{C}}{dt} = A_{\text{sili}} - \overline{A_{\text{sili}}}. \tag{3.26}$$

This relationship between the joint variations of carbon and alkalinity in the ocean-atmosphere system on one hand, and the anomaly of the riverine bicarbonate flux from silicate weathering on the other hand serves as a quantitative basis for the discussion in the next two paragraphs, where we explore the consequences of different scenarios of changing rates of CO_2 consumption by continental silicate and carbonate weathering.

3.3.1 Silicate Weathering as a Mechanism for Atmospheric Carbon Dioxide Variations

Let us first analyse the responses of the ocean and the atmosphere to variations of the bicarbonate input from silicate weathering. As a starting point for the following discussion, we have chosen a rectangular variation of the riverine input of bicarbonate from silicate weathering around its mean value (i.e. of $A_{\text{sili}} - \overline{A_{\text{sili}}}$), with a period similar to that of one glacial-interglacial climate oscillation. Figure 3.2 gives a qualitative overview of the different possible reponses of key variables in the ocean-atmosphere system to such perturbations. In this, for the moment necessarily theoretical discussion, we do not take any response lags into account, supposing that they are negligibly small, when compared to the period of the perturbation. All inputs to the system other than the bicarbonate flux related to silicate weathering are held constant at their glacial-interglacial average value.

Silicate Weathering
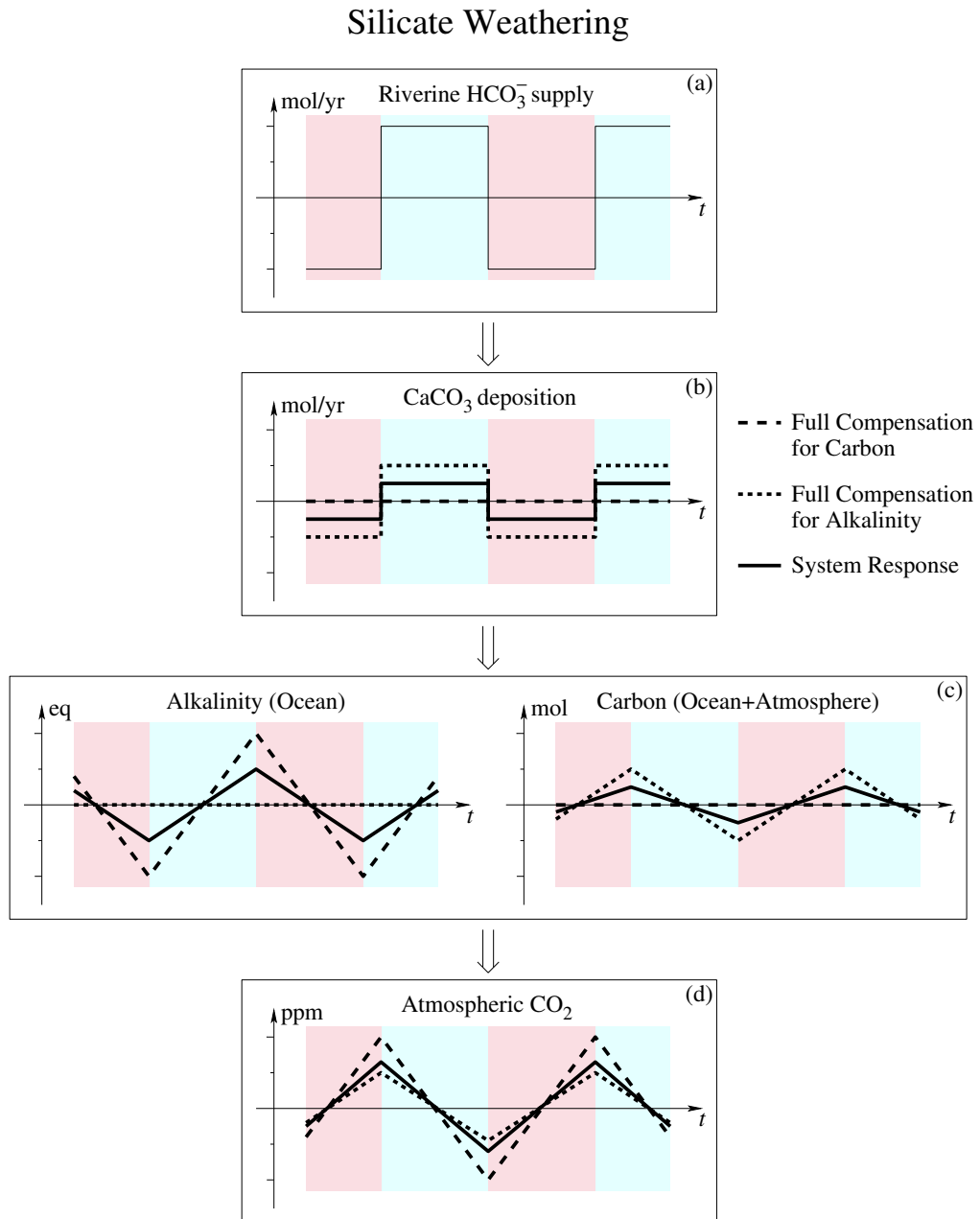
Figure 3.2: Theoretical variations of atmospheric p_{CO_2} (d), and of the total alkalinity and carbon contents in the ocean-atmosphere system (c), induced by a cyclic input of the riverine bicarbonate (a), supposed to arise from *silicate* rock weathering, for different compensation scenarios through carbonate deposition at the sea-floor (b). See text for details and discussion.

From equation (3.26), it becomes clear that it is impossible to balance both the alkalinity and the global carbon budgets simultaneously (unless A_{sili} equals $\overline{A_{\text{sili}}}$ at any time, a case discussed in the next section). The carbonate chemistry of the ocean gets disturbed by this forcing. We can then envisage two end-member scenarios for the response.

(1) **Full compensation for carbon.** The bicarbonate yield from silicate weathering represents a transfer that is internal to the ocean-atmosphere system. The carbonate deposition must hence not deviate from its glacial-interglacial value if the total carbon content of the system is to be conserved. As shown by the long-dashed curves in figure 3.2, the total amount of alkalinity in the ocean then increases while A_{sili} is above average, which leads to a decrease of p_{CO_2} in the atmosphere. While A_{sili} is below average, ocean alkalinity decreases, making p_{CO_2} increase.

(2) **Full compensation for alkalinity.** This scenario is represented by the short-dashed curves in figure 3.2. Here, $d\widehat{A}/dt$ in equation (3.26) vanishes, instead of $d\widehat{C}/dt$. The only way for the ocean to compensate for the imposed alkalinity input variations is through enhanced or decreased deposition of carbonate at the sea-floor. During times of higher-than-average A_{sili}, the total content of carbon in the combined ocean and atmosphere reservoirs thus decreases, making atmospheric p_{CO_2} decrease as well, and vice versa while A_{sili} is below average.

In both scenarios, atmospheric p_{CO_2} increases while A_{sili} is above average $(A_{\text{sili}} - \overline{A_{\text{sili}}} > 0)$, and decreases while A_{sili} is below average $(A_{\text{sili}} - \overline{A_{\text{sili}}} < 0)$.

The effective response of our simple system must be intermediate between these two end-member scenarios, as indicated by the solid lines in figure 3.2. It is probably close to the one that minimizes the perturbations of both the carbon and the alkalinity budgets.

(3) **Minimal variation of carbon and alkalinity.** A more realistic estimate of the effective response can probably be obtained by minimizing $(d\widehat{C}/dt)^2 + (d\widehat{A}/dt)^2$, using the evolution equation (3.26) as a constraint. The so defined minimal response is characterised by

$$\frac{d\widehat{C}}{dt} = -\frac{2}{5}\left(A_{\text{sili}} - \overline{A_{\text{sili}}}\right) \tag{3.27}$$

$$\frac{d\widehat{A}}{dt} = \frac{1}{5}\left(A_{\text{sili}} - \overline{A_{\text{sili}}}\right). \tag{3.28}$$

So far, we have only discussed the effects of such a varying bicarbonate input from silicate weathering from a qualitative point of view. It would of course be interesting to get a quantitative estimate of these effects. This is straightforward for carbonate deposition rates, which are equal to the respective $d\widehat{C}/dt$ and are hence directly related to the amplitude of the perturbation: they are exactly in ratios of $0 : 50 : 40$ for scenarios (1), (2) and (3) respectively. We can expect that the corresponding lysocline variations are more or less in the same ratios, provided the slope in the sea-floor depth distribution does not vary too much in the vicinity of the average level of the CCD.

Because of the complex geochemical feedbacks in the oceanic carbon cycle, this kind of estimate is, however, rather difficult for the atmospheric CO_2 variations, at least regarding their absolute amplitudes. Even for the relative importance of the changes produced in the three scenarios, only crude estimates can be obtained. To first order, the variations of p_{CO_2} in the atmosphere can be related to those of C_T and A_T in the surface ocean by

$$\Delta p_{CO_2} = c\Delta C_T + a\Delta A_T. \qquad (3.29)$$

Solving this equation for $\Delta p_{CO_2} = 0$, at $p_{CO_2} = 200$ ppm and 400 ppm, we can calculate from the A_T-C_T graphs in figures 2.2-c (warm surface water) and 2.3-c (cold surface water) that $c/a = -1.2 \pm 0.1$. This compares well with $|a/c| = 0.84$ calculated by FRANKIGNOULLE (1994). Hence,

$$\Delta p_{CO_2} = -a \times (1.2\,\Delta C_T - \Delta A_T). \qquad (3.30)$$

If we suppose that the perturbations produced by the variable bicarbonate input rate from silicate weathering equally affect the surface and the deep ocean, (3.30) can be interpreted as

$$\frac{dp_{CO_2}}{dt} \propto \left(1.2\frac{d\widehat{C}}{dt} - \frac{d\widehat{A}}{dt}\right). \qquad (3.31)$$

From this relationship, it can be calculated that the expected p_{CO_2} variations in scenarios (1), (2) and (3) are in ratios of $100 : 60 : 68$ respectively.

As said before, these ratios should only be taken as first estimates. They are certainly wrong if the amplitude of the forcing gets large, compared to the average flux, but they should remain acceptable for small deviations. In a more realistic representation of the ocean-atmosphere system, a changing alkalinity input certainly leads to important redistributions of C_T and A_T in order to allow for the correct compensation by carbonate deposition at the sea-floor. Compensation is furthermore not instantaneous, but requires some

time to adjust to the changing input. This response time has consequences for the ocean's carbon and alkalinity contents, and may lead to overshoot phenomena in the p_{CO_2} response for example.

3.3.2 Silicate and Carbonate Weathering in Comparison

For carbonate rock weathering, the analogous mechanism cannot work in the same way. In this case, it is always possible to balance the alkalinity and the carbon budgets simultaneously.

In order to compare the effects from carbonate with those from silicate weathering we analyse the system's response to exactly the same variations of the river bicarbonate input as previously. But here, we suppose that the variations come from changing carbonate weathering. The bicarbonate delivery from silicate weathering, and all the other inputs to the system are assumed constant, at their glacial-interglacial average values. Figure 3.3 gives a qualitative overview of different possible reponses to such perturbations, similarly to figure 3.2. As a consequence of the constant silicate weathering, the relationship (3.26) reduces to

$$\frac{d\widehat{A}}{dt} - 2 \, \frac{d\widehat{C}}{dt} = 0, \tag{3.32}$$

translating now only the well-known fact that carbonate processes involve alkalinity and carbon fluxes in a 2 : 1 ratio. We can again distinguish two end-member scenarios.

(4) **No compensation.** If carbonate deposition does not adjust itself to the varying bicarbonate input, the total content of alkalinity simply increases while the riverine supply is above average, and decreases while it is below average. Its evolution is the same as for scenario (1) since the bicarbonate input is the same. Unlike scenario (1), the total carbon content changes now, in phase with alkalinity (cf. (3.32)) because half of the bicarbonate delivered to the ocean stems from the rock. The joint effects of carbon and alkalinity on p_{CO_2} in the atmosphere partially cancel each other. Alkalinity nevertheless determines the net change, because its variations are twice as important as those of carbon. Hence, p_{CO_2} decreases while the bicarbonate input is above average, and vice versa.

(5) **Full compensation for carbon and alkalinity.** Unlike for silicate weathering, full compensation is possible in the case of carbonate

Carbonate Weathering
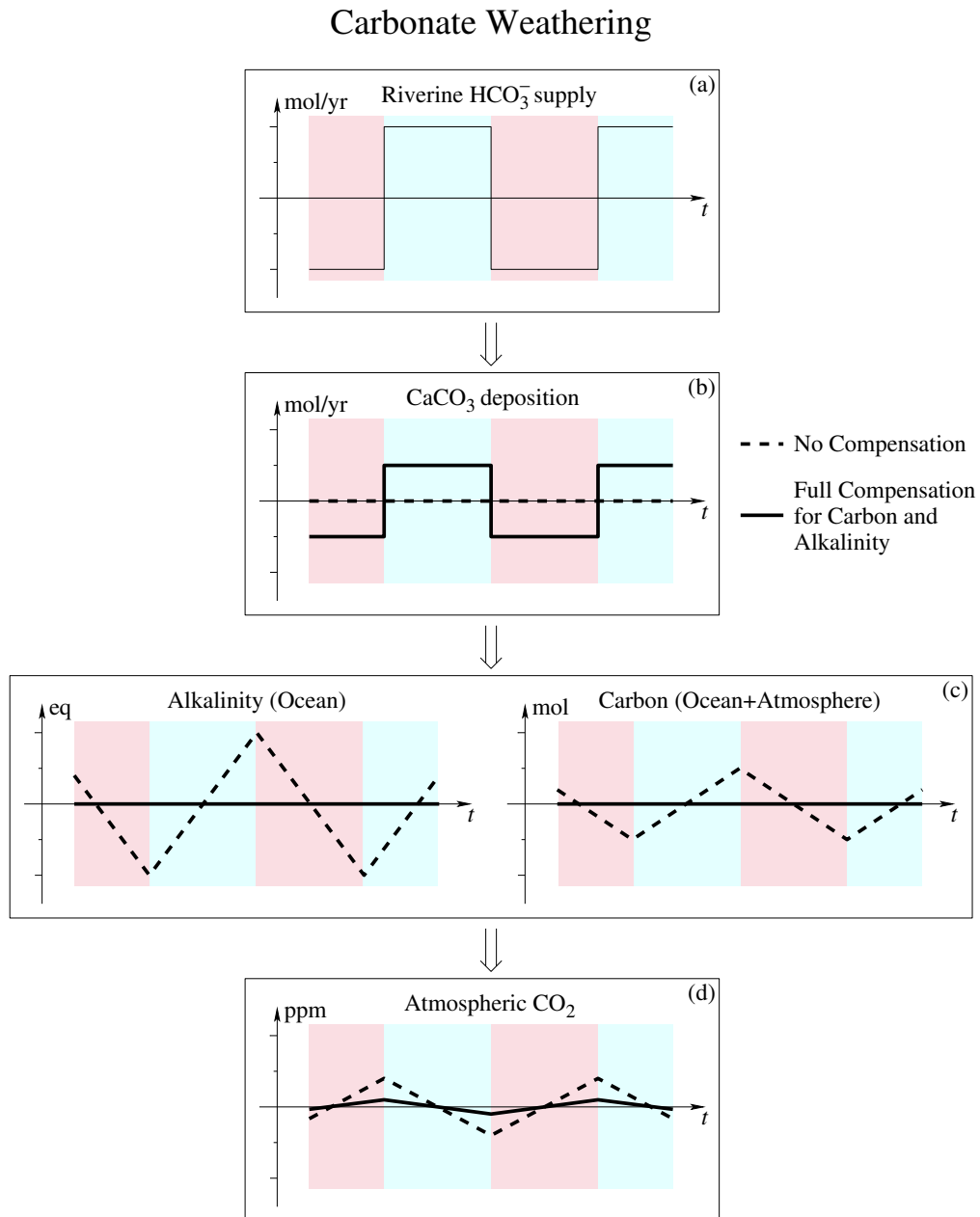
Figure 3.3: Theoretical variations of atmospheric p_{CO_2} (d), and of the total alkalinity and carbon contents in the ocean-atmosphere system (c), induced by a cyclic input of the riverine bicarbonate (a), supposed to arise from *carbonate* rock weathering, for different scenarios of carbon and alkalinity compensation by deposition of $CaCO_3$ at the sea-floor (b).

weathering. In a realistic representation of the system, p_{CO_2} will nevertheless vary, changing in response to the changing lysocline. When this latter moves up and downwards to follow the changing river inputs, the deep-sea $A_T - C_T$ difference is modified. As a consequence, the global distributions of A_T and C_T change and hence atmospheric p_{CO_2}.

For a given river bicarbonate input, the carbonate deposition rates of scenarios (1) – (5) are exactly in ratios of 0 : 50 : 40 : 0 : 50. According to the first order relationship (3.30), we find that the p_{CO_2} variations of the 5 scenarios are in ratios of 100 : 60 : 68 : 40 : 0. Let us emphasize again that the so obtained ratios are only close to the effective ones for moderate variations of the bicarbonate input.

With this limitation in mind, we can nevertheless use them to point out two characteristics that make silicate weathering a more attractive process for explaining the glacial-interglacial change in atmospheric CO_2 rather than carbonate weathering.

1. For a given history of the riverine bicarbonate input to the ocean, we can expect that the effects on atmospheric p_{CO_2} are much larger if silicate weathering rather than carbonate weathering is the driving force. Taking the above ratios at face value, the amplitudes of the silicate- and of the carbonate-driven p_{CO_2} signals would be in a ratio of 60:40 at least. If the overall tendency suggested by the calculated ratios is approximately correct, it is not unreasonable to expect that *silicate weathering is more than two times as efficient in generating atmospheric carbon dioxide variations on glacial-interglacial time scales than is carbonate weathering.*

2. For a given history of the riverine bicarbonate input to the ocean, the lysocline variations should be somewhat smaller if silicate weathering rather than carbonate weathering is the responsible process. The respective amplitudes of the carbonate deposition rate variation brought about by these two processes are probably in a ratio of 40 : 50, taking scenario (3) as close to the true response to changing silicate weathering.

These ratios, relating the effects from carbonate and silicate weathering on the atmospheric CO_2 levels and the lysocline variations, enable us now to get a *first tentative estimate* for the absolute variations that we can await from changing CO_2 consumption rates by silicate weathering. In one of their sensitivity tests, ARCHER and MAIER-REIMER (1994) changed the deep-sea carbonate influx from a present-day value of 12×10^{12} mol $CaCO_3$/yr

to 31×10^{12} mol $CaCO_3$/yr. In terms of alkalinity, this influx must be equal to the riverine bicarbonate input in their model. Accordingly, their bicarbonate input changed from 24×10^{12} to 62×10^{12} mol HCO_3^-/yr, i.e., by 38×10^{12} mol HCO_3^-/yr. As a result of this change, p_{CO_2} in the atmosphere decreased by 70 ppm, from 310 to 240 ppm, and the carbonate ion concentration in the deep Pacific increased by 65 μmol/kg, from 80 to 145 μmol/kg. This latter increase corresponds to a deepening of the calcite lysocline by about 3,200 m. If silicate instead of carbonate weathering is used to produce the same p_{CO_2} variation, the bicarbonate flux only needs to be increased by half (perhaps only even one third) of this. Accordingly, the lysocline deepening would have been $3,200/2 \times 0.8 = 1,300$ m (respectively $3,200/3 \times 0.8 = 850$ m), in much better agreement with the observed deepening of about 600 m for the equatorial Pacific (FARRELL and PRELL, 1989). For a given variation of atmospheric p_{CO_2}, carbonate weathering produces a lysocline variation that is about 2,600 m too large. This discrepancy can possibly be reduced to 250 m by calling upon silicate weathering instead.

3.3.3   The Silicate Weathering Hypothesis

As illustrated in the previous two sections, silicate weathering is an attractive process for generating variations of CO_2 in the atmosphere on glacial-interglacial time scales. In this study, we hence propose to test the following hypothesis:

> **The Silicate Weathering Hypothesis.** Continental weathering, and especially silicate weathering, actively contributes to the glacial-interglacial atmospheric CO_2 variations documented by the Vostok ice-core record. During glacial times, enhanced consumption of atmospheric CO_2 by silicate weathering might be responsible for a significant decrease of CO_2 in the atmosphere.

We focus on silicate weathering because, as discussed in the previous sections, we can expect that it gives rise to more pronounced effects than carbonate weathering due to the inherent short-term decoupling of the alkalinity and inorganic carbon cycles.

It is now legitimate to ask how reasonable such an increase is. In the literature, the opposite opinion generally prevails. During glacial times, the planet was cooler, extensive ice-sheets had developed and covered large parts of the continents at high latitude, especially in the Northern Hemisphere. Additional ice cover was provided by more expanded mountain glaciers. As discussed by KUMP and ALLEY (1994) in a review on the global chemical weathering under ice age conditions, it is generally supposed that chemical

weathering rates should be largely reduced under these circumstances. However, there are compensating effects, such as the production of fine-grained, easily weatherable materials by glaciers or the emergence of parts of the continental shelf area due to the 120–130 m lower sea level, which could still have led to a net increase of CO_2 consumption rates. Most of this shelf exposure takes place at low latitudes, in southeast Asia, Oceania and around Australia, as shown in figure 7.2 on page 222 later in this thesis. Today, land areas close to these shelves are submitted to intense chemical weathering. Large parts of the then exposed shelves are nevertheless carbonate platforms, and not silicate rock outcrops. Kump and Alley (1994) furthermore think that continental ice-sheets largely reduce chemical weathering, perhaps by more than an order of magnitude, except in some marginal regions. Their assumption, that large parts of the ice-sheets were frozen to their beds, is perhaps not correct, at least in the case of the North American Laurentide ice-sheet. Using a numerical ice-sheet model, Clark et al. (1996) have indeed shown that the presence of soft bed (typically wet, deformable till) is fundamental to reproduce the shape and the volume of the Laurentide ice-sheet in agreement with the ICE-4G reconstruction of Peltier (1994), which is based on geodynamic considerations and on observations of relative sea level variations.

Sharp et al. (1995) have shown that glacierization of a catchment can lead to denudation rates far above continental average. The specific cation yield that they calculated from their analyses of the meltwaters from the Haut Glacier d'Arolla in Switzerland is about 70% higher than continental average. They estimate that solute denudation rates on this catchment are about three times the global average. Comparable observations have been made on other glacier-covered alpine catchments (see, e.g., Souchez and Lemmens, 1987). Sharp et al. (1995) also draw attention on the role that glacially driven chemical weathering could have had in carbon cycling over glacial-interglacial time scales. Hallet et al. (1996) made even stronger arguments in their analysis of both chemical and physical erosion by glaciers. They point out that, at present, extensively glaciated basins present chemical weathering rates that are up to 35 times larger than the continental average (see figure 3.4). It appears even that the large basins in Alaska, which are only glaciated for a relatively small fraction, suggest higher chemical weathering rates than the Alpine glaciers. Hallet et al. (1996) indicate that on average, chemical weathering rates are about an order of magnitude higher there than continental average. They also emphasize that extrapolating chemical weathering rates observed on these valley glaciers to ice-sheets is perhaps not justified.
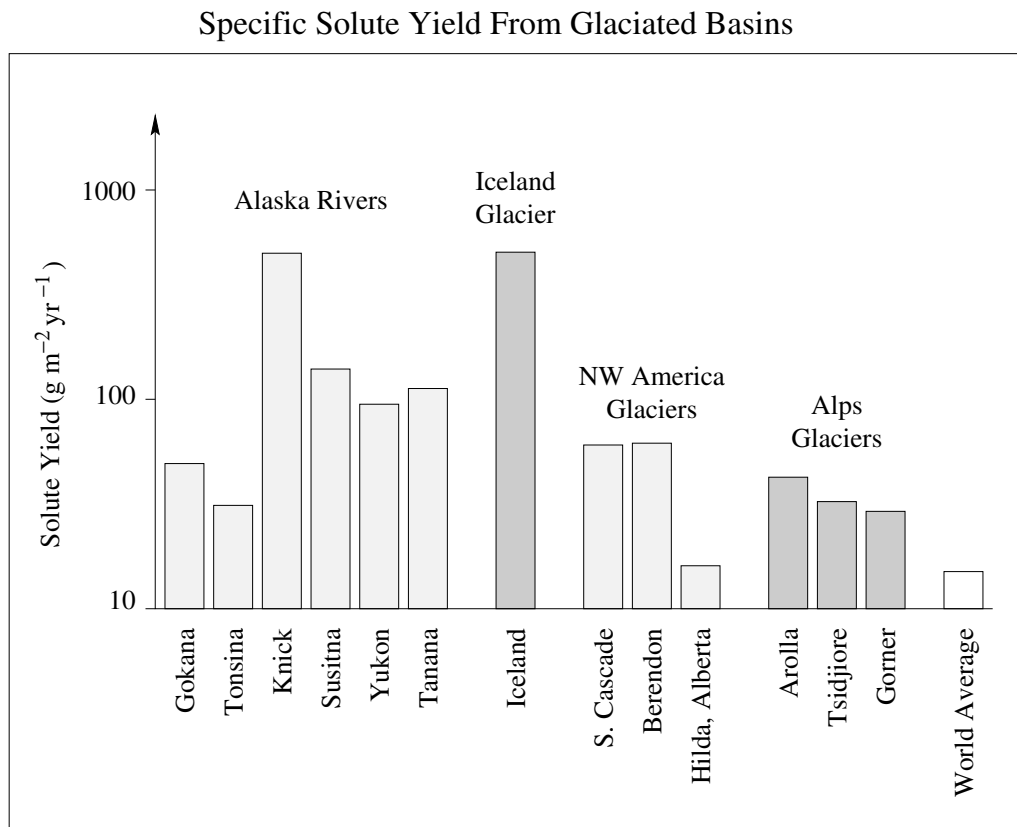
Figure 3.4: Specific solute yields from glaciated basins world-wide compared to the World average chemical denudation rate, estimated at $14.8 \, \mathrm{g \, m^{-2} \, yr^{-1}}$ by SUMMERFIELD (1991). Note the logarithmic scale (figure simplified from HALLET et al., 1996).

Uncertainties in our present knowledge of key factors that control chemical weathering in a glacial world remain too large to draw definite conclusions. We have therefore tried to reconstruct the glacial-interglacial changes in the rate of chemical erosion of the continents, concentrating our efforts on silicate rock weathering. Three different approaches have been adopted: the first two are based on the inversion of the marine $^{87}Sr/^{86}Sr$ and Ge/Si records, the third one is based upon a model of the chemical erosion of the continents. In what follows, we analyse and discuss the limitations of these different approaches. These three methods are used to reconstruct possible histories for the evolution of the atmospheric CO_2 consumption rates and of the resulting river bicarbonate fluxes. These histories are then used as forcing functions to drive a model of the ocean-atmosphere subsystem of the global carbon cycle. Because of the complex interactions between ocean chemistry and carbon cycling, it is very difficult to make quantitative predictions about the atmospheric response to such perturbations. This is especially the case under non-equilibrium conditions as have to be expected for silicate weathering changes and a comprehensive ocean carbon cycle model is needed.

In the next chapter, we give a comprehensive description of the carbon cycle model that we have developed for this study. The three subsequent chapters are then devoted to the different methods proposed to reconstruct the weathering histories.

Chapter 4

The Carbon Cycle Model

The carbon cycle model used for this study has been entirely developed by the author. This chapter is intended to give a comprehensive and detailed description of all its components. The complete set of differential equations used to follow the tracers in time is presented in detail. The first two sections handle the oceanic component, whereas the third one is devoted to the sedimentary component of the model. Finally, the calibration of the model is explained and sensitivity tests with respect to the different adjustable parameters are reported.

Earlier versions of the model have been used to perform the computations for the results published or presented in reports during the realization of this thesis (MUNHOVEN and FRANÇOIS, 1994, 1996; MUNHOVEN and PROBST, 1995). They differ from the present one in several details.

- In the first published version (MUNHOVEN and FRANÇOIS, 1994), the resolution of the depth profiles was only 400 m. Carbonate dissolution in the deep-sea sediments was determined from the lysocline depths, which were calculated from the parameterizations of BROECKER and TAKAHASHI (1978). The mean seawater $\delta^{18}O$ record of LABEYRIE et al. (1987) was used as a sea level proxy. In the following versions, sea level variations were calculated from the SPECMAP stack of IMBRIE et al. (1984). One consequence of this change is a much less chaotic behaviour of the evolution of the carbonate accumulation by coral reefs, which depends on the rate of the sea level fluctuations, as can be seen when comparing figures 4.6 (page 112) and 5.3 (page 175). Furthermore, this early version did not consider a separate flux for shallow-water accumulation of carbonate on banks and shelves besides the coral reef production.

- In the second version (MUNHOVEN and FRANÇOIS, 1996), which was

also used by MUNHOVEN and PROBST (1995), we had already increased the resolution of the depth profiles to 100 m. The parameterizations of BROECKER and TAKAHASHI (1978) were no longer used to determine the carbonate dissolution fluxes. Instead, saturation depths were now directly calculated from the thermodynamic constants. MUNHOVEN and FRANÇOIS (1996) still used the constants of MILLERO (1979), whereas the version described here is based upon the more recent constants discussed in chapter 2.

Relative to earlier versions, the number of adjustable parameters has also been considerably reduced, from 16 to 12.

4.1 Configuration of the Model Ocean

4.1.1 Reservoir Geometry

The carbon cycle model used for this study is a low-resolution box model with a single atmospheric box and 10 oceanic boxes: deep Atlantic, Indo-Pacific, and Antarctic, temperate Atlantic and Indo-Pacific thermoclines and surfaces, high-latitude Atlantic and Pacific surfaces and Antarctic surface. The distribution of the ten reservoirs that make up our model is shown in figure 4.1. The detailed characteristics of the ten reservoirs are given in table 4.1. Table 4.2 shows the typical volumes and surface areas for present-day conditions (i.e. sea level close to maximum) and for 20 kyr BP (sea level 130 m below maximum). The spatial resolution of our model is thus similar to that of BROECKER and PENG's (1989) 10-box PANDORA, KEIR's (1988) 14-box CYCLOPS or the 10-box model of BOLIN et al. (1983).

As indicated in figure 4.1, the reservoirs do not simply have a flat bottom, but they present some structure with depth. The sea-floor relief is described by five depth profiles. Each one of these profiles represents the distribution of sea-floor area as a function of water depth below the five surface reservoirs. They have been calculated from the $1° \times 1°$ bathymetric data of the Scripps Institution of Oceanography (GATES and NELSON, 1975a,b). For computational efficiency reasons, we have converted the raw distribution functions into cumulative ones. These were then sampled at 100 m depth intervals before being included into the model. The five adopted profiles are represented in figure 4.2.

These depth profiles are first used to calculate the volumes and the surface areas of the reservoirs as sea level varies. The sea level fluctuations over the past 120 kyr are assumed to follow linearly the $\delta^{18}O$ signal of the SPECMAP stack (IMBRIE et al., 1984). The so-calculated sea level curve
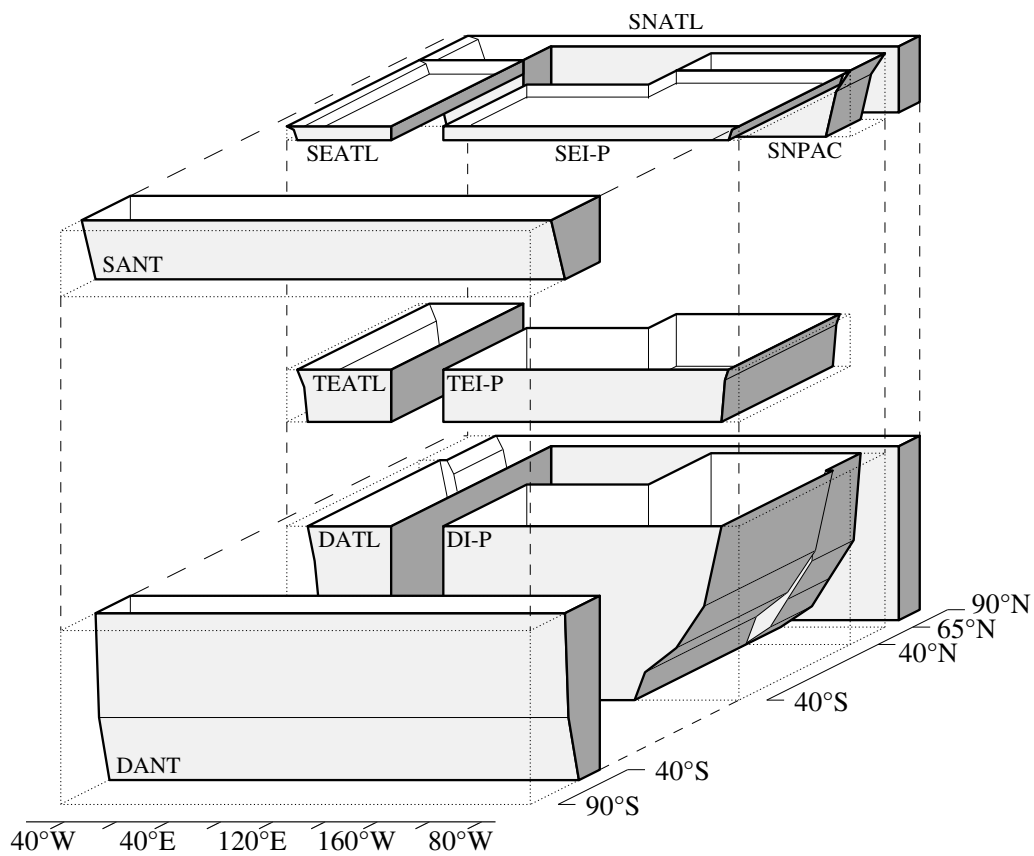
Figure 4.1: Carbon cycle model: distribution of the reservoirs. Not shown is the atmospheric reservoir, which is on top of the surface reservoirs. The exact definitions of the reservoirs can be found in table 4.1.

Table 4.1: Reservoir definitions.

Reservoir	Acronym	Depth Range	Latitude Range
Surface Reservoirs			
North Atlantic	SNATL	$0 - 1000$ m	North of 50°N
Equatorial Atlantic	SEATL	$0 - 100$ m	40°S – 50°N
Antarctic	SANT	$0 - 1000$ m	South of 40°S
Equatorial Indo-Pacific	SEI-P	$0 - 100$ m	40°S – 40°N
North Pacific	SNPAC	$0 - 1000$ m	40°N – 65°N
Thermocline Reservoirs			
Equatorial Atlantic	TEATL	$100 - 1000$ m	40°S – 50°N
Equatorial Indo-Pacific	TEI-P	$100 - 1000$ m	40°S – 40°N
Deep Reservoirs			
Atlantic	DATL	> 1000 m	North of 40°S
Antarctic	DANT	> 1000 m	South of 40°S
Indo-Pacific	DI-P	> 1000 m	40°S – 65°N

Table 4.2: Typical reservoir sizes and surface areas.

Reservoir	Area (10^{12} m^2)		Volume (10^{15} m^3)	
	Present	20 kyr BP	Present	20 kyr BP
SNATL	20	16	12	11
SEATL	65	63	6	6
SANT	76	75	73	73
SEI-P	182	176	18	18
SNPAC	15	14	13	13
TEATL			55	54
TEI-P			156	155
DATL			204	195
DANT			218	209
DI-P			585	561
Total	358	344	1340	1295
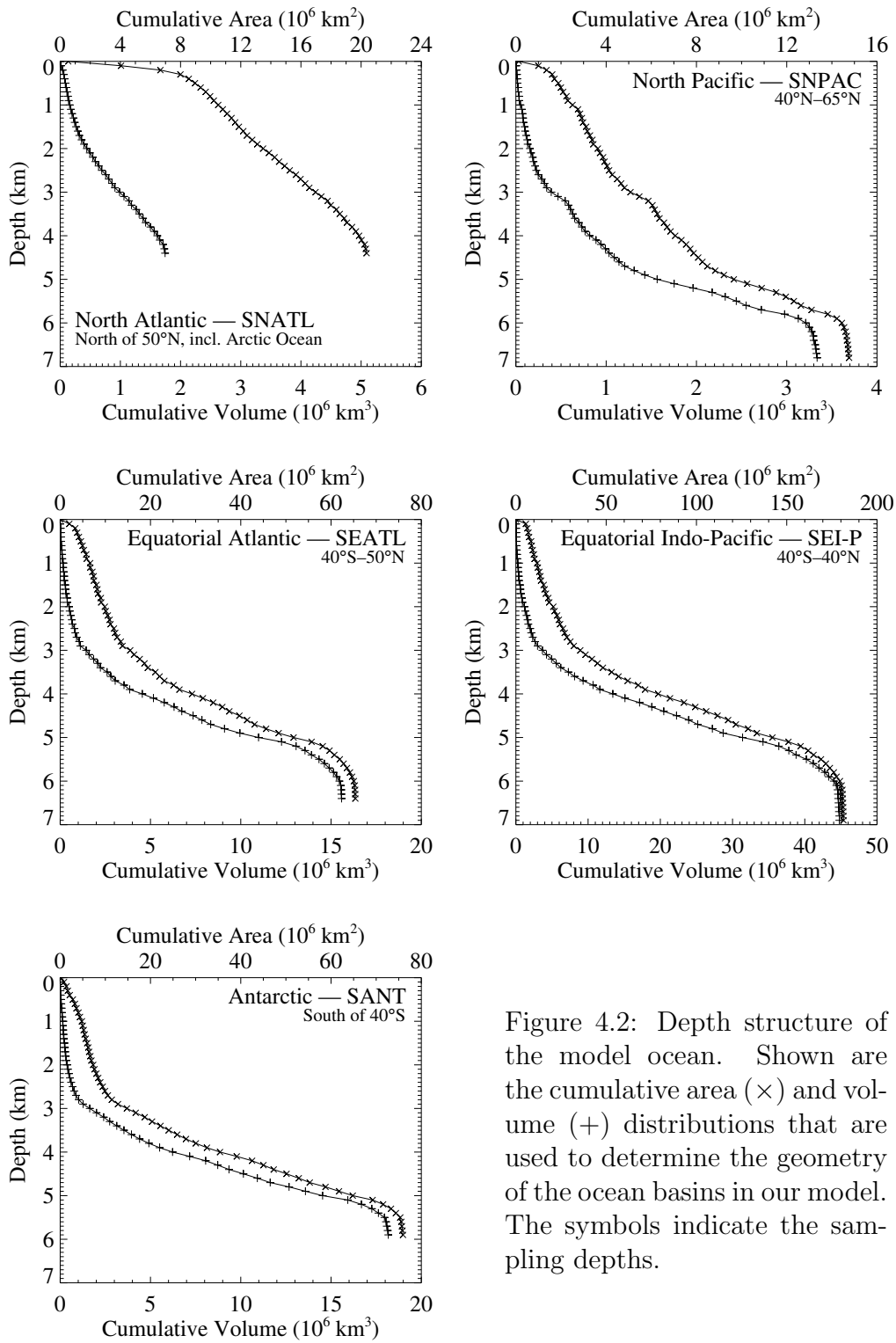
Figure 4.2: Depth structure of the model ocean. Shown are the cumulative area ($\times$) and volume ($+$) distributions that are used to determine the geometry of the ocean basins in our model. The symbols indicate the sampling depths.
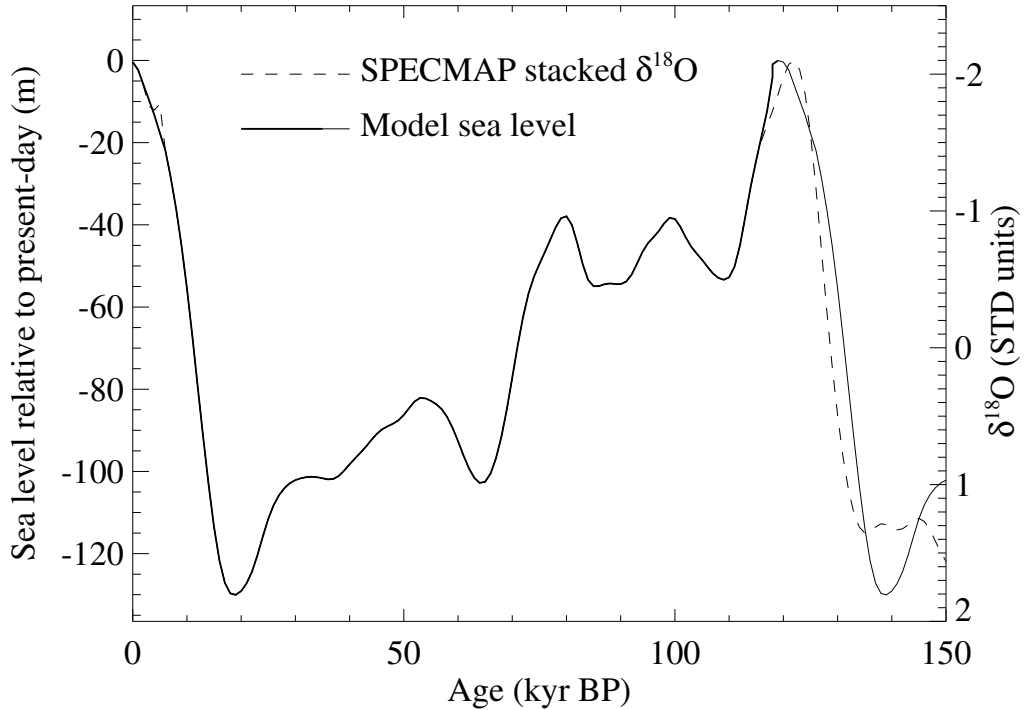
Figure 4.3: Model sea level (solid line) and SPECMAP stacked $\delta^{18}O$ record (dashed line). The thick part of the sea level curve represents one 120 kyr period.

has only been slightly modified so that it leads to a continuous, cyclic history with a period of 120 kyr, when repeated several times. To minimize the influence of arbitrary initial conditions (e.g., carbonate-free sediments) on the calculated evolution of the tracers in the model, the governing system of differential equations described in section 4.2 below is in fact integrated over several repeated 120 kyr cycles, until the solution becomes periodic, i.e., until the contribution from the decreasing exponential part of the solution which results from the initial disequilibrium can be neglected. We have furthermore removed the small peak around 5 kyr BP to avoid a strong oscillation of the sea level variation rate at that time. Figure 4.3 shows both the original SPECMAP $\delta^{18}O$ record and the sea level history adopted in the model.
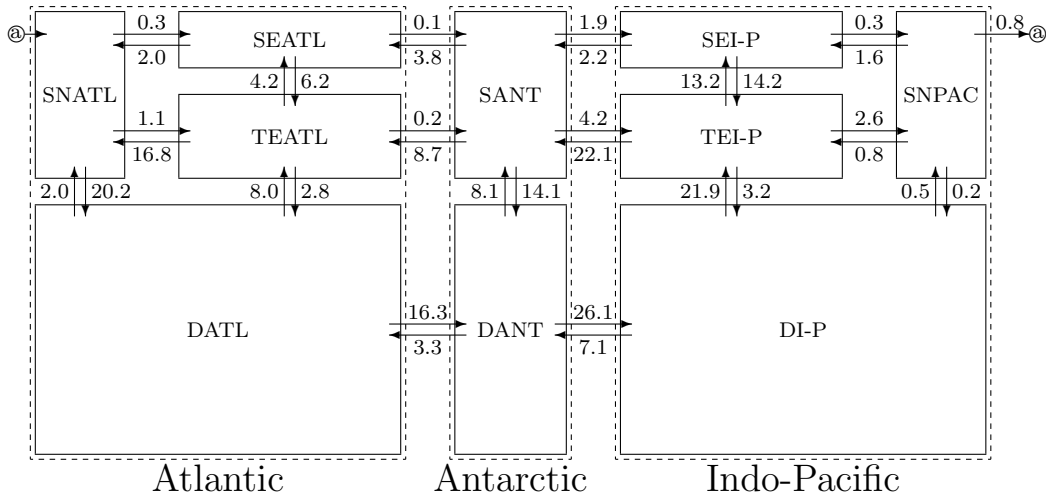
Figure 4.4: Model water circulation (fluxes in Sv).

4.1.2 Water Circulation

Method of Determination

The water exchange (see figure 4.4) between the reservoirs has been derived from the annual mean velocity distribution of the Large-Scale Geostrophic Oceanic General Circulation Model of the Max-Planck-Institut für Meteorologie in Hamburg (MAIER-REIMER et al., 1991, 1993). The velocity field has been integrated over the surfaces separating the different reservoirs and then decomposed into an advective (equal to the net transport) and a mixing component. We have to take only a fraction r_{mix} of the mixing part of the LSG-OGCM into account. This is due to the very large differences in the resolutions of the two models. To lump many small boxes together into one large homogeneous one is in fact identical to increasing the mixing rates between themselves *ad infinitum*. This is exactly what we did when we went from the large scale Hamburg GCM to our box model. To keep the overall ventilation times of the different ocean-basins (i.e. of the reservoirs of the box model) right, it is thus necessary to reduce the mixing through the separating surfaces. r_{mix} is adjusted altogether with the other model parameters that will be presented in the next sections. We finally adopted $r_{mix} = 0.20$, hence taking only 20% of the Hamburg Model mixing component into account. Sensitivity of the model to variations of r_{mix} is discussed in section 4.4.

Comparison with Similar Models

When comparing our transports to those of the models cited before (see
KEIR (1988) for a summary), we find some common points as well as some
striking differences. With the notable exception of North Atlantic Deep
Water (NADW) formation which ranges in the vicinity of 20 Sv for all of
the four models compared here, our transports, like those of PANDORA and
CYCLOPS, are generally much lower than those calculated by BOLIN et al.
(1983). We will thus focus on PANDORA and CYCLOPS for this discussion.
Our upper ocean exchange is similar to that of CYCLOPS in the Atlantic
and to that of PANDORA in the Pacific. Like PANDORA, our model feeds
its NADW source for around 30% from upwelling in the temperate Atlantic,
which is not the case for CYCLOPS. It presents also nearly the same exchange
between the deep Atlantic and Antarctic reservoirs as PANDORA, which is
about half as important as CYCLOPS's. The most important differences
between our model and the other two can be found in the Antarctic-Pacific
interaction and in the intra-Pacific circulation. These two are of course not
independent of each other. Whereas the deep Antarctic-Pacific exchange is
dominated by mixing in both CYCLOPS and PANDORA, our model presents
a well pronounced advection (19 Sv) from the Antarctic to the Pacific. This
advective flux is followed by a strong upwelling into the Pacific intermediate
layer, and a subsequent return flow to the surface Antarctic reservoir. Finally,
our model presents a net formation of deep water inside the Antarctic region,
whereas CYCLOPS and PANDORA present a net upwelling (although their
fluxes differ by a factor of two).

4.1.3   Temperature and Salinity Evolution

The temperature evolution of the different water masses is taken from the
reconstruction of LABEYRIE et al. (1987). We have only removed the warm
peak at 5 kyr B.P. in the deep Atlantic ($2°C$ warmer than today) to avoid spu-
rious CO_2 peaks at that period (see discussion in MUNHOVEN and FRANÇOIS,
1994). In the Antarctic Ocean, we use their record for the southern Indian.
For simplicity, we assume that the surface water has temperature variations
of the same amplitude as the underlying deep water masses ($3°$ in the At-
lantic and $2°$ in the Pacific) with present-day values of $2°C$ in polar and
$19°C$ in temperate regions. Figure 4.5 shows the adopted histories for the
temperature of the deep reservoirs. Salinity is set to an overall mean value
of 35.4 at present-day. Its variations are linked to those of the total volume
of water, in such a way that the product $S \times Volume$ remains constant.
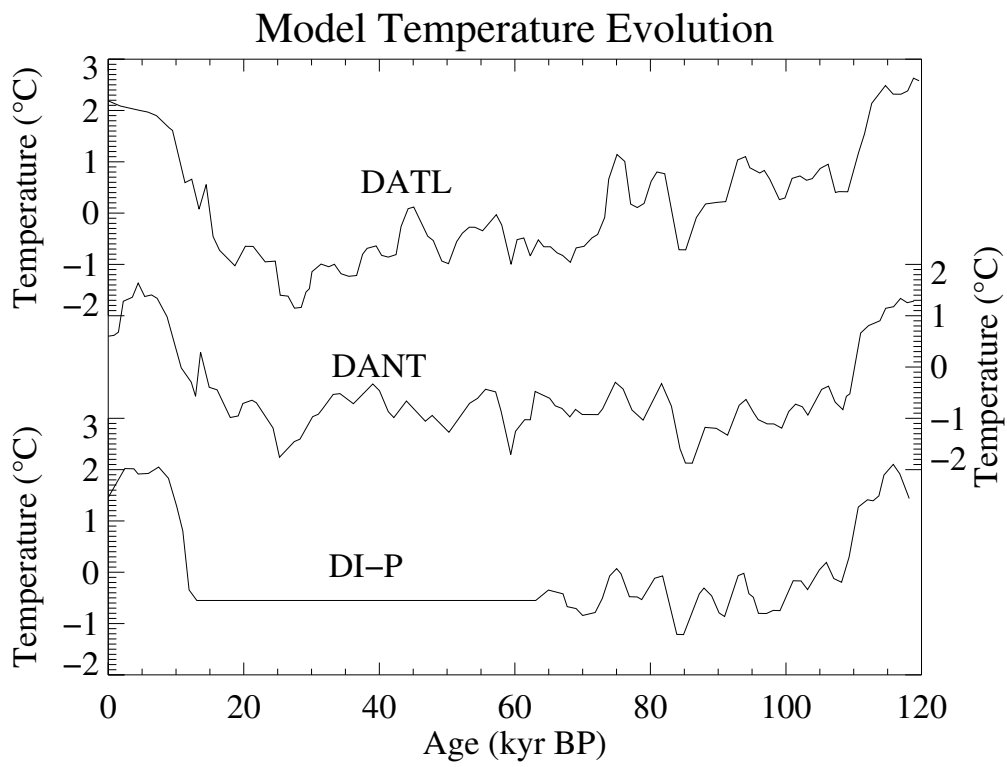
Figure 4.5: Prescribed temperature evolution in the different deep reservoirs.

4.2 Ocean Model Equations

On the next pages, we give a comprehensive description of all the tracers taken into account by the model and of the differential equations governing their evolution in time. First though, we define the symbols, variables and notation used throughout this chapter.

4.2.1 Basic Hypotheses and Definitions

Symbols, Notations and Simplifications

First of all, we define different sets of reservoirs, mostly for notation purposes:

- *Srfc* – the set of surface reservoirs:
$$Srfc = \{\text{SNATL}, \text{SEATL}, \text{SANT}, \text{SNPAC}, \text{SEI-P}\}$$

- *Thcl* – the set of thermocline reservoirs: $Thcl = \{\text{TEATL}, \text{TEI-P}\}$

- *Deep* – the set of deep reservoirs: $Deep = \{\text{DATL}, \text{DANT}, \text{DI-P}\}$

- *WO* – the set of all oceanic reservoirs.

The following symbols are used in the differential equations to denote the geometrical characteristics and physical properties of the reservoirs and the respective tracer quantities:

- Vol_i, $Area_i$ – volume (in m^3) and surface area (in m^2) of reservoir i

- T_i, S_i – temperature (in K) and salinity (dimensionless) of reservoir i

- $W_{i \to j}$ – water flux from reservoir i into j (in Sv)

- $\widehat{A}_i$ – total alkalinity content of reservoir i (in eq)

- $\widehat{C}_i$ – DIC content of reservoir i (in mol)

- $\widehat{O}_i$ – dissolved oxygen content of reservoir i (in mol)

- $\widehat{P}_i$ – phosphate content of reservoir i (in mol)

- $p_{\text{CO}_2\,(i)}$ – CO$_2$ partial pressure of reservoir i (in μatm)

- $\delta\,^{13}\text{C}_i$, $\delta\,^{14}\text{C}_i$ – $\delta\,^{13}\text{C}$ and $\delta\,^{14}\text{C}$ isotopic composition of $\widehat{C}_i$

Additionally, $\widehat{^{13}C_i}$ and $\widehat{^{14}C_i}$ are used to distinguish the DI^{13}C and DI^{14}C contents of the reservoirs. The treatment of carbon isotopes is simplified in our model by supposing that ^{12}C $\simeq$ C $= {}^{12}$C $+ {}^{13}$C $+ {}^{14}$C. We will hence replace the molar ratios ^{13}C/^{12}C in the definition of $\delta\,^{13}$C (equation (1.1)) by molar fractions: if ^{13}R and $^{13}R_*$ are respectively the ^{13}C/C molar fractions of the sample and of the standard reference, we define the $\delta\,^{13}$C of the sample as

$$\delta\,^{13}\text{C} = ({}^{13}R - {}^{13}R_*)/{}^{13}R_* \tag{4.1}$$

For a reservoir i, $\widehat{^{13}C_i}$, $\widehat{C_i}$ and $\delta\,^{13}$C$_i$ are hence related by

$$^{13}R_i = \widehat{^{13}C_i}/\widehat{C_i} \quad \text{and} \quad {}^{13}R_i = (\delta\,^{13}\text{C}_i + 1)\,{}^{13}R_*. \tag{4.2}$$

The relative difference between these simplified $\delta\,^{13}$C values and the original ones is only of the order of 1%. Furthermore, any terms of second order in $\delta\,^{13}$C$_i$ and $\delta\,^{14}$C$_i$ will be neglected.

Generic Form of the Differential Equations

In our model ocean, carbon, phosphate, oxygen and alkalinity get exchanged among the different reservoirs by water circulation, and by biogenic particles settling down from the surface and getting remineralized in the underlying thermocline and deep reservoirs, or buried into the sediments. The generic form of the governing differential equations relative to a reservoir i has the structure of a mass balance equation, i.e.,

$$\frac{d\widehat{Q}_i}{dt} = \sum_j (\mathcal{F}_{\text{in}}^{\text{Q}})_j - \sum_k (\mathcal{F}_{\text{out}}^{\text{Q}})_k + \sum_l (\mathcal{S}_{\text{in}}^{\text{Q}})_l - \sum_m (\mathcal{S}_{\text{out}}^{\text{Q}})_m. \tag{4.3}$$

where $\widehat{Q}_i$ stands for any of the $\widehat{A}_i$, $\widehat{C}_i$, $\widehat{O}_i$ and $\widehat{P}_i$ defined above. $(\mathcal{F}_{\text{in}}^{\text{Q}})_j$ and $(\mathcal{F}_{\text{out}}^{\text{Q}})_k$ are the transport fluxes of Q into and out of the reservoir, $(\mathcal{S}_{\text{in}}^{\text{Q}})_l$ and $(\mathcal{S}_{\text{out}}^{\text{Q}})_m$ are the fluxes related to internal sources and sinks.

$\widehat{Q}$ might of course also stand for $\widehat{^{13}C_i}$ or $\widehat{^{14}C_i}$. We have nevertheless chosen to formulate the equations relative to carbon isotopes in terms of $\delta\,^{13}$C$_i$ and $\delta\,^{14}$C$_i$ instead of $\widehat{^{13}C_i}$ and $\widehat{^{14}C_i}$. For a reservoir i, the generic form of the relevant equations is

$$\widehat{C}_i\,\frac{d\delta_i}{dt} = \sum_j \left((\mathcal{F}_{\text{in}}^{\text{C}})_j \times ((\delta_{\mathcal{F}_{\text{in}}^{\text{C}}})_j - \delta_i) \right) - \sum_k \left((\mathcal{F}_{\text{out}}^{\text{C}})_k \times ((\delta_{\mathcal{F}_{\text{out}}^{\text{C}}})_k - \delta_i) \right)$$

$$+ \sum_l \left((\mathcal{S}_{\text{in}}^{\text{C}})_l \times ((\delta_{\mathcal{S}_{\text{in}}^{\text{C}}})_l - \delta_i) \right) - \sum_m \left((\mathcal{S}_{\text{out}}^{\text{C}})_m \times ((\delta_{\mathcal{S}_{\text{out}}^{\text{C}}})_m - \delta_i) \right) \tag{4.4}$$

where δ_i stands for either $\delta^{13}C_i$ or $\delta^{14}C_i$. This equation is derived from the more general equation (B.9) which can be used to describe the evolution of a ratio of two quantities in terms of a deviation from a standard ratio. Here, the two quantities are ^{13}C and C on one hand, and ^{14}C and C on the other. That equation is established in the appendix, together with two others, applicable to describe variations of absolute ratios ((B.6) and its extended form (B.7) which also takes net exchange fluxes into account). Of those, equation (B.7) will be required to establish the equation for δ^{13}C in the atmosphere.

The exchange fluxes that make up the transport and the source and sink terms of equation (4.3) have been divided into different categories, distinguished by calligraphic letters. Superscripts are used to specify the relevant species, i.e. alkalinity (A), carbon (C), oxygen (O) and phosphate (P); Q again stands for any one of these. The most important of these fluxes are

- $\mathcal{W}_i^{\mathrm{Q\,in}}$, $\mathcal{W}_i^{\mathrm{Q\,out}}$, $\mathcal{W}_i^{\mathrm{Q}}$ – the inflow, outflow and the net gain of species Q for reservoir i, resulting from the transport by water circulation:

$$\mathcal{W}_i^{\mathrm{Q}} = \mathcal{W}_i^{\mathrm{Q\,in}} - \mathcal{W}_i^{\mathrm{Q\,out}},$$

  with

$$\mathcal{W}_i^{\mathrm{Q\,in}} = \sum_{j \in WO} W_{j \to i} \frac{\widehat{Q}_j}{Vol_j} \quad \text{and} \quad \mathcal{W}_i^{\mathrm{Q\,out}} = \sum_{j \in WO} W_{i \to j} \frac{\widehat{Q}_i}{Vol_i};$$

- $\mathcal{X}_i^{\mathrm{C}}$ – the net air-to-sea transfer of CO_2 through the interface of the reservoir i (surface only);

- $\mathcal{U}_i^{\mathrm{Q}}$, $\mathcal{R}_i^{\mathrm{Q}}$ – the uptake and release of species Q within the reservoir i, where Q = C, O or P;

- $\mathcal{P}_i^{\mathrm{A}}$, $\mathcal{D}_i^{\mathrm{A}}$ – the production and destruction of alkalinity (A) within the reservoir i;

- $\mathcal{S}_i^{\mathrm{Q}}$ – the supply of species Q to reservoir i, where Q = A or C.

For convenience, we will also use $\mathcal{I}_i^{\mathrm{Q}}$, $\mathcal{O}_i^{\mathrm{Q}}$ and $\mathcal{T}_i^{\mathrm{Q}}$ to represent the fluxes of species Q respectively into, out of and through the reservoir i, under an other form than the one represented by $\widehat{Q}_i$. $\mathcal{T}_i^{\mathrm{C}}$ might for example stand for the transfer of carbon in organic particles trough the thermocline reservoirs. These do however not appear in any final mass balance equations.

4.2.2   Atmospheric Reservoir

In the atmospheric reservoir, we only consider CO_2, which is given in terms of $p_{CO_2\,(atm)}$, and its carbon isotopic compositions, described by $\delta\,^{13}C$ and $\delta\,^{14}C$ respectively.

Carbon Dioxide

The different fluxes that influence the CO_2 content of the atmospheric reservoir are

- $\mathcal{X}_{atm}^{C}$ – CO_2 exchanged with the surface ocean reservoirs;

- $\mathcal{R}_{atm}^{C}$ – CO_2 released to the atmosphere by volcanic activity;

- $\mathcal{U}_{atm}^{C}$ – CO_2 consumed by chemical rock weathering.

According to equation (1.5) on page 22, the net air-to-sea transfer of CO_2 across the interface of a surface reservoir i is

$$\mathcal{X}_i^{C} = K\,K_0\left(p_{CO_2\,(atm)} - p_{CO_2\,(i)}\right) \times Area_i \qquad (4.5)$$

In our model, we use a uniform, constant value of $0.0572\,\mathrm{mol\,m^{-2}\,yr^{-1}\,\mu atm^{-1}}$ for the *gas transfer coefficient* $K' = K\,K_0$, neglecting its dependence on temperature and wind speed. As the strong variations of both K and K_0 with temperature tend to cancel each other in the product $K\,K_0$, the temperature sensitivity of K' is rather small (SARMIENTO et al., 1992). The dependence of K' on wind speed is much more pronounced and it is at the origin of large latitudinal variations of K', of the order of $\pm 40\%$ around its global average value (SARMIENTO et al., 1992). For simplicity, and because of a lack of information on the evolution of the latitudinal distribution of wind speed over the last glacial-interglacial cycle, we do not take this dependence into account here.

The consumption of CO_2 by chemical rock weathering $\mathcal{U}_{atm}^{C}$ is composed of two independent contributions $\mathcal{U}_{atm}^{C\,Carb}$ and $\mathcal{U}_{atm}^{C\,Sili}$, from carbonate and silicate weathering respectively. $\mathcal{U}_{atm}^{C\,Carb}$ and $\mathcal{U}_{atm}^{C\,Sili}$, as well as $\mathcal{R}_{atm}^{C}$, are prescribed forcings, i.e. time-dependent functions. As shown in chapter 3, they are not independent of each other. They have to meet a number of constraints and they need to be properly set up for each simulation. In chapters 5, 6 and 7, we analyse a number of scenarios for their evolution over the last glacial-interglacial period, based upon different reconstruction methods. For the sake of simplicity, $\mathcal{R}_{atm}^{C}$ also takes into account the CO_2 released by hydrothermal activity at the sea-floor. Although it would be easy to include

separate fluxes for these two contributions, it would be rather difficult to define a realistic partitioning of the global emission — which is the only one that can be derived from the contructed scenarios — into a volcanic and a hydrothermal part. Uncertainties in our present knowledge of these two emissions are simply too large.

The mass balance equation for atmospheric CO_2 finally writes

$$\frac{d\widehat{C}_{\text{atm}}}{dt} = -\mathcal{X}^{\text{C}}_{\text{atm}} + \mathcal{R}^{\text{C}}_{\text{atm}} - \mathcal{U}^{\text{C}}_{\text{atm}} \qquad (4.6)$$

where

$$\mathcal{X}^{\text{C}}_{\text{atm}} = \sum_{i \in Srfc} \mathcal{X}^{\text{C}}_i \qquad (4.7)$$

$$\mathcal{U}^{\text{C}}_{\text{atm}} = \mathcal{U}^{\text{C Carb}}_{\text{atm}} + \mathcal{U}^{\text{C Sili}}_{\text{atm}}. \qquad (4.8)$$

$\widehat{C}_{\text{atm}}$ (in moles) is related to $p_{CO_2 \, (\text{atm})}$ (in μatm, or ppmv) by the relationship $\widehat{C}_{\text{atm}} = 176.73 \times p_{CO_2 \, (\text{atm})}$. For each surface reservoir i, the $p_{CO_2 \, (i)}$ required to determine $\mathcal{X}^{\text{C}}_i$ (equation (4.5)) is calculated from $\widehat{C}_i$ and $\widehat{A}_i$.

Carbon Isotopes

Carbon-13. The exchange fluxes of both CO_2 and $^{13}CO_2$ are only known as net fluxes. In that case, the generic equation (4.4) is difficult to use, and it is preferable to start from the fundamental equation for ^{13}R ((B.7) in the appendix, applied to $^{13}C/C$) to establish the equation for $\delta\,^{13}C_{\text{atm}}$. We thus have

$$\widehat{C}_{\text{atm}} \frac{d\,^{13}R_{\text{atm}}}{dt} = -\sum_{i \in Srfc} \left(\mathcal{X}^{^{13}\text{C}}_i - \mathcal{X}^{\text{C}}_i \times\,^{13}R_{\text{atm}} \right)$$
$$+ \mathcal{R}^{\text{C}}_{\text{atm}} \times (^{13}R_{\mathcal{R}^{\text{C}}_{\text{atm}}} -\,^{13}R_{\text{atm}}) - \mathcal{U}^{\text{C}}_{\text{atm}} \times (^{13}R_{\mathcal{U}^{\text{C}}_{\text{atm}}} -\,^{13}R_{\text{atm}}). \qquad (4.9)$$

It is assumed that CO_2 bears the same isotopic signature when consumed during carbonate and during silicate weathering. $\mathcal{X}^{^{13}\text{C}}_i$ is the net air-to-sea flux of $^{13}CO_2$ across the interface of the surface reservoir i

$$\mathcal{X}^{^{13}\text{C}}_i = K\, K_0 \left(\alpha_{\text{as}}\,^{13}R_{\text{atm}}\, p_{CO_2 \, (\text{atm})} - \alpha_{\text{sa}}\,^{13}R_i\, p_{CO_2 \, (i)} \right) \times Area_i \qquad (4.10)$$

The one-way fractionation factors α_{as} and α_{sa} can be written as $\alpha_{\text{as}} = 1 + \varphi_{\text{as}}$ and $\alpha_{\text{sa}} = 1 + \varphi_{\text{sa}}$. Using the relationship between $\delta\,^{13}C$ and ^{13}R values and neglecting terms of second order in $\delta\,^{13}C$, equation (4.10) becomes

$$\mathcal{X}^{^{13}\text{C}}_i = K\, K_0 \left((\delta\,^{13}C_{\text{atm}} + \varphi_{\text{as}} + 1)\, p_{CO_2 \, (\text{atm})} \right.$$
$$\left. - (\delta\,^{13}C_i + \varphi_{\text{sa}} + 1)\, p_{CO_2 \, (i)} \right)\,^{13}R_* \times Area_i \qquad (4.11)$$

The equation for $\delta^{13}\mathrm{C}_{\mathrm{atm}}$ is then obtained by introducing (4.11) into (4.9) where the different ^{13}R ratios appearing at the right-hand side have been replaced by their respective expressions in $\delta^{13}\mathrm{C}$. After simplification, we obtain

$$
\begin{aligned}
\widehat{C}_{\mathrm{atm}}\,\frac{d\,\delta^{13}\mathrm{C}_{\mathrm{atm}}}{dt} =& \\
& -\sum_{i\in Srfc} K\,K_0\,\left(\varphi_{\mathrm{as}}\,p_{\mathrm{CO}_2\,(\mathrm{atm})} - (\delta^{13}\mathrm{C}_i - \delta^{13}\mathrm{C}_{\mathrm{atm}} + \varphi_{\mathrm{sa}})\,p_{\mathrm{CO}_2\,(i)}\right) \times Area_i \\
& + \mathcal{R}^{\mathrm{C}}_{\mathrm{atm}} \times (\delta^{13}\mathrm{C}_{\mathcal{R}^{\mathrm{C}}_{\mathrm{atm}}} - \delta^{13}\mathrm{C}_{\mathrm{atm}}) - \mathcal{U}^{\mathrm{C}}_{\mathrm{atm}} \times (\delta^{13}\mathrm{C}_{\mathcal{U}^{\mathrm{C}}_{\mathrm{atm}}} - \delta^{13}\mathrm{C}_{\mathrm{atm}})
\end{aligned}
\tag{4.12}
$$

We use $\varphi_{\mathrm{as}} = -0.002$ and $\varphi_{\mathrm{sa}} = -0.010$ as global values, within the ranges calculated by SIEGENTHALER and MÜNNICH (1981). It should however be noticed that the results of these authors have been established for $20°\mathrm{C}$. This approximation does not influence the results to a large extent, given the uncertainties on the other parameters of the $\delta^{13}\mathrm{C}$ treatment in our model. The consequences stemming from the poorly known values for $\delta^{13}\mathrm{C}_{\mathcal{R}^{\mathrm{C}}_{\mathrm{atm}}}$ and $\delta^{13}\mathrm{C}_{\mathcal{U}^{\mathrm{C}}_{\mathrm{atm}}}$ are far more important. We use $\delta^{13}\mathrm{C}_{\mathcal{R}^{\mathrm{C}}_{\mathrm{atm}}} = 0.002$ and $\delta^{13}\mathrm{C}_{\mathcal{U}^{\mathrm{C}}_{\mathrm{atm}}} = \delta^{13}\mathrm{C}_{\mathrm{atm}} - 0.020$. The latter is meant to reflect the fact that the CO_2 consumed during rock weathering mostly stems from the respiration of soil organic matter, on average $20\,^0\!/_{00}$ lighter than the atmospheric CO_2 from which it is formed.

Carbon-14. The atmospheric radiocarbon content is supposed to be at steady state, which translates to

$$
\frac{d\,\delta^{14}\mathrm{C}_{\mathrm{atm}}}{dt} = 0.
\tag{4.13}
$$

$\delta^{14}\mathrm{C}_{\mathrm{atm}}$ is set to -0.038, so that $\Delta^{14}\mathrm{C}_{\mathrm{atm}}$ is close to 0.

4.2.3 Surface Reservoirs

The surface reservoirs are in contact with the overlying atmosphere and with the thermocline reservoirs, or, in the polar regions, the deep reservoirs below. They are the site of biological production, both organic and inorganic. We distinguish between "open ocean" and coastal environments. In the "open ocean" organic and inorganic matter is transferred from the surface to the thermocline and the deep water. A fixed fraction of the phosphate entering each surface reservoir is used for organic matter production, which follows the

Redfield ratios $C:P:N:O_2 = 106:1:16:-138$. Inorganic production (planktonic calcium carbonate) is assumed to be proportional to organic production in each reservoir. In the coastal environment, no separate organic matter transfer is taken into account. Only the accumulation of carbonate material by coral reefs and on banks and shelves are considered there.

Finally, the surface reservoirs also collect the DIC and the alkalinity carried by the bicarbonate transported to the oceans by rivers.

Phosphate

Besides getting transported by ocean circulation, phosphate is only affected by biological cycling: a fixed fraction of the phosphate entering each surface reservoir is used for organic matter production. In any surface reservoir i, the evolution of $\widehat{P}_i$ is hence governed by

$$\frac{d\widehat{P}_i}{dt} = \mathcal{W}_i^{\mathrm{P}} - \mathcal{U}_i^{\mathrm{P}}, \tag{4.14}$$

where

$$\mathcal{U}_i^{\mathrm{P}} = u_i^{\mathrm{P}} \times \mathcal{W}_i^{\mathrm{P\,in}} \tag{4.15}$$

represents the uptake of phosphate for organic matter production. The $u_i^{\mathrm{P}} (i \in Srfc)$ are adjustable parameters.

Oxygen

We suppose that the surface waters are constantly at saturation with respect to oxygen. Hence,

$$\frac{d\widehat{O}_i}{dt} = 0. \tag{4.16}$$

Dissolved Inorganic Carbon

The different fluxes taken into account in the DIC budget for each surface reservoir i are

- $\mathcal{X}_i^{\mathrm{C}}$ – the net air-to-sea flux of CO_2, exchanged with the atmospheric reservoir;

- $\mathcal{W}_i^{\mathrm{C}}$ – the net DIC increase from the transport by water circulation

- $\mathcal{U}_i^{\mathrm{C}}$ – the DIC taken up during biological production (organic and inorganic);

- $\mathcal{S}_i^{\mathrm{C}}$ – the DIC delivered by rivers.

Of these, only $\mathcal{U}_i^{\mathrm{C}}$ and $\mathcal{S}_i^{\mathrm{C}}$ require detailed descriptions. $\mathcal{U}_i^{\mathrm{C}}$ consists of an organic and of an inorganic part:

$$\mathcal{U}_i^{\mathrm{C}} = \mathcal{U}_i^{\mathrm{C\,Org}} + \mathcal{U}_i^{\mathrm{C\,Inorg}} \qquad (4.17)$$

The former is directly linked to the phosphate consumption $\mathcal{U}_i^{\mathrm{P}}$ (equation (4.15)) via

$$\mathcal{U}_i^{\mathrm{C\,Org}} = \mathcal{U}_i^{\mathrm{P}} \times r_{\mathrm{C:P}} \qquad (4.18)$$

where $r_{\mathrm{C:P}} = 106$ is the C:P Redfield ratio. The latter is further subdivided into three parts, for open ocean export to the deep sea on one hand, and for the accumulation by coral reefs and on banks and shelves on the other hand:

$$\mathcal{U}_i^{\mathrm{C\,Inorg}} = \mathcal{U}_i^{\mathrm{C\,InorgOO}} + \mathcal{U}_i^{\mathrm{C\,InorgCR}} + \mathcal{U}_i^{\mathrm{C\,InorgBS}} \qquad (4.19)$$

The export of carbonate material in the open ocean is supposed to be proportional to the export of organic matter:

$$\mathcal{U}_i^{\mathrm{C\,InorgOO}} = r_i^{\mathrm{C}} \times \mathcal{U}_i^{\mathrm{C\,Org}}. \qquad (4.20)$$

The carbonate production consists of calcite and of aragonite, the latter making up a fraction r_{Arag} of each $\mathcal{U}_i^{\mathrm{C\,InorgOO}}$. The rain ratios r_i^{C} ($i \in Srfc$) and r_{Arag} (one global value) are adjustable parameters.

The accumulation of carbonate in the shallow water environments are restricted to the temperate surface reservoirs SEATL and SEI-P. The growth of coral reefs, which produce only aragonite as carbonate mineral, is determined by the combined effect of three factors.

1. They grow only in water shallower than 100 m and on the continental shelf. The favorable area $Area100_i$ thus changes in time as sea level rises and falls.

2. Coral reefs can neither build up during sea level drops nor during too fast rises. The corresponding limiting function $\mathcal{L}$ has a trapezoidal shape (see inset on figure 4.6).

3. Finally, coral reef growth is enhanced when the degree of supersaturation $\Omega_{\mathrm{Arag}\,(i)}$ of seawater with respect to aragonite increases. This is translated by taking it proportional to $(\Omega_{\mathrm{Arag}\,(i)} - 1)^{1.7}$ (OPDYKE and WILKINSON, 1988).

Nonreefal carbonate accumulation on banks and shelves is simply proportional to $Area100_i$. Hence,

$$\begin{cases} \mathcal{U}_i^{\mathrm{C\,InorgCR}} &= k_{\mathrm{CR}} \times Area100_i \times \mathcal{L} \times (\Omega_{\mathrm{Arag}\,(i)} - 1)^{1.7} \\ \mathcal{U}_i^{\mathrm{C\,InorgBS}} &= k_{\mathrm{BS}} \times Area100_i \qquad \text{if } i \in \{\mathrm{SEATL}, \mathrm{SEI\text{-}P}\} \\[2mm] \mathcal{U}_i^{\mathrm{C\,InorgCR}} &= \mathcal{U}_i^{\mathrm{C\,InorgBS}} = 0 \qquad \text{else.} \end{cases} \qquad (4.21)$$
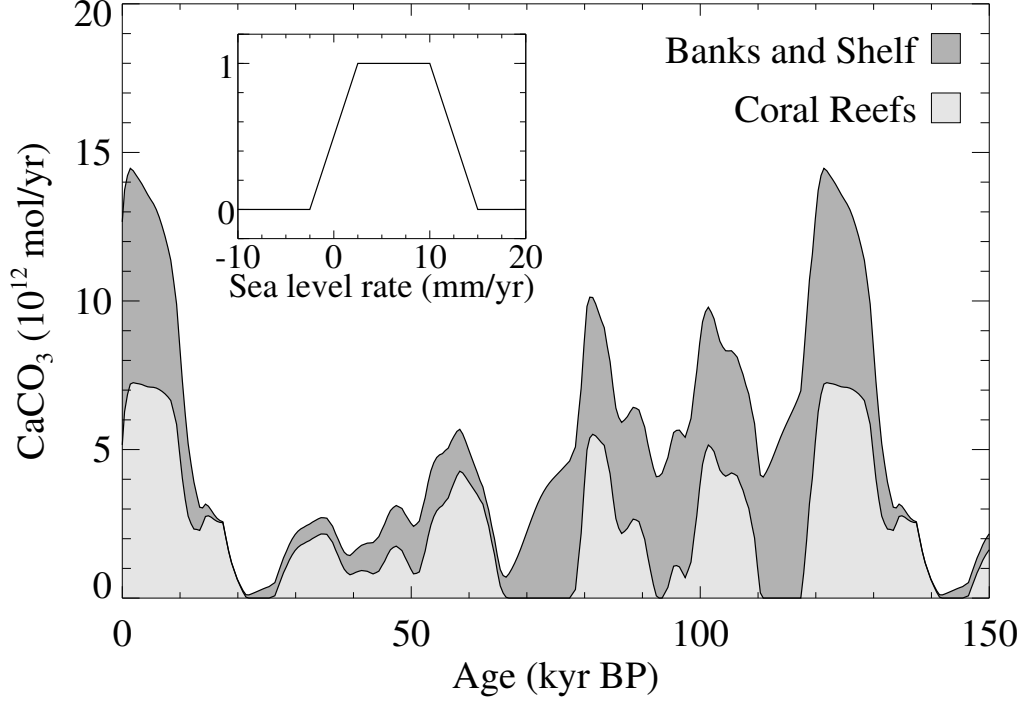
Figure 4.6: Shallow water carbonate precipitation. The inset shows the function $\mathcal{L}$ limiting the coral reef growth with respect to the rate of sea level rise and fall.

Area100$_i$ and $\mathcal{L}$ are evaluated from the sea level curve. $\Omega_{\mathrm{Arag}\,(i)}$ is calculated from $\widehat{C}_i$ and $\widehat{A}_i$. The two parameters k_{CR} and k_{BS} are adjusted to reach a global average CaCO$_3$ accumulation of 7×10^{12} mol CaCO$_3$/yr by coral reefs and of 7.5×10^{12} mol CaCO$_3$/yr on banks and shelves over the last 5000 years (MILLIMAN, 1993). Figure 4.6 shows the histories for these two schemes.

The total bicarbonate delivered by rivers stems from continental weathering. It is hence composed of two parts, one coming from the atmosphere, the other from rock carbonate:

$$\mathcal{S}^{\mathrm{C}} = \mathcal{S}^{\mathrm{C\,Atm}} + \mathcal{S}^{\mathrm{C\,Rock}}. \tag{4.22}$$

Since we assume that carbonic acid is the dominant acid agent and neglect other possible contributors (e.g. sulphuric acid), we know that

$$\mathcal{S}^{\mathrm{C\,Atm}} = \mathcal{U}_{\mathrm{atm}}^{\mathrm{C\,Sili}} + \mathcal{U}_{\mathrm{atm}}^{\mathrm{C\,Carb}} \tag{4.23}$$

and that

$$\mathcal{S}^{\mathrm{C\,Rock}} = \mathcal{U}_{\mathrm{atm}}^{\mathrm{C\,Carb}}. \tag{4.24}$$

For each of $\mathcal{S}^{\mathrm{C\,Atm}}$ and $\mathcal{S}^{\mathrm{C\,Rock}}$, one half is delivered to SEATL, the other one to SEI-P. Hence,

$$\begin{cases} \mathcal{S}_i^{\mathrm{C\,Atm}} &= \frac{1}{2}\mathcal{S}^{\mathrm{C\,Atm}} \\ \mathcal{S}_i^{\mathrm{C\,Rock}} &= \frac{1}{2}\mathcal{S}^{\mathrm{C\,Rock}} \qquad \text{if } i \in \{\mathrm{SEATL, SEI\text{-}P}\} \\[2mm] \mathcal{S}_i^{\mathrm{C\,Atm}} &= \mathcal{S}_i^{\mathrm{C\,Rock}} = 0 \qquad \text{else.} \end{cases} \tag{4.25}$$

The individual contribution $\mathcal{S}_i^{\mathrm{C}}$ to each reservoir i is then obtained from

$$\mathcal{S}_i^{\mathrm{C}} = \mathcal{S}_i^{\mathrm{C\,Atm}} + \mathcal{S}_i^{\mathrm{C\,Rock}}. \tag{4.26}$$

The variations of $\widehat{C}_i$ are now completely determined by

$$\frac{d\widehat{C}_i}{dt} = \mathcal{W}_i^{\mathrm{C}} + \mathcal{X}_i^{\mathrm{C}} + \mathcal{S}_i^{\mathrm{C}} - \mathcal{U}_i^{\mathrm{C}}. \tag{4.27}$$

Total Alkalinity

The relevant fluxes of alkalinity into and out of the surface reservoirs are

- $\mathcal{W}_i^{\mathrm{A}}$ – the alkalinity exchanged with the other water reservoirs;

- $\mathcal{P}_i^{\mathrm{A}}$ – the creation during organic matter production;

- $\mathcal{D}_i^{\mathrm{A}}$ – the destruction during carbonate precipitation;

- $\mathcal{S}_i^{\mathrm{A}}$ – the alkalinity carried by riverine bicarbonate.

$\mathcal{P}_i^{\mathrm{A}}$ is linked to the uptake of phosphate $\mathcal{U}_i^{\mathrm{P}}$ (from equation (4.15)) by

$$\mathcal{P}_i^{\mathrm{A}} = \mathcal{U}_i^{\mathrm{P}} \times (1 + r_{\mathrm{N:P}}) \tag{4.28}$$

where $r_{\mathrm{N:P}} = 16$ is the N:P Redfield ratio. This equation translates the fact that one equivalent of alkalinity is produced for each mole of phosphate consumed, and another one for each mol of nitrate. $\mathcal{D}_i^{\mathrm{A}}$ equals twice the uptake of DIC for carbonate production ($\mathcal{U}_i^{\mathrm{C\,Inorg}}$, from equations (4.19) – (4.21))

$$\mathcal{D}_i^{\mathrm{A}} = 2 \times \mathcal{U}_i^{\mathrm{C\,Inorg}} \tag{4.29}$$

and $\mathcal{S}_i^{\mathrm{A}}$ is equal to the delivery of bicarbonate by rivers $\mathcal{S}_i^{\mathrm{C}}$ (from equations (4.22) – (4.26))

$$\mathcal{S}_i^{\mathrm{A}} = \mathcal{S}_i^{\mathrm{C}}. \tag{4.30}$$

The evolution of the surface reservoir alkalinity is then completely described by

$$\frac{d\widehat{A}_i}{dt} = \mathcal{W}_i^{\mathrm{A}} + \mathcal{S}_i^{\mathrm{A}} + \mathcal{P}_i^{\mathrm{A}} - \mathcal{D}_i^{\mathrm{A}}. \tag{4.31}$$

Carbon Isotopes

Carbon-13. The most complicated term in the $\delta^{13}C$ equation in surface reservoirs is the one related to the air-sea exchange. Since its expression has been determined before (equation (4.11)), the equation for $\delta^{13}C_i$ is now straightforward to establish:

$$\widehat{C}_i \, \frac{d\,\delta^{13}C_i}{dt} = \sum_{j \in WO} W_{j \to i} \frac{\widehat{C}_j}{Vol_j} (\delta^{13}C_j - \delta^{13}C_i) \tag{4.32}$$

$$+ K\,K_0 \left((\delta^{13}C_{atm} - \delta^{13}C_i + \varphi_{as})\,p_{CO_2\,(atm)} - \varphi_{sa}\,p_{CO_2\,(i)} \right) \times Area_i$$
$$+ \mathcal{S}_i^{C\,Atm} \times (\delta^{13}C_{\mathcal{S}_i^{C\,Atm}} - \delta^{13}C_i) + \mathcal{S}_i^{C\,Rock} \times (\delta^{13}C_{\mathcal{S}_i^{C\,Rock}} - \delta^{13}C_i)$$
$$- \mathcal{U}_i^{C\,Org} \times (\delta^{13}C_{\mathcal{U}_i^{C\,Org}} - \delta^{13}C_i) - \mathcal{U}_i^{C\,Inorg} \times (\delta^{13}C_{\mathcal{U}_i^{C\,Inorg}} - \delta^{13}C_i).$$

We only need to specify the $\delta^{13}C$ values which characterize the different fluxes. $\delta^{13}C_{\mathcal{S}_i^{C\,Atm}}$ is simply equal to $\delta^{13}C_{\mathcal{U}_{atm}^C}$. $\delta^{13}C_{\mathcal{S}_i^{C\,Rock}}$, the $\delta^{13}C$ of the carbon originating from the lithosphere, is set to 0.002. In order to avoid a slow drift of the mean $\delta^{13}C$ of our system, we had to use a somewhat smaller value of 0.00175 $(1.75\,\%_{00})$ in some experiences. Both are nevertheless well within the range of $1.8 \pm 0.2\,\%_{00}$ given by DERRY and FRANCE-LANORD (1996). Regarding the two remaining fluxes, the biogenic ones, we suppose that there is no fractionation during carbonate precipitation (i.e., $\delta^{13}C_{\mathcal{U}_i^{C\,Inorg}} - \delta^{13}C_i = 0.000$) and that organic carbon is $20\,\%_{00}$ lighter than the DIC used to produce it (i.e., $\delta^{13}C_{\mathcal{U}_i^{C\,Org}} - \delta^{13}C_i = -0.020$).

Carbon-14. The $\delta^{14}C$ and the $\delta^{13}C$ equations are of course very similar. The $\delta^{14}C$ can easily be established by transposing that for $\delta^{13}C$, considering that the fractionation differences for ^{14}C are twice those of ^{13}C and completing it by a supplementary sink term to take the radiodecay into account. For a given reservoir i, the loss of DIC by radiodecay of ^{14}C is equal to $\lambda \times \widehat{^{14}C_i}$, where $\lambda = 1/8267$ yr^{-1} is the decay constant of ^{14}C and $\widehat{^{14}C_i} = \widehat{C}_i(\delta^{14}C_i + 1)^{14}R_*$. This loss consists only of ^{14}C and its $\delta^{14}C$ is equal to $(1 - {}^{14}R_*)/{}^{14}R_*$. The additional term is

$$-\lambda \times \widehat{C}_i(\delta^{14}C_i + 1)\,{}^{14}R_* \times ((1 - {}^{14}R_*)/{}^{14}R_* - \delta^{14}C_i)$$
$$\simeq -\lambda \times \widehat{C}_i(\delta^{14}C_i + 1) \tag{4.33}$$

to first order in $\delta^{14}C_i$. The full equation used for $\delta^{14}C_i$ is then

$$\widehat{C}_i \, \frac{d\,\delta^{14}C_i}{dt} = \sum_{j \in WO} W_{j \to i} \frac{\widehat{C}_j}{Vol_j} (\delta^{14}C_j - \delta^{14}C_i) \tag{4.34}$$

$$+ K K_0 \left((\delta^{14}C_{atm} - \delta^{14}C_i + 2\varphi_{as}) \, p_{CO_2 \, (atm)} - 2\varphi_{sa} \, p_{CO_2 \, (i)} \right) \times Area_i$$
$$+ \mathcal{S}_i^{C \, Atm} \times (\delta^{14}C_{\mathcal{S}_i^{C \, Atm}} - \delta^{14}C_i) + \mathcal{S}_i^{C \, Rock} \times (\delta^{14}C_{\mathcal{S}_i^{C \, Rock}} - \delta^{14}C_i)$$
$$- \mathcal{U}_i^{C \, Org} \times (\delta^{14}C_{\mathcal{U}_i^{C \, Org}} - \delta^{14}C_i) - \lambda \times \widehat{C}_i(\delta^{14}C_i + 1).$$

The term relative to $\mathcal{U}_i^{C \, Inorg}$ has already been omitted since it vanishes as a consequence of the absence of carbon isotope fractionation during the precipitation of $CaCO_3$. The remaining unknown $\delta^{14}C$ values are related to their $\delta^{13}C$ counterparts, considering that

- the fractionation of ^{14}C during organic matter production is twice that of ^{13}C

$$\delta^{14}C_{\mathcal{U}_i^{C \, Org}} - \delta^{14}C_i = 2 \times (\delta^{13}C_{\mathcal{U}_i^{C \, Org}} - \delta^{13}C_i) = -0.040; \qquad (4.35)$$

- the atmospheric CO_2 consumed during chemical rock weathering has been twice as much fractionated with respect to ^{14}C than for ^{13}C

$$\delta^{14}C_{\mathcal{S}_i^{C \, Atm}} - \delta^{14}C_{atm} = 2 \times (\delta^{13}C_{\mathcal{S}_i^{C \, Atm}} - \delta^{13}C_{atm}). \qquad (4.36)$$

Finally, it is assumed that continental carbonate rocks are devoid of ^{14}C, i.e., $\delta^{14}C_{\mathcal{S}_i^{C \, Rock}} = -1.000$.

4.2.4   Thermocline and Deep Reservoirs

The two thermocline reservoirs are merely transit reservoirs but their presence is required to avoid unrealistic behaviour, especially with regard to dissolved oxygen, as often observed in two-box models (see, e.g., Sarmiento, 1986, 1992). In our model, they collect the organic matter raining down from the overlying surface reservoirs. A large fraction of this matter gets remineralized, the rest gets transferred to the underlying deep reservoirs, where remineralization completes. As already shortly pointed out before, organic matter remineralization follows the same Redfield ratios as its production in the surface waters.

The inorganic fraction of the biogenic rain is supposed not to dissolve on its way through the thermocline water column. Dissolution of biogenic carbonate particles is supposed to take place only in the deep sea, and all of the carbon and alkalinity coming from it is accounted for in the deep reservoirs. There are neither carbon nor alkalinity sources related to carbonate dissolution in the thermocline reservoirs.

The deep reservoirs are in contact with the thermocline reservoirs in the equatorial region and with the surface reservoirs in the polar regions. They are furthermore the site of exchange of carbon with the sedimentary shell.

There is no need for specific thermocline equations because they are special cases of those for the deep reservoirs, with irrelevant fluxes set to 0.

Dissolved Inorganic Carbon

The general introduction to this section has already presented the most important fluxes that influence the inorganic carbon content of the thermocline and deep reservoirs. The complete list for any reservoir i of these contains two more:

- $\mathcal{W}_i^{\mathrm{C}}$ – the net DIC increase from the transport by water circulation;

- $\mathcal{R}_i^{\mathrm{C}}$ – the DIC released during organic matter remineralization and by carbonate dissolution (deep reservoirs only).

Organic Matter Fluxes.   In terms of carbon, the inputs of organic matter raining down from the surface to the thermocline reservoirs are respectively

$$\mathcal{I}_{\mathrm{TEATL}}^{\mathrm{C\,Org}} = \mathcal{U}_{\mathrm{SEATL}}^{\mathrm{C\,Org}} \quad \text{and} \quad \mathcal{I}_{\mathrm{TEI\text{-}P}}^{\mathrm{C\,Org}} = \mathcal{U}_{\mathrm{SEI\text{-}P}}^{\mathrm{C\,Org}}.$$

A fraction r_{oxyd} of this organic matter gets remineralized, releasing its carbon back to solution. For $i \in \textit{Thcl}$, the remineralization and transfer fluxes are then

$$\mathcal{R}_i^{\mathrm{C\,Org}} = \mathcal{I}_i^{\mathrm{C\,Org}} \times r_{\mathrm{oxyd}} \quad \text{and} \quad \mathcal{T}_i^{\mathrm{C\,Org}} = \mathcal{I}_i^{\mathrm{C\,Org}} - \mathcal{R}_i^{\mathrm{C\,Org}}. \tag{4.37}$$

r_{oxyd} is another of the adjustable parameters.

Organic matter fluxes reaching the different deep reservoirs are then

$$\begin{aligned}
\mathcal{I}_{\mathrm{DATL}}^{\mathrm{C\,Org}} &= \mathcal{U}_{\mathrm{SNATL}}^{\mathrm{C\,Org}} + \mathcal{T}_{\mathrm{TEATL}}^{\mathrm{C\,Org}} \\
\mathcal{I}_{\mathrm{DANT}}^{\mathrm{C\,Org}} &= \mathcal{U}_{\mathrm{SANT}}^{\mathrm{C\,Org}} \\
\mathcal{I}_{\mathrm{DI\text{-}P}}^{\mathrm{C\,Org}} &= \mathcal{U}_{\mathrm{SNPAC}}^{\mathrm{C\,Org}} + \mathcal{T}_{\mathrm{TEI\text{-}P}}^{\mathrm{C\,Org}}.
\end{aligned}$$

All of this gets remineralized, which means that

$$\mathcal{R}_i^{\mathrm{C\,Org}} = \mathcal{I}_i^{\mathrm{C\,Org}} \tag{4.38}$$

for any deep reservoir i.

Carbonate Fluxes. The fate of the carbonate particles raining down from the surface reservoirs in the open ocean depends on several factors, of which the position of the aragonite and calcite saturation depths — ASD and CSD — are the most important. The rationale of the carbonate dissolution in the thermocline and deep reservoirs of our model is based on the following hypotheses.

1. The carbonate rain is uniformly distributed over the whole open ocean area, defined as the area where water is deeper than 200 m, the approximate depth of the continental shelf break.

2. Neither calcite nor aragonite particles get dissolved in waters supersaturated with respect to them. Hence, all of the aragonite produced in waters shallower than the ASD and all of the calcite particles produced in waters shallower than the CSD reach the sea-floor and are preserved in the sedimentary mixed layer. For aragonite, it is further assumed that it gets transformed into calcite by diagenetic processes during its residence in the sediments.

3. Aragonite produced in waters where the sea-floor lies deeper than the ASD gets dissolved within the water column in the deep sea below, and does not reach the sea-floor.

4. Calcite particles on the other hand always reach the sea-floor where they are taken up by the sedimentary mixed layer. Below the CSD, a more or less important fraction dissolves, depending on the degree of saturation with respect to calcite in the overlying water and on the fraction of carbonate material already present in the mixed layer. The rest is preserved and may later get buried or also dissolved. Dissolution products diffuse out of the sedimentary mixed layer and get released to the deep reservoirs. If conditions are favourable, old carbonate (i.e. calcite, since all of the aragonite in the sediments becomes calcite) from below the sedimentary mixed layer may get unburied and also dissolved, representing a source of DIC and alkalinity to the ocean. A complete description of the adopted dissolution scheme, the theory behind it and the basic hypotheses that it is based upon is given in section 4.3.

5. No carbonate dissolution takes place in the thermocline reservoirs. As a consequence,
$$\mathcal{R}_{\text{TEATL}}^{\text{C Inorg}} = \mathcal{R}_{\text{TEI-P}}^{\text{C Inorg}} = 0. \tag{4.39}$$

The main purpose of this hypothesis is to simplify the computational model overhead when coupling the ocean and the sediment modules.

It is however reasonable, because in our model, even the ASD rarely gets shallower than 1000 m.

The complete equation governing the evolution of $\widehat{C}_i$ in a thermocline or a deep reservoir i is then

$$\frac{d\widehat{C}_i}{dt} = \mathcal{W}_i^{\mathrm{C}} + \mathcal{R}_i^{\mathrm{C}}, \tag{4.40}$$

where

$$\mathcal{R}_i^{\mathrm{C}} = \mathcal{R}_i^{\mathrm{C\,Org}} + \mathcal{R}_i^{\mathrm{C\,Inorg}}. \tag{4.41}$$

The different $\mathcal{R}_i^{\mathrm{C\,Org}}$ are given by the equations (4.37) and (4.38). The $\mathcal{R}_i^{\mathrm{C\,Inorg}}$ for the deep reservoirs are computed by the sediment model described in section 4.3 hereafter.

Phosphate and Oxygen

Besides transport by the water circulation, the phosphate and oxygen of any thermocline or deep reservoir are influenced by organic matter remineralization. Their differential equations are respectively

$$\frac{d\widehat{P}_i}{dt} = \mathcal{W}_i^{\mathrm{P}} + \mathcal{R}_i^{\mathrm{P}}, \tag{4.42}$$

and

$$\frac{d\widehat{O}_i}{dt} = \mathcal{W}_i^{\mathrm{O}} - \mathcal{U}_i^{\mathrm{O}}. \tag{4.43}$$

$\mathcal{R}_i^{\mathrm{P}}$ represents the phosphate released during remineralization and is related to the corresponding DIC release (equations (4.37) and (4.38)) by

$$\mathcal{R}_i^{\mathrm{P}} = \mathcal{R}_i^{\mathrm{C\,Org}}/r_{\mathrm{C:P}}. \tag{4.44}$$

$\mathcal{U}_i^{\mathrm{O}}$ is the oxygen consumption, which we calculate from the phosphate release (from the previous equation) by

$$\mathcal{U}_i^{\mathrm{O}} = \mathcal{R}_i^{\mathrm{P}} \times r_{\mathrm{O_2:P}}. \tag{4.45}$$

In this latter equation, $r_{\mathrm{O_2:P}} = 138$ is the O_2:P Redfield ratio.

Total Alkalinity

The equation governing the evolution of alkalinity in the thermocline and the deep reservoirs is essentially the reverse of that in the surface reservoirs: organic matter remineralization now acts as a sink and carbonate dissolution as a source. We thus have

$$\frac{d\widehat{A}_i}{dt} = \mathcal{W}_i^{\mathrm{A}} + \mathcal{P}_i^{\mathrm{A}} - \mathcal{D}_i^{\mathrm{A}} \tag{4.46}$$

where the source term $\mathcal{P}_i^{\mathrm{A}}$ is related to the release of DIC by carbonate dissolution $\mathcal{R}_i^{\mathrm{C\,Inorg}}$ (from the sediment model) by

$$\mathcal{P}_i^{\mathrm{A}} = 2 \times \mathcal{R}_i^{\mathrm{C\,Inorg}} \tag{4.47}$$

and the sink term $\mathcal{D}_i^{\mathrm{A}}$ is related to the phosphate remineralization flux (equation (4.44)) by

$$\mathcal{D}_i^{\mathrm{A}} = \mathcal{R}_i^{\mathrm{P}} \times (1 + r_{\mathrm{N:P}}) \tag{4.48}$$

by analogy with equation (4.28).

Carbon Isotopes

Carbon-13. According to the previous list of the different carbon fluxes, the $\delta\,^{13}\mathrm{C}$ equation for a thermocline or a deep reservoir i can immediately be written by using the generic equation (4.4):

$$\widehat{C}_i \frac{d\,\delta\,^{13}\mathrm{C}_i}{dt} = \sum_{j \in WO} W_{j \to i} \frac{\widehat{C}_j}{Vol_j} (\delta\,^{13}\mathrm{C}_j - \delta\,^{13}\mathrm{C}_i)$$
$$+ \mathcal{R}_i^{\mathrm{C\,Org}} \times (\delta\,^{13}\mathrm{C}_{\mathcal{R}_i^{\mathrm{C\,Org}}} - \delta\,^{13}\mathrm{C}_i) + \mathcal{R}_i^{\mathrm{C\,Inorg}} \times (\delta\,^{13}\mathrm{C}_{\mathcal{R}_i^{\mathrm{C\,Inorg}}} - \delta\,^{13}\mathrm{C}_i). \tag{4.49}$$

Remineralization is supposed to proceed without fractionation for carbon isotopes. The different $\delta\,^{13}\mathrm{C}_{\mathcal{R}_i^{\mathrm{C\,Org}}}$ are hence obtained from the $\delta\,^{13}\mathrm{C}$ of the incoming organic carbon, i.e. from the $\delta\,^{13}\mathrm{C}_{\mathcal{U}_j^{\mathrm{C\,Org}}}$ of the respectively overlying surface reservoirs j. Since the sedimentary mixed layer model does not track carbon isotopes, we use a global mean value of $2\,\%_{00}$ for the carbonate dissolution source: $\delta\,^{13}\mathrm{C}_{\mathcal{R}_i^{\mathrm{C\,Inorg}}} = 0.002$.

Carbon-14. The equation for radiocarbon is again almost identical to that for $^{13}\mathrm{C}$, with the additional sink term for radiodecay:

$$\widehat{C}_i \frac{d\,\delta\,^{14}\mathrm{C}_i}{dt} = \sum_{j \in WO} W_{j \to i} \frac{\widehat{C}_j}{Vol_j} (\delta\,^{14}\mathrm{C}_j - \delta\,^{14}\mathrm{C}_i)$$

$$+ \mathcal{R}_i^{\mathrm{C\,Org}} \times (\delta^{14}\mathrm{C}_{\mathcal{R}_i^{\mathrm{C\,Org}}} - \delta^{14}\mathrm{C}_i) + \mathcal{R}_i^{\mathrm{C\,Inorg}} \times (\delta^{14}\mathrm{C}_{\mathcal{R}_i^{\mathrm{C\,Inorg}}} - \delta^{14}\mathrm{C}_i)$$

$$- \lambda \times \widehat{C}_i (\delta^{14}\mathrm{C}_i + 1). \tag{4.50}$$

The $\delta^{14}\mathrm{C}_{\mathcal{R}_i^{\mathrm{C\,Org}}}$ and $\delta^{14}\mathrm{C}_{\mathcal{R}_i^{\mathrm{C\,Inorg}}}$ are related to the $\delta^{14}\mathrm{C}$ of the organic carbon raining down from the surface in exactly the same way as for $\delta^{13}\mathrm{C}$ above. The carbonate dissolution source is assigned an average $\delta^{14}\mathrm{C}$ of -0.580, obtained by assuming a typical age of about 4,000 yr for the carbonate in the sedimentary mixed layer and an average initial $\delta^{14}\mathrm{C}$ of -0.060.

4.3   The Sedimentary Shell

The biological activity in the surface reservoirs leads to a particle rain of organic and of inorganic (carbonate) matter to the deep sea. While the organic component is completely remineralized in the water column of our model, this is not the case for the carbonate component. Carbonate particles collect in the sedimentary mixed layer which blankets the sea-floor. This sedimentary mixed layer serves as an interface between the ocean and the deep sediment below. Large variations of the calcite lysocline depth have been observed for the last several glacial-interglacial cycles, at various places in the ocean (VOLAT et al., 1980; BALSAM, 1983; CROWLEY, 1983, 1985; FARRELL and PRELL, 1989). These records are still not fully understood and the driving mechanisms — production and preservation cycles, dissolution cycles or dilution cycles — remain subject of debate.

We have therefore decided to include a representation of the sedimentary shell in our carbon cycle model, to take the interaction between the oceanic and the sedimentary environments into account. We require that our sediment-water carbonate exchange scheme should fulfil the following fundamental conditions.

1. The main features of carbonate preservation patterns in the modern ocean should be reproduced. Above a given horizon (corresponding to a lysocline) carbonate gets well preserved. Below this horizon, there is steadily increasing dissolution through a transition zone, down to another horizon (corresponding to a compensation depth) below which it gets completely dissolved. The positions of these two characteristic horizons may vary in time, in response to changing chemical conditions. The model sediment must hence have a sufficiently good structure along water depth.

2. Post-depositional chemical erosion must be possible. Carbonate matter only definitly escapes from the ocean once it has been buried to

sufficiently great depth in the sediments. The representation of the sediment column must therefore have some vertical structure, enabling to keep track of the accumulation history of carbonate.

3. The non-linearity of the carbonate dissolution kinetics is taken into account.

Since we want to use our model to perform long-term simulations (running over at least two glacial cycles), it is clear that a very fast and therefore simple scheme is required. Such a scheme will necessarily be conceptual. Many of our simplifying hypotheses are also commonly adopted in other similar, albeit more complex models (e.g., GUINASSO, JR. and SCHINK, 1975; SCHINK and GUINASSO, JR., 1977; TAKAHASHI and BROECKER, 1977; BERNER, 1980; BROECKER and PENG, 1982; KEIR, 1984; ARCHER, 1991). Several of these authors explicitly solve the general diagenetic equations for the different constituents of the sediment column. In our case, this would lead to prohibitive computation times and we have preferred to develop a model which is governed by a system of equations that can be solved analytically as far as possible. Basically, the sedimentary mixed layer representation of our sediment stacks is very similar to the model of KEIR and BERGER (1983) with which it shares several basic hypotheses.

On the next pages, we give a comprehensive description of the adopted representation of the sediments in our model, along with a presentation and discussion of the underlying theory and fundamental hypotheses.

4.3.1   Sediment Stack Configuration

The deep-sea sedimentary shell which exchanges matter with seawater is associated with the profiles used to describe the sea-floor depth distribution. As specified before, these profiles have a resolution of 100 m along water depth. The "horizontal" resolution of the sedimentary shell follows accordingly. In the first published version of the model, this resolution was set to 400 m (MUNHOVEN and FRANÇOIS, 1994). This was later changed to 100 m in order to improve the representation of the transition zone, about 400–1,000 m thick, and the significance of the lysocline and compensation depth variations in time.

Each one of the five depth profiles thus comes with a series of up to 80 stacks of sedimentary layers, depending on the maximum depth of the respective ocean basin, as illustrated in figure 4.7. These stacks represent the sediment profiles for the corresponding 100-m depth intervals. Each stack is composed of a bioturbated layer atop of a sequence of "memory"
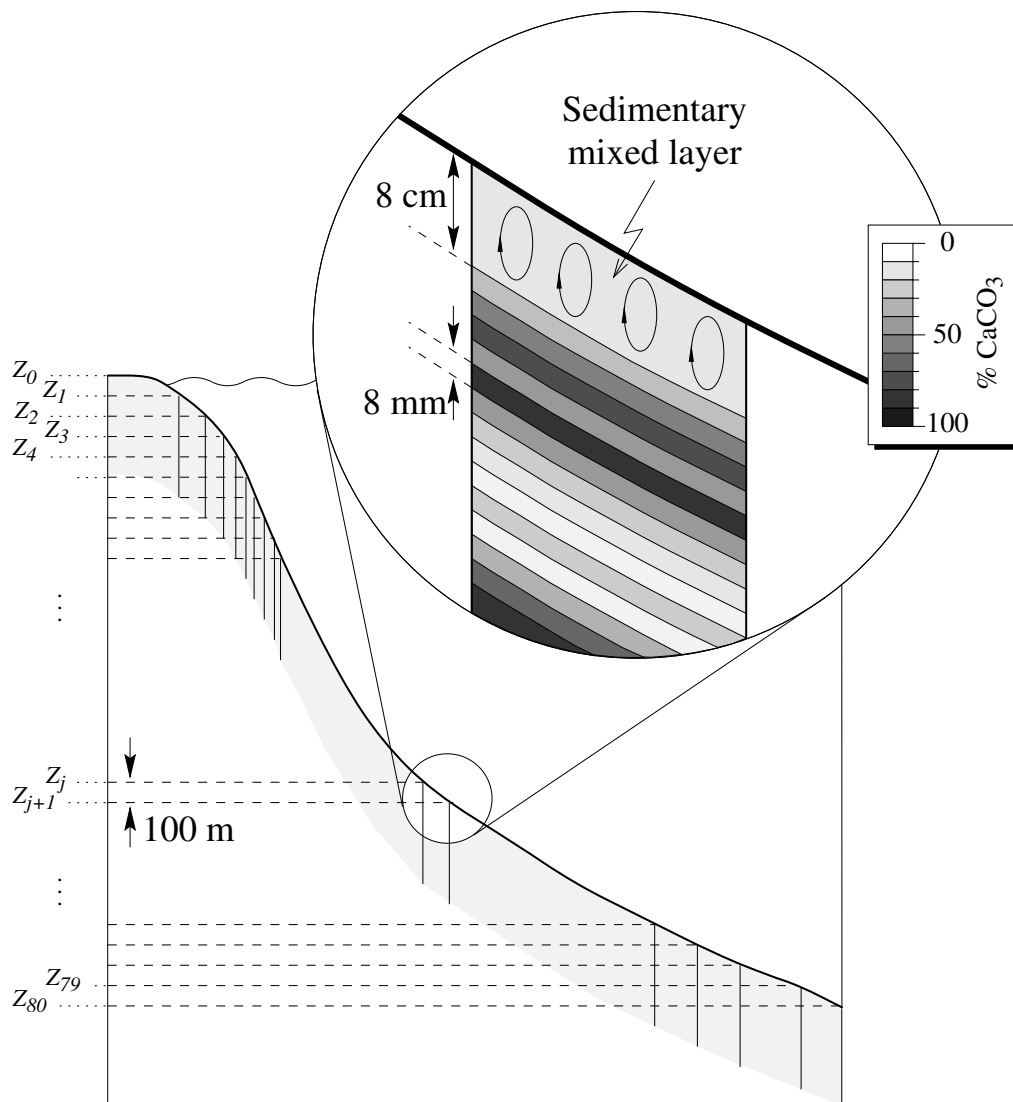
Figure 4.7: Depth profile and sedimentary layers. The enlargening shows an example of a typical sediment stack.

layers. The bioturbated layer can be seen as a reservoir of 8 cm height. The thickness of the memory layers is everywhere 10% (i.e. 8 mm) of their top bioturbated layer. This latter is in contact with the overlying seawater. Carbonate particles raining down from the surface get collected and may either accumulate or dissolve there, depending on the chemical conditions. Dissolution products are released back to the seawater by diffusion through the sediment porewater. To avoid production of a pure carbonate sediment, the particle rain falling down to the sea-floor is supposed to contain also non-soluble, chemically inert material. The mass ratio of inert material to carbonate matter is set to 1:10 (kg/kg), constant everywhere and in time.

The height of the mixed layer reservoirs given above is only a nominal one. Because of the exchange of matter with the overlying seawater, they may be more or less filled. If one of them gets overfilled during sediment growth by more than 6% of its nominal height, i.e. 60% of the height of a memory layer, a new memory layer gets created and filled up by sediment material taken out of the mixed layer. If it gets emptied to less than 94% of its nominal level, the most recently created memory layer gets unburied, and its content transferred into the mixed layer. The memory layers are assumed to be isolated from one other. They do not exchange any matter, except for having their content completely remixed into the bioturbated layer when they get unburied.

4.3.2 Sedimentary Carbonate Dissolution

The sedimentary mixed layer of a given stack is supposed to behave like a semi-infinite porous environment. We furthermore take it as well-mixed with respect to its solid fraction as a consequence of bioturbation.

For solids, we use simple mass balance equations. If $M_{i,j}^{\mathrm{C}}$ and $M_{i,j}^{\mathrm{nC}}$ are respectively the amounts of carbonate (in mol) and non carbonate solids (in kg) in the mixed layer of a given stack j ($j = 0, \ldots, 79$), covering the water depth interval $[Z_j, Z_{j+1}]$ in a profile i ($i \in Srfc$) as shown in figure 4.7, the two corresponding equations are

$$\frac{dM_{i,j}^{\mathrm{C}}}{dt} = (\mathcal{F}_{\mathrm{in}}^{\mathrm{C}})_{i,j} - (\mathcal{R}_{\mathrm{out}}^{\mathrm{C}})_{i,j} - (\mathcal{X}^{\mathrm{C}})_{i,j} \tag{4.51}$$

and

$$\frac{dM_{i,j}^{\mathrm{nC}}}{dt} = (\mathcal{F}_{\mathrm{in}}^{\mathrm{nC}})_{i,j} - (\mathcal{X}^{\mathrm{nC}})_{i,j}. \tag{4.52}$$

In these equations

- $(\mathcal{F}_{\text{in}}^{\text{C}})_{i,j}$ and $(\mathcal{F}_{\text{in}}^{\text{nC}})_{i,j}$ respectively denote the fluxes of carbonate and of non carbonate particles entering the sedimentary mixed layer reservoir from the oceans;

- $(\mathcal{X}^{\text{C}})_{i,j}$ and $(\mathcal{X}^{\text{nC}})_{i,j}$ are the corresponding exchanges with the memory layer pool, considered here as sink terms as it will generally be the case in a growing sediment column;

- $(\mathcal{R}_{\text{out}}^{\text{C}})_{i,j}$ is the sink of carbonate related to dissolution and subsequent diffusion of the produced carbonate ions out of the sediment into the seawater.

The carbonate rain out of a given surface reservoir in our model is uniformly distributed and it is homogeneous with respect to its aragonite:calcite composition. As stated before in section 4.2.4, dissolution of carbonate only concerns calcite. Aragonite simply accumulates in the sediments above the aragonite saturation depth and gets converted to calcite there. All of the aragonite in the carbonate rain that falls into undersaturated waters of our model gets instantaneously dissolved and does not even reach the sea-floor. Calcite always reaches the sea-floor where it gets mixed into the bioturbated layer. Above the calcite saturation depth, it accumulates; below it is more or less rapidly dissolved, depending on the amount of calcite already present within the sediment, and on the degree of undersaturation.

For a given profile i, the total flux of carbonate ions from the sedimentary mixed layer to the overlying seawater is thus

$$\mathcal{R}_i^{\text{C Calc}} = \sum_{j=0}^{79} (\mathcal{R}_{\text{out}}^{\text{C}})_{i,j}, \tag{4.53}$$

where all the $(\mathcal{R}_{\text{out}}^{\text{C}})_{i,j}$ terms of the stacks situated above the calcite lysocline corresponding to the profile are zero. With $\mathcal{R}_i^{\text{C Arag}}$ denoting the amount of aragonite which falls below the aragonite saturation depth and hence gets dissolved, the $\mathcal{R}_i^{\text{C Inorg}}$ fluxes required to complete the mass balance equations for dissolved inorganic carbon and total alkalinity in the deep sea (equations (4.40)/(4.41) and (4.46)/(4.47)) can be written

$$\begin{aligned}
\mathcal{R}_{\text{DATL}}^{\text{C Inorg}} &= (\mathcal{R}_{\text{SNATL}}^{\text{C Calc}} + \mathcal{R}_{\text{SNATL}}^{\text{C Arag}}) + (\mathcal{R}_{\text{SEATL}}^{\text{C Calc}} + \mathcal{R}_{\text{SEATL}}^{\text{C Arag}}) \\
\mathcal{R}_{\text{DANT}}^{\text{C Inorg}} &= \mathcal{R}_{\text{SANT}}^{\text{C Calc}} + \mathcal{R}_{\text{SANT}}^{\text{C Arag}} \\
\mathcal{R}_{\text{DI-P}}^{\text{C Inorg}} &= (\mathcal{R}_{\text{SNPAC}}^{\text{C Calc}} + \mathcal{R}_{\text{SNPAC}}^{\text{C Arag}}) + (\mathcal{R}_{\text{SEI-P}}^{\text{C Calc}} + \mathcal{R}_{\text{SEI-P}}^{\text{C Arag}}).
\end{aligned}$$

While the contribution from aragonite dissolution to the $\mathcal{R}_i^{\text{C Inorg}}$ is simply proportional to the area of sea-floor deeper than the aragonite saturation

depth, that from calcite dissolution is a more complicated function of the geochemical state of the ocean water and of the sediment porewater. In the next section, we give a thorough description of the theoretical framework used to construct the interface which handles the chemical exchange of carbonate ions across the sediment-water interface, i.e., which determines the different $(\mathcal{R}_{\text{out}}^{\text{C}})_{i,j}$. Hence, all of the carbonate stored in the sediments of our carbon cycle model and transiting through it is calcite. The model developed below only treats sediments located at depths where seawater is undersaturated with respect to calcite. The rest of the sea-floor is simply an accumulation zone.

Mass Balance of Dissolved CO_3^{2-} in an Undersaturated Sediment

To calculate the sediment-to-seawater flux of CO_3^{2-} due to carbonate dissolution, we follow the developments of TAKAHASHI and BROECKER (1977), BERNER (1980) and BROECKER and PENG (1982). We have adapted the model described by BROECKER and PENG (1982) to non-linear kinetics of carbonate dissolution, using the formalism presented by BERNER (1980). Furthermore, the influence of a benthic boundary layer is reanalysed.

General Diagenetic Equation. Let us consider a well-located sediment column at the sea-floor (e.g. a sediment core), at a given depth Z. According to BERNER (1980), the general diagenetic equation for the CO_3^{2-} ions in the porewater of our sediment column, schematically represented in figure 4.8, is

$$\frac{\partial(\phi C)}{\partial t} = \frac{\partial}{\partial z}\left(D_{\text{B}}\frac{\partial(\phi C)}{\partial z} + \phi(D_{\text{S}} + D_{\text{I}})\frac{\partial C}{\partial z}\right) - \frac{\partial(\phi v C)}{\partial z} + R_{\text{d}} + \sum_i R_i, \quad (4.54)$$

where:

- ϕ is the porosity of the sediment, defined by

$$\phi = \frac{\text{volume of interconnected water}}{\text{volume of total sediment}};$$

- C is the porewater concentration of CO_3^{2-} ions, expressed here in moles per unit volume of porewater (mol/m^3);

- D_{B}, D_{S} and D_{I} are respectively the *biodiffusion coefficient*, the *whole-sediment diffusion coefficient* and the *irrigation biodiffusion coefficient*, in unit surface area of total sediment per unit time (m^2/s);
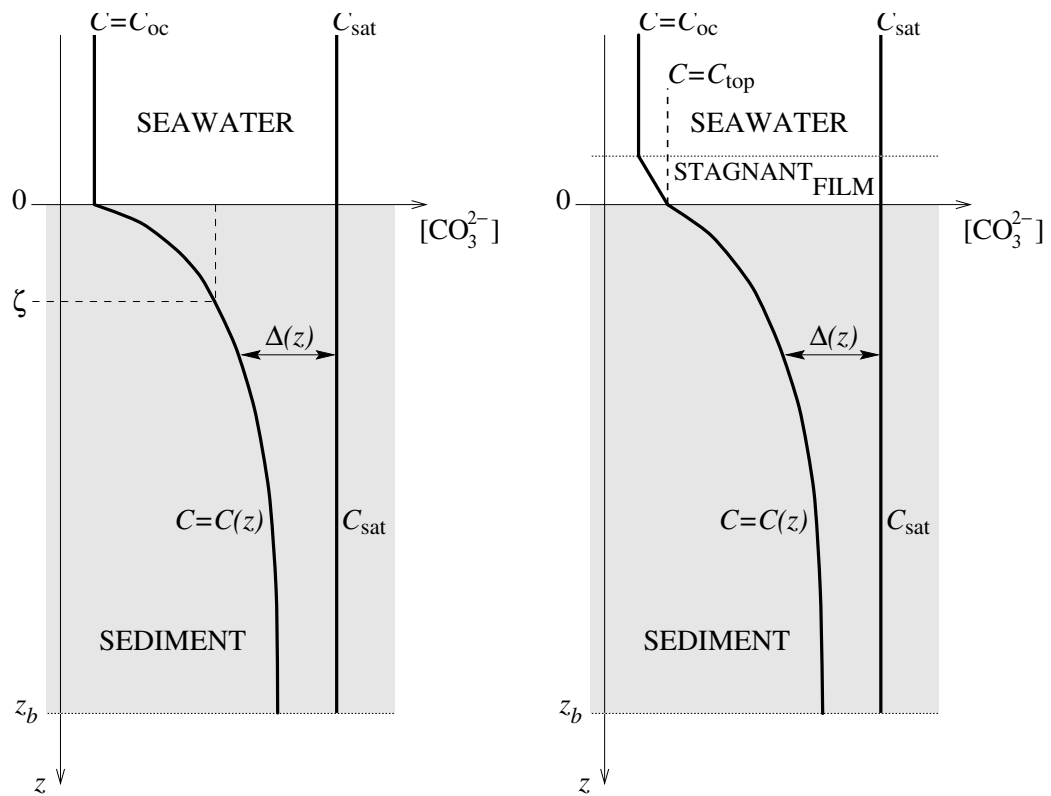
Figure 4.8: Porewater profiles of CO_3^{2-} in a calcite bearing sediment column below the CSD, for given boundary conditions (C_{sat} and C_{oc}). On the lefthand side, the sediment column is in direct contact with the seawater. On the righthand side, a boundary layer, represented by a diffusive stagnant film, is taken into account.

- v is the porewater velocity relative to the sediment-water interface (m/s);

- R_{d} is the rate of dissolution of $CaCO_3$, per unit volume of total sediment (mol/m³);

- $\sum_i R_i$ is the net rate of CO_3^{2-} production by all chemical reactions other than carbonate dissolution, per unit volume of total sediment (mol/m³).

The sediment-to-seawater flux of carbonate ions across the sediment-water interface, per unit surface of total sediment, is

$$\mathcal{R}^{\mathrm{C}} = \phi D_{\mathrm{S}} \left.\frac{\partial C}{\partial z}\right|_{z=0} - \phi v C|_{z=0}. \tag{4.55}$$

$(\mathcal{R}_{\mathrm{out}}^{\mathrm{C}})_{i,j}$, the total flux out of carbonate ions out of the mixed layer of a sediment stack (i,j), is obtained by integrating $\mathcal{R}^{\mathrm{C}}$ over its top surface, extending between water depths Z_j and Z_{j+1}:

$$(\mathcal{R}_{\mathrm{out}}^{\mathrm{C}})_{i,j} = \int_{a(Z_j)}^{a(Z_{j+1})} \mathcal{R}^{\mathrm{C}} \, da. \tag{4.56}$$

$a(Z)$ denotes here the sea-floor area shallower than the depth Z. Values for a are only stored at the sampling depths Z_j. Between these, it is evaluated by linear interpolation:

$$a(Z) = a(Z_j) + \frac{a(Z_{j+1}) - a(Z_j)}{Z_{j+1} - Z_j} \times (Z - Z_j), \quad Z_j \leq Z \leq Z_{j+1}. \tag{4.57}$$

Using this expression, (4.56) can immediately be transformed into

$$(\mathcal{R}_{\mathrm{out}}^{\mathrm{C}})_{i,j} = \frac{a(Z_{j+1}) - a(Z_j)}{Z_{j+1} - Z_j} \int_{Z_j}^{Z_{j+1}} \mathcal{R}^{\mathrm{C}} \, dZ. \tag{4.58}$$

The purpose of the next paragraphs is now simply to determine an expression for $\mathcal{R}^{\mathrm{C}}$ as a function of depth.

Simplifying Hypotheses. A number of hypotheses are made to simplify equation (4.54) in the framework of our idealized sediment mixed layer. Some of them have already been mentioned before. They are repeated here for the sake of clarity and completeness.

1. We assume that diagenesis is in a steady state regime.

2. Porosity is constant with depth and time: we have chosen $\phi \equiv 0.7$. As a consequence (see BERNER, 1980),

$$\frac{\partial \phi}{\partial t} = 0, \quad \frac{\partial \phi}{\partial z} = 0 \quad \text{and} \quad \frac{\partial v}{\partial z} = 0.$$

   This supposes in particular that the dissolution of carbonate does not have any influence on porosity, which can be justified by the fact that carbonate-free and carbonate-rich samples of deep-sea sediments have indeed very similar porosities.

3. Irrigation of the sediment is not explicitly taken into account and therefore $D_{\mathrm{I}} = 0$ here.

   Biodiffusion is much slower than molecular diffusion, meaning that $D_{\mathrm{S}} \gg D_{\mathrm{B}}$ (GUINASSO, JR. and SCHINK, 1975).

   D_{S} is furthermore supposed to be constant. Its value is related to the molecular diffusion coefficient of CO_3^{2-} in seawater, D, and to the sediment *tortuosity* θ by $D_{\mathrm{S}} = D/\theta^2$. θ can be parameterized in terms of ϕ: $\theta^2 = \phi F$ and $F = \phi^{-s}$, where F is the *formation factor*, and $s \simeq 1.8$ for deep-sea sediments (see, e.g., BERNER, 1980, for details and references). Since molecular diffusion is known to be strongly dependent on temperature, assuming a constant D_{S} is basically equivalent to assuming a constant temperature. This is certainly justified in the uppermost few tens of centimeters of the sediment column.

4. There is no externally impressed flow (e.g. hydrothermal etc.). As a consequence, v becomes equal to the bulk sediment accumulation rate.

5. Dissolved CO_3^{2-} is not affected by chemical reactions other than carbonate dissolution: $\sum_i R_i = 0$. Enhanced dissolution resulting from organic matter degradation in the sediment column is neglected.

With these hypotheses, the general equation (4.54) simplifies to

$$\frac{\partial C}{\partial t} = D_{\mathrm{S}} \frac{\partial^2 C}{\partial z^2} - v \frac{\partial C}{\partial z} + \frac{R_{\mathrm{d}}}{\phi} = 0. \tag{4.59}$$

Calcite Dissolution Kinetics. For the dissolution kinetics of calcite, we adopt a law of the form

$$\bar{R}_{\mathrm{d}} = \bar{k}' \times (C_{\mathrm{sat}} - C)^n, \tag{4.60}$$

where $\bar{R}_{\mathrm{d}}$ is expressed in moles of $CaCO_3$ dissolved per unit surface area of carbonate particles, per unit time. C_{sat} is the saturation concentration of

CO_3^{2-} under *in situ* conditions, i.e. for a given Ca^{2+} concentration, temperature, pressure and salinity. n is an exponent describing the rate order of the dissolution reaction. We adopt here $n = 4.5$ (KEIR, 1980).

In the literature, this rate law is generally presented under a slightly different form (BERNER, 1980; KEIR, 1980, 1984; KEIR and BERGER, 1983, 1985; BERGER and KEIR, 1984; ARCHER et al., 1989; MORSE and MACKENZIE, 1990; ARCHER, 1991):

$$\bar{R}_d' = \bar{k}' \times (1 - \Omega_{\text{Calc}})^n = \bar{k}' \times (1 - C/C_{\text{sat}})^n. \tag{4.61}$$

When these two laws are calibrated for a given C_{sat}^*, the two rate constants $\bar{k}$ and $\bar{k}'$ are related by $\bar{k}' = \bar{k}(C_{\text{sat}}^*)^n$ and $\bar{R}_d' = (C_{\text{sat}}^*/C_{\text{sat}})^n \times \bar{R}_d$. Because C_{sat} varies with pressure (from about 0.050 $\mu\text{mol m}^{-3}$ at 1,000 m to 0.115 $\mu\text{mol m}^{-3}$ at 5,000 m depth for calcite — see figure 1.11), the two approaches are not compatible. The differences are considerable: for $n = 4.5$, $(C_{\text{sat}})^n$ varies by a factor of 40 between 1,000 and 5,000 m depth. For aragonite, ACKER et al. (1987) have nevertheless shown that (4.60) is more appropriate than (4.61). According to ARCHER et al. (1989), this most probably also holds for calcite.

In order to make use of $\bar{R}_d$ in equation (4.59), we have to convert it into the correct units. R_d and $\bar{R}_d$ are related by

$$
\begin{aligned}
R_d &= \bar{R}_d \times \bar{A}_v \times f \times (1 - \phi) \\
&= \bar{k} \times \bar{A}_v \times f \times (1 - \phi) \times (C_{\text{sat}} - C)^n \\
&= k \times f \times (1 - \phi) \times (C_{\text{sat}} - C)^n,
\end{aligned} \tag{4.62}
$$

where

- $\bar{A}_v$ is the average specific surface area of $CaCO_3$ per unit volume of carbonate particles, which we take constant and include in the rate constant, using $k = \bar{k} \times \bar{A}_v$;

- f is the volume fraction of $CaCO_3$ in the particulate fraction of the sediment;

- $(1 - \phi)$ represents the volume fraction of particulate sediment in the total sediment (particles + porewater).

Equation (4.59) hence transforms into

$$D_S \frac{\partial^2 C}{\partial z^2} - v \frac{\partial C}{\partial z} + \frac{1 - \phi}{\phi} f \, k \, (C_{\text{sat}} - C)^n = 0. \tag{4.63}$$

C_{sat} can be considered as constant along a porewater profile taken at a given place at the sea-floor. It depends mostly on pressure, which is determined by the height of the water column above the sediment-water interface (of the order of hundreds to thousands of meters). Pressure variations at the 0.01–1 m scale of the model sediment column are therefore clearly negligible. The concentration of Ca^{2+} is only poorly affected by $CaCO_3$ dissolution, and temperature and salinity are identical to those of the seawater impregnating the sediment. We can thus safely suppose that C_{sat} remains constant with z, and depends only on the water depth Z at which the sea-floor is located. Defining

$$\Delta = C_{\text{sat}} - C, \tag{4.64}$$

we find that

$$\frac{\partial^2 C}{\partial z^2} = -\frac{\partial^2 \Delta}{\partial z^2} \quad \text{and} \quad \frac{\partial C}{\partial z} = -\frac{\partial \Delta}{\partial z}. \tag{4.65}$$

The steady-state equation to solve now writes

$$-D_{\text{S}} \frac{\partial^2 \Delta}{\partial z^2} + v \frac{\partial \Delta}{\partial z} + \frac{1-\phi}{\phi} f \, k \, \Delta^n = 0. \tag{4.66}$$

The presence of the advection term $v \, \partial \Delta / \partial z$ makes it impossible to proceed analytically. According to LERMAN (1978), it can be neglected in deep-sea environments, where accumulation rates are low. For our sediment model, the fundamental equation governing the transport of carbonate ions through the porewater column and, most important, across the sediment-water interface becomes then

$$-D_{\text{S}} \frac{\partial^2 \Delta}{\partial z^2} + \frac{1-\phi}{\phi} f \, k \, \Delta^n = 0. \tag{4.67}$$

This equation, from which $(\partial \Delta / \partial z)|_{z=0}$ is to be derived, must be completed by appropriate boundary conditions:

$$\lim_{z \to 0} \Delta(z) = \Delta_{\text{top}} \tag{4.68}$$

$$\lim_{z \to z_{\text{b}}} \frac{\partial \Delta}{\partial z} = 0. \tag{4.69}$$

where Δ_{top} is of course equal to $C_{\text{sat}} - C_{\text{top}}$ and z_{b} is the depth of the bottom of our sedimentary mixed layer (see figure 4.8). *A priori* we may not assume that C_{top} is equal to C_{oc}, which depends only on the total dissolved inorganic carbon content, C_{T}, and on the total alkalinity, A_{T}, of the overlying seawater and could thus easily be calculated. The presence of a diffusive boundary layer could possibly lead to differences between these two concentrations. We will nevertheless show below that the role of such a boundary layer can be

neglected, unless it becomes very thick. In our model, we hence assume that $C_{\text{top}} = C_{\text{oc}}$.

These hybrid boundary conditions give rise to a great deal of complications for the resolution of this differential equation. This holds especially for the condition on the derivative in $z = z_{\text{b}}$, translating the fact that we do not allow for diffusive exchange with the memory sediment layers below the mixed layer. Normally, either the values of Δ at both endpoints $z = 0$ and $z = z_{\text{b}}$, or values for both Δ and $\partial\Delta/\partial z$ at one of these two endpoints would be required to solve this equation in an explicit way. With the above boundary conditions, this is not possible, except for $n = 1$, i.e. for linear dissolution kinetics. These problems are discussed below.

Solution of the Diagenesis Equation. The first step to integrate equation (4.67) is to multiply it by $\partial\Delta/\partial z$

$$\frac{\partial^2\Delta}{\partial z^2}\frac{\partial\Delta}{\partial z} = \frac{fk(1-\phi)}{D_{\text{S}}\phi}\Delta^n\frac{\partial\Delta}{\partial z},$$

which can then be rewritten as

$$\frac{1}{2}\frac{\partial}{\partial z}\left(\frac{\partial\Delta}{\partial z}\right)^2 = \frac{fk(1-\phi)}{D_{\text{S}}\phi}\frac{1}{n+1}\frac{\partial\Delta^{n+1}}{\partial z}. \tag{4.70}$$

In this equation, k and ϕ are constants; f is assumed to be constant in the uppermost parts of the sediment column because of sufficiently intense homogenization through bioturbation. The previous equation can therefore be easily integrated. Using the boundary condition (4.69), we obtain

$$\left(\frac{\partial\Delta}{\partial z}\right)^2 = \frac{2fk(1-\phi)}{(n+1)D_{\text{S}}\phi}\left(\Delta^{n+1} - \Delta_{\text{b}}^{n+1}\right) \tag{4.71}$$

where $\Delta_{\text{b}} = \lim_{z\to z_{\text{b}}}\Delta(z)$. Because $\frac{\partial\Delta}{\partial z} < 0$, the depth profile $\Delta(z)$ in the sediment column is solution of the first-order equation

$$\frac{\partial\Delta}{\partial z} = -\left(Kf\left(\Delta^{n+1} - \Delta_{\text{b}}^{n+1}\right)\right)^{\frac{1}{2}}, \tag{4.72}$$

with

$$K = \frac{2k(1-\phi)}{(n+1)D_{\text{S}}\phi}. \tag{4.73}$$

For our purpose the explicit knowledge of $\Delta(z)$ would *a priori* not be required, since we are only interested in $(\partial\Delta/\partial z)|_{z=0}$. In order to eliminate the unknown Δ_{b}, it is nevertheless necessary to proceed and to integrate

equation (4.67) completely. Δ_b can only be eliminated by taking into account the as yet unused boundary condition (4.68).

Despite the simplifications already made, an explicit analytical solution of equation (4.72) can only be obtained if $n = 1$. The complete solution is

$$\Delta(z) = \Delta_{\text{top}} \times \frac{\cosh(\sqrt{Kf}(z_b - z))}{\cosh(\sqrt{Kf}z_b)}, \qquad (4.74)$$

where $\Delta_b = \Delta_{\text{top}}/\cosh(\sqrt{Kf}z_b)$ has already been substituted. If $n \neq 1$, which is obviously the case of interest here, it is not possible to derive a simple analytical expression for $\Delta(z)$. Several possibilities may now be considered to address the problem in this case.

1. *Numerical determination of Δ_b.* Δ_b can be calculated by iteratively solving the initial-value problem defined by (4.72) and (4.68) numerically. Once a value for Δ_b is obtained, $(\partial\Delta/\partial z)|_{z=0}$ can immediately be calculated from (4.72) too.

   Although such a determination is perfectly possible, it is not feasible to include it in our model because of the enormous computing costs it represents[*].

2. *Refinement of the sediment representation.* The representation of the sedimentary shell of our model could be reformulated, allowing for carbonate dissolution in layers below the mixed layer. Again, this would considerably increase the computing costs of our model experiments. With one single diffusive layer, the sedimentary part of the model requires already about 60–70% of the total computing time[†].

3. *Approximation-function solution.* Instead of the exact solution of the problem defined by the equation (4.67) and the boundary conditions (4.68) – (4.69), we might use an approximation of it. This approximation could either satisfy the differential equation or the boundary conditions exactly. The appropriateness of such an approximation has to be carefully studied, both from a qualitative and from a quantitative point of view.

For this study, we have adopted the last one of these possibilities. We use an approximation-function satisfying the differential equation (4.67) exactly, but

---

[*]The calculation of the 4823 data points used to draw figure 4.10 required 25 hours of CPU time on one processor of a SUN SPARCstation 10-514.

[†]A 240,000-year transient simulation with our model requires about 150 minutes of raw CPU time on one processor of a SUN SPARCstation 10-514, a 20,000-year steady-state one 11–12 minutes.

not the original boundary conditions. Instead of defining the lower boundary condition at the actual depth z_{b} of the mixed layer, we formally define them at an infinite depth. Condition (4.69) is replaced by

$$\lim_{z \to +\infty} \Delta(z) = 0 \quad \text{and} \quad \lim_{z \to +\infty} \frac{\partial \Delta}{\partial z} = 0, \qquad (4.75)$$

which is equivalent to neglecting Δ_{b} in equation (4.72). KEIR and BERGER (1983) call upon these same conditions, as do BROECKER and PENG (1982) in their first-order model, although the latter authors do not explicitly state their boundary conditions[‡]. Accordingly, we use the simpler equation

$$\frac{\partial \Delta}{\partial z} = -\sqrt{Kf}\Delta^{\frac{n+1}{2}}, \qquad (4.76)$$

to derive the flux of carbonate ions across the sediment-water interface. As a consequence, this flux becomes

$$\mathcal{R}^{\mathrm{C}} = \phi D_{\mathrm{S}} \left.\frac{\partial C}{\partial z}\right|_{z=0} = -\phi D_{\mathrm{S}} \left.\frac{\partial \Delta}{\partial z}\right|_{z=0} = k_{\mathrm{sed}}\sqrt{f}(\Delta_{\mathrm{top}})^{\frac{n+1}{2}}, \qquad (4.77)$$

where k_{sed}, defined by

$$k_{\mathrm{sed}} = \phi D_{\mathrm{S}}\sqrt{K} = \sqrt{\frac{2k(1-\phi)\phi D_{\mathrm{S}}}{(n+1)}}, \qquad (4.78)$$

is constant in our model. The required $\mathcal{R}_i^{\mathrm{C\,Calc}}$ (equations (4.53) and (4.58)) can now be obtained by integrating the expression $\mathcal{R}^{\mathrm{C}}$ over each depth profile i. $\mathcal{R}^{\mathrm{C}}$ depends on the water depth Z through Δ_{top} and on the sedimentary mixed-layer reservoir (i, j) through f. Noting $f_{i,j}$ the carbonate fraction in the mixed layer of the sediment stack (i, j), we can rewrite equation (4.58) as

$$(\mathcal{R}_{\mathrm{out}}^{\mathrm{C}})_{i,j} = k_{\mathrm{sed}}\sqrt{f_{i,j}} \times \frac{a(Z_{j+1}) - a(Z_j)}{Z_{j+1} - Z_j} \times \int_{Z_j}^{Z_{j+1}} \left(\Delta_{\mathrm{top}}(Z)\right)^{\frac{n+1}{2}} dZ. \quad (4.79)$$

$f_{i,j}$ is calculated from $M_{i,j}^{\mathrm{C}}$ (equation (4.51)) and $M_{i,j}^{\mathrm{nC}}$ (equation (4.52)). Δ_{top} is evaluated at the sampling depths Z_j, and then linearly interpolated between them. For $Z_j \leq Z \leq Z_{j+1}$, we thus have

$$\Delta_{\mathrm{top}}(Z) = \Delta_{\mathrm{top}}(Z_j) + \frac{\Delta_{\mathrm{top}}(Z_{j+1}) - \Delta_{\mathrm{top}}(Z_j)}{Z_{j+1} - Z_j} \times (Z - Z_j) \qquad (4.80)$$

[‡]Our general solution for $n = 1$ (equation (4.74)) can easily be transformed into the one given by BROECKER and PENG (1982) since $\lim_{z_{\mathrm{b}} \to +\infty} \Delta(z) = \Delta_{\mathrm{top}} \exp(-Kz)$, and noting that they include the porosity ϕ in their definition of the whole sediment diffusion coefficient D_{S}.

which, when introduced into (4.79), finally gives us

$$(\mathcal{R}_{\text{out}}^{\text{C}})_{i,j} = \frac{k_{\text{sed}}}{\frac{n+1}{2}+1} \times (a(Z_{j+1}) - a(Z_j)) \times \sqrt{f_{i,j}} \qquad (4.81)$$

$$\times \frac{\left(\Delta_{\text{top}}(Z_{j+1})\right)^{\frac{n+1}{2}+1} - \left(\Delta_{\text{top}}(Z_j)\right)^{\frac{n+1}{2}+1}}{\Delta_{\text{top}}(Z_{j+1}) - \Delta_{\text{top}}(Z_j)}$$

This is the expression for $(\mathcal{R}_{\text{out}}^{\text{C}})_{i,j}$ that we have used in our model to calculate the releases of dissolved inorganic carbon and of alkalinity to the deep reservoirs due to carbonate dissolution at the sea-floor.

4.3.3   Calibration and Properties

Two problems remain to be addressed before we can integrate the sediment model described over the previous pages into our global carbon cycle model.

1. We need to find or to determine an appropriate value for the dissolution rate constant, either for k, K or for k_{sed}.

2. In the formulation above, $(\mathcal{R}_{\text{out}}^{\text{C}})_{i,j}$ depends on Δ_{top}, the sediment-top deviation of the actual carbonate ion concentration from the concentration at saturation. From the model variables, we can only calculate Δ_{oc}, which might be considerably different from Δ_{top} if the diffusion of the carbonate ions out of the sediment is inhibited by a benthic boundary layer, as illustrated in figure 4.8.

These topics are discussed in the next paragraphs, where we also analyse the consequences of having adopted an approximation-function solution for the diagenesis equation, both regarding its departure from the true solution and the degree of coherence with the basic definition of the mixed layer model. Finally, we also analyse the impact that the presence of a diffusive boundary layer could have on the behaviour of our model sediment.

Dissolution Rate Constant

Although the general calibration of the model is the subject of section 4.4 hereafter, the description of our sedimentary mixed-layer model would not be complete without a discussion on the dissolution constant k_{sed}, which is in fact its key parameter. There are different methods to calculate k_{sed}. Depending on the scale of the properties used to define k_{sed}, these methods can be divided into *macroscopic* and *microscopic* ones.

k_{sed} in our model. The value for k_{sed} adopted in our model is based upon a macroscopic consideration. The constraint used to determine it is the thickness of the transition zone, i.e. the distance separating the carbonate saturation depth CSD from the carbonate compensation depth CCD: k_{sed} is chosen such that this transition zone is about 600–800 m thick. Accordingly, we have adopted $k_{\text{sed}} = 2 \times 10^4 \, \text{mol} \, \text{m}^{-2} \, \text{yr}^{-1} \, (\text{mol} \, \text{m}^{-3})^{-(n+1)/2}$, where n is the dissolution rate order, set to 4.5 in our model. In the following we will not specifiy these complicated units anymore. All values given for k_{sed} and k will be such that $(\mathcal{R}_{\text{out}}^{\text{C}})_{i,j}$, as obtained from equation (4.81), comes out in moles per year if concentrations are expressed in mol/m^3 and areas in m^2. For $k_{\text{sed}} = 2 \times 10^4$, we calculate that $k = 5.53 \times 10^{11}$ from equation (4.78), using $\phi = 0.7$ and $D_{\text{S}} = 3 \times 10^{-10}$ m^2 s^{-1} (LERMAN, 1978).

How do these values compare with other published values from modelling and from experimental studies, and with those obtained by other methods ?

The model of ARCHER. To compare with the results of ARCHER (1991) who has published the most complete model of the calcite lysocline, it is easiest to use the specific dissolution rate R_{d}, given by equation (4.62). In ARCHER's model, $R_{\text{d}} = k_{\text{C}} \times f \times (\rho_{\text{Calc}}/M_{\text{Calc}}) \times (1 - \Omega_{\text{Calc}})^n$, where $k_{\text{C}} = 0.3$–1.0 day^{-1}, ρ_{Calc} is the density of calcite $(2,900 \, \text{kg/m}^{-3})$ and M_{Calc} its molecular mass $(0.1 \, \text{kg/mol})$. ARCHER (1991) uses the same dissolution rate order $n = 4.5$ as we do. Rewriting equation (4.62) in terms of Ω_{Calc}, we obtain that $R_{\text{d}} = (1 - \phi) \times k \times f \times (C_{\text{sat}})^n \times (1 - \Omega_{\text{Calc}})^n$. As already mentioned in the discussion of the dissolution kinetics law on page 129, the values of k and k_{C} can only be correctly related to each other at a given C_{sat}, i.e. at a given depth. Using our value of 5.53×10^{11} for k, we calculate that the range of 0.3–1.0 day^{-1} for k_{C} quoted by ARCHER (1991) can be reproduced for C_{sat} between 0.090 and 0.120 mol/m^{-3}, typical of depths between about 3,750 m (the average depth of the oceans) and 5,500 m. We consider that this agreement is rather good, taking into account that the average dissolution depth of calcite in the Pacific for example is of 4,900 m (KEIR and BERGER, 1985).

The model of KEIR and BERGER. Another model that has been widely used to study the last glacial-interglacial transition is that of KEIR (1984) (see KEIR and BERGER (1983, 1985); BERGER and KEIR (1984)). The formulation of the dissolution law that they have adopted is very similar to that of ARCHER (1991). In the notation style of this thesis, their dissolution flux,

called *dissolution response* in KEIR and BERGER (1985), writes

$$\mathcal{R}_{\text{Keir}}^{\text{C}} = k'_{\text{sed}} \sqrt{f} \left(1 - \frac{C_{\text{top}}}{C_{\text{sat}}}\right)^{\frac{n+1}{2}} = \frac{k'_{\text{sed}}}{(C_{\text{sat}})^{\frac{n+1}{2}}} \sqrt{f} (\Delta_{\text{top}})^{\frac{n+1}{2}}, \qquad (4.82)$$

where k'_{sed} is set to 10^2 mg $CaCO_3/cm^2/yr$ (10 mol $CaCO_3/m^2/yr$). This expression is to be compared with equation (4.77) above, and as before, the problem is to find an appropriate C_{sat} for this purpose. KEIR (1984) based his estimate for k'_{sed} on his own laboratory measurements (KEIR, 1980), carried out in synthetic seawater at 1 atm and 20 °C. From the characteristics reported in (KEIR, 1980), we may calculate that $C_{\text{sat}} \simeq 0.045$ mol/m³ under these conditions. In KEIR and BERGER's (1985) study, where they coupled this sediment model to a single-depth, flat-bottom, two-box model of the ocean, they use the C_{sat} at 4,100 m depth, which equals 95 μmol/kg-SW (0.099 mol/m³). By identifying k_{sed} and $k'_{\text{sed}}/(C_{\text{sat}})^{(n+1)/2}$, we obtain k_{sed} values of about 5,800 (for $C_{\text{sat}} = 0.099$ mol/m³) and of 50,000 (for $C_{\text{sat}} = 0.045$ mol/m³). Our value of 20,000 fits without any difficulty into the range defined this way. It should be noticed that the use of these two values would lead to a transition zone thickness of 1,000–1,200 m, and of 300–400 m respectively. The latter of these is surely far from the average observed within the oceans.

The resaturation-time estimate. Another method to estimate the dissolution rate constant is described by BROECKER and PENG (1982). It can be qualified as a microscopic method, and it is based upon the equilibration time of a sample of undersaturated seawater with solid calcite as measured from *in situ* saturometer experiments. Basically, a saturometer is a device composed of a recipient, filled with carbonate sediment or grains, coupled to a pH-meter to monitor the evolution of the pH in the interstitial water. It can be lowered to a given depth in the water column, where a connected pump periodically flushes it with seawater at ambient pressure. During the time when the pump is switched off, a valve closes the recipient and isolates it from the water around. The carbonate ion concentration in seawater previously pumped in then progressively equilibrates with the solid carbonate. For a complete and more precise description of this instrument we refer to BEN-YAAKOV and KAPLAN (1971).

The environment in the recipient may thus be seen as a synthetic sediment, composed of pure calcite in the case we are interested in. The appropriate equation for the evolution of the carbonate ion concentration C in the interstitial water can be derived from (4.54), by dropping the terms related to gradients, and by substituting R_{d} for its expression from equation
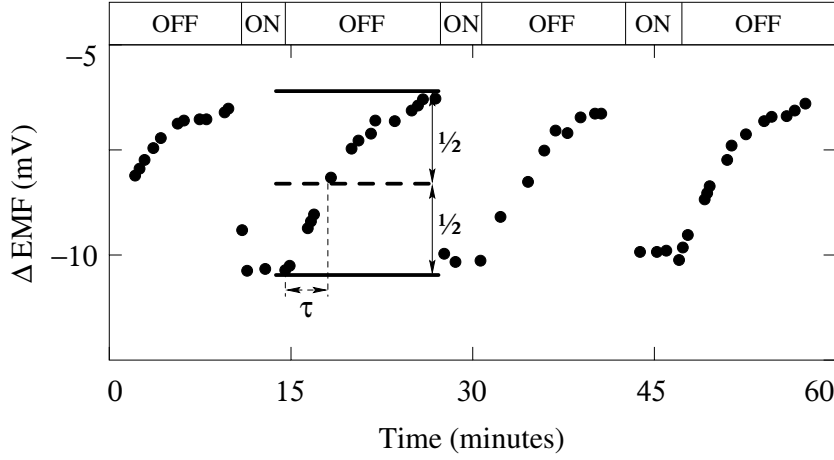
Figure 4.9: Saturometer experiment results at GEOSECS station 341 in the Pacific, carried out at a depth of 4.5 km. Shown is the potential between the pH electrodes of the saturometer, immersed into a calcite sample. The ON/OFF cycles shown on top of the graph indicate whether the pump is flushing the calcite sample with fresh seawater (ON) or the recipient is isolated from seawater (OFF) and the interstitial water is equilibrating with the solid phase (adapted from BROECKER and PENG, 1982).

(4.62). Taking furthermore into account that $f = 1$ in this environment, the evolution of C at a given depth in the seawater column is described by

$$\frac{dC}{dt} = -\frac{d\Delta}{dt} = \frac{1 - \phi}{\phi}\, k\, \Delta^n, \qquad \Delta(t_0) = C_{\text{sat}} - C_{\text{oc}} = \Delta_{\text{oc}}. \qquad (4.83)$$

The *half-saturation time* τ, which we are using as a measure of the equilibration time, is defined as the time required for the interstitial water to reduce the initial difference from saturation by one half: $\Delta(t_0 + \tau) = \Delta_{\text{oc}}/2$. By integrating equation (4.83) between t_0 and $t_0 + \tau$, we find that

$$\begin{cases} k = \dfrac{\phi \ln 2}{\tau(1 - \phi)} & \text{if } n = 1 \\[3mm] k = \dfrac{\phi(2^{n-1} - 1)}{\tau(1 - \phi)(n - 1)(\Delta_{\text{oc}})^{n-1}} & \text{if } n \neq 1. \end{cases} \qquad (4.84)$$

The results of saturometer experiments represented in figure 4.9 (from BROECKER and PENG, 1982) indicate that $\tau \simeq 3$ min. C_{T} and A_{T} have not been measured at GEOSECS station 341 where these results come from. We rely therefore on the data from the neighbouring station 340: at a depth of 4,518 m, $S = 34.691$, $t_{\text{pot}} = 1.076\,°\text{C}$, $C_{\text{T}} = 2,313\ \mu\text{mol/kg-SW}$ and

$A_T = 2,414$ μeq/kg-SW, leading to $C_{oc} = 74$ μmol/kg-SW. From relationship (2.45), we find that $[Ca^{2+}] = 10.19$ mmol/kg-SW. Accordingly, $C_{sat} = 103$ μmol/kg-SW, and hence $\Delta_{oc} = 29$ μmol/kg-SW (0.030 mol/m^3). Unfortunately, the values for k calculated from (4.84) are sensitive to the porosity of the calcite sample in the saturometer, which is not known. For ϕ ranging between 0.7 and 0.9, k ranges between 2.58×10^{11} and 9.94×10^{11}, leading to k_{sed} between 13,660 and 26,810. Our preferred values are obtained for $\phi \simeq 0.83$. Here again, we observe that there is a fairly good agreement between the values adopted for k (and k_{sed}) and the independent estimates.

Quality of the Approximation-Function Solution

To analyse the quality of the approximation-function solution adopted in our model, we have performed a high-precision numerical resolution of the initial-value problem defined by (4.72) and (4.68). The most important results of this analysis are reported in figure 4.10. Part (a) of that figure shows the variations of the specific dissolution flux calculated from the approximation-function, as a function of the calcite fraction f in the sediment, and the dissolution strength Δ_{top} at the sediment-water interface. As can be seen in part (b), this flux is in excellent agreement with the exact solution. The largest deviations (of the order of 10%) are observed where both f and Δ_{top} are small. This is of no importance at all since here the dissolution flux is more than two orders of magnitude less than average. This error does hence not have any influence on the global carbonate dissolution flux from the seafloor. Tests have shown that this remains true, even if a value as low as 800 is used for k_{sed}.

By definition, the approximation-function solution adopted to calculate the carbonate dissolution in our model sediment does not exactly satisfy the boundary condition at the bottom of the mixed layer. The deviation is nevertheless small, as shown in part (c), where the flux across the bottom interface that the non-zero gradient of the approximate solution theoretically implies is compared with the the flux across the sediment-water interface at the top. Differences in excess of 10% are again only observed where the dissolution is 1–2 orders of magnitude lower than average. The incoherency introduced into the model by the adopted approximation is hence negligible, in the sense that the resulting carbonate ion profile in the sediment porewater does not imply any significant transport across the bottom.
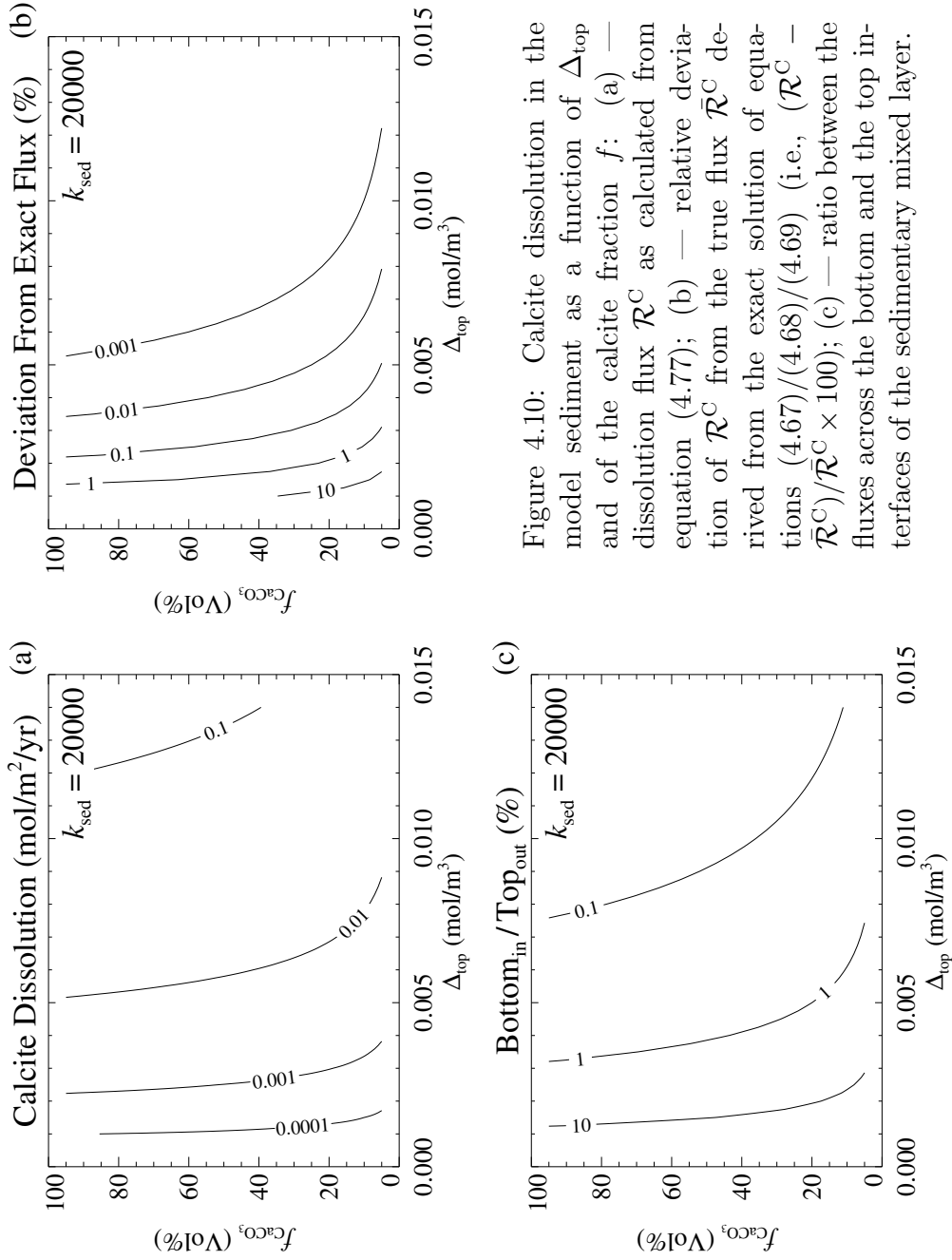
Figure 4.10: Calcite dissolution in the model sediment as a function of Δ_{top} and of the calcite fraction f: (a) — dissolution flux $\mathcal{R}^C$ as calculated from equation (4.77); (b) — relative deviation of $\mathcal{R}^C$ from the true flux $\bar{\mathcal{R}}^C$ derived from the exact solution of equations (4.67)/(4.68)/(4.69) (i.e., $(\mathcal{R}^C - \bar{\mathcal{R}}^C)/\bar{\mathcal{R}}^C \times 100)$); (c) — ratio between the fluxes across the bottom and the top interfaces of the sedimentary mixed layer.

Quantitative Role of a Diffusive Boundary Layer

We have already shortly addressed the possible effect of a benthic boundary layer separating the sediment column from the overlying seawater, across which carbonate ion transport would only take place by diffusion. As a consequence, the top sediment dissolution strength Δ_{top} could be smaller than Δ_{oc} in the seawater, as illustrated in figure 4.8. The carbonate ion flux $\mathcal{F}$ across such a diffusive film, of thickness z, is given by

$$\mathcal{F} = \frac{D}{z}(C_{\mathrm{top}} - C_{\mathrm{oc}}) = \frac{D}{z}(\Delta_{\mathrm{oc}} - \Delta_{\mathrm{top}}), \qquad (4.85)$$

where D is the diffusion coefficient of carbonate ions in seawater. At the interface between the sediment and the benthic boundary layer, mass conservation requires that $\mathcal{F} = \mathcal{R}^{\mathrm{C}}$. By combining the previous equation with (4.77), we obtain the following relationship between Δ_{top} and Δ_{oc}:

$$\frac{D}{z}(\Delta_{\mathrm{oc}} - \Delta_{\mathrm{top}}) = k_{\mathrm{sed}}\sqrt{f}(\Delta_{\mathrm{top}})^{\frac{n+1}{2}}. \qquad (4.86)$$

For a given Δ_{oc}, this equation can be analytically solved for Δ_{top} only for some discrete values of n (e.g. $n = 1, 3$). If $n = 4.5$, the case of interest here, there is no analytical solution. We have therefore solved this equation numerically using a NEWTON-RAPHSON iteration scheme, for Δ_{oc} ranging between 0.001 and 0.014 mol/m^3 and for f between 5 and 95%. k_{sed} was set to the standard value of 20,000, D to 5×10^{-10} m^2/s. Different thicknesses were tested for the diffusive film (100 μm, 300 μm and 1,000 μm). The results of these calculations are summarized in figure 4.11, where we show the relative difference between the approximate flux (obtained by assuming that $\Delta_{\mathrm{top}} = \Delta_{\mathrm{oc}}$), and the exact flux (obtained by using the calculated actual Δ_{top}, which is lower than Δ_{oc}). It should be noticed that BROECKER and PENG use $D = 10 \times 10^{-10}$ m^2/s in their developments (BROECKER and PENG, 1982, p. 90). If we had used this twice larger value in our calculations, the results presented in figure 4.11 would correspond to a layer that is twice as thick as indicated. In choosing $D = 5 \times 10^{-10}$ m^2/s, we tried to make a compromise between the results of LI and GREGORY (1974), and the value obtained by relating it to the adopted whole sediment diffusion coefficient $D_{\mathrm{S}} = 3 \times 10^{-10}$ m^2/s (LERMAN, 1978). This figure shows that the boundary layer can perfectly well be neglected if $z = 100$ μm (a). In this case, the difference between the approximate and the actual flux exceeds 10% only where carbonate-rich sediments get bathed by corrosive waters. If z becomes as large as $1,000$ μm on the other hand (c), the 10% error from (a) grows to 50%. In this case, it would be unreasonable to disregard the benthic
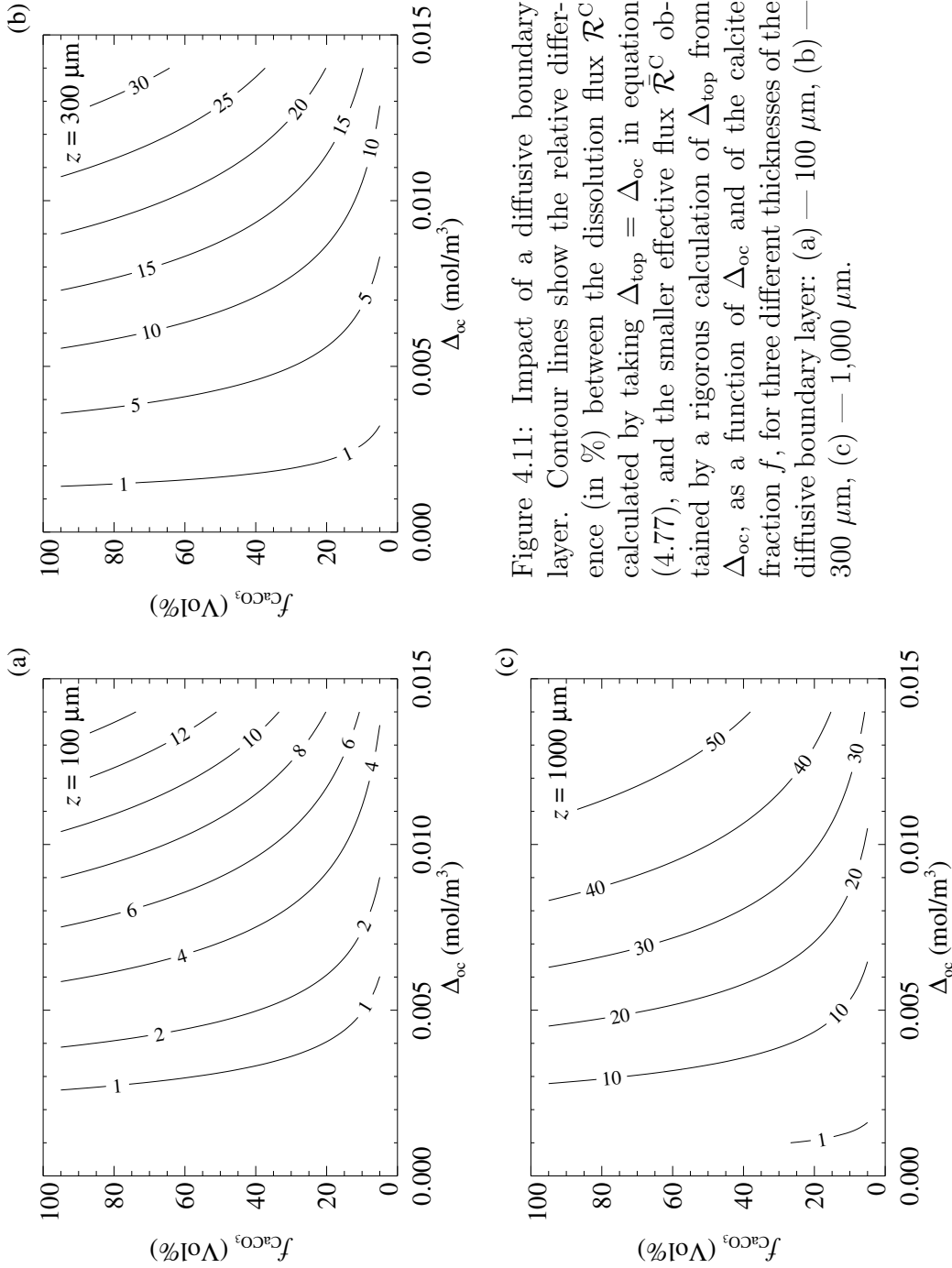
Figure 4.11: Impact of a diffusive boundary layer. Contour lines show the relative difference (in %) between the dissolution flux $\mathcal{R}^C$ calculated by taking $\Delta_{top} = \Delta_{oc}$ in equation (4.77), and the smaller effective flux $\bar{\mathcal{R}}^C$ obtained by a rigorous calculation of Δ_{top} from Δ_{oc}, as a function of Δ_{oc} and of the calcite fraction f, for three different thicknesses of the diffusive boundary layer: (a) — 100 μm, (b) — 300 μm, (c) — 1,000 μm.

boundary layer. A thickness of 300 μm seems to be about the threshold value below which the layer can be neglected. BROECKER and PENG (1982) report that measurements of this thickness have yielded results of about 120 μm. They nevertheless indicate that the average thickness might be somewhat larger, due to above-average current velocities at the site of measurement. As this is much smaller than 300 μm, we have decided not to include any boundary layer in the formulation of our model, as ARCHER (1991) does in his much more complete model as well.

4.4 Calibration and Sensitivity

4.4.1 Model Calibration

Model Parameters

All of the parameters of our model have been identified in the description of the model configuration (section 4.1) and the presentation of the equations (section 4.2). The parameters in our model can roughly be divided into two major classes: (1) *external* ones, such as temperature and salinity, and also the depth profiles, which are prescribed *a priori* and do not depend on other model variables, and (2) *adjustable* ones, for which values need to be determined in order for the model to reproduce tracer distributions that can be verified against data from the "real" world. We furthermore distinguish two groups of adjustable parameters.

- The first group includes the shallow-water carbonate precipitation constants k_{CR} and k_{BS} (see p. 111), and the sediment dissolution constant k_{sed} (see p. 133). Their values are determined from single constraints and they are only weakly dependent on the state of our model ocean. The adopted constraints for these parameters are based upon observations (*cf.* chapter 1). They are as follows:

  k_{CR} − to reach a global average accumulation rate of 7×10^{12} moles of CaCO$_3$ per year by coral reefs over the past 5,000 years;

  k_{BS} − to reach a global average accumulation rate of 7.5×10^{12} moles of CaCO$_3$ per year on banks and shelves over the past 5,000 years;

  k_{sed} − to produce a transition zone thickness (CCD-minus-CSD) of 600 to 800 m.

- The second group includes all the others: the water circulation upscaling parameter r_{mix} (see p. 101), the phosphate uptake efficiencies

u_i^{P}, $i \in Srfc$ (see p. 110), the fraction r_{oxyd} of organic matter rem-
ineralized in the thermocline (see p. 116), the rain ratios r_i^{C}, $i \in Srfc$
(see p. 111) and the aragonite fraction in the carbonate rain r_{Arag} (see
p. 111).

When going through the description of the model, one can count 16 ad-
justable parameters for which values must be provided. But in fact the
model can be completely determined by only 12 *general parameters*. Several
parameters appearing with distinct names in the equations are in fact equal
to one single general parameter. For example the phosphate uptake efficien-
cies for the Surface Equatorial Atlantic and Indo-Pacific reservoirs, $u_{\mathrm{SEATL}}^{\mathrm{P}}$
and $u_{\mathrm{SEI-P}}^{\mathrm{P}}$ are always set to the same value, that of the general parameter
$u_{\mathrm{SE}}^{\mathrm{P}}$ which represents the surface equatorial phosphate uptake efficiency. The
correspondences can be found in the first two columns of table 4.7 where the
final results of the two adjustment procedures are presented.

Data Constraints

Parameter values are determined for the model tracer distribution to reach
the best possible agreement with a set of oceanic and atmospheric data con-
straints. This is done by minimizing a weighted residual R defined by

$$R^2 = \sum_n \left(\frac{\bar{X}_n - X_n}{\sigma_n} \right)^2 . \qquad (4.87)$$

In this definition the $\bar{X}_n$ represent the data constraints and the X_n represent
the corresponding model results. The σ_n are weights, used to normalize the
individual deviations to a common scale. Table 4.3 presents the oceanic data
that we have compiled and which are intended to be representative of the
pre-industrial state of the modelled system. Most of these data have been
presented in chapter 1 and derive from the sources given there. Here we
only want to emphasize a few details. DIC concentrations for the surface
reservoirs have been obtained from the GEOSECS distributions by subtract-
ing 0.030 mol/m^3 to account for the fossil fuel CO$_2$ invasion into the upper
ocean. KROOPNICK (1985) estimates this correction at 40 μmol/kg. The
surface distribution of DIC resulting from this larger correction is neverthe-
less impossible to reproduce. The Antarctic data have also been adjusted
in order to take into account that our Antarctic reservoir reaches farther
North than the 50°S limit used by TAKAHASHI et al. (1981b). The data for
our Antarctic reservoirs have been obtained by averaging the original profiles
from TAKAHASHI et al. (1981b) for the Antarctic, the South Atlantic, South
Indian and South Pacific Oceans, using ratios of $3 : \frac{1}{4} : \frac{1}{4} : \frac{1}{2}$.

Not all of the data from table 4.3 are taken into account to form the residual R. We have chosen to use only the atmospheric p_{CO_2}, the distributions of DIC, alkalinity, phosphate and Δ^{14}C, and the calcite saturation depth CSD. Oxygen is neglected since it does not play a limiting role in our model. Furthermore, it should be noticed that its concentration is prescribed in the surface reservoirs, and that the deep reservoirs come very close to the given values anyway. The distribution of δ^{13}C is well correlated to that of phosphate, so that it does not really represent an additional constraint. The aragonite and calcite saturation depths ASD and CSD are separated by a nearly constant distance of 2,000 m.

Table 4.4 lists the weights σ_n required to evaluate R from these data. Their values have been chosen to reflect the data variability and uncertainty, but also the relative importance of the respective reservoirs. The DIC and alkalinity data for the North Atlantic are not taken into account for the calculation of R for lack of reliability. In our model atmosphere, Δ^{14}C is set to a constant value of 0 $^0\!/\!_{00}$ and it does hence not make much sense to include it in the definition of R.

Calibration Procedure and Parameter Best-Fit Values

Two sets of best-fit values for the parameters have been determined: a first one for steady-state and a second one for the transient experiments.

Parameters for steady-state conditions.   The set of best-fit parameter values for steady-state experiments is represented by that combination of parameter values which leads to the best agreement of the calculated model tracer distribution with the adopted data constraints (i.e., the combination of parameter values that minimizes the residual R) when the model is run to steady state with its configuration frozen at the present-day situation. Steady state is generally reached after 20,000 simulation years. Starting with estimates for the parameters derived from the literature, their best-fit values are determined by using a simple iteration scheme. At each step, we calculate approximations of the one-dimensional sub-minima of R, i.e., of the minima that R takes as a function of each of the parameters individually). Only the value of the parameter corresponding to the lowest of the calculated sub-minima is adjusted, and the process is repeated for the next iteration.

The one-dimensional sub-minimizations of R with respect to each of the parameters individually are done by parabolic interpolation, using a parabola fitted through a triplet of points derived from parameter values which bracket a minimum of R. Such triplets can generally be determined by evaluating R for small perturbations of the parameter around its current value (perturba-

tions are typically $\pm 10\%$ early in the iteration process and $\pm 5\%$ in the later stages). If this fails to provide an adequate triplet, additional steps (of the same size as the first perturbation) are taken along the direction of decreasing R, until we obtain three consecutive values that bracket a minimum.

This iteration scheme is only used to determine values for the parameters of the second group. It is rather easy to get good values for the parameters of the first group, and they require only little fine-tuning after those of the second group have been determined.

For the steady-state determination, we had to consider an additional "parameter", b_{riv}. The model in fact absolutely needs to be fed by an input of carbon and alkalinity. If such an input is not provided, it becomes impossible for the system to maintain its calcite and aragonite saturation horizons at realistic depths because else, it would simply run out of alkalinity and carbon. To avoid this, the model ocean is fed by a constant input b_{riv} of bicarbonate. It is assumed that this bicarbonate originates from carbonate mineral dissolution. Half of the carbon is taken from the atmosphere. Silicate mineral dissolution is not explicitly taken into account and set to 0, as are the related inputs of volcanic and hydrothermal CO_2. In a steady-state situation with *constant* inputs of carbon and alkalinity, the two weathering sources would anyway be indistinguishable. The optimal value for b_{riv} is determined together with those for other parameters.

Parameters for transient conditions. For the parameter determination under transient conditions, we anticipate somewhat on the results described later in this thesis. Parameter values are obtained almost the same way as in the steady-state case, except that the complete model is run with one of the weathering scenarios of chapter 6 over two successive glacial-interglacial climate oscillations (240,000 years), starting with the steady-state set of parameters. The final tracer distribution is then used as a basis for minimization of R. It has been verified that the obtained best-fit values depend only weakly on the chosen scenario.

Results and Discussion. The obtained best-fit parameter values are reported in table 4.7, separately for steady-state and for transient conditions. The two parameter sets have many values in common, but where there are differences, they are important. The corresponding model results can be found in tables 4.5 and 4.6. The obtained minima of R are 5.36 for steady-state and 5.03 for transient conditions. The sensitivity of R to the model parameters will be discussed in section 4.4.2 below.

There are no surprises among the values found for the parameters which

Table 4.3: Oceanic and atmospheric data constraints.

	Atmos.	SNATL	SEATL	SANT	SEI-P	SNPAC	TEATL	TEI-P	DATL	DANT	DI-P
p_{CO_2}	280										
DIC		2.15	2.02	2.26	2.04	2.36	2.25	2.28	2.30	2.36	2.42
Alkalinity		2.40	2.42	2.45	2.40	2.49	2.41	2.42	2.44	2.46	2.52
Phosphate		1.00	0.29	1.60	0.44	1.00	1.58	1.97	1.66	2.27	2.60
Oxygen		0.35	0.25	0.35	0.25	0.35	0.18	0.16	0.25	0.23	0.15
$\delta^{13}C$	−6.4	1.25	1.72	0.85	1.60	1.25	0.85	0.60	0.75	0.40	0.15
$\Delta^{14}C$	0	−70	−50	−100	−50	−100	−80	−120	−105	−156	−200
ASD									2,300	1,300	1,000
CSD									4,300	3,400	3,000

Units are as follows: p_{CO_2} – ppmv, DIC and Oxygen – mol/m^3, Alkalinity – eq/m^3, Phosphate – mmol/m^3, $\delta^{13}C$ and $\Delta^{14}C$ – ‰, ASD and CSD – m.

Table 4.4: Weights adopted in the definition of the residual.

	Atmos.	SNATL	SEATL	SANT	SEI-P	SNPAC	TEATL	TEI-P	DATL	DANT	DI-P
p_{CO_2}	5										
DIC		—	0.03	0.05	0.03	0.05	0.03	0.03	0.01	0.01	0.01
Alkalinity		—	0.03	0.05	0.03	0.05	0.03	0.03	0.01	0.01	0.01
Phosphate		0.50	0.05	0.50	0.05	0.50	0.10	0.10	0.02	0.02	0.02
$\Delta^{14}C$	—	10	10	10	10	10	20	20	10	10	10
CSD									250	250	250

Units are the same as in table 4.3 above. Variables not considered in the definition of the residual have been omitted here.

Table 4.5: Model results for the distribution of tracers and saturation depths for steady-state adjustment.

	Atmos.	SNATL	SEATL	SANT	SEI-P	SNPAC	TEATL	TEI-P	DATL	DANT	DI-P
p_{CO_2}	280	254	286	277	284	275					
DIC		2.22	2.06	2.24	2.04	2.24	2.24	2.30	2.31	2.36	2.42
Alkalinity		2.43	2.41	2.44	2.38	2.45	2.43	2.44	2.45	2.46	2.51
Phosphate		0.90	0.30	1.46	0.41	1.29	1.47	2.10	1.66	2.25	2.60
Oxygen		*0.35*	*0.25*	*0.35*	*0.25*	*0.35*	0.24	0.14	0.24	0.20	0.14
$\delta^{13}C$	*−6.4*	1.45	1.90	1.27	1.91	1.42	1.00	0.48	0.79	0.42	0.15
$\Delta^{14}C$	*0*	−79	−46	−97	−50	−81	−95	−138	−114	−141	−193
ASD									2,300	1,100	950
CSD									4,300	3,050	2,900

Units are the same as in table 4.3. Values typeset in *italics* are prescribed.

Table 4.6: Model distribution of tracers and saturation depths for transient adjustment.

	Atmos.	SNATL	SEATL	SANT	SEI-P	SNPAC	TEATL	TEI-P	DATL	DANT	DI-P
p_{CO_2}	281	256	287	278	285	276					
DIC		2.22	2.05	2.25	2.04	2.25	2.24	2.31	2.30	2.36	2.42
Alkalinity		2.43	2.40	2.45	2.39	2.45	2.43	2.45	2.44	2.47	2.52
Phosphate		0.90	0.30	1.46	0.41	1.29	1.47	2.10	1.66	2.25	2.60
Oxygen		*0.35*	*0.25*	*0.35*	*0.25*	*0.35*	0.24	0.14	0.24	0.20	0.14
$\delta^{13}C$	*−6.4*	1.43	1.86	1.25	1.88	1.40	0.97	0.46	0.77	0.39	0.12
$\Delta^{14}C$	*0*	−79	−42	−98	−49	−81	−94	−139	−115	−143	−196
ASD									2,200	1,150	1,050
CSD									4,200	3,100	3,000

Units are the same as in table 4.3. Values typeset in *italics* are prescribed.

Table 4.7: Model Parameter Best-Fit Values.

Parameter		Best-fit value	
General name	Name in equations	Steady state	Transient
r_{mix}	—	0.20	0.20
$u_{\mathrm{SE}}^{\mathrm{P}}$	$u_{\mathrm{SEATL}}^{\mathrm{P}}$, $u_{\mathrm{SEI-P}}^{\mathrm{P}}$	0.79	0.79
$u_{\mathrm{SN}}^{\mathrm{P}}$	$u_{\mathrm{SNATL}}^{\mathrm{P}}$, $u_{\mathrm{SNPAC}}^{\mathrm{P}}$	0.35	0.35
$u_{\mathrm{SANT}}^{\mathrm{P}}$	$u_{\mathrm{SANT}}^{\mathrm{P}}$	0.27	0.27
r_{oxyd}	r_{oxyd}	0.72	0.72
$r_{\mathrm{SEATL}}^{\mathrm{C}}$	$r_{\mathrm{SEATL}}^{\mathrm{C}}$	0.42	0.35
$r_{\mathrm{SEI-P}}^{\mathrm{C}}$	$r_{\mathrm{SEI-P}}^{\mathrm{C}}$	0.30	0.25
$r_{\mathrm{polar}}^{\mathrm{C}}$	$r_{\mathrm{SNATL}}^{\mathrm{C}}$, $r_{\mathrm{SANT}}^{\mathrm{C}}$, $r_{\mathrm{SNPAC}}^{\mathrm{C}}$	0.09	0.09
r_{Arag}	r_{Arag}	0.67	0.37
[*]k_{CR}	k_{CR}	0.172	0.172
[*]k_{BS}	k_{BS}	0.920	0.920
[*]k_{sed}	k_{sed}	20,000	20,000
b_{riv}	$\mathcal{S}^{\mathrm{C}}$	44.0×10^{12}	—

Best-fit values for all of these parameters are determined by minimization of the residual R, except for those marked by an asterix [*] which are adjusted independently to reproduce fluxes or other characteristics of the carbon cycle. See text for details.

If different equation parameters are listed under the same general entry, they all share the same value.

Signification (and units) of the parameters are as follows: r_{mix} — upscaling factor applied to the mixing component of the oceanic circulation (dimensionless); $u_{\mathrm{SE}}^{\mathrm{P}}$, $u_{\mathrm{SN}}^{\mathrm{P}}$ and $u_{\mathrm{SANT}}^{\mathrm{P}}$ — phosphate utilization efficiencies (dimensionless); r_{oxyd} — fraction of organic matter remineralized in the thermocline (dimensionless); $r_{\mathrm{SEATL}}^{\mathrm{C}}$, $r_{\mathrm{SEI-P}}^{\mathrm{C}}$ and $r_{\mathrm{polar}}^{\mathrm{C}}$ — carbonate-C/organic-C rain ratio (mol $CaCO_3$/mol C-Org); r_{Arag} — aragonite fraction in the carbonate rain (mol Arag/mol $CaCO_3$); k_{CR} and k_{BS} — shallow-water carbonate production constants (mol $CaCO_3$/m^2/yr); k_{sed} — sediment calcite dissolution rate constant (complicated units, such that the dissolution flux comes out in mol $CaCO_3$/m^2/yr when concentrations are expressed in mol/m^3); b_{riv} — riverine bicarbonate input, parameter required to run the model under steady-state conditions (mol HCO_3^-/yr).

Table 4.8: Steady-state carbon fluxes.

	SNATL	SEATL	SANT	SEI-P	SNPAC	Totals
Air-to-Sea	28.5	−23.1	10.8	−42.4	4.2	−23.0
Organic	36.5	37.4	68.1	113.7	8.7	264.4
Inorganic	3.3	15.7	6.1	34.1	0.8	60.0
Coral reefs		1.0		2.6		3.6
Banks and shelves		1.9		5.1		7.0
Ocean-to-sediment	2.4	4.7	0.8	3.4	0.1	11.4
Sediment-to-ocean	0.0	0.0	0.0	0.0	0.0	0.0

All fluxes are in 10^{12} mol C/yr.

Table 4.9: Pre-industrial carbon fluxes for the transient adjustment.

	SNATL	SEATL	SANT	SEI-P	SNPAC	Totals
Air-to-Sea	28.4	−20.9	13.0	−38.3	4.4	−13.4
Organic	36.5	37.4	68.1	113.7	8.7	264.4
Inorganic	3.3	13.1	6.1	28.4	0.8	51.7
Coral reefs		1.8		4.8		6.5
Banks and shelves		1.9		5.1		7.0
Ocean-to-sediment	2.8	5.8	1.3	5.0	0.2	14.9
Sediment-to-ocean	0.0	2.0	4.1	7.2	0.2	13.5

All fluxes are in 10^{12} mol C/yr.

drive the organic matter production/remineralization cycle (u_{SE}^P, u_{SN}^P, u_{SANT}^P and r_{oxyd}). In the warm equatorial reservoirs, phosphate uptake efficiency is close to 80%; in the cold high-latitude reservoirs it is only around 30%. This illustrates the high potential of the latter for an increased fixation of carbon through bioproduction, called upon as a means to reduce atmospheric CO_2 levels during glacial times (BROECKER, 1982; KNOX and MCELROY, 1984; SARMIENTO and TOGGWEILER, 1984; SIEGENTHALER and WENK, 1984; KNOX-ENNEVER and MCELROY, 1985; TOGGWEILER and SARMIENTO, 1985; WENK and SIEGENTHALER, 1985). In the Antarctic surface reservoir, phosphate uptake efficiency could nearly triple before reaching the same level as that found for the warm surface ocean. With 72% of the export production getting remineralized between 100 and 1,000 m depth (i.e. in the thermocline reservoirs) our model compares well with the 80% estimated for the real ocean. As can be seen in table 4.7, the transient and steady-state adjustments yield identical values for these parameters.

On the other hand, there are surprises when looking at the parameters related to the production of inorganic matter (r_{SEATL}^C, r_{SEI-P}^C, r_{polar}^C and r_{Arag}). r_{SEATL}^C and r_{SEI-P}^C, the two carbonate-C/organic-C rain-ratios of the equatorial reservoirs, are almost 20% higher for the steady-state than for the transient adjustment; r_{Arag}, the aragonite fraction is even 80% higher. While the steady-state values for r_{SEATL}^C and r_{SEI-P}^C are already somewhat high, $r_{Arag} = 0.67$ is almost certainly much too high. The values obtained for the transient adjustment are much more realistic. The adopted value of 0.37 for r_{Arag} is even somewhat smaller than the 0.40 used by OPDYKE and WALKER (1992b). The high steady-state values are actually artefacts of the steady-state assumption itself, when forcing our model to comply with the set of data constraints. The most important keys to understand this are the aragonite and calcite saturation and compensation horizons. Normally, the model dynamically adjusts the depths of these two so that the global accumulation of carbonate in the sea-floor sediments gets closest to balancing the ocean's supply of alkalinity and carbon. In a steady-state situation, the sediments below the CCD in our model cannot become a net source of carbon and alkalinity to the deep sea: dissolution is limited by the supply from the carbonate raining down from the surface. During the adjustment, the model is forced to reproduce or at least to come close to given saturation and compensation depths. This means that the fractions of the calcite and aragonite productions that accumulate on the sea-floor are set, since the carbonate rain is uniformly distributed in our model.

Besides, the surface- to deep-sea gradients of alkalinity prescribed by the data constraints imply a net transfer of alkalinity from the surface to the deep reservoirs (in fact they tell us that there must be a sink in the surface

and/or a source in the deep waters, which may very well be independent of each other). Since the sinking carbonate particles are the main surface- to deep-sea vectors of alkalinity in our model, this means that the overall production of carbonate is also more or less fixed: it has to be large enough for the dissolution in the deep-sea to account for this net transfer. The aragonite fraction in the carbonate rain finally represents an additional and significant degree of freedom to achieve the constraints: the larger the fraction of aragonite, the larger the carbon and alkalinity releases in the deep sea, for given situations of the aragonite and calcite saturation depths (see figure 4.12). Once the inorganic production and accumulation-dissolution cycle is settled, the inputs of carbon and alkalinity corresponding to the carbonate burial in the sea-floor sediments is also determined. Practically, r_{Arag} also takes into account the part of calcite that dissolves above the calcite saturation depth (see, e.g., ARCHER, 1996, and references therein).

This is also the reason for the high value obtained for the riverine input of bicarbonate b_{riv}, which is almost 40% higher than the 32×10^{12} mol HCO$_3^-$/yr commonly cited (MEYBECK, 1979). Let us nevertheless recall that this latter figure might be an underestimate, as noticed in the discussion of the global oceanic carbon budget (see page 35).

Under transient conditions, one major difference makes the model behave in a completely different way. When the model reaches the pre-industrial era, it has had a period of intense carbonate deposition on the sea-floor a few ten thousands of years earlier. The saturation depths have been rising since then, progressively exposing the previously deposited carbonates to corrosive waters. They become gradually exposed and dissolve. In the deep sea, below the CCD, the global releases of alkalinity and of carbon have thus become much larger than the supply from carbonate raining down from the surface. The source of carbon and alkalinity in the deep sea that is required to comply with the given distributions of DIC and total alkalinity do not need any longer to come from the carbonate rain alone, but a large part comes from the sea-floor weathering of old sedimentary carbonates. As a consequence, the best-fit values for $r_{\mathrm{SEATL}}^{\mathrm{C}}$, $r_{\mathrm{SEI-P}}^{\mathrm{C}}$ and, most important, for r_{Arag} are smaller for transient than for steady-state conditions. It is possible that $r_{\mathrm{polar}}^{\mathrm{C}}$ would also be smaller, if we had better data constraints for the high-latitude reservoirs.

Not much can be said about k_{CR} and k_{BS}. It is always possible to exactly fulfil the constraints that they are subject to. Let us only emphasize here that they should not be interpreted as specific accumulation rates, although their units might suggest this. k_{CR} for example takes into account that coral reef growth is limited to latitudes where water temperature does not fall below a given annual minimum temperature, a variable that is of course not
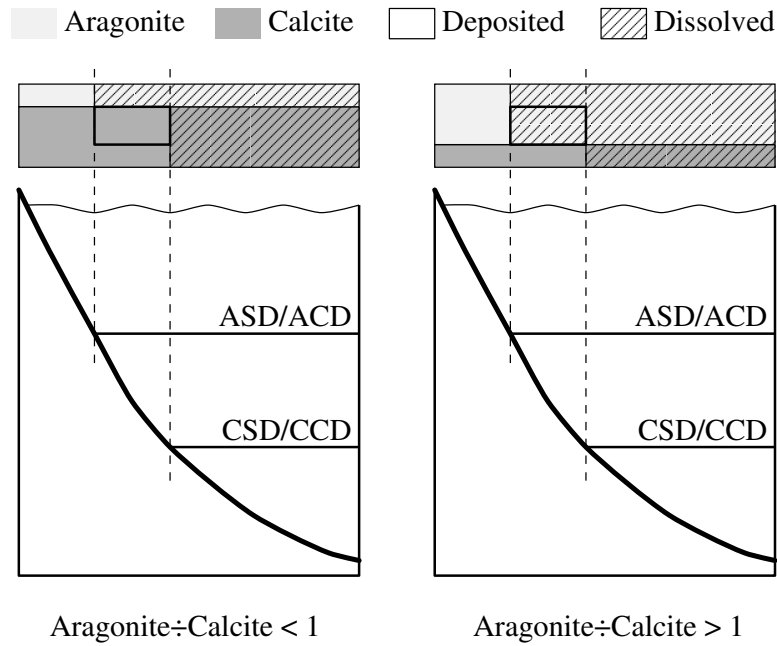
Figure 4.12: Partitioning of the carbonate rain into a part that gets dissolved and a part that gets deposited, for a given depths of the ASD/ACD and CSD/CCD systems. The shaded rectangles drawn on top of the oceans represent the total carbonate rain (aragonite in light plus calcite in dark grey), supposed to be homogeneous over the whole surface area. The dissolved part of the rain corresponds to the hatched and the deposited part to the plain area. The thick rectangle indicates the fraction that gets deposited if the aragonite:calcite ratio is low (on the left), but gets dissolved if this ratio is high (on the right).

resolved within our reservoirs.

4.4.2   Model Sensitivity

The sensitivity of the coupled ocean-sediment model to its parameters has been systematically tested for steady-state conditions only. We will limit our discussion here to the following two aspects:

- How do the tracer distributions globally respond to parameter changes ?

- How does the atmospheric CO_2 content respond to parameter changes ?

To quantify this sensitivity, we have determined the variations of the residual R around the obtained minimum for perturbations of each single parameter around its best-fit value. The results of these experiments, intended to address the first of the two questions above, are shown in figure 4.13. Each curve of this figure represents the variation of R (normalized to its minimum of 5.36) for changes of the parameter indicated. The scales of the three parts of that figure have been made rigorously identical in order to make a significant comparison possible. It is clear that, the narrower the parabola-shaped curve, the more significant the best-bit value of the corresponding parameter.

Surprisingly, the best-defined of all of the parameters is the "fake" parameter b_{riv} that we had to introduce in order to close the model. This already illustrates what potential we may expect from changing continental weathering to disturb the whole ocean's geochemistry. For the moment, it should not be considered more than an illustration. We have indeed to keep in mind the artefacts that led to several anomalous parameter values in the steady-state calibration. Similar caution must be taken to avoid an overinterpretation of r_{Arag}, another parameter to which the model is surprisingly sensitive. This parameter represents in fact the only way for our model to handle carbonate dissolution in the water column and calcite dissolution above the CSD, processes that are not explicitly taken into account in the present version.

The least-well defined of our parameters are those with the flattest curves: $u_{\mathrm{SN}}^{\mathrm{P}}$ and $r_{\mathrm{polar}}^{\mathrm{C}}$. This on the other hand is not very surprising since both rely on boreal reservoirs, for which the quality of the constraining data is worst. Considering the very low sensitivity of R to variations of $u_{\mathrm{SN}}^{\mathrm{P}}$, and taking into account that its best-fit value is fairly similar to that of $u_{\mathrm{SANT}}^{\mathrm{P}}$, one might ask if it would not be preferable to use a unique parameter for the high-latitude reservoirs: as can be seen from figure 4.13, R does only increase by 4% when the value of $u_{\mathrm{SN}}^{\mathrm{P}}$ is decreased by 20%, which is enough to reduce it to the same value as $u_{\mathrm{SANT}}^{\mathrm{P}}$.
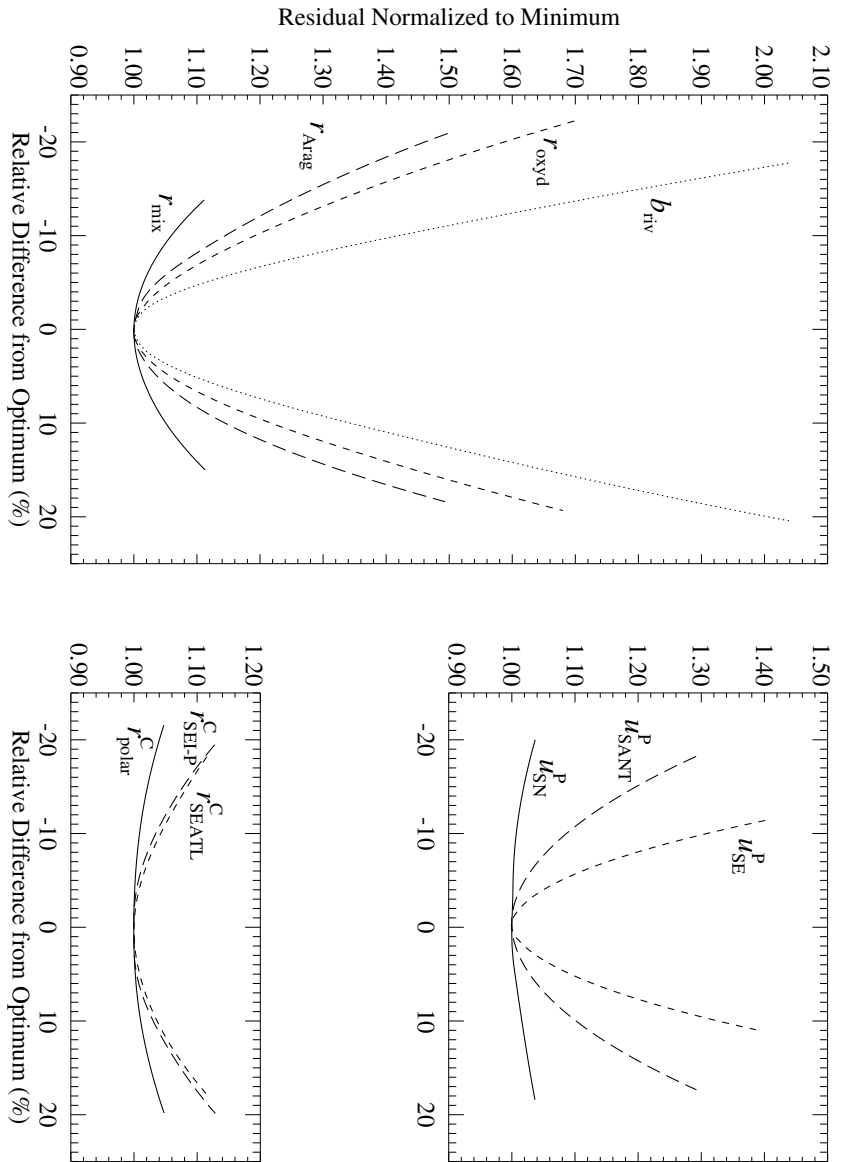
Figure 4.13: Model sensitivity to its parameters in a steady-state situation. Each curve describes the variations of the normalized residual in the vicinity of its minimum value due to changes of a given parameter around its best-fit value, all others being held constant (see table 4.7).

The reason for not having made this simplification becomes clear when analysing the model's sensitivity in terms of atmospheric CO_2 changes, illustrated in figure 4.14. This figure is strictly analogous to figure 4.13: instead of the variations of R around its minimum, we have plotted those of p_{CO_2} around the value of 279.6 it takes at the minimum of R. On the upper right panel, it can in particular be seen that p_{CO_2} is more sensitive to perturbations of u_{SANT}^P than of u_{SN}^P. The slopes of the two corresponding curves are in a ratio of $-20:-11$. We have therefore decided to keep separate phosphate uptake parameters for the boreal and the austral reservoirs. Once again, b_{riv} appears to be the most influential parameter, and once again, the role of r_{Arag} is unexpectedly important. This latter represents a factor whose impact on the oceanic carbonate balance has never been explored (as confirmed by MILLIMAN, personal communication). This is most probably due to the fact that the current knowledge of inorganic carbon cycling in the oceans barely allows one to reach a significant estimate of its magnitude. u_{SE}^P, previously the second-best constrained parameter — see figure 4.13 — does not play any significant role with regard to atmospheric CO_2. This is a striking example of the action of the solubility pump (VOLK and HOFFERT, 1985), which is often neglected relative to the biological pump: this latter is only efficient if coupled to the former. Organic production increases can only lead to large reductions of the atmospheric p_{CO_2} if they take place in regions where deep water formation is important. If they take place in regions where upwelling dominates, their overall effect is much weaker. It should however be noticed that the curves relative to the phosphate uptake efficiency parameters in figure 4.14 do not represent the pure response of organic production changes. As a consequence of the model formulation, the phosphate uptake parameters determine the global biological production and not only the organic part, since the inorganic production is calculated from the organic one via the rain ratios. The concomitant changes of the inorganic production partly counterbalance the effects from changes of the organic one.

4.5 Numerical Methods

4.5.1 Integration Scheme

The system of ordinary differential equations which describes the evolution of our model carbon system is solved numerically using an explicit RUNGE-KUTTA-type method. Because of the various forcing functions used with the model, we have looked for a method with an adaptative stepsize.

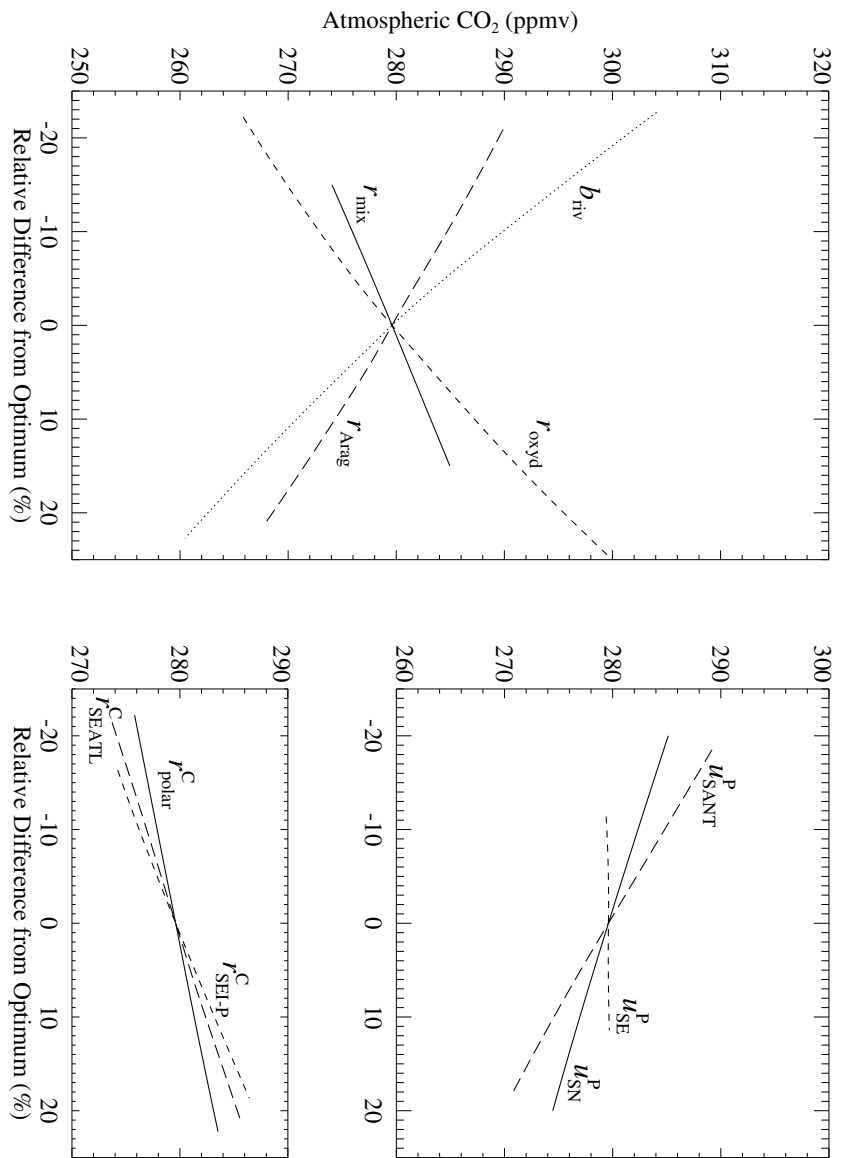We have selected the method of DORMAND and PRINCE of order 5(4).

Figure 4.14: Model sensitivity to its parameters in a steady-state situation: variations of the atmospheric CO_2 level due to changes of single parameters around their best-fit value, analogous to figure 4.13. Line styles for the different parameters are the same as in that figure .

This is basically a method of order 4, having embedded a method of order 5. The latter is used to step forward in time, the former is used for the purpose of stepsize control. For an ordinary differential equation defined by

$$\frac{dx}{dt} = f(t, x) \quad \text{and} \quad x(t_0) = x_0,$$

the numerical approximation x_{n+1} of the solution $x(t)$ in $t_{n+1} = t_n + \Delta t_n$ is calculated from the approximation x_n for $x(t)$ in t_n using the following system of intermediate steps:

$$
\begin{aligned}
k_1 &= f(t_n, x_n) \\
k_2 &= f(t_n + \tfrac{1}{5}\Delta t_n, x_n + (\tfrac{1}{5}k_1)\Delta t_n) \\
k_3 &= f(t_n + \tfrac{3}{10}\Delta t_n, x_n + (\tfrac{3}{40}k_1 + \tfrac{9}{40}k_2)\Delta t_n) \\
k_4 &= f(t_n + \tfrac{4}{5}\Delta t_n, x_n + (\tfrac{44}{45}k_1 - \tfrac{56}{15}k_2 + \tfrac{32}{9}k_3)\Delta t_n) \\
k_5 &= f(t_n + \tfrac{8}{9}\Delta t_n, x_n + (\tfrac{19372}{6561}k_1 - \tfrac{25360}{2187}k_2 + \tfrac{64448}{6561}k_3 - \tfrac{212}{729}k_4)\Delta t_n) \\
k_6 &= f(t_n + \Delta t_n, x_n + (\tfrac{9017}{3168}k_1 - \tfrac{355}{33}k_2 + \tfrac{46732}{5247}k_3 + \tfrac{49}{176}k_4 - \tfrac{5103}{18656}k_5)\Delta t_n) \\
k_7 &= f(t_n + \Delta t_n, x_n + (\tfrac{35}{384}k_1 + 0k_2 + \tfrac{500}{1113}k_3 + \tfrac{4125}{192}k_4 - \tfrac{2187}{6784}k_5 + \tfrac{11}{84}k_6)\Delta t_n)
\end{aligned}
$$

and

$$\Delta_5 x_n = \tfrac{35}{384}k_1 + 0k_2 + \tfrac{500}{1113}k_3 + \tfrac{4125}{192}k_4 - \tfrac{2187}{6784}k_5 + \tfrac{11}{84}k_6$$

$$\Delta_4 x_n = \tfrac{5179}{57600}k_1 + 0k_2 + \tfrac{7571}{16695}k_3 + \tfrac{393}{640}k_4 - \tfrac{92097}{339200}k_5 + \tfrac{187}{2100}k_6 + \tfrac{1}{40}k_7$$

The numerical approximation x_{n+1} of the solution $x(t)$ at $t_{n+1} = t_n + \Delta t_n$ is then defined as the fifth order approximation $x_{n+1} = x_n + \Delta t_n \Delta_5 x_n$. The fourth order approximation $x'_{n+1} = x_n + \Delta t_n \Delta_4 x_n$ of $x(t)$ at t_{n+1} is used by the step control mechanism.

This mixed RUNGE-KUTTA method has computational advantages over the classical step-doubling procedure with RICHARDSON extrapolation of the discretization error, applied to the well-known RUNGE-KUTTA method of order 4. Whereas this latter procedure requires at least 11 evaluations of the second member of the differential equation, the DORMAND-PRINCE method used here requires only 7 such evaluations, more than 30% less.

The adopted stepsize control mechanism works as follows: after x_{n+1} and x'_{n+1} have been obtained, an overall error *err* is determined as the maximum of the relative differences between corresponding components of the two vectors x_{n+1} and x'_{n+1} where they are larger than 10^{-8}, and of the absolute differences where they are smaller. If *err* > *tol*, *tol* being a fixed tolerance, both x_{n+1} and x'_{n+1} are rejected and recalculated with Δt_n reduced to $0.8 \times \Delta t_n \times (tol/err)^{1/4}$. If *err* < *tol*, then x_{n+1} is accepted as an approximation for $x(t)$ at $t_{n+1} = t_n + \Delta t_n$. The next iteration is then started, with a

new (larger) trial stepsize calculated by $\Delta t_{n+1} = 0.8 \times \Delta t_n \times (tol/err)^{1/5}$, but with $\Delta t_{n+1} < 2$ yr for stability reasons. We use $tol = 0.05$ in our integration scheme.

Variables relative to the sedimentary part of the model (i.e. $M_{i,j}^{\mathrm{C}}$ and $M_{i,j}^{\mathrm{nC}}$, with $i \in Srfc$ and $j = 0, \ldots, 79$) are not taken into account when calculating err. Their variations are generally very small and their evolution is partially calculated asynchronously with the rest of the model. After completion of each step by the general integration scheme define above, it is checked if all the sedimentary mixed layer reservoirs are still filled within $\pm 6\%$ of their nominal height. Where necessary, they get emptied by creation of a new memory layer, or refilled by remixing the content of the most recently formed memory layer in its stack into it, in order to get their level back within the adopted range of 8 cm $\pm\, 6\%$. Practically, this means that the terms $(\mathcal{X}^{\mathrm{C}})_{i,j}$ and $(\mathcal{X}^{\mathrm{nC}})_{i,j}$ in equations (4.51) and (4.52) respectively are set to zero while performing the calculations to step forward from time t_n to t_{n+1}.

4.5.2 Carbonate System Speciation

Simplified Equations of State for Seawater

In our model, concentrations can *a priori* only be obtained in units of mol/m^3, while the stoechiometric equilibrium constants presented in chapter 2 are given in mol/kg-SW. Their use thus requires the knowledge of an equation of state for seawater, such as the International Equation of State for Seawater EOS80 (UNESCO, 1981, 1983). This equation relates the density of seawater to temperature, salinity and pressure, within a standard error of about 0.009 kg/m^3. It is valid for salinities ranging from 0 to 42, for temperatures between -2 and 40°C, and for pressures between 0 and 1,000 bar.

Its evaluation is nevertheless very costly. For our purposes, we have therefore established two simple parameterizations for the density of seawater (ρ, in kg/m^3) as a function of temperature (T, in K), salinity (S) and pressure (P, in bar):

$$
\begin{aligned}
\rho_1(S, T, P) \;=\; & 1{,}039.9044 + 0.77629393\,(S - S_0) \\
& - 0.19692738\,(T - T_0) \\
& + 0.044038615\,(P - P_0)
\end{aligned} \tag{4.88}
$$

$$
\begin{aligned}
\rho_2(S, T, P) \;=\; & 1{,}040.0145 + 0.77629393\,(S - S_0) \\
& - 0.25013591\,(T - T_0) \\
& + 0.042026266\,(P - P_0) \\
& - 4.7473116 \times 10^{-3}\,(T - T_0)^2 \\
& - 4.7974224 \times 10^{-6}\,(P - P_0)^2 \\
& - 2.1404592 \times 10^{-4}\,(T - T_0)(P - P_0)
\end{aligned} \tag{4.89}
$$

where $S_0 = 35.5$, $T_0 = 285.16$ K and $P_0 = 300$ bar.

The coefficients of these two parameterizations were obtained by a least squares fit to EOS80, for S ranging from 34.5 to 36.5, and for T ranging from 271.16 K to 299.16 K ($-2°$C to $27°$C) if $P \leq 100$ bar, and from 271.16 K to 278.16 K ($-2°$C to $5°$C) if $P > 100$ bar. For this domain, which covers all of the combinations of salinity, temperature and pressure values encountered by our model, the standard deviation of ρ_1 from EOS80 is estimated at about 0.23 kg/m^3 (with $-0.34 < \rho_1 - \rho_{\mathrm{EOS80}} < 0.90$ everywhere), and that of ρ_2 at 0.02 kg/m^3 (with $-0.12 < \rho_2 - \rho_{\mathrm{EOS80}} < 0.10$ everywhere). It must be stressed that these two expressions are *fitting functions* and *not expansions at* (S_0, T_0, P_0). They are hence not exact at that point, which explains the difference between their respective constant terms.

Speciation Calculation Algorithms

Many processes in the oceanic environment of our model are directly dependent on the concentration of a given species of dissolved inorganic carbon: air-sea exchange depends on $[\mathrm{CO_{2(aq)}}]$, deep-sea carbonate dissolution on $[\mathrm{CO_3^{2-}}]$. We therefore need to include a precise speciation calculation module into our model. According to the theoretical sensitivity experiments regarding the different approximative representations of total alkalinity (section 2.5), it is necessary to perform these calculations by including at least $\mathrm{HCO_3^-}$, $\mathrm{CO_3^{2-}}$ and $\mathrm{B(OH)_4^-}$ among the alkalinity contributors. A_{CB} is the minimal approximation to be used for total alkalinity and the procedure should hence solve at least the cubic equation (2.55), rewritten here as

$$H^3 + a_2 H^2 + a_1 H + a_0 = 0, \tag{4.90}$$

where

$$
\begin{aligned}
a_2 &= K_{\mathrm{B}}(1 - B_{\mathrm{T}}/A_{\mathrm{CB}}) + K_1(1 - C_{\mathrm{T}}/A_{\mathrm{CB}}) \\
a_1 &= K_1\big(K_{\mathrm{B}}(1 - B_{\mathrm{T}}/A_{\mathrm{CB}} - C_{\mathrm{T}}/A_{\mathrm{CB}}) + K_2(1 - 2C_{\mathrm{T}}/A_{\mathrm{CB}})\big) \\
a_0 &= K_1 K_2 K_{\mathrm{B}}\big(1 - B_{\mathrm{T}}/A_{\mathrm{CB}} - 2C_{\mathrm{T}}/A_{\mathrm{CB}}\big)
\end{aligned}
$$

with H as a shorthand for $[\mathrm{H_3O^+}]$. In the oceans, we generally have $C_{\mathrm{T}} < A_{\mathrm{CB}} < 2C_{\mathrm{T}}$ and $B_{\mathrm{T}} < A_{\mathrm{CB}}$, C_{T} and B_{T} being expressed in moles, A_{CB} in equivalents. The sum of the roots of equation (4.90) (equal to $-a_2$) is thus negative, and their product (equal to $-a_0$) is positive. This equation therefore has either two negative real roots or two complex roots with negative real parts, and it has only one positive, physically meaningful root. Algebraic methods of resolution have proved to be of no use here, because of a lack of

precision (MUNHOVEN, 1990). We therefore use a NEWTON-RAPHSON iteration scheme to determine $H = [\mathrm{H}^+]_\mathrm{SWS}$ from equation (4.90). The overall efficiency of such an iteration scheme depends on the ability to determine a starting value H_0 from which convergence is warranted. In our case, an appropriate H_0 can be obtained from the following:

1. determine the position of the local minimum of the cubic;

2. write the TAYLOR expansion to second degree, at this position;

3. set H_0 equal to the largest of the two roots of the Taylor expansion;

We have verified that the local minimum of the cubic is always negative if $1.5 < C_\mathrm{T} < 3.0$ and $1.8 < A_\mathrm{CB} < 3.2$. The above method thus always yields a valid H_0. Starting from this H_0, the NEWTON-RAPHSON iterations generate a monotonically decreasing sequence, which quadratically converging to the root of interest. The adopted stopping criterion $(H_n - H_{n-1})/H_n < 10^{-5}$ is often already fulfilled at $n = 3$; sometimes it is necessary to go for $n = 4$.

For our carbon cycle model, the above routine is sufficient. For the calculations in section 2.4, we have nevertheless developed an algorithm to determine the carbonate speciation when the more precise approximation of A_T which takes $[\mathrm{OH}^-]_\mathrm{SWS}$ and $[\mathrm{H}^+]_\mathrm{SWS}$ into account is used. In this case, we solve equations (4.90) and (2.54), which writes

$$A_\mathrm{CB} - A_\mathrm{T} + K_\mathrm{W}/H - H = 0, \qquad (2.54)$$

simultaneously for H and A_CB, using this time a NEWTON-KANTOROVICH iteration scheme. The starting value H_0 is calculated as above, after formally replacing A_CB by A_T in equation (4.90). $(A_\mathrm{CB})_0$ is obtained by introducing H_0 into (2.54). With the same stopping criterion $(H_n - H_{n-1})/H_n < 10^{-5}$ as before, this algorithm generally stops after 3 to 4 iterations, in some very rare cases 5 iterations are required.

Chapter 5

Strontium Isotopes as Indicators of Glacial-Interglacial Weathering Changes

5.1   Strontium and ^{87}Sr/^{86}Sr in Seawater

FAURE et al. (1965) were probably among the first to recognize the potential of the seawater ^{87}Sr/^{86}Sr isotopic ratio as an indicator of continental weathering. Using the data from GOLDSTEIN and JACOBSEN (1987), we may calculate that the present-day oceans contain about $121 \pm 4 \times 10^{15}$ mol Sr. The oceans are very homogeneous with respect to strontium isotopic ratios, with ^{87}Sr/^{86}Sr $= 0.709174 \pm 0.000030$ (HODELL et al., 1990). FAURE et al. (1965) have shown that this ratio is controlled by the blending of three distinct isotopic varieties of strontium:

1. strontium deriving from the *weathering of old crustal sialic rocks* on the continents, relatively enriched in ^{87}Sr due to the decay of ^{87}Rb to ^{87}Sr with isotopic ratios typically between 0.712 and 0.730;

2. strontium deriving from the *weathering of young volcanic rocks*, both on the continents and in the ocean basins (including Sr-exchange taking place during the reaction of seawater with basalt at mid-ocean ridges and on the sea-floor), a source for which ^{87}Sr/^{86}Sr ratios are typically between 0.703 and 0.706;

3. strontium originating from the *weathering of marine carbonates and sulphates* (the latter, however, only to a minor extent) of Phanerozoic

age, both on the continents and in the ocean basins (also including recycling of Sr during early diagenesis of carbonate sediments on the sea-floor), giving rise to Sr fluxes with $^{87}Sr/^{86}Sr$ ratios ranging between 0.706 and 0.709, but generally very close to 0.708 (HOLLAND, 1984; FAURE, 1986).

With emphasis on the cycling pathways within the global strontium cycle rather than on the sources, the seawater strontium content and its isotope composition are generally considered to be controlled by the *riverine input from the continents*, collecting contributions from all of the three sources above, by the *sea-floor alteration of basalt*, both at high-temperature ridge crest hydrothermal systems and at low-temperature alteration sites, and by *diagenetic Sr recycling fluxes* out of carbonate sediment porewaters.

The largest of these fluxes is the riverine one, currently estimated at 33.3×10^9 mol Sr/yr, with an $^{87}Sr/^{86}Sr$ ratio of of 0.7119 (PALMER and ED-MOND, 1989). These authors indicate that the error on the flux magnitude is almost certainly lower than 30% and that it is more likely to be an under- than an overestimate. The other two types of fluxes are much less well known. ELDERFIELD and GIESKES (1982), who have analysed the Sr^{2+} concentration gradients in the interstitial waters of sediments in a number of DSDP cores, calculate that the recycling of Sr from carbonate sediments represents an annual input of about 2.5–5×10^9 mol Sr for the oceans, with an average $^{87}Sr/^{86}Sr$ ratio of 0.7087. They furthermore find that the low-temperature alteration of basalt represents only a flux of 0.5–0.7×10^9 mol Sr/yr, with an average $^{87}Sr/^{86}Sr$ ratio of 0.7064, almost two orders of magnitude less than the riverine flux. Adopting this relatively small value for the contribution from low-temperature basalt alteration reactions, PALMER and ED-MOND (1989) calculate that the high-temperature alteration processes provide $15.1 \pm 3.8 \times 10^9$ mol Sr/yr. They assume that this flux bears a $^{87}Sr/^{86}Sr$ signature of 0.7035. HOLLAND (1984) arrives at a very similar global contribution from the sea-floor alteration of basalt of about 17×10^9 mol Sr/yr, but he attributes 10×10^9 mol Sr/yr of these to high- and 7×10^9 mol Sr/yr to low-temperature sites. From these flux estimates, we find that the residence time of strontium in the oceans must be on the order of 2.5×10^6 years.

Due to the distinct Sr isotope signatures of the dissolved weathering products originating from the continents, the $^{87}Sr/^{86}Sr$ ratio of seawater has been interpreted as an indirect weathering indicator. Accordingly, changes in the relative importance of the different sources have been made responsible for the variations documented in the seawater $^{87}Sr/^{86}Sr$ record for the Cenozoic and the Phanerozoic (PETERMAN et al., 1970; VEIZER and COMPSTON, 1974; BURKE et al., 1982; PALMER and ELDERFIELD, 1985; HESS et al.,

1986; KOEPNICK et al., 1988; CAPO and DEPAOLO, 1990; HODELL et al., 1990; JONES et al., 1994). For example, the uplift of continental blocks and their subsequent weathering and erosion are generally made responsible for the late Cenozoic increase in the seawater $^{87}Sr/^{86}Sr$ ratio (RAYMO et al., 1988; HODELL et al., 1990; RICHTER et al., 1992). Especially the uplift of the Himalaya-Tibetan Plateau region is thought to play major roles in this context (RAYMO et al., 1988). It is nevertheless not yet clear how much of the observed increase can be attributed to enhanced weathering, and how much to source redistributions leading to more radiogenic river Sr loads. The complete interpretation for the observed changes on that time scale remains nevertheless subject to discussion (see, e.g., FRANÇOIS and WALKER, 1992; BERNER and RYE, 1992; FRANÇOIS et al., 1993; GODDÉRIS and FRANÇOIS, 1995, 1996; GODDÉRIS, 1997).

5.2 Glacial-Interglacial Sr Isotope Records

The first opportunity to perform a study of the impact of changing continental weathering rates on atmospheric CO_2 over glacial-interglacial climate cycles — going beyond purely theoretical considerations and relying to some extent on observational constraints — came when DIA et al. (1992) published their seawater strontium isotope record for the past few hundred kiloyears. This record was based upon the analysis of the $^{87}Sr/^{86}Sr$ ratio of foraminifera in the core V28-238 from the equatorial Pacific. Over the 250 kyr period spanned by their record, they observed cyclic variations with an amplitude of about 20 ppm (relative to the $^{87}Sr/^{86}Sr$ ratio of 0.709168 measured on modern foraminifera), fairly well correlated to the $\delta^{18}O$ signal in the same core. Due to the short time scales of these variations, they concluded that the most viable explanation for the obtained signal were changes in the riverine supply of strontium to the oceans. They calculated that either a $\pm 50\%$ change of the supply itself, or a deviation of 0.0005 around the present-day river $^{87}Sr/^{86}Sr$ of 0.7119 were sufficient.

We used our carbon cycle model to analyse the potential impact of such variations of the continental weathering processes on the evolution of the CO_2 content in the atmosphere. The results of our study were published in MUNHOVEN and FRANÇOIS (1994), which is reproduced *in extenso* hereafter. The study of DIA et al. (1992) was in fact only the first part of a multi-episode story. While the MUNHOVEN and FRANÇOIS (1994) paper was in press, another record of seawater $^{87}Sr/^{86}Sr$ was published (CLEMENS et al., 1993). These authors based their reconstruction on $^{87}Sr/^{86}Sr$ ratios of planktonic foraminifera from ODP Site 758 in the equatorial Indian. Spanning 450 kyr

and having a much higher temporal resolution than that of DIA et al. (1992), it was suitable for a spectral analysis. This analysis showed that there was a non-zero coherency (at the 95% confidence level) between the reconstructed $^{87}Sr/^{86}Sr$ and the SPECMAP stacked oxygen isotope record (IMBRIE et al., 1984). They did not find any significant phase difference, which suggests that one can expect a rather direct link between seawater $^{87}Sr/^{86}Sr$ and global climate.

In both cases, the claimed variability was very close to the instrumental precision. To further investigate on the rather puzzling records, CLEMENS et al. also analysed samples in the Chain 84-24 core from the North Atlantic (CLEMENS et al., 1994, 1995). In this new record, they were not able to resolve any significant glacial-interglacial cycles. But they had to correct their results for a systematic positive relationship between instrumental mass fractionation inherent to the thermal ionization processus and the measured $^{87}Sr/^{86}Sr$ values. Without that correction, their signal presented a similar 100 kyr variability than the V28-238 record of DIA et al. (1992) and their own ODP Site 758 record (CLEMENS et al., 1993). However, they could not detect a similar bias in this latter. But, it did not stand a high-precision re-analysis by HENDERSON et al. (1994b,a). These authors had redone measurements on the V28-238 core and on key-sections of the ODP Site 758 core. In contrast to DIA et al. (1992), they did not find any support for cyclic variations in seawater $^{87}Sr/^{86}Sr$ over the past 350,000 years in the V28-238 record. Furthermore, they were not able to reproduce the largest shifts found by CLEMENS et al. (1993) in the ODP Site 758 record. A statistical analysis showed that their new measurements could instead be well represented by a simple linear increase, which is distinguishable from the well-known trend over the past 2.5 Myr pointed out by HODELL et al. (1990) and CAPO and DEPAOLO (1990). Finally, they calculate that the amplitude of any possible glacial-interglacial cycles that would be present but that are currently unresolvable due to instrumental limitations cannot exceed $\pm(6$–$9)$ ppm, or $\pm(0.000004$–$0.000006)$ on the absolute $^{87}Sr/^{86}Sr$ ratio itself.

On the following pages, we reproduce the complete text of MUNHOVEN and FRANÇOIS (1994). Although the Sr isotope record that this paper is based upon has been withdrawn since it was published, the discussion concerning the different parts of the model response to the weathering induced forcing remains of interest for the present thesis, and the main conclusions are still valid as well.

Glacial-Interglacial Changes in Continental Weathering: Possible Implications for Atmospheric CO$_2$

Guy Munhoven and Louis M. François

Institut d'Astrophysique
Université de Liège
Avenue de Cointe, 5
B–4000 Liège
Belgium

Abstract. An eleven-box model of the ocean-atmosphere sub-system of the global carbon cycle is developed to study the potential contribution of continental rock weathering and oceanic sedimentation to variations of atmospheric CO$_2$ pressure over glacial-interglacial time scales. The model is capable of reproducing the distribution of total dissolved inorganic carbon, total alkalinity, phosphate, $\delta\,^{13}$C, and Δ^{14}C between the various ocean basins today, as well as the partial pressure of atmospheric CO$_2$. A simple sedimentation scheme at 20 different depth levels drives carbonate deposition and dissolution as a function of the depths of carbonate and aragonite lysoclines in each ocean basin considered (Atlantic, Antarctic and Indo-Pacific). The coral reef erosion-deposition cycle is also taken into account. Furthermore, a simple cycle of oceanic strontium isotopes has been added to this model to take advantage of the ^{87}Sr/^{86}Sr data recently published by DIA et al. (1992) for the last 300,000 years. These data emphasize the importance of weathering of continental silicate rocks at glacial-interglacial time scales. They are used to construct several scenarios of changes of continental weathering over the last glacial cycles. They suggest that the flux of alkalinity delivered to the ocean from continental silicate weathering may have been substantially larger during glacial times than today. We show that such variations of continental weathering may explain at least in part the observed changes of the partial pressure of atmospheric CO$_2$ between glacial and interglacial periods.

Introduction

Analyses of air bubbles trapped in Antarctica (Vostok) ice sheets have shown that the concentration of atmospheric CO_2 has fluctuated between 180 and 280 ppm during the last glacial-interglacial cycle (BARNOLA et al., 1987). The reason for this variation of atmospheric CO_2 over time scales of 10–100 kyr is not yet understood, but many authors have speculated on an oceanic cause, invoking changes in the dynamics, the chemistry or the biology of the world ocean (e.g., BROECKER, 1982; KNOX and McELROY, 1984; SARMIENTO and TOGGWEILER, 1984; BROECKER and PENG, 1989; MARTIN, 1990). The oceanic circulation has a characteristic time of $\approx$ 1000 yr and involves carbon and alkalinity fluxes of rather important magnitude. Changes in the rates of dynamical and chemical oceanic processes have thus the ability to modify substantially the atmospheric CO_2 content over time scales of several thousand years.

Simple box models of the glacial ocean have been developed and widely used to test the numerous mechanisms hypothesized to explain the CO_2 changes. However, the authors of these models have often considered the global ocean as a closed system, neglecting the long-term cycle of rock weathering on the continents followed by sedimentary deposition on the sea-floor. Nevertheless KEIR and BERGER (1983) were the first to explicitly take into account the interactions with shelf and deep-sea sediments in a two-box model of the oceanic carbon cycle used to test the phosphate-extraction mechanism proposed by BROECKER (1982). Further

BERGER and KILLINGLEY (1982) and BERGER and KEIR (1984) proposed that large atmospheric CO_2 variations could be driven by coral reef growth accompanying sea level rise. The resulting drop in surface alkalinity propagates to the deep sea where dissolution of sea-floor carbonate occur. Dissolution spikes are indeed observed in deep sea-floor carbonate sequences and FARRELL and PRELL (1989) have summarized the past changes of the calcite lysocline and compensation depth over the last million years in the Central Equatorial Pacific. The time lag between coral reef buildup and deep sea-floor carbonate dissolution is critical to generate a significant atmospheric CO_2 signal. The so-called coral reef hypothesis has been recently reconsidered by OPDYKE and WALKER (1992b) who used a 2-box model of the oceanic carbon and alkalinity cycles.

In this paper, we analyse the importance of chemical weathering of both silicate and carbonate minerals for the glacial-interglacial changes in atmospheric CO_2. For this purpose, we use a 10-box model of the world ocean taking into account river input as well as sea-floor sedimentation. Our study considers recent observations which are possible indicators of past weathering intensities.

$^{87}Sr/^{86}Sr$: Indicator of Past Weathering ?

Recently, DIA et al. (1992) have published data from planktonic foraminifera and corals in the Pacific recording the evolution of the $^{87}Sr/^{86}Sr$ ratio of seawater over the last 250 kyr, i.e. over the last two glacial cycles. The stron-

tium isotope data show cyclic variations with a periodicity of $\approx$ 100 kyr. A good correlation with $\delta^{18}O$ in the same core is observed. The amplitude of the signal is rather important with the $^{87}Sr/^{86}Sr$ ratio varying between 0.709155 and 0.709175. In view of the rather long residence time of strontium in the ocean (2–4 Myr) compared with the 100 kyr period of the cyclicity, such a variation of the isotopic signal suggests that important changes in the river flux of oceanic strontium have occured over glacial-interglacial times. River strontium comes from the weathering of continental silicates and carbonates. The weathering of carbonate rocks is not of major importance because carbonate rocks have been precipitated from ancient seawater and thus have a mean isotopic ratio relatively close to the oceanic value. Igneous silicate rocks in contrast show a wide range of isotopic compositions with $^{87}Sr/^{86}Sr$ ratios generally higher (at least for the old granitic shield) than the oceanic value (HOLLAND, 1984). A change in silicate rock weathering, either in the global flux or in the distribution over the continents, can significantly alter the strontium isotopic ratio of seawater. The isotopic fluctuations recorded over the last two glacial cycles thus possibly signify an important change in the global rate of silicate weathering during the same period. Such drastic changes in weathering intensity over glacial cycles are supported by Ge/Si data recently reported by FROELICH et al. (1992), suggesting a variation in the mean river concentration of dissolved silica originating from weathering by a factor of 2–3.

The strontium isotopic record of an-cient seawater over Cenozoic and even Phanerozoic time scales has been known for many years (PETERMAN et al., 1970; VEIZER and COMPSTON, 1974; BURKE et al., 1982; KOEPNICK et al., 1988). For these time periods, which are much longer than the residence time of strontium in the ocean, the isotopic changes are large and easily measured. The interpretation of the Cenozoic and Phanerozoic records is still much debated. Some authors (e.g., BRASS, 1976; BERNER and RYE, 1992) call upon variations of the isotopic composition of the material from igneous rock weathering entering the oceans due to changes in the relative importance of the continental shields (characterized by a high $^{87}Sr/^{86}Sr$ ratio) versus young volcanic rocks as sources of strontium. EDMOND (1992) provides a plausible mechanism for this hypothesis: taking the Himalaya as an example, he shows that rock metamorphism during collisions between continental plates may transfer radiogenic from K-rich minerals into Ca- and Na-rich ones, which, when uplifted, weather more rapidly and thus become a source of ^{87}Sr. Several other studies (RAYMO et al., 1988; RAYMO, 1991) have proposed that the isotopic signal is an index of past intensities of continental weathering. FRANÇOIS and WALKER (1992) and FRANÇOIS et al. (1993) have shown that, on the basis of this hypothesis, it is possible to reconstruct in a numerical simulation an atmospheric CO_2 history consistent with the timing of Phanerozoic glaciations, as well as CCD and carbonate deposition rates compatible with the Cenozoic records.

Over time scales of several million years, it is usually assumed that atmo-

spheric carbon dioxide is controlled primarily by the balance between the input from volcanoes and the loss in weathering reactions of continental silicate rocks (WALKER et al., 1981; BERNER et al., 1983; LASAGA et al., 1985). The role of silicate weathering in the glacial-interglacial carbon budget of the ocean-atmosphere system has nevertheless often been neglected, because of the rather long residence time of oceanic carbon with respect to continental weathering and sedimentation ($\approx$ 150 kyr) or more specifically with respect to silicate weathering followed by carbonate deposition on the sea-floor ($\approx$ 400 kyr). However this simple argument regarding the oceanic residence time of carbon is not really relevant as far as atmopheric CO_2 is concerned, because of the high non-linearity of CO_2 dissolution and carbonate reactions in seawater. The long-term mean release of CO_2 from volcanoes (and hence the global weathering rate of continental silicates) is not well-known but estimates generally fall in the range of 5–10×10^{12} mol/yr (WALKER, 1977; WALKER et al., 1981; BERNER et al., 1983; MEYBECK, 1987). Following FRANÇOIS and WALKER (1992), let us assume an intermediate value of 7×10^{12} moles for the amount of Ca-Mg originating from continental silicate weathering and entering the ocean each year. This flux corresponds to an alkalinity input of 14×10^{12} eq/yr. With a volume of 1.35×10^{18} m^3 for the world ocean, a flux of this magnitude, if not compensated by carbonate deposition on the sea-floor, has the ability to raise the average alkalinity of seawater by 0.2 meq/kg in only 20 kyr. Such a drop in global alkalinity, if reflected in

surface water, can induce a drop in atmospheric CO_2 by $\approx$ 130 ppm, a change larger than the amplitude of the glacial-interglacial signal. Of course, in the real system, the rise in alkalinity would be accompanied by a rise in carbonate ion concentration and thus by an increase in the deposition rate of sea-floor carbonates, an increase which compensates at least partly for the initial rise in alkalinity.

As mentioned above, the isotopic data of DIA et al. (1992) show a cyclic change of 28 ppm in the $^{87}Sr/^{86}Sr$ ratio of seawater over the last two glacial cycles. What is the change in the weathering rate required to sustain such an isotopic shift, if we assume that weathering intensity is the only important factor that has varied ? Is this needed change significant with respect to that postulated in the simple example discussed previously ? The effect of a variation ΔF_{riv} of the river flux of strontium on the $^{87}Sr/^{86}Sr$ isotopic ratio of ocean water r_o can be measured by the quantity $(r_{riv} - r_o) \cdot (\Delta F_{riv}/q_o) \cdot (9.43 + r_o)/(9.43 + r_{riv})$ which is numerically equal to the time derivative of r_o induced by the flux variation (the factor $(9.43 + r_o)/(9.43 + r_{riv})$ is close to unity and it comes from the consideration of not only ^{87}Sr and ^{86}Sr but also ^{84}Sr and ^{88}Sr in the streontium budget; for details see HOLLAND (1984)). In this expression, r_{riv} is the river strontium isotopic ratio which today is close to 0.7119 (WADLEIGH et al., 1985) and q_o is the amount of strontium in the oceanic reservoir (0.12×10^{18} moles today). The data of DIA et al. (1992) record changes of r_o between 0.709155 and 0.709175 over typical time inter-

vals of 40 kyr. The necessary variation of the strontium river flux required to sustain such an isotopic shift is thus $\Delta F_{\text{riv}} = 2.2 \times 10^{10}$ mol/yr, which is about 70% of the present-day river flux of strontium. It is clear that some fraction of the isotopic shift can be induced by a variation in r_{riv} in response to a change in the type of rock weathered, due for example to a change in the distribution of precipitation and runoff worldwide. However, a change in the type of rock weathered, if due to a totally independent factor (such as runoff distribution) can act with an equal probability towards an increase or a decrease in r_{riv}, the latter possibility leading to an even higher estimate of ΔF_{riv}. Note also that metamorphic effects (invoked by EDMOND (1992)) have not the ability to change substantially the value of r_{riv} on the geologically short time scale of the glacial-interglacial cycle. We can thus conclude that the isotopic data suggest variations of the weathering intensity over the continents of the order of 70% of the present-day flux. As shown before, if silicate weathering has varied by this amount, then atmospheric CO_2 must have been strongly affected by these changes.

In the following sections, we will discuss these topics by constructing a coupled model of the carbon and strontium geochemical cycles to be applied over glacial-interglacial time scales. We will focus on the description of the long-term exchanges of carbon between the continental crust, the ocean-atmosphere system and sea-floor sediments. We believe that the changes in atmospheric CO_2 recorded at Vostok are certainly not due solely to changes in continen-

tal weathering of rocks. Presumably many other factors are at work, such as the much discussed effect of a redistribution of oceanic carbon in response to dynamical changes. Thus we do not aim at an explanation for the Vostok record, but the available strontium isotopic record suggests that silicate weathering has changed dramatically over the last two glacial cycles and we will show that these changes cannot be neglected as far as atmospheric carbon dioxide is concerned.

Model Characteristics

The model of the ocean-atmosphere subsystem of the global carbon cycle which we have been using for this study is a low resolution box model with one single atmospheric box and ten oceanic boxes: deep Atlantic, Indo-Pacific, and Antarctic, temperate Atlantic and Indo-Pacific thermoclines and surfaces, high-latitude Atlantic and Pacific surfaces and Antarctic surface (figure 5.1). The volumes of these different reservoirs are calculated as a function of sea level, which is allowed to vary in time. For this purpose we use five depth profiles (one per surface reservoir) obtained by sampling the $1° \times 1°$ bathymetric data of the Scripps Institution of Oceanography at 400 m depth intervals and by linear interpolation between these sampling points. Furthermore, we have associated a series of twenty sedimentary layers with each one of these profiles (each layer thus covering a depth interval of 400 m).

A set of 264 ordinary differential equations is used to determine the following tracers: total dissolved inor-
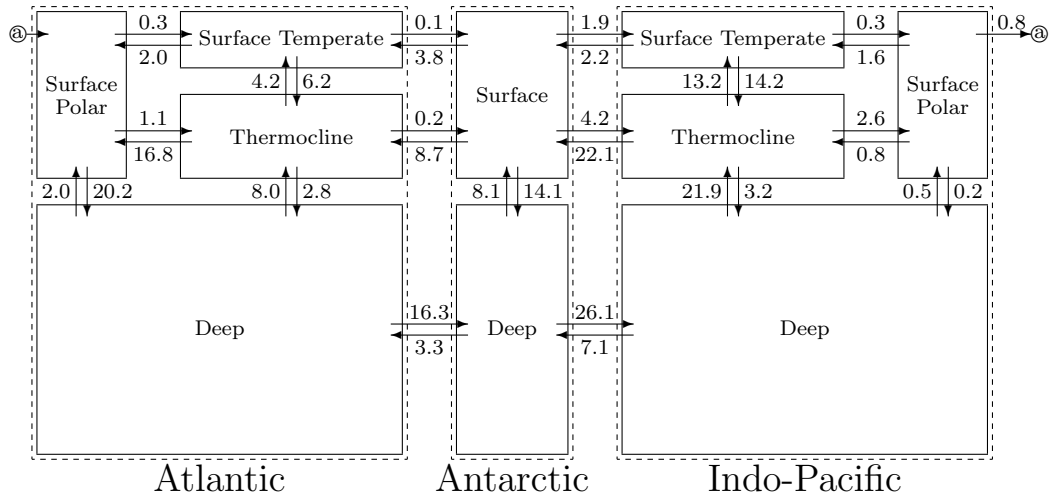
Figure 5.1: Ocean circulation. Arrows indicate water fluxes in Sverdrups (i.e. 10^6 m^3/yr).

ganic carbon, total alkalinity, phosphate and dissolved oxygen for the oceanic reservoirs, the partial pressure of CO_2 in the atmosphere, the $\delta^{13}C$ and $\Delta^{14}C$ for all of the precedent carbon species and finally the carbonate content and the $^{87}Sr/^{86}Sr$ ratio of the sedimentary reservoirs. The water exchange is fixed and has been determined from the annual mean velocity distribution of the Large Scale Geostrophic Oceanic General Circulation Model of the Max-Planck-Institut für Meteorologie in Hamburg, FRG (MAIER-REIMER and MIKOLAJEWICZ, 1991). This velocity field has been integrated over the surfaces separating the different boxes and then been decomposed into an advective and a mixing component. To reproduce the observed $\Delta^{14}C$ distribution of the real ocean we must take only 15% of the mixing part of the Hamburg model into account. This is due to the very large

differences in the resolutions of the two models. Lumping many small boxes together into a single large homogeneous reservoir is equivalent to increasing the mixing rates between them *ad infinitum.* This is exactly what is done when moving from the large scale Hamburg GCM to our box model. To keep the overall ventilation times of the different ocean basins (i.e. of the reservoirs of the box model) right, it is thus necessary to reduce the mixing through the separating surfaces.

The resulting circulation is presented in figure 5.1. When comparing our transports to those of earlier box models of equivalent complexity (BOLIN et al. (1983), BROECKER and PENG's (1986, 1989) PANDORA and KEIR's (1988) CYCLOPS — see KEIR (1988) for a summary), we find some common features as well as some striking differences. With the notable exception of

North Atlantic Deep Water (NADW) formation which ranges in the vicinity of 20 Sv (1 Sv $= 10^6$ m^3/yr) for all of the four models compared here, our transport rates, like those of PANDORA and CYCLOPS, are in general much lower than those calculated by Bolin et al. (1983). We will thus focus on PANDORA and CYCLOPS for this discussion. Our upper ocean exchange is similar to that of CYCLOPS in the Atlantic and to that of PANDORA in the Pacific. Like PANDORA, our model derives 30% of its NADW source waters from upwelling in the temperate Atlantic, which is not the case for CYCLOPS. It presents also nearly the same exchange between the deep Atlantic and Antarctic reservoirs as PANDORA, which is about half as important as that in CYCLOPS. The most important differences between our model and the other two can be found in the Antarctic-Pacific interaction and in the intra-Pacific circulation. These two are of course not independent. Whereas the deep Antarctic-deep Pacific exchange is dominated by mixing in both CYCLOPS and PANDORA, our model presents a well pronounced advection (19 Sv) from the Antarctic into the Pacific. This advective flux is followed by a strong upwelling in the temperate Pacific and a returning flow from the Pacific intermediate layer to the surface Antarctic reservoir. Finally, our model presents a net formation of deep water inside the Antarctic region, whereas CYCLOPS and PANDORA present a net upwelling (although their fluxes differ by a factor of two).

Besides this advective transport of matter by the marine circulation, we have considered the transfer of organic and inorganic matter from the surface to the thermocline and deep water: a fixed fraction of the phosphate entering each surface reservoir is used for organic matter production and the inorganic (calcium carbonate) production is supposed to be proportional to the organic production. We take 30% of the inorganic production as aragonite, the rest as calcite. The ratio $CaCO_3/C_{org}$ varies from 0.05 in the Northern Pacific reservoir to 0.4 in the Equatorial Indo-Pacific. These ratios have been adjusted to get for total alkalinity the best possible agreement with GEOSECS data. The organic matter is entirely recycled in the thermocline and the deep ocean. Production as well as recycling of organic matter are constrained by the Redfield ratio C/P/N = 106/1/16. One part of the calcium carbonate is transferred to sediments and the remaining part is dissolved in the deep ocean reservoirs, depending on the depth of the calcite and aragonite lysoclines (i.e. the saturation depths with respect to each of these minerals). Carbonate sediments are allowed to redissolve when these lysoclines become shallower.

Sea level variations over the period of interest for our problem are assumed to follow linearly the mean seawater δ^{18}O. Furthermore, we suppose that sea level variations by themselves do not change the total amounts of dissolved inorganic carbon, of total alkalinity and of phosphate, as well as of salt in the oceans. This means that when sea level is falling oceanic compounds become more concentrated, and *vice-versa*. The temperature evolution of the different water masses is taken from

the reconstruction of LABEYRIE et al. (1987). These reconstructions only deal with deep basins and as no data were available to us for the surface reservoirs, the surface temperature variations have been given the same amplitude as their deep counterparts (3° in the Atlantic and 2° in the Pacific) with present-day values of 2°C in polar and 19°C in temperate regions.

Model Runs and Discussion

Among the numerous model experiments performed, four have been selected to illustrate the sensitivity of the system to changes in continental weathering. The results of these simulations are summarized in figures 5.2 and 5.4 to 5.7. The first experiment (Run #1) shows the response of the model ocean-atmosphere to the glacial-interglacial variations in sea level and temperature, including the associated change in seawater salinity. When sea level is falling, the volume of oceanic water is reduced but no exchange of carbon and alkalinity with crustal pools (either through river runoff or carbonate sedimentation) is allowed, meaning that total inorganic carbon, alkalinity and phosphate are slightly more concentrated, with potential effects on the atmospheric CO_2 pressure. The opposite applies when sea level rises. Temperature and salinity changes also influence atmospheric CO_2 through the dependence of carbonate speciation and CO_2 solubility on these factors. Finally, ocean productivity can react to the slight change in phosphate concentration. The overall response of the

model atmospheric CO_2 pressure to the combination of these effects is given by curve #1 of figure 5.2. This curve may be considered as the response of a *closed* ocean to the temperature and salinity changes, without any change in circulation. The amplitude of the CO_2 signal is about 30 ppm. Note however that a CO_2 peak is obtained in the model near 5 kyr BP. This peak, not observed in the Vostok core, is due to a similar peak in the Atlantic temperature history (≈ 2°C warmer today than 5 kyr BP) reconstructed by LABEYRIE et al. (1987): when the Atlantic temperature peak is removed from the model data, the CO_2 peak disappears. If this peak at 5 kyr BP is not considered, then the amplitude of the signal is only 20 ppm, a value slightly higher than the rough estimate of 12 ppm made recently by BROECKER (1992). It must be emphasized however that our result contains internal oceanic feedbacks which are not considered in simple estimates of the direct effect of temperature and salinity.

Model run #2 illustrates the importance of considering the ocean-atmosphere as an *open* system. In this experiment, the ocean is fed by *constant* river fluxes of, first, carbon and alkalinity (in a 1:2 ratio, as in $CaCO_3$) originating from weathering of "ancient" (as opposed to freshly deposited coral reefs) continental carbonate rocks, and, second, of alkalinity from continental silicate weathering. Because silicate weathering adds alkalinity alone (i.e. without carbon) to seawater and because $CaCO_3$ (i.e. carbon and alkalinity in a 1:2 ratio) deposition is the only flux out of the model ocean-atmosphere, an additional
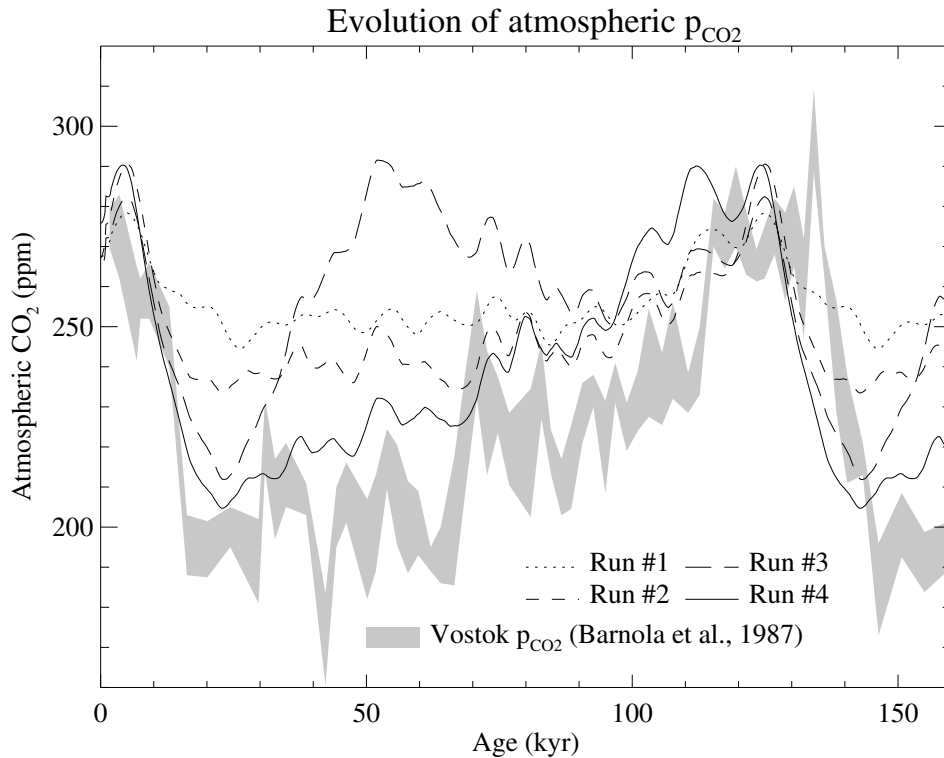
Figure 5.2: Model-generated variations of atmospheric CO_2 pressure compared with the observations from ice cores (Vostok). Four runs have been performed with the following characteristics (a more detailed description of model runs is given in the text):

Run #1: sea level, salinity and temperature changes only, no weathering-sedimentation cycle;

Run #2: sea level, salinity and temperature changes, with cycle of coral reef erosion and deposition, but with constant continental weathering rates;

Run #3: sea level, salinity and temperature changes, with cycle of coral reef erosion and deposition, and variations of the weathering rate of continental silicate rocks from figure 5.6 (curve #3), but fixed isotopic composition of the weathering products;

Run #4: sea level, salinity and temperature changes, with cycle of coral reef erosion and deposition, both the weathering rate of continental silicate rocks (figure 5.6, curve #4) and the isotopic composition of the weathering products (figure 5.5, curve #4) vary. Note the large difference in the silicate weathering rate with respect to run #3 (see figure 5.5).

input of carbon to the system equal to half the source of alkalinity from silicate weathering is needed to balance the carbon and alkalinity budgets. This additional carbon input is provided by the release of CO_2 from volcanic origin (hydrothermal and metamorphic), a flux which is also assumed to be *constant* with time.

Coral reefs build up on continental shelves during sea level high stands and are eroded due to exposition when sea level is low. This simple coral reef buildup and erosion scheme is important since the coral reef flux to limestones has represented almost 11×10^{12} mol $CaCO_3$ per year over the last 5000 yrs (KINSEY and HOPLEY, 1991), compared to a total net oceanic sink of about 30×10^{12} mol $CaCO_3$ per year. The growth of coral reefs in our model is determined by the combined effect of the following factors. (1) They are supposed to grow only in water shallower than 100 m on the continental shelf. The favourable area S_{100} thus changes in time as sea level rises and falls. (2) Furthermore and similar to OPDYKE and WALKER (1992a) and WALKER and OPDYKE (submitted[†]; and personal communication), we suppose that their growth depends on the rate of sea level variation: coral reefs can neither build up during sea level drops, nor during very rapid rises. The corresponding limiting function L has the shape of a trapezoid. It is equal to 0 for sea level variations lower than -5 mm/yr (i.e. for sea level drops faster than 5 mm/yr) or higher then $+25$ mm/yr (i.e. for sea level rises faster

than 25 mm/yr) and is equal to 1 between $+5$ mm/yr and $+15$ mm/yr. Between -5 mm/yr and $+5$ mm/yr it varies linearly from 0 to 1, and between $+15$ mm/yr and $+25$ mm/yr, from 1 to 0. (3) Finally, we assume that coral reef growth is enhanced when the degree of supersaturation Ω_{CaCO_3} of seawater with respect to $CaCO_3$ increases. The total precipitation G of $CaCO_3$ by coral reefs (see figure 5.3) is then $G = k \times S_{100} \times L \times (\Omega_{CaCO_3} - 1)$, where we have chosen $k = 0.7$ mol/m^2/yr to produce a mean $CaCO_3$ production of 11×10^{12} mol/yr over the last 5000 years (KINSEY and HOPLEY, 1991). This approach differs from that of OPDYKE and WALKER (1992b) who have forced their model with a hypothetical net variation, including as well precipitation as erosion. The above scheme only drives net precipitation. In our model, erosion of coral reefs is proportional to the exposed area, with a rate of the same order of magnitude as the growth rate, in terms of $CaCO_3$ fluxes per unit area. The $CaCO_3$ flux originating from coral reef (i.e. "freshly" deposited carbonates) erosion is added to that originating from weathering of "ancient" continental carbonate rocks.

Planktonic carbonates deposited on the ocean bottom above the lysocline are kept in sedimentary reservoirs until a rise of the lysocline exposes them to sufficiently corrosive waters so that they can be redissolved. Above the lysocline, there is no dissolution and below, we take it proportional to $([CO_3^{2-}]_{loc} - [CO_3^{2-}]_{sat})^{4.5}$, following KEIR (1980), where $[CO_3^{2-}]_{loc}$ is

---

[†]Note added in the present thesis version: now published as WALKER and OPDYKE (1995).

Coral Reef CaCO$_3$ Production

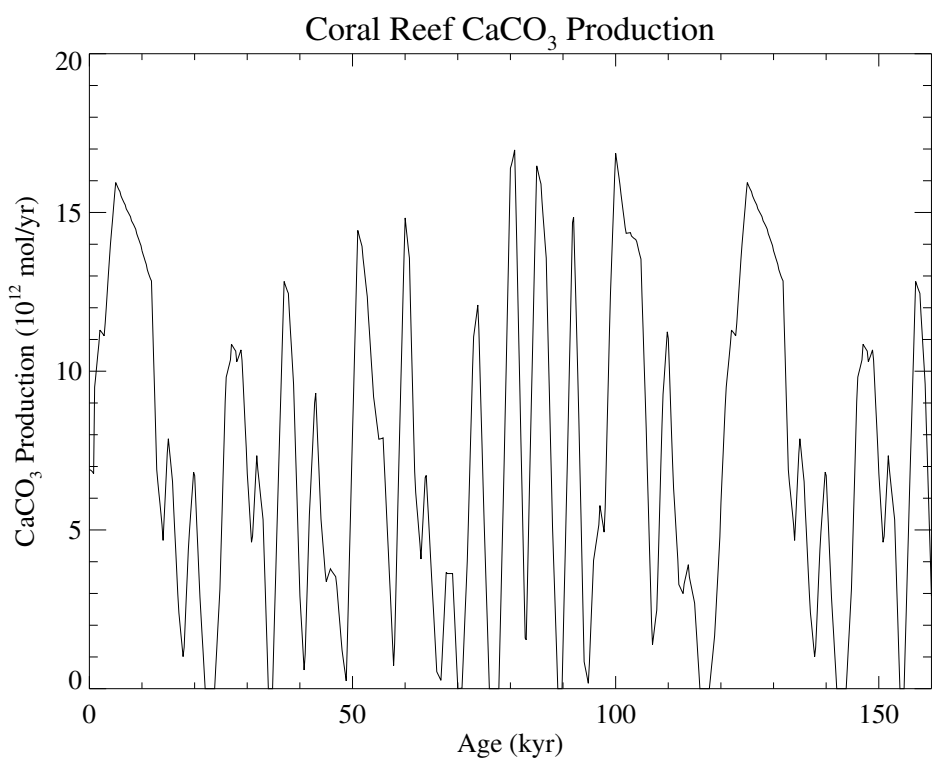

Figure 5.3: Model-generated coral reef growth evolution.

the local carbonate ion concentration given by the model and $[CO_3^{2-}]_{sat}$ is the carbonate ion concentration at saturation calculated from the relationship of BROECKER and TAKAHASHI (1978). We have integrated this law over the top surface of each sedimentary reservoir. The dissolution constant has been fixed at 10^4 mol/m^2/yr, a value consistent with the transition zone thicknesses (CCD−lysocline) of the Atlantic (≈ 800 m) and the Pacific (≈ 600 m).

The variation of the atmospheric CO_2 pressure (p_{CO_2}) in this model run #2 is also presented in figure 5.2. Compared with run #1, the opening of the ocean-atmosphere system, which comprises the addition of river inputs as well as the cycles of coral reef buildup-erosion and of pelagic carbonate sedimentation-dissolution, has increased substantially the amplitude of the CO_2 signal, which is now of $\approx$ 55 ppm. The overall shapes of the two signals also differ slightly. The peak at 5 kyr BP mentioned previously and due to the Atlantic temperature history has also been stengthened, so that the difference between pre-industrial and glacial minimum p_{CO_2} is only ≈ 35 ppm. This value is too small by a factor of more than 2, compared with the corresponding difference in the Vostok record ($\approx$ 80 ppm). This means that, in our model, the Vostok signal cannot be explained by the coral reef hypothesis alone, despite the rather important coral reef fluxes involved. Presumably, the reason is the inclusion of negative feedbacks such as the partial compensation of the coral reef signal by lysocline shifts.

The previous discussion of runs #1 and #2 has overlooked the data on oceanic strontium isotopic composition recently published by DIA et al. (1992). These data are shown as the shaded area (detrended data including error bars) in figure 5.4. As discussed earlier these data support major changes of continental weathering through time, the rate of which has precisely been held constant in run #2. Before a comparison of model results with the observed strontium isotopic signal can be performed, we need to know the isotopic composition of the weathered material, so that the effect of continental weathering on the $^{87}Sr/^{86}Sr$ ratio of seawater can be estimated. Whereas the $Sr/(Ca+Mg)$ ratio of 0.0015 and the $^{87}Sr/^{86}Sr$ ($r_{carb} = 0.708$) for carbonate rocks are quite well-defined (HOLLAND, 1984), this is not the case for silicate (igneous) material. Rivers draining continental silicate rocks show $^{87}Sr/^{86}Sr$ ratios of 0.704–0.706 for young volcanics and of 0.710–0.730 for old shield crustal rocks (HOLLAND, 1984). When using a ratio of 13:17 (WADLEIGH et al., 1985) between the present-day riverine fluxes of Sr coming respectively from silicate (igneous) rocks and from carbonates, we need to assume a typical $^{87}Sr/^{86}Sr$ ratio $r_{sil} = 0.717$ for the mean silicate (igneous) material weathered today to get the observed riverine ratio $r_{riv} = 0.7119$ (WADLEIGH et al., 1985). To get rid of any long-term trend, the strontium isotopic budget equation of the ocean has to be equilibrated by the Sr exchange with oceanic basalts presenting a ratio $r_{bas} = 0.704$, a mean for the interactions with mid-ocean ridge basalts at high temperature (0.703) and with pelagic crustal material at low temperature (0.705).
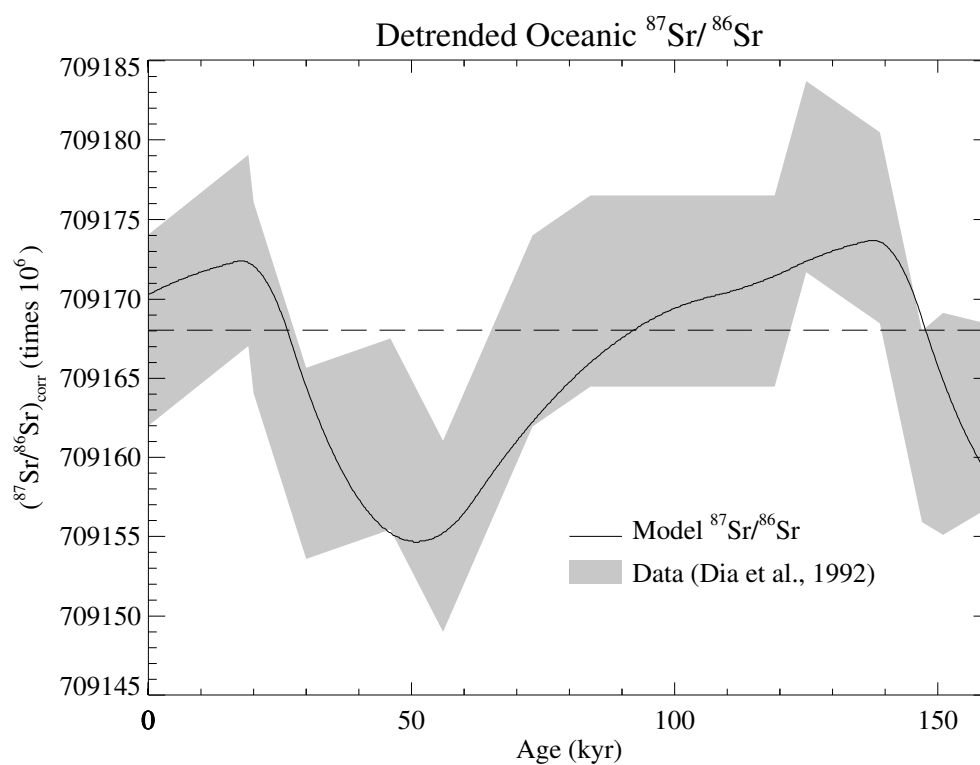
Figure 5.4: Variation (solid line) of the $^{87}Sr/^{86}Sr$ ratio of seawater obtained in runs #2, #3 and #4 when the model silicate weathering follows the isotopic compositions and rates of figures 5.5 and 5.6 respectively. The model signal is compared with the observed range (shaded area).
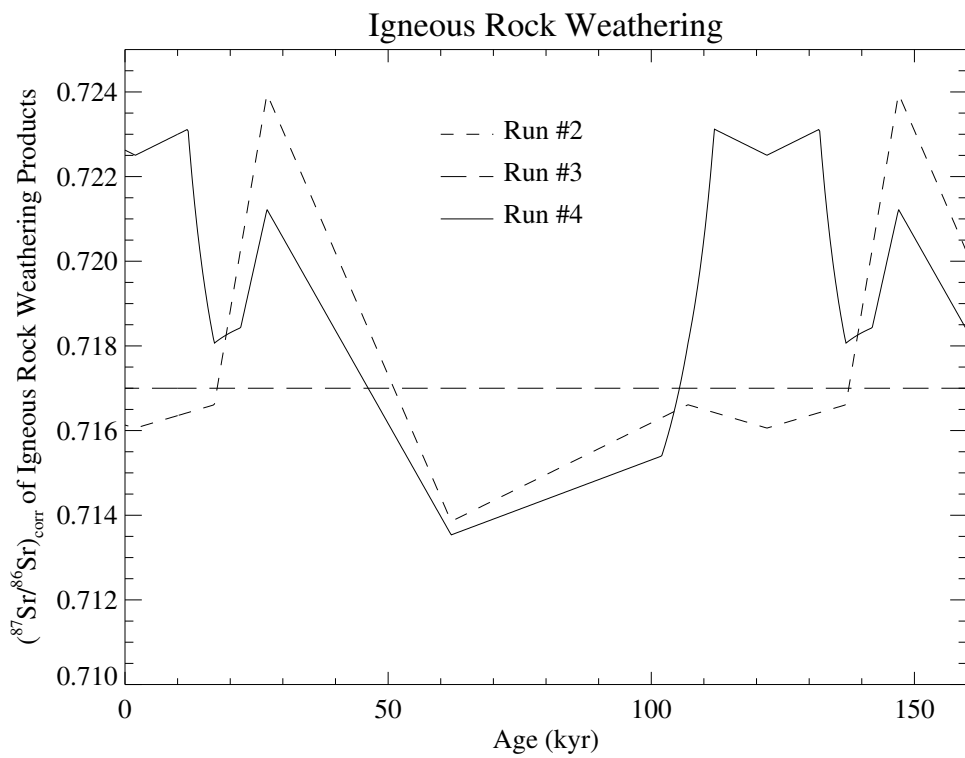
Igneous Rock Weathering

Figure 5.5: Isotopic compositions of the weathering products from continental (igneous) silicate rocks adopted in model runs #2, #3 and #4.
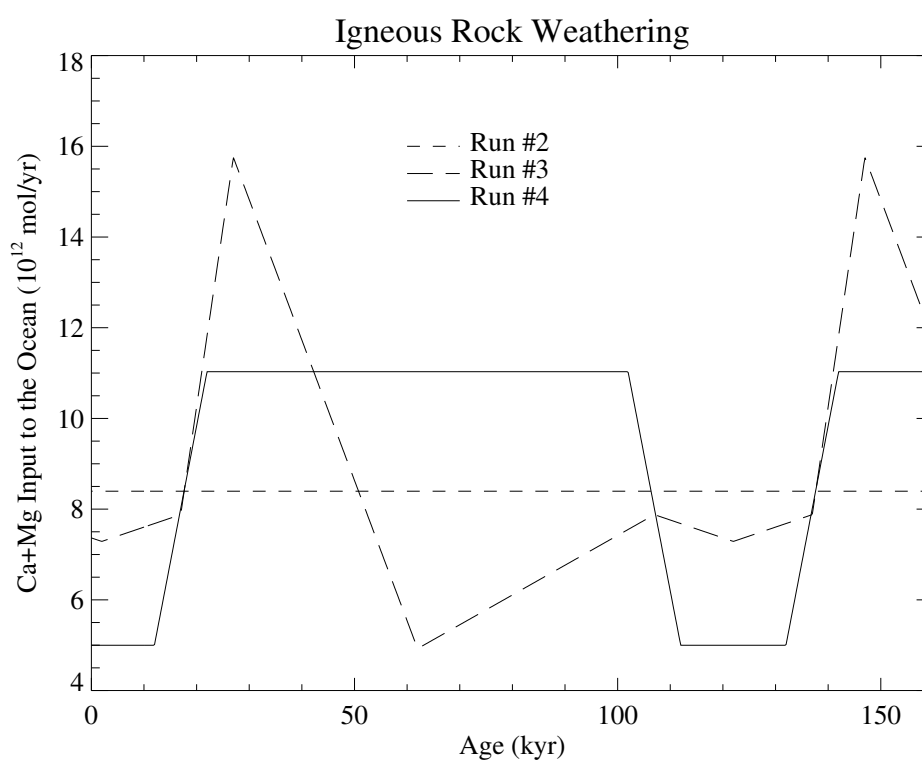
Figure 5.6: Rates of continental weathering of (igneous) silicate rocks adopted in model runs #2, #3 and #4 (in terms of Ca+Mg input to the ocean).

The most probable candidate for the cause of the variation of the strontium isotopic ratio of seawater shown in figure 5.4 is silicate weathering. Indeed it is unlikely that the oceanic basaltic flux or its isotopic composition r_{bas} show changes with a periodicity close to that of the glacial-interglacial cycle. The connection between climatic cycles and continental weathering is much more direct, through changes in runoff or in the rate of mechanical and chemical breakdown of rocks. Of the continental components, carbonate weathering is also a poor candidate, because its isotopic ratio $r_{\text{carb}} \approx 0.708$ is too close to the mean oceanic value $r_{\text{o}} = 0.70916$: the present-day flux should be enhanced by a factor of at least four to explain the observed isotopic shifts. By contrast, silicate rocks have a mean isotopic ratio r_{sil} much more different from that of seawater, with a very wide spectrum of values. Two end-member scenarios thus come to mind: *either* the mean isotopic ratio r_{sil} of the silicate weathering has changed through time (due to a worldwide change in the distribution of precipitation, runoff and erosion) while its global intensity F_{sil} remained constant, *or* its global intensity F_{sil} has varied without any changes of the mean isotopic ratio.

For the first one of these two scenarios — constant global rate of silicate weathering F_{sil}, but varying mean isotopic composition r_{sil} — the variation in r_{sil} necessary to reproduce the observed glacial-interglacial change of the isotopic ratio of seawater is shown by the short-dashed line labeled 'Run #2' in figure 5.6. The amplitude of the signal is relatively important with r_{sil} vary-

ing between 0.714 and 0.724. Such a variation is not precluded, since it falls within the observed range of $^{87}\text{Sr}/^{86}\text{Sr}$ ratios of rivers draining different types of igneous rocks (0.704–0.730), but we might question whether or not it is compatible with the expected change in the distribution over the continents of precipitation, runoff and weathering during glacial cycles. This question is outside the scope of this paper, because it would require an atmospheric general circulation model to be run and coupled with a model of rock weathering taking into account the detailed lithology of the Earth's surface. Of course, because the rate of silicate weathering is held constant in this second scenario, the variation of the atmospheric CO_2 pressure is that of run #2 presented earlier: the shape of the signal is approximately correct, but not the amplitude.

The second of these two scenarios is investigated in run #3, where the (igneous) silicate weathering input F_{sil} has been adjusted empirically until a best fit of the model seawater isotopic composition with the observed data is obtained, for r_{sil} fixed at 0.717. The shape of the F_{sil} signal (figure 5.6, 'Run #3') is the same as that of r_{sil} in the previous scenario (figure 5.5, 'Run #2') because in both experiments the product $(r_{\text{sil}} - r_{\text{o}}) \cdot F_{\text{sil}}$ must be essentially the same. As can be seen in figure 5.4, the isotopic ratio r_{o} of model seawater (solid line) falls within the range of observed values. For this best fit experiment, the input of Ca+Mg (proportional to that of Sr, F_{sil}) from silicate weathering has the glacial-interglacial variation shown by the long-dashed line of figure 5.6. It presents a very marked peak to-

ward high weathering rates centred near 30 kyr BP and a small depression toward low values between 100 and 50 kyr BP. When the carbon cycle model of run #2 — which includes variations of temperature and salinity, as well as the coral reef and pelagic deposition cycles — is forced with this alkalinity input, the atmospheric CO_2 pressure varies as shown by the curve labelled 'Run #3' in figure 5.2. The peak in silicate weathering centred near 30 kyr results in a sharp minimum of atmospheric CO_2 at ≈ 22 kyr BP, when Vostok's signal is also at minimum. The sharp rise in CO_2 during the last deglaciation is also approximately reproduced. However, if we go further back in time, we meet a distinct maximum in model CO_2 near 60–50 kyr with peak values as high as 290 ppm (i.e. characteristic of an interglacial), in sharp conflict with the observations. The reason for this maximum is the small depression in silicate weathering between 100 and 60 kyr. If the observed strontium isotopic ratio of seawater is to be reproduced without changing r_{sil}, this depression and hence the increased CO_2 cannot be avoided, because of its necessity for yielding decreasing r_o values in the period 90–60 kyr BP.

None of the two end-member weathering scenarios adopted to reproduce the seawater strontium isotopic cycle observed by DIA et al. (1992) is entirely successful as far as atmospheric CO_2 is concerned. In each case some features of the Vostok CO_2 are captured, but major disagreements remain. Of course, to keep the model as simple as possible, we ignored some mechanisms (such as oceanic dynamical response or biological fertilization) of po-

tential importance for atmospheric CO_2 variations. Such mechanisms could be invoked to solve the apparent disagreement between observed Sr isotopic ratios and atmospheric CO_2.

It is however possible to reproduce *simultaneously* both observed signals in the same run, provided that F_{sil} and r_{sil} are both allowed to vary. Indeed it is relatively easy to create "something like" the observed atmospheric p_{CO_2}, if it is assumed that the rate of silicate weathering has been higher during glacial times than today. The physical basis for such an assumption is that during glacial times mechanical breakdown of rocks was probably more extensive (because continental areas subject to seasonal freezing and unfreezing can be expected to have been larger) and that enhanced mechanical breakdown should lead to higher rates of chemical weathering in response to larger areas of rock surface available to the weathering reactions. Ge/Si data (FROELICH et al., 1992) further support glacial weathering rates higher than today. In run #4, we have thus adopted a two-step function for the rate of silicate weathering F_{sil} (figure 5.6) through time, with glacial rates higher than interglacial ones by a factor of 2.2 (in the range of values suggested by Ge/Si data). The resulting p_{CO_2} (figure 5.2) resembles the Vostok signal, with a correct amplitude and a good general trend. The history of the mean isotopic composition r_{sil} of weathered silicate rocks which must be assumed to reproduce oceanic strontium isotopic data is shown in figure 5.5. During interglacial times, r_{sil} reaches a value of ≈ 0.723, while during the early phase of the glacial period (100–60 kyr BP) it
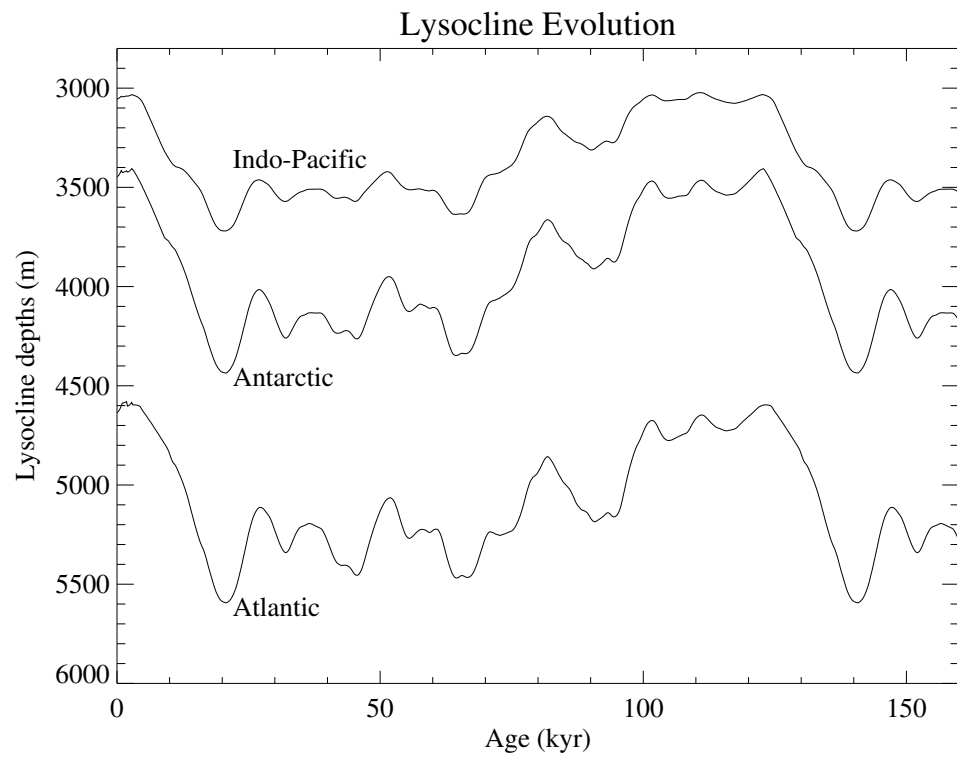
Figure 5.7: Histories of the lysocline depths of the model ocean basins calculated in run #4.

decreases to values between 0.714 and 0.716.

Finally, figure 5.7 shows the history of the Atlantic, Antarctic and Indo-Pacific lysocline depths generated by this model run #4. The model Indo-Pacific lysocline is about 600 meter deeper during glacial times than at present with a major drop occuring near 80 kyr and a rise near 20 kyr BP, in good agreement with the data of FARRELL and PRELL (1989) for the equatorial Pacific. The behaviour of the observed Pacific lysocline has the biggest chance to be of global significance, because of the large size of the basin. The lysoclines of other basins are certainly more affected by possible circulation changes which have been ignored here. Because of the constancy of the oceanic circulation, model Atlantic and Antarctic lysoclines changes are parallel to those of the Indo-Pacific basin.

Conclusions

In this paper we have analysed the contribution of continental rock weathering to the glacial-interglacial cycles of atmospheric CO_2. For this purpose, a 10-box model of the oceanic carbon cycle has been built, in which sedimentary processes have been particularly emphasized. The model ocean has been fed by weathering fluxes. Of these fluxes, specific attention has been given to the weathering of silicate rocks. Indeed cyclic variations in the strontium isotopic ratio of seawater have been observed recently by DIA et al. (1992) at glacial-interglacial time scales. Although large error bars exist on these data, they suggest that continen-

tal weathering rates, and more specifically silicate weathering, have changed markedly throughout glacial-interglacial cycles. These observations are strenghtened by recent data on the Ge/Si ratio of Pleistocene seawater reported by FROELICH et al. (1992). The interpretation of the strontium isotopic signal remains speculative, because the mean isotopic composition of the weathering products may have changed with time, and no simple estimate of its history can be derived. However our model shows that it is important to take weathering into account in studies of the glacial-interglacial oceanic carbon cycle and that the contribution of continental weathering cannot be neglected. It is even possible to construct a scenario in which both the rate of silicate weathering and the isotopic ratio of its products change through time, and for which the model predicts correctly the observed variation of the strontium isotopic ratio of seawater as well as that of the atmospheric CO_2 pressure. The glacial-interglacial change in atmospheric CO_2 in this scenario is due in large part to silicate weathering, with the rest originating from variations in temperature and salinity as well as from coral reef erosion-deposition cycles. The scenario looks *a priori* fully plausible, but would need to be tested with a detailed global model of continental weathering, a model still to be constructed. Anyway it is likely that other oceanic processes not considered here, such as circulation which for simplicity was held constant, are also at work. Future studies should include these topics, but this simplification does not alter the main conclusion reached here that the contribution of silicate

weathering to the glacial-interglacial cycles of atmospheric CO_2 was not negligible.

Acknowledgments

Chapter 6

Ge/Si: Tracer of Glacial-Interglacial Weathering Changes

The results of the previous chapter have shown that seawater $^{87}Sr/^{86}Sr$ did not represent a very restrictive constraint on the history of the consumption of atmospheric CO_2 over glacial-interglacial climate cycles. $^{87}Sr/^{86}Sr$ ratios merely translate the fact that terrestrial silicate rocks are generally older than carbonate rocks. Most of the Sr delivered to the ocean by rivers nevertheless derives from the weathering of carbonates. Furthermore, the fact that $^{87}Sr/^{86}Sr$ ratios in waters draining silicate rocks are so widely spread has turned out to be a major hindrance to its use as an accurate tracer for the evolution of continental silicate weathering. On a global scale, $^{87}Sr/^{86}Sr$ ratios simply do not sufficiently well characterize products originating from silicate weathering.

In a second attempt we therefore use the marine Ge/Si record to reconstruct the glacial-interglacial history of the CO_2 consumption by continental silicate rock weathering. The interpretation of the marine Ge/Si ratio is not biased by interferences from carbonate rock weathering, as it was the case for the $^{87}Sr/^{86}Sr$ ratio, because carbonate rocks do not contain any Ge. But then, the Ge/Si ratio can at most be used to reconstruct the glacial-interglacial evolution of the riverine silica input to the oceans and the interpretation of this input in terms of an equivalent flux of bicarbonate is unfortunately not straightforward because of the incongruent weathering of silicate rock minerals. Furthermore, there remain major unknowns in our present knowledge of the global Ge cycle.

The results of this second study, including a complete discussion of these problems and of their possible impacts, have been published as MUNHOVEN and FRANÇOIS (1996). The text of that paper (corrected for a few minor errors) is reproduced on the next pages.

Glacial-Interglacial Variability of Atmospheric CO$_2$ due to Changing Continental Silicate Rock Weathering: A Model Study

Guy Munhoven and Louis M. François

Laboratoire de Physique Atmosphérique et Planétaire, Institut d'Astrophysique, Université de Liège, Liège, Belgium

Abstract. An 11-box model of the oceanic carbon cycle including sedimentary processes is used to explore the role chemical weathering of continental silicate rocks might play in driving atmospheric CO$_2$ levels on glacial-interglacial time scales. Histories for the consumption of CO$_2$ by silicate rock weathering processes are derived from the marine Ge/Si record. Taking the major uncertainties in the knowledge of the Ge and Si cycles into account, several histories for the evolution of the riverine dissolved silica fluxes are calculated from this record. The investigation of the systematics between riverine dissolved silica and bicarbonate fluxes under different weathering regimes leads us to the tentative conclusion that although there is no correlation between dissolved silica and total bicarbonate concentrations in the major rivers, there may exist a negative correlation between weathering intensity and the ratio of bicarbonate derived from silicate weathering alone to dissolved silica. With this correlation as a working hypothesis, it is possible to interpret the dissolved silica fluxes in terms of equivalent CO$_2$ consumption rates. The calculated histories indicate that glacial rates of CO$_2$ consumption by chemical silicate rock weathering could have been twice, and possibly up to 3.5 times, as high as they are today. When used to force the carbon cycle model, they are responsible for glacial-interglacial pCO$_2$ variations in the atmosphere of typically 50–60 ppm and up to 95–110 ppm. These variations are superimposed to a basic

oscillation of 60 ppm generated by the model, mainly in response to coral reef buildup and erosion processes. The total pCO$_2$ signal has an amplitude of about 80–90 ppm and up to 125–135 ppm. Although these large amplitudes indicate that silicate weathering processes should be taken into account when studying glacial-interglacial changes of CO$_2$ in the atmosphere, it also raises new problems, such as too high CO$_2$ levels during the period from 110–70 kyr B.P., requiring further study.

Introduction

Almost all of the studies dealing with the glacial-interglacial atmospheric CO$_2$ variations have focused on oceanic processes (biological, dynamical, and chemical ones) to find possible mechanisms to explain the evolution well documented by the Vostok ice core record (BARNOLA et al., 1987; JOUZEL et al., 1993). The ocean-atmosphere system was considered to be more or less isolated from the continents, and the CO$_2$ fluxes involved in rock erosional processes were disregarded. It was generally assumed that these fluxes were small and that their potential for changes on glacial-interglacial cycles was too limited to have had a significant impact on atmospheric CO$_2$ levels. KEIR and BERGER (1983) were the first to include an exchange flux with the deep-sea and shelf sediments in their two-box model, paired with a constant riverine supply of Ca^{2+} and HCO$_3^-$. Later, OPDYKE and WALKER (1992b) and WALKER and OPDYKE (1995) used a more complex representation of the sedimentary shell with 15 separate depth intervals in their two-box model when they reanalysed the "coral reef" hypothesis (originally proposed by BERGER (1982)). Like KEIR and BERGER (1983), they forced their model ocean by constant riverine

supplies of dissolved CaCO$_3$. They also let the partitioning between the deep-sea and the shelf depositional areas vary in time to simulate the effects of the geometric changes induced by sea level variations. MUNHOVEN and FRANÇOIS (1994), who also took these geometric variations into account, have, nevertheless, pointed out that the differences between carbonate and silicate rock weathering processes require an uncoupling of the riverine carbon and alkalinity supplies to the ocean, even on the geologically short time scale of the glacial-interglacial cycles of the Pleistocene. Parts of the low atmospheric CO$_2$ levels during the last glacial period can then be explained by an enhanced consumption of CO$_2$ by continental silicate rock weathering processes at that time. Unfortunately, the glacial-interglacial marine ^{87}Sr/^{86}Sr record (DIA et al., 1992) that they used as a proxy for continental weathering turned out to be an analytical artifact (HENDERSON et al., 1994a). MUNHOVEN and FRANÇOIS (1994) had already pointed out that seawater ^{87}Sr/^{86}Sr was not a very restrictive constraint for this weathering history. Continental ^{87}Sr/^{86}Sr ratios simply do not characterize sufficiently well the products originating from silicate weathering. The basic conclusion of MUNHOVEN and FRANÇOIS (1994)

is, nevertheless, supported by the results of SHARP et al. (1995), who have shown that glacierization can tremendously increase net chemical weathering rates. In the glacier-covered catchment that they have studied, the specific yield of total, dissolved weathering products reaches almost 3 times the world average. In terms of specific cation equivalents, chemical denudation rates there are about 70% higher than world average. They report that specific cation yields of up to 2.6 times the world average have been observed on other glacierized catchments. Glacially driven changes of chemical weathering could therefore play a role in the global cycling of carbon because of the involved atmospheric CO_2 drawdown.

Concerns about the plausibility of the mechanism proposed by MUNHOVEN and FRANÇOIS (1994) were expressed by GIBBS and KUMP (1994). They have applied statistical relationships for riverine bicarbonate as a function of runoff (BLUTH and KUMP, 1994) to the "recent" lithological map of BLUTH and KUMP (1991) adapted to the last glacial maximum (LGM) geography. Compared to nowadays, they found only a 20% increase (versus 100% found by MUNHOVEN and FRANÇOIS (1994)) in the global riverine bicarbonate delivery to the oceans at 18 kyr B.P. This increase was primarily due to more extended exposure of carbonates on the continental shelves. However, they admit that their bicarbonate flux-runoff relationships, which are calibrated for the present day cannot be directly applied to LGM conditions if the weathering regime at that time was different from today's. One of the factors

that is likely to undergo important variations between a glacial and an interglacial period is mechanical weathering. Because of more contrasted annual thaw and freeze cycles over larger parts of the Earth surface during a glaciation, enhanced fragmentation of rock material could possibly increase the reactive surface of rock actually subject to chemical weathering. GODDÉRIS and FRANÇOIS (1995) have calculated that, through the action of mechanical breakdown, chemical weathering per unit ground area is presently more than an order of magnitude more efficient in the Himalayan region than elsewhere. This could theoretically counterbalance the reduction of the specific chemical weathering rates arising from a typical temperature decrease of 20 K (GODDÉRIS and FRANÇOIS, 1995).

On the other hand, when repeating GIBBS and KUMP (1994) study for silica, we also observe only a very small increase between the present interglacial and the glacial maximum fluxes. The surplus again stems from the continental shelves (dissolution of interbedded opal in the carbonate sediments (BLUTH and KUMP, 1994)) rather than from the continents. FROELICH et al. (1992) have, however, shown that the rivers transported probably more than twice as much dissolved silica to the oceans at LGM as today, because of a globally decreased weathering intensity. It would now be hard to understand that this doubling of the dissolved silica flux at the LGM did not have any consequences for the atmospheric CO_2 consumption by silicate rock weathering. Disregarding the complexity of silicate mineral degradation pathways and fol-

lowing first-order logic, one could be tempted to admit that a doubling of the dissolved silica yield should go together with a doubling of the CO_2 consumption. Such a priori quantifications are, however, too simplistic, and changing weathering regimes will complicate the problem even further. Unlike carbonate rocks, silicate rocks weather incongruently. The chemical weathering of silicate rock minerals leads to the formation of a variety of secondary minerals (mostly clays) and of dissolved silica. Different minerals lead to different ratios of silica dissolved versus CO_2 consumed. At the global scale, the dissolved phase also carries only a relatively small fraction of the total silicon released. Clay minerals take up the largest part of it. The partitioning between these two phases is related to chemical weathering intensity, defined as the fraction of total Si which gets dissolved from bedrock during weathering (MURNANE and STALLARD, 1990). The marine Ge/Si record can at most be used to reconstruct the history of the dissolved silica fluxes. However, both clays and dissolved silica in the riverine sediment load represent "consumed CO_2." Furthermore, a small part of the dissolved silica in rivers stems from the dissolution of amorphous silica which does not require any CO_2. Estimating the total CO_2 consumption by silicate weathering from the dissolved silica yield alone, if possible at all, requires a careful and thorough look at the global scale silica-bicarbonate systematics in the world rivers. We will show in this paper that it is possible to get a reasonable estimate for the lower bound of this CO_2 consumption from the evolu-

tion of the dissolved silica fluxes to the ocean on glacial-interglacial time scales. If dissolved silica load in the rivers was higher and weathering intensity lower at LGM than at present (FROELICH et al., 1992), there was also a relatively more important fraction of Si weathered from bedrock put into the solid phase. We can furthermore expect a reduced formation of the typical weathering products of high-intensity weathering regimes (such as kaolinite, Al-, and Fe-sesquioxides). We will present clues indicating that this should go together with more CO_2 being consumed for the same amount of silica dissolved. We propose that on the global mean, the ratio between SiO_2 dissolved and CO_2 consumed during silicate weathering alone is at present probably close to its minimum value over a glacial-interglacial cycle. This hypothesis enables us to reconstruct the minimum amount of CO_2 consumed by silicate rock weathering processes from the history of riverine dissolved silica fluxes.

Carbon Cycling by Rock Weathering

Atmospheric CO_2 levels are driven by the dissolved inorganic carbon ($DIC = [CO_2] + [HCO_3^-] + [CO_3^=]$) and the total alkalinity ($TA \simeq [HCO_3^-] + 2 \times [CO_3^=] + [B(OH)_4^-]$) in the surface ocean. Figure 6.1 gives a schematic overview of the sources and sinks of these two quantities. On 100-kyr and longer time scales, their evolution is determined by the interaction of the ocean (and the atmosphere) with the lithospheric crust. In this study, we will focus on the inorganic exchanges of carbon between these two
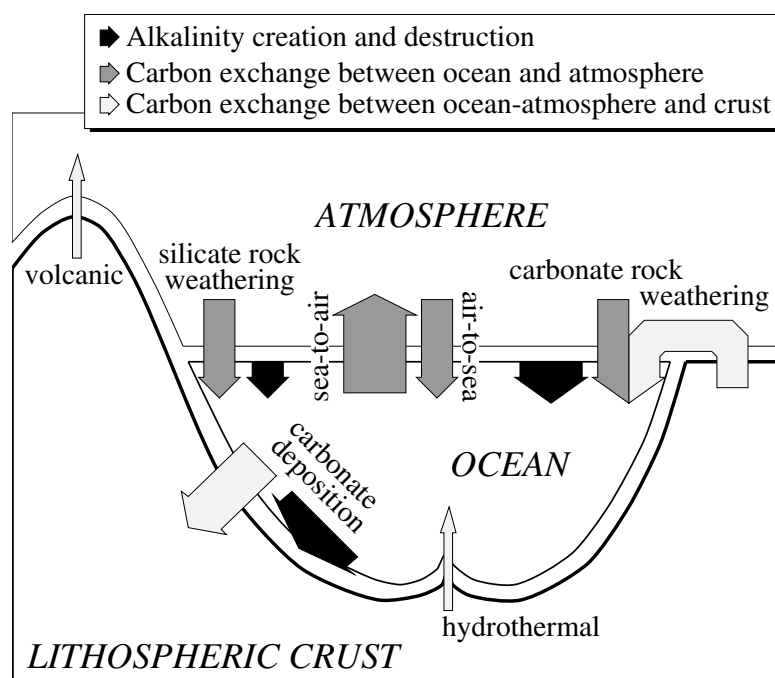
Figure 6.1: Schematic view of the global carbon cycle on geological time scales.

reservoirs. Rigorously speaking, organic carbon exchanges may not be neglected: although organic matter transferred to the deep ocean is almost entirely recycled ($\sim 99\%$), the deposition of organic matter on the continental shelf areas are by no means negligible. We will assume that this deposition is constantly balanced by the riverine input of "elemental" carbon or kerogen from continental shale erosion, and we will thus disregard organic exchanges. The only sink of carbon and alkalinity of the ocean-atmosphere system is then the deposition of biogenic $CaCO_3$ (including coral reef production). The source originates carbonate and silicate rock erosion.

No significant accumulation of CO_2 in the atmosphere has been observed over the last several hundred thousands of years, as documented by different re-constructions of atmospheric and surface ocean pCO_2 (BARNOLA et al., 1987; JOUZEL et al., 1993; WESTERNHAUSEN et al., 1994). The oceanic carbon and alkalinity budgets must hence have been close to equilibrium on the 100-kyr scale, let us say for the last 0.5 Myr at least. It has been demonstrated in studies of the Phanerozoic carbon cycle (see, e.g., WALKER et al., 1981; BERNER et al., 1983; BERNER, 1990, 1991; FRANÇOIS and WALKER, 1992; FRANÇOIS et al., 1993) that the simultaneous balance of these two budgets requires an additional carbon flux from the crust to the ocean-atmosphere system. This flux has to supply half of the CO_2 consumed by silicate weathering. It is represented by the outgassing of CO_2 through volcanic processes (hydrothermal and metamorphic). As MUNHOVEN and FRANÇOIS

(1994) have pointed out, this balancing only concerns the long-term mean. On shorter time scales (from kiloyears to tens of kiloyears), it is perfectly possible that the CO_2 supply by volcanoes temporarily covers more than half of the consumption by silicate rock weathering or that it becomes less. On the time span of interest for this study, the CO_2 consumption by silicate rock weathering is likely to exhibit a much higher variability than volcanic activity. The former is in fact mostly climate-controlled, whereas the latter is more dependent on global tectonic activity. Despite the very high interannual variability of volcanic activity, its 100- to 1000-year mean can be taken as constant over the time span of interest for us. Ice core proxies of volcanic activity (e.g. the abundance of volcanic ashes) show only very little variability over the last glacial-interglacial cycle. It is therefore reasonable to assume that the volcanic CO_2 release remained constant over the last few 100 kyr. As long as the CO_2 consumption by chemical silicate rock weathering processes is higher than its long-term average, so is the alkalinity flux which comes with it. To counteract the resulting accumulation of alkalinity, the carbonate chemistry of the ocean will work to increase the deposition of $CaCO_3$ on the sea-floor. Because of the resulting loss of carbon, a complete balancing is, however, not possible. The system has thus to run with an alkalinity balance in excess and a carbon balance in deficit. As a consequence, atmospheric pCO_2 must decrease. The reverse happens while the CO_2 demand by silicate rock weathering is lower than long-term mean.

For carbonate rock weathering, the analogous mechanism cannot work the same way. In this case, it is always possible to balance the alkalinity and the carbon budgets simultaneously. Some response will nevertheless come from the changing carbonate saturation depth. While it moves upward and downward to follow the changing river inputs, it modifies the deep-sea *TA–DIC* difference. As a consequence, the global distributions of *TA* and *DIC* change and hence atmospheric pCO_2. Sensitivity tests (not reported here) performed with our model indicate that the pCO_2 variations resulting from carbonate weathering are only about half as large as those from silicate weathering, for a similar production of river bicarbonate.

Oceanic Silicon and Germanium Cycles

Present-Day State

The geochemistry of Ge is dominated by its ability to replace Si in the different geochemical processes. The Ge cycle can thus simply be determined from the Ge/Si characteristics of the different sources, sinks, and reservoirs in the Si cycle.

The present-day oceans contain about 140×10^{15} mol of dissolved silica (HOLLAND, 1978; BROECKER and PENG, 1982). They are quite homogeneous with respect to Ge/Si, with $(Ge/Si)_{seawater} = 0.735 \times 10^{-6}$ mol/mol for water masses not too close to hydrothermal vents (FROELICH et al., 1989). Dissolved Si is removed from the oceans virtually only by accumulation of biogenic silica on the sea-

floor (mostly opal in siliceous remains of diatoms). The net accumulation rates can be estimated to be $7.5 \pm 2.3 \times 10^{12}$ mol Si/yr (DeMaster, 1981; Lisitzin, 1985; Tréguer et al., 1995). In order to reconstruct the history of the marine Ge/Si ratio from the record in the siliceous remains of diatoms, it is essential to know how diatoms take up Ge and to what extent this record needs to be corrected for fractionation effects. Froelich et al. (1992) have shown that these effects are probably negligible, the discrimination factor $K_D = $ (Ge/Si)$_{\mathrm{opal}}$/(Ge/Si)$_{\mathrm{ocean}}$ being 1.0 ± 0.2. Previous studies based upon a two-box representation of the oceanic Ge and Si cycles had favored $K_D = 0.5 \pm 0.2$ (Froelich et al., 1989; Murnane and Stallard, 1988). This small K_D is possibly just an artifact of the two-reservoir structure of the model and its inherent assumptions and simplifications. More complex models do not support such a large discrimination (Froelich et al., 1992; Froelich, 1995). In this paper, we generally take $K_D = 1.0$, except for one sensitivity experiment where we use $K_D = 0.8$. We are aware that this problem which is fundamental for the interpretation of the marine Ge/Si signal still has to be definitely settled.

The inputs of dissolved Si to the oceans divide into continental and submarine ones. The largest contribution comes in by rivers. For this work, we have retained Meybeck's (1979) estimate of 6.47×10^{12} mol Si/yr. It is the only one for which the corresponding bicarbonate flux was available. It is still in good agreement with the pre-industrial value of $6.2 \pm 0.6 \times 10^{12}$ mol Si/yr derived from Tréguer et al.'s (1995) recent

reevaluation. As extensively discussed by Froelich et al. (1992), weathering intensity and silica partitioning into clays control the riverine dissolved silica concentrations and Ge/Si ratios. High, dissolved silica concentrations are observed under extreme weathering-limited conditions, where weathering intensity is low. Low concentrations are common under extreme transport-limited conditions, where weathering intensity is highest. The opposite holds for the Ge/Si signatures: weathering-limited catchments exhibit the lowest Ge/Si ratios, whereas streams from transport-limited regions have the highest ratios. The secondary aluminosilicates (mostly clays) formed during chemical weathering find themselves enriched in Ge relative to Si. As a consequence, rivers generally carry dissolved Ge/Si ratios considerably lower than the rocks they drain. Crustal average rock displays Ge/Si ratios of $1.4 \pm 0.1 \times 10^{-6}$ mol/mol (Mortlock and Froelich, 1987). Ninety percent of today's uncontaminated rivers have Ge/Si ratios between 0.2×10^{-6} mol/mol and 1.2×10^{-6} mol/mol, the global discharge-weighted mean being close to 0.6×10^{-6} mol/mol.

Tréguer et al. (1995) list an additional continental source. They suggest that $0.5 \pm 0.5 \times 10^{12}$ mol Si/yr get dissolved out of the aeolian dusts that reach the sea surface. Because the magnitude of this source is smaller than the uncertainty on the riverine flux and since we can only speculate on its Ge/Si characteristics, we will consider this as a kind of deferred chemical weathering. The composition of the aeolian dusts (many clays) makes us expect, however,

that this source has a Ge/Si ratio above the ocean average.

The submarine contribution stems from the sea-floor weathering of basalt at hydrothermal sites and from low-temperature leaching of the basaltic crust. WOLERY and SLEEP (1988) estimated that hydrothermal emanations deliver about 0.9×10^{12} mol Si/yr to the oceans. More recently, MORTLOCK et al. (1993) have determined a typical Ge/Si ratio of 10×10^{-6} mol/mol for this source. Using this ratio in a simultaneous balance of the oceanic Ge and Si budgets, they derive a much smaller hydrothermal flux of $0.25 \pm 0.15 \times 10^{12}$ mol Si/yr. Their study does, however, not take any separate low-temperature alteration source into account. The most recent estimates for this last source are in the range of $0.4 \pm 0.3 \times 10^{12}$ mol Si/yr (WOLLAST and MACKENZIE, 1983; WOLERY and SLEEP, 1988; TRÉGUER et al., 1995). Nothing is known about its Ge/Si signature. Fortunately, this will not affect our results, unless it is orders of magnitude different from that of the hydrothermal one.

Glacial-Interglacial Ge/Si Variations

MORTLOCK et al. (1991) and FROELICH et al. (1992) have presented a 140-kyr and a 600-kyr record for the history of marine Ge/Si. Both come from the Southern Ocean and exhibit pronounced glacial-interglacial oscillations, with low ratios during glacial and high ones during interglacial times. FROELICH et al. (1992) have shown that the most plausible interpretation of these records is that

they reflect global ocean changes due to variations of the riverine dissolved silica supply. Variations of the riverine input of dissolved silica on glacial-interglacial time scales are not unlikely because it is the one which is most directly linked to climate. Because rivers represent the largest source of dissolved silica and at the same time the only one with Ge/Si ratios lower than the present-day ocean average, they must play a major role. Contributions from the other sources can of course not be completely excluded, but they must be much smaller than the riverine one. FROELICH et al. (1992) have also made a simple estimation of the magnitude of the changes required to reproduce the 600-kyr record. This estimation was made for an ocean at instantaneous steady state (where inputs and outputs balance at every moment), submitted to a rectangular input of dissolved riverine Si. Biogenic fractionation effects were neglected, and opal accumulation on the sea-floor was supposed to follow a residence-time approach.

In this work, we focus on the 140-kyr record (represented in figure 6.2). We use it to reconstruct histories for the riverine silica supply to the oceans. Using a fully transient approach (without any steady state assumptions), we reconstruct histories for the riverine silica supply to the oceans. As previously mentioned, the correct interpretation of this record requires us to know whether diatoms fractionate Ge during their shell buildup or not. If they fractionate, productivity changes must be considered. We therefore adopt $K_D = 0.8$ for one set of experiments. We furthermore include a gradual variation of the silica ex-
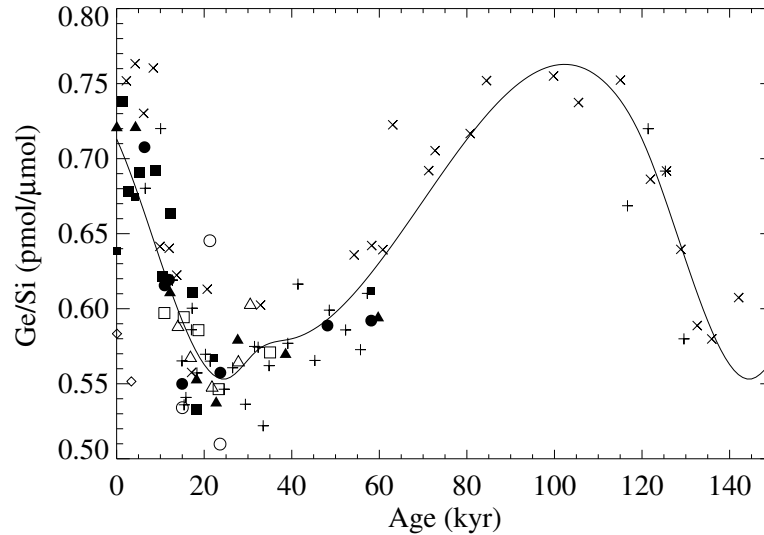
Figure 6.2: Marine Ge/Si history (FROELICH et al., 1992). The different symbols denote the cores used to compile this record (see FROELICH et al. (1992) for details). Also represented is the least squares spline used to parameterize this evolution.

traction efficiency from 95% at present day to 50% at LGM, even lower than the 65% given by FROELICH et al. (1989). These important changes are required to produce any substantial effect. According to LISITZIN (1985), the overall opal accumulation rate has remained fairly constant for the past several hundred thousand years. There have only been some temporary geographical redistributions, associated with the glacial cycles.

Dissolved Silica and Bicarbonate in the World Rivers

To derive a history for the CO_2 consumption by silicate rock weathering from the evolution of the riverine dissolved silica flux, the most difficult and critical step is to determine the contribution of silicate weathering processes to the global riverine bicarbonate load from a reconstructed silica evolution. There is no correlation between total bicarbonate and dissolved silica concentrations in the world rivers. Lithological heterogeneities, different weathering regimes and types, and most importantly, carbonate dissolution inevitably mask any potential characteristics of silicate dissolution in terms of bicarbonate yield. It is hence not straightforward to characterize the contribution from silicate weathering to the total bicarbonate load in the world rivers as a function of climatic zones and weathering regimes.

The riverine bicarbonate pool results from the mixture of the atmospheric and the carbonate sources:

$[HCO_3^-]_{tot} = [HCO_3^-]_{atm} + [HCO_3^-]_{carb}$. The atmospheric contribution can be divided into two parts, one equaling the contribution from carbonate rocks and one having gone through silicate rock weathering: $[HCO_3^-]_{atm} = [HCO_3^-]_{sili} + [HCO_3^-]_{carb}$. Hence $[HCO_3^-]_{sili}/[HCO_3^-]_{tot} = 2\,[HCO_3^-]_{atm}/[HCO_3^-]_{tot} - 1$.

In order to interpret riverine dissolved silica fluxes in terms of CO_2 consumption, we need to know how $[HCO_3^-]_{sili}$ and $[H_4SiO_4]$ vary together, under different weathering conditions. In the geochemical and mineralogical characterization of hydrolitic weathering processes of CHAMLEY (1989), it appears that cation removal, which is the acid-consuming step of the weathering process, is most important during early stages of silicate dissolution. If carbonic acid is supposed to be the dominant acid agent, CO_2 consumption must then also be highest during these stages. At the same time, the leaching of silicon is low. It gets more important as hydrolysis intensity progresses. Base cations (Na, K, Ca, and Mg) get removed before silicon and the final stages where silicon removal completes do not require any additional CO_2. The lowest $[HCO_3^-]_{sili}/[H_4SiO_4]$ ratios can then be expected under the most intense weathering conditions, where the dissolution of the parent rock is most complete and the fraction of bedrock Si dissolved into the draining waters is most important.

MEYBECK (1987) estimates that 67% of the present-day riverine bicarbonate load stems from the atmosphere. We infer from this that 34% has gone through silicate weathering. According to BERNER and BERNER (1987), $HCO_{3(sili)}^-$ represents 38% of the total weathering derived bicarbonate in world average river water. Accordingly, we take $[HCO_3^-]_{sili}/[HCO_3^-]_{tot} = 0.36 \pm 0.02$. With average concentrations of 846 $\mu mol/L$ for $[HCO_3^-]_{tot}$ and of 173 $\mu mol/L$ for dissolved silica (MEYBECK, 1979), we find that $[HCO_3^-]_{sili}/[H_4SiO_4] = 1.76 \pm 0.10$ mol/mol. Part of the dissolved silica in rivers may, however, come from the (congruent) dissolution of amorphous silica, which does not consume any CO_2: $[H_4SiO_4] = [H_4SiO_4]_{sili} + [H_4SiO_4]_{amor}$. Global estimates for $[H_4SiO_4]_{amor}/[H_4SiO_4]$ are highly variable. Both HOLLAND (1978) and BERNER and BERNER (1987) neglect this source. BLUTH and KUMP (1994) observe high proportions of dissolved silica in rivers draining carbonated catchments. They ascribe this to the dissolution of biogenic silica disseminated or interbedded in the carbonate rocks. From BLUTH and KUMP's (1994) relationships (integrated for runoff values from 10 to 3000 mm/yr), we can calculate an average $[HCO_3^-]/[H_4SiO_4]$ ratio of about 16 mol/mol for carbonate drainages. Amorphous silica probably also dissolves from shales, but so do carbonates. If we assume that the association between amorphous silica and carbonates is general and that the influence of silicate rocks is negligible on carbonated terrains, we reach a world average $[H_4SiO_4]_{amor}/[H_4SiO_4]$ close to 0.20. Accordingly, $[HCO_3^-]_{sili}/[H_4SiO_4]_{sili}$ would be of the order of 2.18 ± 0.12 mol/mol. Using the same methodology with

the data set of MEYBECK (1986), we find a typical bicarbonate to silica ratio of 60–70 mol/mol for carbonated drainages. With this value, $[H_4SiO_4]_{amor}/[H_4SiO_4]$ would fall close to 0.05. For comparison, MEYBECK (1987) estimates the contribution from amorphous silica dissolution at 7.5% of the total. With this latter figure, we get a global $[HCO_3^-]_{sili}/[H_4SiO_4]_{sili}$ ratio of 1.90 ± 0.11 mol/mol. This is in excellent agreement with the ratios derived from the bicarbonate-runoff and silica-runoff regressions of BLUTH and KUMP (1994) for basaltic ($[HCO_3^-]/[H_4SiO_4] = 1.86$ mol/mol) and for granitic ($[HCO_3^-]/[H_4SiO_4] = 1.93$ mol/mol) catchments, averaged over a runoff ranging from 10 to 3000 mm/yr. In this study, we do not consider any correction for amorphous silica, neither in histories of riverine silica fluxes that we calculate nor in the conversion factors used to calculate the equivalent consumption rates of atmospheric CO_2. This means that we assume that the relative contribution from amorphous silica dissolution to the total riverine dissolved silica is constant in time.

At drainage basin level, only a very few studies on the partitioning of bicarbonate between the atmospheric and the carbonate sources have been published. For the Amazon, the $[HCO_3^-]_{atm}/[HCO_3^-]_{tot}$ ratio has been estimated at 0.705 (STALLARD, 1980) and 0.674 (PROBST et al., 1994). Using the corresponding data, we arrive at $[HCO_3^-]_{sili}/[H_4SiO_4]$ ratios of 1.10 mol/mol (STALLARD and EDMOND, 1987) and 1.04 mol/mol (PROBST, 1992). For the Congo

(Zaïre), PROBST et al. (1994) find that $[HCO_3^-]_{atm}/[HCO_3^-]_{tot} = 0.747$. The corresponding $[HCO_3^-]_{sili}/[H_4SiO_4]$ ratio is 0.55 mol/mol (data from PROBST et al. (1992)).

In PEDRO's (1968) maps of the global distribution of the different weathering types, the regions where weathering is most intense (the allitization and the monosialitization or kaolinization zones) are clearly restricted to the tropics. The Congo and the Amazon are the dominating rivers of that climatic belt. In the morphoclimatic classification of dissolved matter transport by rivers of MEYBECK (1979), the Amazon drainage basin is located in the very humid tropical zone. Most of it is of subtype "plain," but it includes contributions from regions of subtype "mountaineous." The Congo basin is almost completely located in the humid tropics. For a first estimation, we take the above ratios as typical for the respective zones. According to MEYBECK (1979), 10.2% of total dissolved silica in the world rivers comes from the humid tropics and 55.2% comes from the very humid tropics, plain and mountaineous subtypes altogether. This partitioning leads to an average $[HCO_3^-]_{sili}/[H_4SiO_4]$ ratio of about 1.0 mol/mol for these two zones. To reach a global average of 1.76 mol/mol, a typical ratio of 3.2 mol/mol is then required for the rest of world, which, however, still includes a small tropical part. Because of these markedly different ratios for the tropical zone, which covers the high weathering intensity part of the world, and for the rest of the world, the $[HCO_3^-]_{sili}/[H_4SiO_4]$ ratio might turn out to be a valu-

able indicator of weathering intensity. Rivers draining regions of low weathering intensity would be characterized by high $[HCO_3^-]_{sili}/[H_4SiO_4]$ ratios and vice versa. Qualitative support for this idea comes from the work of AMIOTTE SUCHET (1995), who has built a geochemical weathering model to calculate the basin by basin partitioning between the atmospheric and the carbonate rock sources for riverine bicarbonate. Results from this model can be used to determine $[HCO_3^-]_{sili}/[H_4SiO_4]$ ratios for a few rivers where sufficiently reliable data are available. For these, it seems that when $[HCO_3^-]_{sili}/[H_4SiO_4]$ increases, there is first a population shift from tropical to temperate (and boreal) rivers and later to those draining semiarid and arid regions. This latter shift is, however, already more tentative. Below our average value of 1.76 mol/mol, we find only tropical rivers. The average ratio for the tropical rivers that can be derived from this model is in excellent agreement with our typical value of 1.0 mol/mol. Unfortunately, for the moment, this model does not help to get a more representative $[HCO_3^-]_{sili}/[H_4SiO_4]$ ratio for temperate and boreal rivers than the one calculated above. Critical data are missing for almost all of the important boreal and for many of the large temperate rivers. The remaining ones do not provide a sufficiently representative sample.

If our simple two-pole model linking weathering intensity and $[HCO_3^-]_{sili}/[H_4SiO_4]$ ratios in river waters is correct, the world average $[HCO_3^-]_{sili}/[H_4SiO_4]$ increases when weathering intensity globally decreases, in other words, if the relative contribution from the regions with high weathering intensity (where weathering to kaolinite and further to Fe- and Al-sequioxides is dominant) lessens. Unfortunately, there are no reconstructions of the distribution either of weathering or of continental climatic zones at LGM available that are directly based upon data. The best information on the climatic zones can probably be obtained from reconstructions of the vegetation distribution at LGM (ADAMS et al., 1990; VAN CAMPO et al., 1993). These reconstructions indicate a much smaller extent of the zones covered by vegetation types characteristic of the tropical climate conditions at LGM than today. It is therefore likely that the surface of tropical climate zone was much reduced compared to nowadays. Accordingly, intense weathering areas were probably also less wide, indicating a potential weakening of the low-$[HCO_3^-]_{sili}/[H_4SiO_4]$ pole. Following SHARP et al.'s (1995) findings, we should furthermore expect a more important glacially driven chemical weathering. The environmental parameters characterizing the weathering regime in a glacier-covered terrain (SHARP et al., 1995) are typically those of a weathering-limited one as described by FROELICH et al. (1992). The weakening of the low-$[HCO_3^-]_{sili}/[H_4SiO_4]$ pole is hence likely to go together with a strengthening of the high-$[HCO_3^-]_{sili}/[H_4SiO_4]$ pole. Average glacial rivers were probably closer to the high-$[HCO_3^-]_{sili}/[H_4SiO_4]$ pole of the temperate and cool regions than they are in the present interglacial. The glacierization effect has certainly not completely decayed since the last

deglaciation. We, nevertheless, think that it has rarely been smaller during the last glacial-interglacial cycle than it is now. The present-day value of 1.76 ± 0.10 mol/mol should therefore be close to the minimum of a glacial-interglacial cycle. More reliable climate reconstructions as well as a better understanding of the climate-weathering intensity relationship are required to confirm (or reject) this conclusion, which is very important for the rest of this work. Because of the remaining uncertainties, we use a constant $[\mathrm{HCO_3^-}]_{\mathrm{sili}}/[\mathrm{H_4SiO_4}]$ ratio of 1.76 mol/mol to convert the riverine silica fluxes derived from the evolution of the marine Ge/Si ratio into the corresponding amounts of atmospheric CO_2 consumed by the responsible silicate weathering processes. If the actual ratio was higher than the adopted 1.76 mol/mol during times of low weathering intensity, we are likely to underestimate the consumption of atmospheric CO_2 by silicate rock weathering over the whole glacial-interglacial cycle. This approach can hence be regarded as rather conservative, and it does not artificially amplify the efficiency of the mechanism.

Model Description

Reconstruction of the Evolution of Riverine Dissolved Silica Supply

The budget for the ocean's dissolved silica pool can be written as

$$\frac{dSi_{\mathrm{oc}}}{dt} = F_{\mathrm{riv}} + F_{\mathrm{hyd}} - F_{\mathrm{opal}} \qquad (6.1)$$

where Si_{oc} is the dissolved silica content (in moles) and F_{riv}, F_{hyd}, and F_{opal} are the riverine and the hydrothermal silica fluxes and the opaline silica accumulation rates (in moles/year), respectively. With $r = \mathrm{Ge/Si}$ (r in moles/mole), the germanium budget becomes

$$\frac{dr_{\mathrm{oc}}Si_{\mathrm{oc}}}{dt} = r_{\mathrm{riv}}F_{\mathrm{riv}} + r_{\mathrm{hyd}}F_{\mathrm{hyd}} - r_{\mathrm{opal}}F_{\mathrm{opal}} \qquad (6.2)$$

We also take advantage of the weathering intensity relationship between r_{riv} and $[\mathrm{Si}]_{\mathrm{riv}}$, parameterized as $r_{\mathrm{riv}} = r_{\mathrm{riv}}^0 + g/[\mathrm{Si}]_{\mathrm{riv}}$, where $r_{\mathrm{riv}}^0 = 0.33 \times 10^{-6}$ mol/mol and $g = 38 \times 10^{-12}$ mol (FROELICH et al., 1992). This relationship has only a limited influence on the histories constructed here. Its use, instead of a global mean value, for instance, has a dampening effect on the amplitude of the calculated changes for the dissolved silica flux because of the negative correlation between r_{riv} and $[\mathrm{Si}]_{\mathrm{riv}}$ it introduces. While increasing the magnitude of this flux in order to get a more important supply of Ge-depleted dissolved matter, the induced parallel decrease of the Ge/Si ratio acts as an moderating mechanism. The amplitude of the required flux magnitude variations is therefore smaller than if this relationship were not taken into account.

Noting that $F_{\mathrm{riv}} = [\mathrm{Si}]_{\mathrm{riv}}W_{\mathrm{riv}}$, where W_{riv} is the water discharge, (6.2) can be rewritten as

$$\frac{dr_{\mathrm{oc}}Si_{\mathrm{oc}}}{dt} = r_{\mathrm{riv}}^0 F_{\mathrm{riv}} + gW_{\mathrm{riv}} + r_{\mathrm{hyd}}F_{\mathrm{hyd}} - r_{\mathrm{opal}}F_{\mathrm{opal}} \qquad (6.3)$$

If we eliminate F_{riv} between (6.1) and

(6.3) and take into account that

$$\frac{dr_{\mathrm{oc}}Si_{\mathrm{oc}}}{dt} = r_{\mathrm{oc}}\frac{dSi_{\mathrm{oc}}}{dt} + \frac{dr_{\mathrm{oc}}}{dt}Si_{\mathrm{oc}} \quad (6.4)$$

we obtain the following equation describing the evolution of $Si_{\mathrm{oc}}(t)$:

$$\begin{aligned}
\frac{dSi_{\mathrm{oc}}}{dt} =\ & \frac{gW_{\mathrm{riv}} + (r_{\mathrm{hyd}} - r_{\mathrm{riv}}^0)F_{\mathrm{hyd}}}{r_{\mathrm{oc}} - r_{\mathrm{riv}}^0} \\
& - \frac{r_{\mathrm{opal}} - r_{\mathrm{riv}}^0}{r_{\mathrm{oc}} - r_{\mathrm{riv}}^0}F_{\mathrm{opal}} \\
& - \frac{dr_{\mathrm{oc}}}{dt}\left(\frac{Si_{\mathrm{oc}}}{r_{\mathrm{oc}} - r_{\mathrm{riv}}^0}\right)
\end{aligned}$$

$$(6.5)$$

where $r_{\mathrm{opal}} = r_{\mathrm{oc}}$ if diatoms do not discriminate Ge against Si during their shell buildup. We solve the differential equation (6.5) to get the evolution of Si_{oc} under different working hypotheses outlined below. F_{riv} can then be obtained from (6.1). The evolution of $r_{\mathrm{oc}}(t)$ is parameterized by a cubic spline fitted to the marine Ge/Si record (see figure 6.2) through a least squares procedure. This cubic spline is also used to calculate the time derivative of r_{oc}. As initial values, we use $Si_{\mathrm{oc}} = 140 \times 10^{15}$ mol (HOLLAND, 1978; BROECKER and PENG, 1982) and $F_{\mathrm{riv}} = 6.47 \times 10^{12}$ mol Si/yr (MEYBECK, 1979). We assume that neither Si nor Ge accumulate in the oceans over one glacial-interglacial oscillation. This means the time derivatives of Si_{oc} and of $r_{\mathrm{oc}}Si_{\mathrm{oc}}$ have a zero average over one oscillation.

F_{hyd}, which is the poorest known of all, is then used to balance the budgets. Therefore we fix r_{hyd} at a typical value of 10×10^{-6} mol/mol (MORTLOCK et al., 1993), and for each case, we determine the appropriate F_{hyd} (constant in time) to meet the above constraints. Different sensitivity tests have shown that the exact value adopted for r_{hyd} (alternative values adopted were 5×10^{-6} mol/mol and 20×10^{-6} mol/mol) does not play any significant role for the evolution of the so-calculated evolution of F_{riv}[†].

Because of the lack of knowledge concerning the evolution of the global opal accumulation rate, we take two laws for F_{opal} into consideration: a constant accumulation rate model, in agreement with LISITZIN's (1985) results and also a classical residence-time oriented or first-order model, where $F_{\mathrm{opal}} = Si_{\mathrm{oc}}/\tau$, with $\tau = 20,000$ years. We also analyse the sensitivity for changes in W_{riv} using a constant discharge at the present-day value of 37,400 km³/yr (MEYBECK, 1979) and a discharge reduced (or increased) by 20% at LGM.

Oceanic Carbon Cycle Model

Model Geometry, Water Circulation, and Temperature Evolution. The oceanic carbon cycle model used for this study is an improved version of the one described by MUNHOVEN and FRANÇOIS (1994). This is a low-resolution box model with a single atmo-

---

[†]Note added in the thesis manuscript : Equation (6.5) is of the type $dR/dt = f(t)\,R + g(t)$, where the coefficients f and g are periodic, of the same period. The solution $R(t)$ of such an equation can always be written as $R(t) = G(t) + H(t)E(t)$, where both G and H are periodic, and where E is either an exponential or a linear function. The proof of this general mathematical result, which we have established for this study, is given in appendix B.2. This result can be used to calculate F_{hyd}, and the correct F_{opal}-F_{hyd} combination in case F_{opal} is taken as a constant.
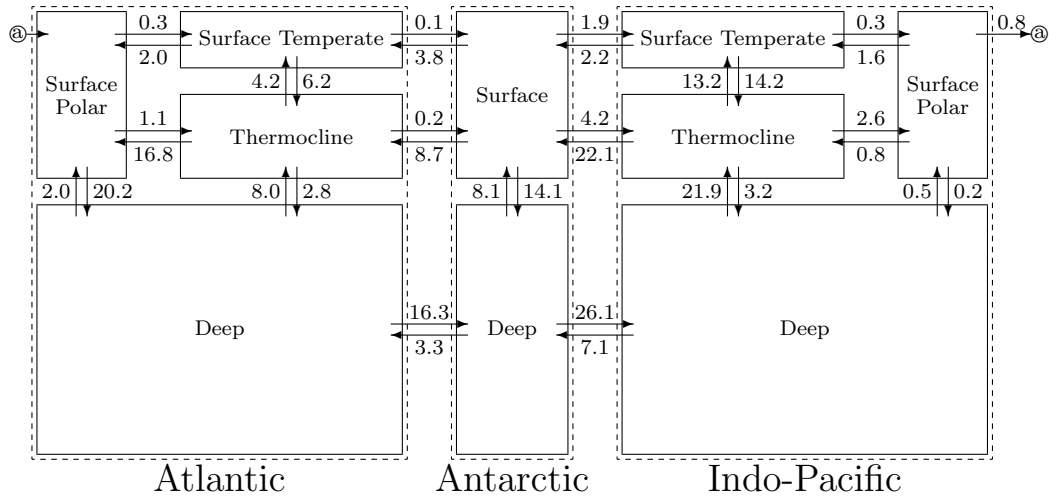
Figure 6.3: Model circulation (water fluxes in sverdrups, 1 Sv = 10^6 m^3/s).

spheric box and 10 oceanic boxes (figure 6.3). The volumes of the oceanic reservoirs are sea level dependent and vary in time. The sea level variations over the period of interest for our problem are now assumed to follow linearly the $\delta^{18}O$ signal of the Spectral Mapping Project (SPECMAP) stack. Five depth profiles (one per surface reservoir) obtained by linear interpolation of the $1° \times 1°$ bathymetric data of the Scripps Institution of Oceanography sampled at 100-m depth intervals are used for this purpose. Each one of these profiles comes with a series of 80 stacks of sedimentary layers. These stacks represent the sediments for the corresponding 100-m depth intervals. Each stack is composed of a bioturbated layer atop of a sequence of "memory" layers. The bioturbated layer has a typical thickness decreasing from 8 cm in shallow waters to 2 cm at a water depth of 6000 m and below. The thickness of the memory layers is 10%

of their top bioturbated layer. Because of exchange of matter with the overlying seawater, the thickness of the bioturbated layer varies in time. Once its actual thickness differs from its typical one by more than 10%, a new memory layer is filled up, or the most recent of these gets unburied and remixed into the bioturbated one. A set of ordinary differential equations is then used to trace the evolution of total dissolved inorganic carbon *DIC*, total alkalinity *TA*, phosphate and dissolved oxygen for the oceanic reservoirs, the partial pressure of CO_2 in the atmosphere, the $\delta^{13}C$ and $\Delta^{14}C$ for all of the carbon species listed before, and finally the carbonate content of the sedimentary layers. The water exchange (see figure 6.3) between the reservoirs has been determined from the annual mean velocity distribution of the Large Scale Geostrophic Oceanic General Circulation Model of the Max-Planck-Institut für Meteorologie (Ham-

burg, Germany) (MAIER-REIMER et al., 1991, 1993). The temperature evolution of the different water masses is taken from the reconstruction of LABEYRIE et al. (1987). We have only removed the warm peak at 5 kyr B.P. in the deep Atlantic (2°C warmer than today) to avoid a spurious 10 ppm CO_2 peak at that period (MUNHOVEN and FRANÇOIS, 1994). For simplicity, we assume that the surface water has temperature variations of the same amplitude as the underlying deep water masses (3° in the Atlantic and 2° in the Pacific) with present-day values of 2°C in polar and 19°C in temperate regions.

Biological Production: Organic and Inorganic Carbon Fluxes. The model includes different kinds of biological production. In the "open ocean," organic and inorganic matter is transferred from the surface to the thermocline and the deep water. A fixed fraction of the phosphate entering each surface reservoir is used for organic matter production. Inorganic production (planktonic calcium carbonate) is supposed to be proportional to the organic production. Forty percent of the inorganic production are assumed to be aragonite; the rest is assumed to be calcite. The $CaCO_3/C_{org}$ ratio varies from 0.05 in the northern Pacific reservoir to 0.30 in the equatorial Atlantic. These values have been adjusted to get for total alkalinity the best possible agreement with Geochemical Ocean Sections Study (GEOSECS) data. The organic matter is entirely recycled in the thermocline and the deep ocean; none is buried in the sediments. Both production and recycling of or-

ganic matter follow the Redfield ratio C:P:N:O = 106:1:16:−138. Part of the calcium carbonate is transferred to the sediments, and the rest is dissolved in the deep ocean reservoirs, depending on the depth of the calcite and aragonite lysoclines. We use the thermodynamic lysoclines defined as the saturation depths with respect to calcite and aragonite here. Planktonic carbonates that are deposited on the ocean bottom above the lysocline depth are kept in the sedimentary reservoirs until a rise of the lysocline exposes them to sufficiently corrosive waters so that they can be redissolved. No dissolution occurs above the lysocline; below, it is proportional to $([CO_3]_{loc}-[CO_3]_{sat})^{2.75}$. This is the diffusive flux out of the bioturbated layer that is obtained by using the dissolution law of order 4.5 (KEIR, 1980) instead of the linear one in the model of BROECKER and PENG (1982). The value $[CO_3]_{loc}$ is the local carbonate ion concentration derived from the *TA* and *DIC* concentrations in the deep reservoirs, and $[CO_3]_{sat}$ is the depth-dependent carbonate ion concentration at saturation calculated separately for calcite and aragonite. This law has been integrated over the top surface of each sedimentary reservoir, representing an 8-cm-thick sedimentary mixed layer. The dissolution constant has been determined to get a mean transition zone thickness (calcite compensation depth minus calcite saturation depth) of about 800 m.

Besides this open ocean biological activity, the shallow water regions must also be considered. Over the late Holocene, the coral reef flux to limestone has represented around 7 ×
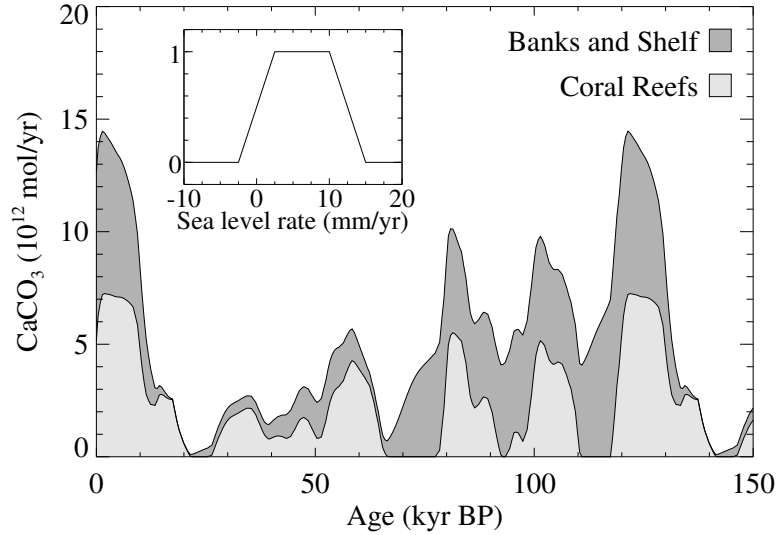
Figure 6.4: Shallow water carbonate precipitation. The inset shows the function $\mathcal{L}$ limiting the coral reef growth with respect to the rate of sea level rise and fall.

10^{12} mol $CaCO_3$ each year and another 7.5×10^{12} mol accumulate in banks and embayments and on the continental shelves (MILLIMAN, 1993; WOLLAST, 1994). This is almost half of the total net oceanic sink of about 32×10^{12} mol $CaCO_3$/yr (MILLIMAN, 1993; WOLLAST, 1994). Our model therefore includes a simple coral reef growth scheme. The growth of coral reefs is determined by the combined effect of three factors. (1) They grow only in water shallower than 100 m and on the continental shelf. The favorable area $\mathcal{A}_{100}$ thus changes in time as sea level rises and falls. (2) Coral reefs can neither build up during sea level drops nor during too fast rises. The corresponding limiting function $\mathcal{L}$ has a trapezoidal shape (see inset on figure 6.4). (3) Finally, coral reef growth is enhanced when the degree of su-

persaturation Ω_{CaCO_3} of seawater with respect to $CaCO_3$ increases (OPDYKE and WILKINSON, 1988). The total precipitation of $CaCO_3$ by coral reefs in our model is hence $k \times \mathcal{A}_{100} \times \mathcal{L} \times (\Omega_{CaCO_3} - 1)^{1.7}$. The value k is calculated to reach a mean $CaCO_3$ accumulation of 7×10^{12} mol/yr over the last 5000 years (MILLIMAN, 1993). An additional flux handles nonreefal carbonate accumulation in shallow waters. This one is proportional to the area of flooded continental shelf, averaging 7.5×10^{12} mol $CaCO_3$/yr, again over the last 5000 years (MILLIMAN, 1993). Figure 6.4 shows the histories for the two schemes.

We would like to emphasize several differences to similar models previously published. Unlike OPDYKE and WALKER (1992b), who prescribed a hypothetical net variation (precipitation

minus erosion) in shallow water regions, the two schemes described above only handle precipitation. Erosion of carbonate platforms is independent and is taken proportional to the exposed area. Assuming a typical runoff of 1000 mm/yr over the continental shelf areas, we calculate a specific dissolution rate of 1.1 mol $CaCO_3/m^2/yr$ from the relationships of BLUTH and KUMP (1994). MUNHOVEN and FRANÇOIS (1994) already treated the deposition and dissolution fluxes separately as is now also done by WALKER and OPDYKE (1995). The function governing their total shallow water $CaCO_3$ accumulation (reefal plus nonreefal) is similar to the one that is used here for reef buildup alone. Following MILLIMAN (1993), who indicates that most reefs were probably outpaced by the rapid sea level rises of 8–12 mm/yr, we definitely cut off carbonate precipitation at 15 mm/yr. WALKER and OPDYKE (1995) (and also MUNHOVEN and FRANÇOIS (1994)) allow it until 25 mm/yr. Part of this difference is compensated by the separate nonreefal flux used in our model which is independent of the rates of sea level variations. Besides these more conceptual differences, we must also mention that quite diverse total shelf accumulation rates have been adopted in these models. OPDYKE and WALKER (1992b) and WALKER and OPDYKE (1995) obtain an average deposition of 23×10^{12} mol $CaCO_3/yr$ for the late Holocene, compared to 14.5×10^{12} mol /yr in our model (and even 11×10^{12} mol /yr in the previous version (MUNHOVEN and FRANÇOIS, 1994)). This has some important consequences which will be discussed in the next section.

Numerical Simulations and Discussion

We have selected a few of the numerous possible experiments to illustrate the potential of continental silicate rock weathering to drive the atmospheric CO_2 levels on glacial-interglacial time scales. All of the experiments include the sea level and temperature variations and the coral reef buildup and erosion scheme described in the model section. The history for the carbonate part in the riverine bicarbonate flux is also the same for all of the experiments. This flux includes a constant input steming from the dissolution of continental carbonates (at the present-day value of 20.6×10^{12} mol/yr) to which we add the contribution from shelf erosion (up to a maximum of 17.6×10^{12} mol/yr, depending on the shelf area exposed). Half of this bicarbonate is taken from the atmosphere, the other half comes from the dissolving carbonate minerals. Besides these common features, each experiment includes a different scenario for the $HCO_3^-{}_{\text{sili}}$ flux to complete the riverine bicarbonate input. These are calculated from the Ge/Si based reconstructions of the river Si delivery by using the $[HCO_3^-]_{\text{sili}}/[H_4SiO_4]$ ratio of 1.76 mol/mol, according to the previous discussion.

We use a kind of control run to quantify the role of continental silicate rock weathering in the evolution of atmospheric CO_2 concentration. For this control run, the varying $HCO_3^-{}_{\text{sili}}$ flux is replaced by a constant average one. Hence there are, in fact, several control

runs, because this constant $HCO_3^-{}_{\text{sili}}$ input has to be adjusted for each of the input scenarios considered below. A consistent picture for the net contributions of continental silicate rock weathering can only be obtained if we compare the CO_2 evolution that each scenario yields with the one its own constant mean would yield. This net contribution from silicate weathering-related CO_2 consumption is obtained from the difference between the atmospheric CO_2 history a given scenario yields and the one from its corresponding control run. Different constant inputs produce slightly different responses for atmospheric CO_2 because the resulting surface ocean to deep-sea *TA* and *DIC* gradients are not the same. The resulting CO_2 signals, however, differ by less than 10 ppm.

This type of control run obviously takes into account all of the components that make up the coral reef (or basin to shelf partitioning) scenario. The CO_2 history it generates can immediately be compared to the results of OPDYKE and WALKER (1992b) and WALKER and OPDYKE (1995). Their model makes this mechanism a much more efficient motor for glacial-interglacial CO_2 variations than ours because of its almost 60% higher Holocene carbonate accumulation rates in shallow water areas. In our control run experiments, the total bicarbonate inputs that force the model reach present-day values of $40 \pm 4 \times 10^{12}$ mol/yr. This compares well to the 43×10^{12} mol/yr in the work of WALKER and OPDYKE (1995). When submitted to the complete weathering scenarios with variable $HCO_3^-{}_{\text{sili}}$ contributions, the model ocean, however, re-

ceives only 32×10^{12} mol/yr at present day, in much better agreement with observational data (MEYBECK, 1979). In our model scenarios, the contribution of bicarbonate from silicate weathering at present day is close to the glacial-interglacial minimum. Table 6.1 gives a summary of the main characteristics of the riverine Si scenarios calculated from the inversion of the marine Ge/Si signal. The corresponding control runs are based upon the reported $\overline{F}_{\text{riv}}$ values.

We first analyse the sensitivity of our system with respect to the two silica accumulation schemes adopted. The results are represented in figures 6.5 (constant opal accumulation rate) and 6.6 (first-order model). For each of the two accumulation laws, three experiments have been performed to illustrate that time variations in continental runoff only play a secondary role. Atmospheric CO_2 changes remain within ± 5 ppm for the $\pm 20\%$ runoff variations that we have used. The top and middle panels show the scenarios for CO_2 consumption by silicate rock weathering and the resulting evolutions of atmospheric CO_2, respectively. For comparison, the Vostok CO_2 curve (BARNOLA et al., 1987) is also reported (middle). The curves for the variable silicate weathering scenarios have been drawn on a light grey background to distinguish them from the control runs. The bottom panel gives the net contribution of silicate rock weathering processes to the total variation of atmospheric CO_2. This contribution is calculated from the difference between the full scenarios and their respective control runs, both taken from the middle panel. CO_2 variations have quite large amplitudes in both series. If

Table 6.1: Characteristic Riverine Dissolved Si Fluxes.

Model	$\dfrac{W^{\text{LGM}}}{W^{\text{present}}}$	$\overline{F}_{\text{opal}}$	$F^{\text{present}}_{\text{opal}}$	F_{hyd}	$\overline{F}_{\text{riv}}$	$\dfrac{F^{\text{max}}_{\text{riv}}}{F^{\text{present}}_{\text{riv}}}$
No Fractionation of Ge/Si by Diatoms ($K_D = 1.0$)						
Constant opal accumulation	0.8	10.09	10.09	0.211	9.88	2.53
	1.0	10.48	10.48	0.211	10.26	2.65
	1.2	10.93	10.93	0.211	10.72	2.80
First order ($\tau = 20,000$ years)	0.8	11.72	8.61	0.248	11.47	3.08
	1.0	12.36	8.99	0.255	12.11	3.29
	1.2	13.12	9.42	0.263	12.86	3.55
$K_D = 0.8$ and Variable Silica Extraction Efficiency						
Constant opal accumulation	1.0	9.09	9.09	0.164	8.92	1.94
First order ($\tau = 20,000$ years)	1.0	10.00	8.09	0.184	9.81	2.28

$W^{\text{LGM}}/W^{\text{present}}$ is the river runoff variation factor, $\overline{F}_{\text{opal}}$ and $F^{\text{present}}_{\text{opal}}$ are the calculated mean and the present-day accumulation rates of biogenic opal on the sea-floor, respectively, F_{hyd} is the hydrothermal input of dissolved silica to the oceans, $\overline{F}_{\text{riv}}$ is the glacial-interglacial average dissolved Si input by rivers and the ratio $F^{\text{max}}_{\text{riv}}/F^{\text{present}}_{\text{riv}}$ compares the maximum with the present-day riverine silica transport of 6.47×10^{12} mol Si/yr. All fluxes are in 10^{12} mol Si/yr.
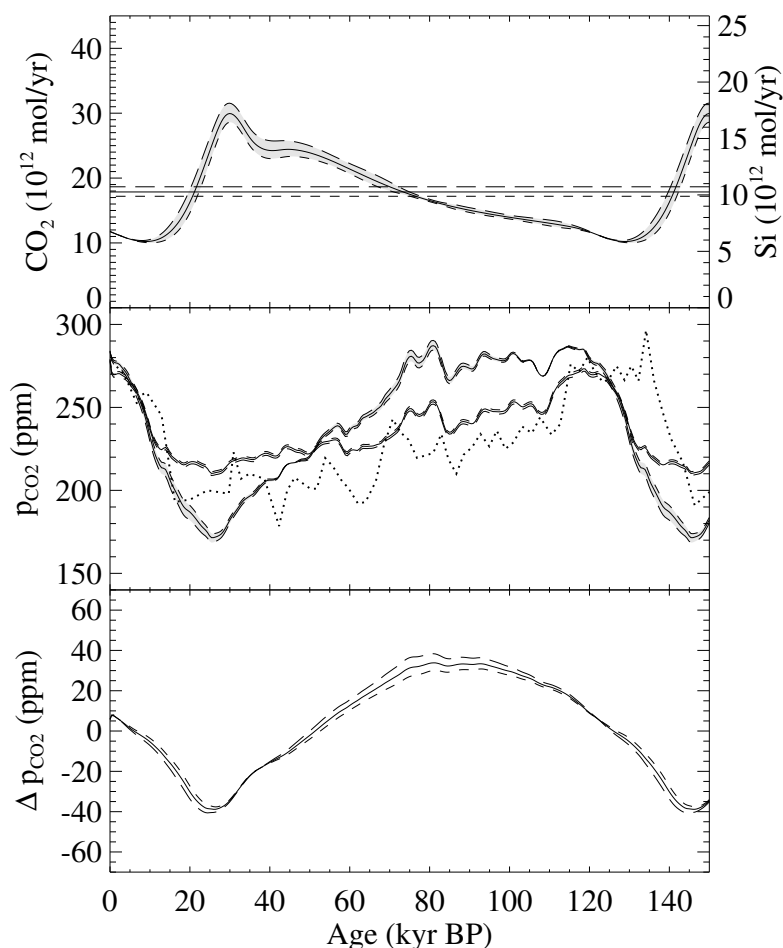
Figure 6.5: Ge/Si signal inversion with constant silica accumulation rates. (top) Scenarios for the consumption of atmospheric CO_2 by silicate rock weathering processes alone. Complete scenarios are represented on a light grey background, their corresponding control runs unshaded. (middle) Calculated evolutions of atmospheric CO_2. The heavy dotted line represents the Vostok ice core data (Barnola et al., 1987). (bottom) Net contribution of silicate rock weathering processes in the total variation of atmospheric CO_2. The three curves of each group correspond to different evolutions of the continental runoff: long dashes for a 20% lower, short dashes for a 20% higher and solid line for unchanged global runoff at the last glacial maximum, compared to today's 37,400 km^3/yr.
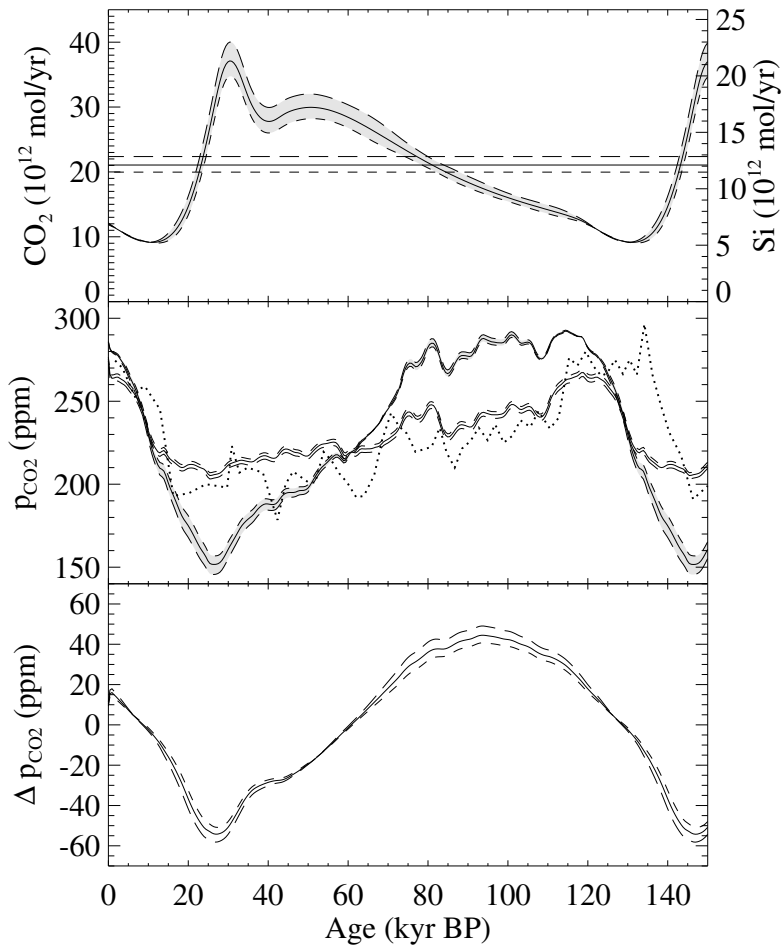
Figure 6.6: Ge/Si signal inversion with silica accumulation following a first-order law (residence-time model). See figure 6.5 for other details.

the Ge/Si inversion is performed under the hypothesis of constant opal accumulation rates, the calculated CO_2 consumption scenario leads to 110–120 ppm changes, including a net variation of 70–80 ppm due to the variable silicate weathering (figure 6.5); if the first-order model is used for the inversion, we obtain the considerable amplitude of 135–145 ppm for atmospheric CO_2, silicate weathering bringing in a 95–110 ppm oscillation (figure 6.6). These amplitudes are not additive because the histories calculated during the control and the complete experiments do not have exactly the same shape and they are not fully in phase. The CO_2 variations obtained for the control runs all have amplitudes very close to 60 ppm.

In a second series of simulations, we explore to what extent the inversion of the marine Ge/Si signal could be influenced by discrimination effects of diatoms while feeding on Si and Ge. As a guidance, we take the Rayleigh distillation law from FROELICH et al. (1989) stating that

$$\frac{r_{\text{opal}}}{r_{\text{oc}}} = \frac{1 - F^{K_D}}{1 - F}. \qquad (6.6)$$

In this law, F is the preformed nutrient fraction, that is, the fraction of upwelled silica that remains after biological uptake has completed. For this set of scenarios, we use $K_D = 0.8$ as noted above, $F = 0.05$ (FROELICH et al., 1989) for the peak interglacial and $F = 0.50$ for the peak glacial. A time-dependent evolution for $r_{\text{opal}}/r_{\text{oc}}$ is then constructed by linear interpolation between the basic glacial and the interglacial values of $(1 - 0.50^{0.8})/(1 - 0.50) = 0.85$ and $(1 - 0.05^{0.8})/(1 - 0.05) = 0.96$. The cor-

responding results are represented in figure 6.7. Although the response is less pronounced than before, even these important changes cannot explain the observed Ge/Si record without any variations in the riverine supply. The latter remain large enough to produce a significant atmospheric CO_2 response: the overall amplitude still reaches 90–100 ppm, with a net oscillation of 50–65 ppm coming from the changing silicate weathering.

All of our modelling results suffer from a common shortcoming: they predict much too high atmospheric CO_2 levels during isotope stage 5, especially over the substages 5a-5d (i.e. 70–115 kyr B.P.). Oxygen isotope stages are used here only as approximate time indications and not as absolute time-intervals. During that period, the inclusion of the CO_2 drawdown by silicate weathering cancels the decrease observed for the control runs, which compared rather well with the Vostok signal. The model also completely misses the drop in atmospheric CO_2 at the beginning of this relatively warm period (in terms of oxygen isotopes), and it produces, in fact, a pure interglacial, as far as atmospheric CO_2 is concerned, whereas the Vostok ice core record witnesses CO_2 levels of 230–240 ppm, intermediate between the typical interglacial maxima of about 270 ppm and the full glacial minima around 200 ppm (BARNOLA et al., 1987; JOUZEL et al., 1993). The net distinction between the 110–70 kyr B.P. and the 70–20 kyr B.P. time intervals in the Vostok CO_2 record may indicate two completely different behaviors of the global carbon cycle during these periods.
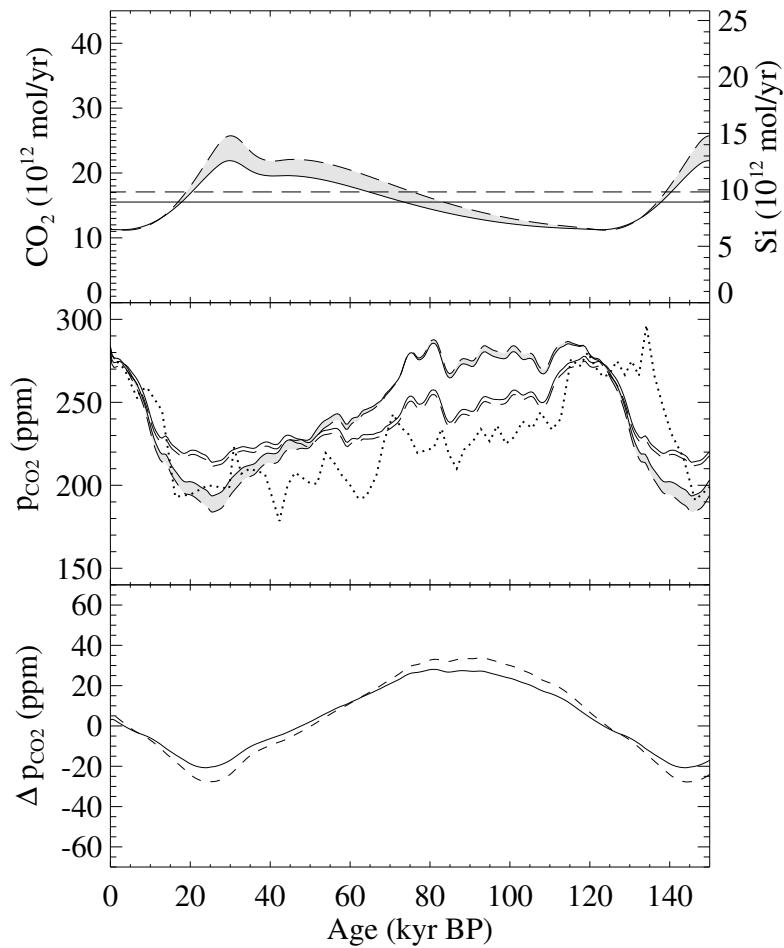
Figure 6.7: Ge/Si signal inversion allowing for fractionation (see text for details). (top, middle, and bottom) Same distribution as in figures 6.5 and 6.6, except that solid lines correspond here to the constant opal accumulation model and dashed lines correspond to the first-order model. River runoff is assumed not to vary in time.

The reason for this discrepancy is simply the strong tie of the CO_2 consumption scenarios to the marine Ge/Si signal, which is markedly high (i.e. above mean) from 120 to 70 kyr B.P., whereas it is low (i.e. below mean) from 70 to 10 kyr B.P., this latter interval covering the whole isotope stages 2, 3, and 4. This correlation dictates the shapes of the different calculated evolutions of the riverine Si supply and of the corresponding CO_2 consumption and hence of the system's global response. This link becomes particularly obvious on the graphs showing the net contribution of chemical continental silicate rock weathering in figures 6.5, 6.6, and 6.7 (bottom).

The model is, however, able to reproduce the glacial-interglacial pH difference as calculated from the marine boron isotopic record (Sanyal et al., 1995). It also points out an alternative pathway on the *TA–DIC* diagram to perform the transition between the glacial and the interglacial pH values, requiring less drastic changes than the full carbonate change scenario proposed by Sanyal et al. (1995). The observed pH variation can be achieved with much smaller *TA* and *DIC* variations. Figure 6.8 shows the evolution of the model's deep Indo-Pacific and equatorial surface Indo-Pacific reservoirs with respect to *TA* and *DIC*, for both control (dotted) and variable silicate weathering (solid lines) experiments. The results from the experiments with variable silicate weathering are in fair agreement with Sanyal et al.'s (1995) findings. The model only yields a somewhat smaller variation in the deep sea (ΔpH = 0.24, compared to the reconstructed 0.31 ±

0.12 (Sanyal et al., 1995)) than in the surface waters (ΔpH = 0.30, compared to 0.20 ± 0.11 (Sanyal et al., 1995)). In the control run, both deep-sea and surface waters exhibit peak-to-peak variations of only 0.08 pH units. On the other hand, the variations of the calcite saturation depth that accompany the pH variations shown in figure 6.8 exceed 2 km and are even larger than those of Opdyke and Walker (1992b) and Walker and Opdyke (1995). So large a variation is unfortunately difficult to reconcile with the history of the different characteristic sedimentary carbonate depths reconstructed by Farrell and Prell (1989). Even our weakest scenarios (figure 6.7) make the calcite saturation depth move up and down by about 1.5 km. However, then the ΔpH is also only half as important as in the example previously discussed. Sanyal et al. (1995) have already pointed out this incompatibility between their boron isotope-based pH reconstruction and the results of Farrell and Prell (1989) and have discussed possible reasons. Several questions arise in this context. To what extent might Farrell and Prell's (1989) reconstructions be biased by dissolution effects during times of lysocline shoaling? In our model, deep-sea dissolution of ancient carbonates is rather important with present-day dissolution rates of 6×10^{12} mol $CaCO_3$/yr for the control runs and 8–10×10^{12} mol $CaCO_3$/yr for the complete experiments. Because of the important disequilibria of the present-day marine cycles of calcium, magnesium and inorganic carbon (Morse and Mackenzie, 1990; Milliman, 1993; Wollast, 1994) we think that this kind
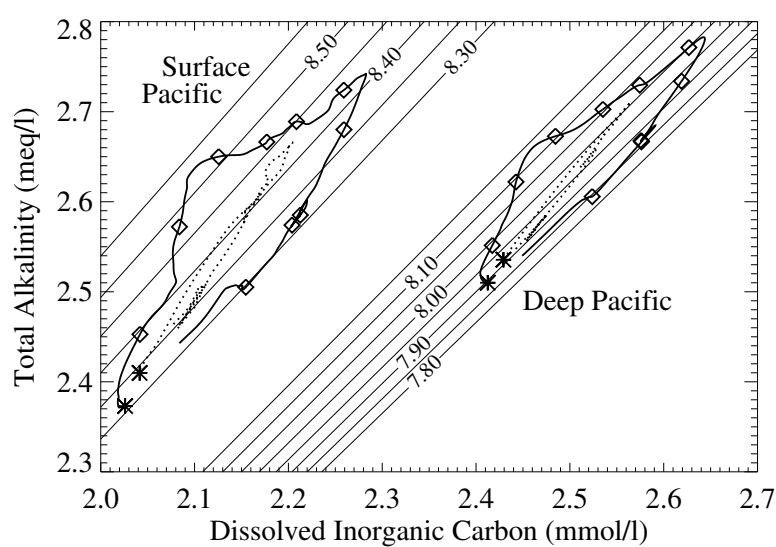
Figure 6.8: Evolution of the model Pacific surface and deep reservoirs over the past 110 kyr in a *DIC-TA* diagram with *p*H contour lines. Diamonds delimit 10-kyr intervals, stars mark pre-industrial (final) state. The underlying scenario stems from the Ge/Si inversion based upon variable opal accumulation without river runoff variations (solid line on grey background in figure 6.6). Solid lines represent the results for the complete run; the dotted lines correspond to the control run.

of dissolution cannot be precluded a priori. Such dissolution effects have also been discussed by OPDYKE and WALKER (1992b) and WALKER and OPDYKE (1995), who have also shown how they can alter the preserved record. In a reconstruction like FARRELL and PRELL's (1989), they would inevitably shift low-carbonate lines into shallower depths. Sediment layers in a core which are now found to be poor in carbonate could have been much richer at the time when they represented the sedimentary mixed layer, before they first got buried. They could then have lost part of their carbonate at a later time during a lysocline shoaling. Another explanation could come from a possible offset between the classical sedimentary lysocline and the calcite saturation depth (thermodynamic lysocline) that we are using here. Respiration-driven carbonate dissolution in the sedimentary mixed layer could possibly take place above the saturation depth (ARCHER and MAIER-REIMER, 1994).

Conclusions

We have calculated several histories for the evolution of the CO_2 consumption by silicate rock weathering over the last glacial-interglacial cycle. The marine Ge/Si record for the last 140 kyr (MORTLOCK et al., 1991; FROELICH et al., 1992) has been used as a basis for these histories. We have inverted this record in terms of silica fluxes into and out of the ocean. This has been done in a fully transient way (no steady state behavior), under the only assumption that the Ge and Si budgets are balanced on the glacial-

interglacial mean. The resulting histories for the riverine dissolved silica transport have then been converted into equivalent histories of CO_2 consumption by silicate rock weathering. To perform this conversion, we have studied the systematics of $[HCO_3^-]_{sili}/[H_4SiO_4]$ ratio in the world rivers. The $[HCO_3^-]_{sili}$ is that part of the total bicarbonate load that has gone through silicate weathering processes. The data available in the literature suggest that this ratio is possibly an indicator for weathering intensity. Rivers draining regions with high weathering intensity exhibit low $[HCO_3^-]_{sili}/[H_4SiO_4]$ ratios and vice versa. This finding requires, however, more thorough validation. There is some qualitative support for this idea, but the existing data on individual rivers are not sufficiently representative. If this relationship is correct, the global average river $[HCO_3^-]_{sili}/[HCO_3^-]_{total}$ in a glacial world (with low global weathering intensity (FROELICH et al., 1992)) should be higher than at present day. The modern value of 1.76±0.10 mol/mol is hence probably close to the glacial-interglacial minimum. We have used the present-day value for the whole glacial-interglacial cycle. The calculated scenarios for the consumption of CO_2 by silicate rock weathering processes are thus merely minimum estimates for this period. We are, however, fully aware that it can only be considered as a working hypothesis.

When used as a forcing for our carbon cycle model, the so-constructed CO_2 consumption histories generate glacial-interglacial atmospheric CO_2 variations between 50 and 110 ppm. These are superimposed to a basic

oscillation of about 65 ppm because of other varying factors such as salinity and temperature variations, coral reef buildup, and erosion. Both signals have different shapes and phases. The overall variation is between 90 and 145 ppm. Compared to the Vostok ice core record (BARNOLA et al., 1987), concentrations are generally too high between 110 and 70 kyr B.P. Part of this problem is due to the fact that we have considered the whole glacial-interglacial cycle as a single entity. This approach requires that not only constraints at a few key dates or periods (like pre-industrial and LGM atmospheric CO_2 levels or the present-day riverine silica flux) must be taken into account. Long-term means have also to be considered, for example, to keep the whole system stable over hundreds of kiloyears.

Constrained by the most recent carbonate cycling data of MILLIMAN (1993) and WOLLAST (1994), our model confirms the efficiency of coral reef buildup and erosion as a driving force for atmospheric CO_2 variations on glacial-interglacial time scales. It shows at the same time that climate driven changes of the CO_2 consumption by chemical silicate rock weathering have the potential to generate pCO_2 changes in the atmosphere that are much too large to be neglected. This conclusion is somewhat mortgaged by the uncertainties affecting the procedure used to calculate the CO_2 consumption scenarios. Further study is required, in particular, on the systematics of CO_2 consumption during chemical weathering of silicate rocks under weathering regimes of different intensities.

Chapter 7

Erosion Model Based Approach to Glacial-Interglacial Weathering Changes

The two approaches presented in the previous two chapters considered the continents more or less as a black box: CO_2 consumption scenarios were deduced from a marine signal by mass balance considerations and the problem of finding possible mechanisms to explain them could only be addressed from a qualitative point of view. In this chapter, we take the continents themselves as a starting point to determine the riverine bicarbonate flux to the oceans. This flux is derived from PH. AMIOTTE SUCHET's erosion model GEM-CO_2 (Global Erosion Model for CO_2 fluxes). This model directly calculates the amount of atmospheric/soil CO_2 consumed by erosion processes and the corresponding bicarbonate transfer to the oceans as a function of lithology and of runoff. By applying GEM-CO_2 first under present-day and then under LGM climate conditions, we construct simple histories for the river bicarbonate transport to the oceans, to be used as forcings in the carbon cycle model. In the next section, we give a brief presentation of this model. We then describe how the problem of the boundary conditions required to apply it under LGM conditions is addressed. Finally, we present the results from the carbon cycle model simulations, using the obtained bicarbonate fluxes, and draw some conclusions.

7.1   GEM-CO_2 — A Global Erosion Model

As already mentioned, GEM-CO_2 (AMIOTTE SUCHET and PROBST, 1993a,b, 1995; AMIOTTE SUCHET, 1995) calculates the consumption of atmospheric

Table 7.1: Runoff-CO_2 consumption laws used in GEM-CO_2.

Rock type	$\mathcal{F}_{CO_2} = a \times Q$	$\mathcal{F}_{HCO_3^-} = b \times \mathcal{F}_{CO_2}$
	a (mmol/l)	b (mol/mol)
basalts & gabbros	0.479	1
acid volcanic	0.222	1
evaporitic	0.293	2
plutonic & metamorphic	0.095	1
shales	0.627	1
carbonates	1.586	2
sandstones	0.152	1

In this table, $\mathcal{F}_{CO_2}$ denotes the CO_2 consumption rate (typically in moles per unit outcrop surface area per unit time), Q the runoff, and $\mathcal{F}_{HCO_3^-}$ the corresponding bicarbonate flux.

(soil) CO_2 by weathering processes on the continents, and the resulting bicarbonate transfer to the oceans, as a function of lithology, i.e., the type of rock undergoing weathering, and of drainage intensity. The fundamental hypothesis it rests upon is hence that continental runoff is the primary climatic factor driving CO_2 consumption. Rocks outcropping at the Earth's surface have been classified into seven classes. For each of these, an empirical linear relationship between the CO_2 consumption rate and runoff has been derived using published chemical analyses of stream water from 232 small, non-polluted and monolithologic watersheds in France (MEYBECK, 1986). The rock classification together with their respective relationships are given in table 7.1. The proportion of carbonate minerals in the outcropping rocks is highly variable and difficult to assess. In GEM-CO_2, it is supposed that only waters draining 'carbonate' and 'evaporite' rock types follow the carbonate dissolution stoichiometry, as shown by the $\mathcal{F}_{HCO_3^-}/\mathcal{F}_{CO_2}$ ratio b in table 7.1. GEM-CO_2 does not allow for any weathering in ice-covered areas.

GEM-CO_2 was validated against field data on the Garonne, the Congo and the Amazon river basins (AMIOTTE SUCHET and PROBST, 1993a,b; AMIOTTE SUCHET, 1995). For this validation, the three basins were divided into small grid cells, each of them being considered as a monolithologic watershed. The distribution of exposed rock types was derived from regional geological maps; adopted resolutions were 2.5×2.5 km^2 for the Garonne, and 50×50 km^2 for the Congo and the Amazon basins.

For its application at the global scale (AMIOTTE SUCHET and PROBST,

1995; AMIOTTE SUCHET, 1995), a new map of the global lithology was constructed, based upon available lithological and soil maps (AMIOTTE SUCHET and PROBST, Present-day continental lithology: Implications for global erosion, *in prep.*). This map, which gives the distributions of the seven rock types and of ice on the present-day continents in a $1° \times 1°$ longitude-latitude grid is shown in figure 7.1. Using the runoff distribution from the water balance model of WILLMOTT et al. (1985), AMIOTTE SUCHET and PROBST (1995) and AMIOTTE SUCHET (1995) produced maps of $\mathcal{F}_{CO_2}$ and of $\mathcal{F}_{HCO_3^-}$.

Here, we cannot get into the details of the distributions of these two carbon fluxes. They have been discussed by AMIOTTE SUCHET and PROBST (1995). The maps are available in the Data Base 1012 from the Carbon Dioxide Information Analysis Center (CDIAC) in Oak Ridge, Tennessee. We only want to emphasize one interesting characteristic concerning the total fluxes that can be calculated from these global distributions. The overall CO_2 consumption rate of 19.6×10^{12} mol/yr represents 70% of the total bicarbonate production of 27.9×10^{12} mol/yr[†]. This partitioning is in good agreement with the commonly cited estimates of 65–67% (HOLLAND, 1978; BERNER and BERNER, 1987; MEYBECK, 1987; PROBST, 1992)[‡]. GIBBS and KUMP (1994), who have constructed a model similar to GEM-CO$_2$ (but using a $2° \times 2°$ grid) by combining the bicarbonate-runoff relationships of BLUTH and KUMP (1994) with the lithology map derived from the work of BLUTH and KUMP (1991), find a ratio of 0.80. There is a huge difference between these two values. A ratio of 0.80 means that only 20% of the total riverine bicarbonate comes from the carbonate rock minerals, an equivalent amount being furthermore taken from the atmosphere. Accordingly, 60% has gone through silicate rock weathering processes, all of which stems from the atmosphere. For an atmospheric fraction of 67% on the other hand, only 34% come from silicate rock weathering and the other $2 \times 33\%$ have gone through carbonate rock weathering. This good agreement of the partitioning of the CO_2 consumption rates between silicate and carbonate weathering derived from GEM-CO$_2$ on one hand and the estimates taken from the literature on the other hand was already observed for the large river basins (AMIOTTE SUCHET and PROBST, 1993b, 1995; AMIOTTE SUCHET, 1995).

From this summary presentation, it clearly follows that two problems have

---

[†]If used with the maps from the UNESCO Atlas of World Water Balance (KORZOUN et al., 1977) instead of the model of WILLMOTT et al. (1985), GEM-CO$_2$ yields slightly different values of 21.0×10^{12} mol/yr and 29.4×10^{12} mol/yr repectively, as shown below.

[‡]Also WOLLAST and MACKENZIE (1983) and MORSE and MACKENZIE (1990), who find that 35% of the total river bicarbonate stem from the weathered carbonate minerals, 56% directly from the soil/atmosphere, and 9% from the oxidation of fossil organic matter, which we may also include in the soil CO_2 source.
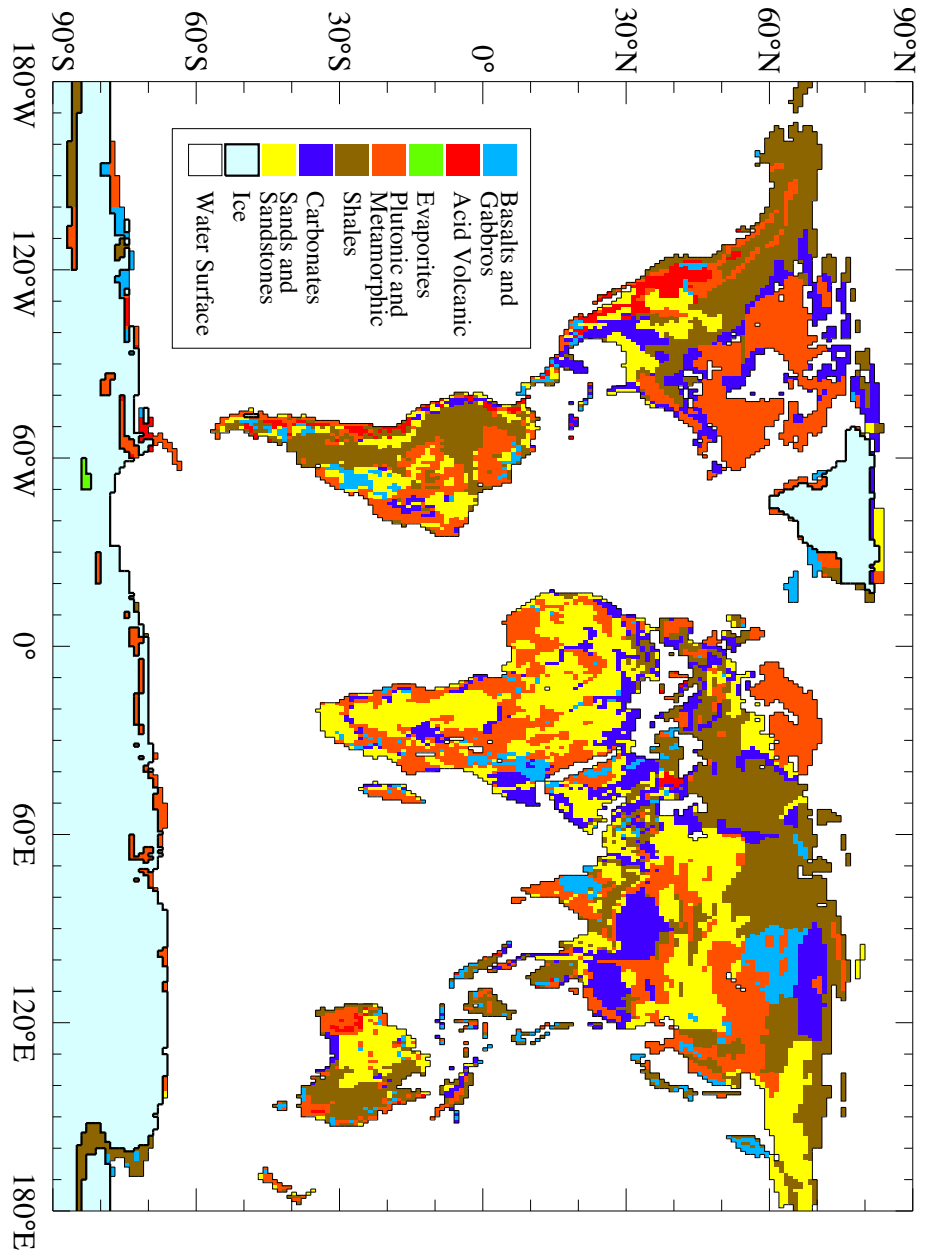
Figure 7.1: Lithological map of the present-day continents used by GEM-CO$_2$.

to be addressed in order to apply GEM-CO$_2$ under LGM climate conditions:

1. adaptation of the GEM-CO$_2$ lithological map to LGM geography, including the ice coverage appropriate to this colder climate;

2. reconstruction of the LGM runoff distribution.

7.2 LGM Geography and Lithology

7.2.1 Reconstruction of the Ice Age Topography

The Earth's surface conditions at the Last Glacial Maximum were considerably different from today's. Huge ice sheets, up to several kilometers thick, covered large parts of the northern latitude shield areas and of the high mountainous regions. Sea level stood about 120–130 m lower than today (CHAPPELL and SHACKLETON, 1986; FAIRBANKS, 1989) and large parts of the continental shelves laid free and were subject to erosion. With a model of the Earth's crust, PELTIER (1994) has reconstructed a history of the Earth's topography and ice cover at 1,000 yr intervals since the LGM (taken as 21 kyr BP), with a longitude-latitude resolution of $1° \times 1°$. The corresponding ice sheet extension history is currently being used as a standard boundary condition for the GCM experiments in the international PaleoModeling Intercomparison Project (PMIP).

Before adapting the lithology map of GEM-CO$_2$ to LGM conditions, we have to check if the present-day coastlines of GEM-CO$_2$ can be overlaid with PELTIER's (1994) ice-cover and topological maps. The continental outlines on the lithology map of GEM-CO$_2$ were determined directly from a geographical atlas. Each grid element was defined to be of continental or oceanic nature depending on which of both covered the most important surface. On PELTIER's (1994) map continental grid elements were defined as being those with a positive elevation. Both methods do not necessarily give the same results everywhere.

This is why we also considered the high-resolution ($5' \times 5'$) elevation database ETOPO5, distributed by the National Geophysical Data Center (NGDC) Boulder, Colorado). We have down-gridded these data to a $1° \times 1°$ grid and used the resulting heights to distinguish between continental and oceanic grid elements. Among these three maps, the best agreement is found between the lithology map and the $1° \times 1°$ version of ETOPO5. We therefore only used PELTIER's (1994) maps to calculate glacial-interglacial topographical anomalies. These anomalies are then applied to the ETOPO5-derived map in order to reconstruct the LGM topography. Grid elements with heights

Table 7.2: Surface Area Distribution.

	Present-day	LGM
Ocean	361.3	336.3
Continent		
Endoreic	32.0	32.0
Exoreic	117.9	142.9
Ice-covered	14.1	45.6
Ice-free	135.8	129.3
Total	149.9	174.9

All areas are in 10^6 km^2.

Table 7.3: Ice-covered and ice-free areas of the continents at LGM.

	Exoreic		Endoreic	
	Ice-free	Ice-covered	Ice-free	Ice-covered
Present-day Land	84.2	33.7	32.0	0.0
Emerged Shelf	13.1	11.9	0.0	0.0
Total LGM Continent	97.3	45.6	32.0	0.0

All areas are in 10^6 km^2.

below 0 and not covered by ice are taken as the oceanic ones. Continental grid elements not corresponding to exposed points in the lithology map of GEM-CO$_2$ were supposed to belong to the non flooded continental shelves. Tables 7.2 and 7.3 summarize the resulting changes in the distribution of Earth surface at the global scale, and the partitioning between endoreic and exoreic, as well as between ice-free and ice-covered areas.

7.2.2 Ice Age Shelf Lithology

To construct the ice age lithology, the following guidelines were used:

1. Grid elements that belong to the continental area on both present-day and LGM maps, and that were not covered by ice at LGM, are supposed not to have changed their lithological class.

2. The ice-cover at 21 kyr BP given by PELTIER (1994) is used as is. A

few isolated spots between the ice sheet margins and the ocean have been covered by ice too.

3. Continental shelf points around Australia and in the Caribbean area, where annual average and annual minimum temperatures are high enough for important biogenic carbonate production, are considered to consist of carbonates. Exceptions to this rule are points near large river mouths and points where the closest present-day coastal zones are dominated by shales, reflecting swamp areas, as is the case in parts of the Indonesian islands. We suppose that these points, as well as the remaining shelf elements at high latitudes were covered by shales at the LGM. As far as the CO_2 consumption rate is concerned, this is a rather conservative assumption.

The resulting map for the continental margin lithology, represented in figure 7.2, compares very well to the one used by GIBBS and KUMP (1994).

7.3 LGM Runoff Reconstruction

7.3.1 Glacial-Interglacial Runoff Variation

Observational constraints on the runoff variation between the last glacial and the present interglacial periods are cruelly missing. Even for precipitation, indicators are at most qualitative and their interpretation not unambiguous (see, e.g., BROECKER, 1992). We therefore decided to use General Circulation Models (GCMs) for the reconstruction of the runoff distribution at the LGM. The GCMs that have been used to carry out climate simulation experiments for the Last Glacial Maximum often have only a simplified representation of the hydrologic budget at the land-atmosphere interface. It is generally assumed that, although the absolute runoff distributions they provide are not necessarily correct, they are useful to calculate anomalies like the glacial-interglacial one which we need for our purpose. The effective runoff distribution is then obtained by applying the GCM-derived anomaly to the actually observed modern distribution:

$$R_{\text{LGM}} = R_{\text{present}} + (R_{\text{LGM}}^{\text{GCM}} - R_{\text{present}}^{\text{GCM}}). \qquad (7.1)$$

This commonly adopted method helps to root the interpretation of the CO_2 consumption in the observed runoff distribution.
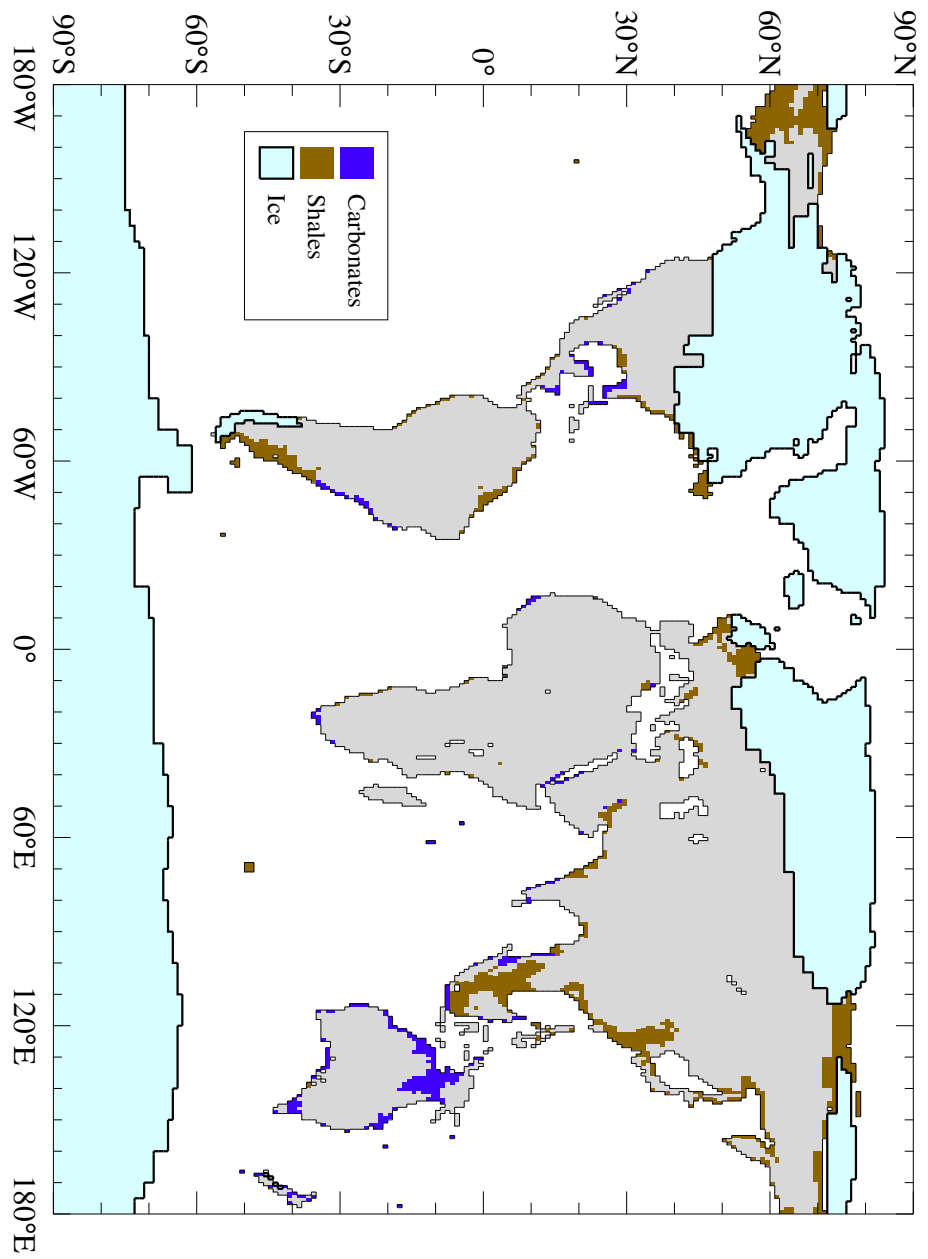
Figure 7.2: LGM continental margin lithology and ice sheet extension. Continental outlines are drawn in thin and ice sheet boundaries in heavy lines. Grey zones represent shelf areas exposed at LGM but presently flooded, with carbonates in lighter and shales in darker grey tones.

7.3.2 Construction of a Digital Database for the Present-Day Runoff

The runoff distribution originally used by AMIOTTE SUCHET (1995) for his study of present-day erosion and which he derived from the water balance model of WILLMOTT et al. (1985), was not sufficiently consistent with global river discharge data (see, e.g., LUDWIG, 1996). It was thus necessary to reconsider the present-day situation and to get a more accurate distribution, preferably on the same $1° \times 1°$ grid as GEM-CO_2. No appropriate digital database was available to us and we therefore decided to digitize and grid the runoff distribution maps from the UNESCO Atlas of World Water Balance (KORZOUN et al., 1977). We preferred these maps to those of BAUMGARTNER and REICHEL (1975) for two reasons:

1. KORZOUN et al. (1977) primarily use river gauging data to construct their maps, whereas that of BAUMGARTNER and REICHEL (1975) is completely derived from the difference between observed precipitation and empirically calculated evapotranspiration;

2. KORZOUN et al. (1977) indicate that they used an azimuthal equal-area projection for their maps, BAUMGARTNER and REICHEL (1975) do not give any information about the type of projection used for their maps.

Method of Map Inversion. The inversion of these maps, i.e., the conversion from the rectangular cartesian coordinates of the contour lines on the printed map to a longitude-latitude coordinate system is a non-linear problem. For each map, six parameters had to be determined: the longitude and latitude of the origin of the projection (i.e. the point of tangency), the x, y coordinates of this pole on the map, and the scaling factors along the x (horizontal) and y (vertical) directions. We determined these parameters by a least-squares procedure applied to the nodes of the grid, for which the actual longitudes and latitudes were known. The NELDER-MEAD downhill simplex algorithm was used to perform the minimization (see, e.g., PRESS et al., 1989). The analytical expressions for transforming the geographical longitude-latitude into map x, y coordinates were taken from MALING (1992). To minimize errors, each map grid was read in at least twice, generally four times.

The digitized runoff contour lines were then interpolated on a regular longitude-latitude grid of $0.25° \times 0.25°$ resolution, using a DELAUNAY triangulation method. This resolution, which is much higher than that of GEM-CO_2, was necessary for the validation step of the map. While the construction of the digital runoff database was purposely performed for this

study, its validation was carried out by LUDWIG (1996). This validation was done by integrating the map over the surfaces of 60 major rivers basins of the world for which sufficiently accurate discharge data were available in the literature. The results compare rather well to the literature data, although part of them are more recent than 1977, the year when UNESCO published the World Water Balance Atlas. LUDWIG (1996) finds that the original map may be overestimating the actual runoff by about 10%. Since GEM-CO$_2$, when used together with this original map underestimates the overall river bicarbonate flux by about the same fraction (29.4×10^{12} mol/yr instead of 32.0×10^{12} mol/yr), the correction proposed by LUDWIG (1996) was not taken into account for the present study.

Before use with GEM-CO$_2$, the map was regridded onto the appropriate $1° \times 1°$ grid by simple fusion of arrays of 4×4 cells.

The resulting map at a $1° \times 1°$ resolution is shown in figure 7.3.

7.3.3 GCM-Based Runoff Distributions

Two ways can be considered to get runoff distributions from GCMs. For a few of them calculated runoff distributions R are readily available. Else, the difference between the calculated precipitation, P, and evapotranspiration, E, fields can be used. There are several problems with both approaches. On the long-term mean, R and $P - E$ should balance over the continents. Unfortunately, this is not always the case in the GCM results that were available for our study. In a few cases, the annual mean water budget over the continents was not balanced. One possible explanation for this would be that steady-state had not been reached by the end of the experiments. The results from one of the GCMs (NCAR-CCM0 (KUTZBACH and GUETTER, 1986; WRIGHT et al., 1993) nevertheless used by GIBBS and KUMP (1994) in a study similar to the present one) could not be used because its annual mean $P - E$ was negative over large continental areas, which does not make any physical sense. This can be seen in figure 7.4, where the distribution of the annual mean $P - E$ is compared with corresponding data from the UNESCO runoff distribution. Although there is some similarity between the two distributions, the differences are very large. The average $P - E$ over the global continental area (endoreic + exoreic regions) calculated from this GCM is only about 180 mm/yr, compared to 314 mm/yr obtained from the UNESCO map. Also represented in this figure is the LGM-minus-Present difference of $P - E$, used by GIBBS and KUMP (1994) to estimate the glacial-interglacial runoff variation. At low latitudes, it comes out that the calculated variation is almost of the same order of magnitude as the calculated present-day values. This points out that the glacial simulation presents negative $P - E$ values
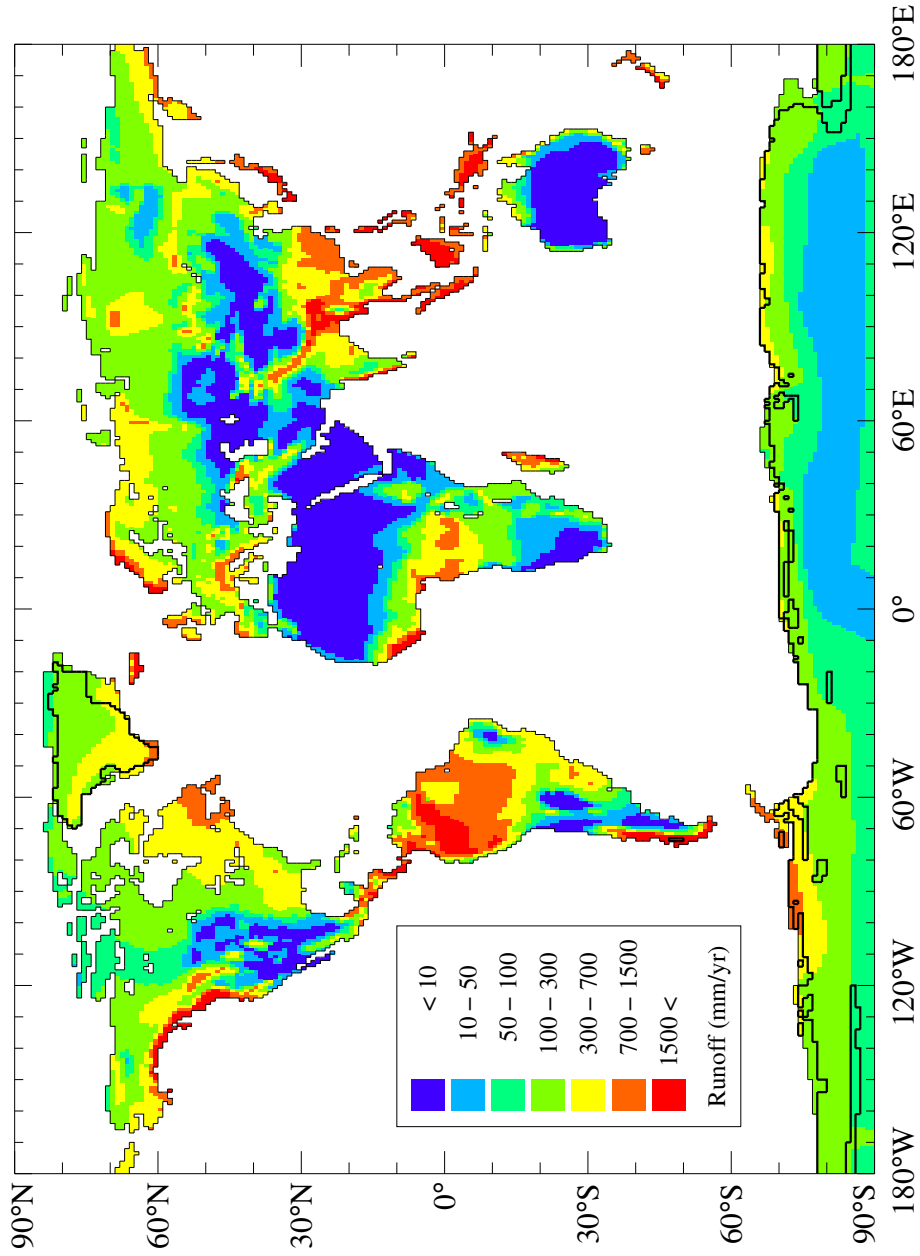
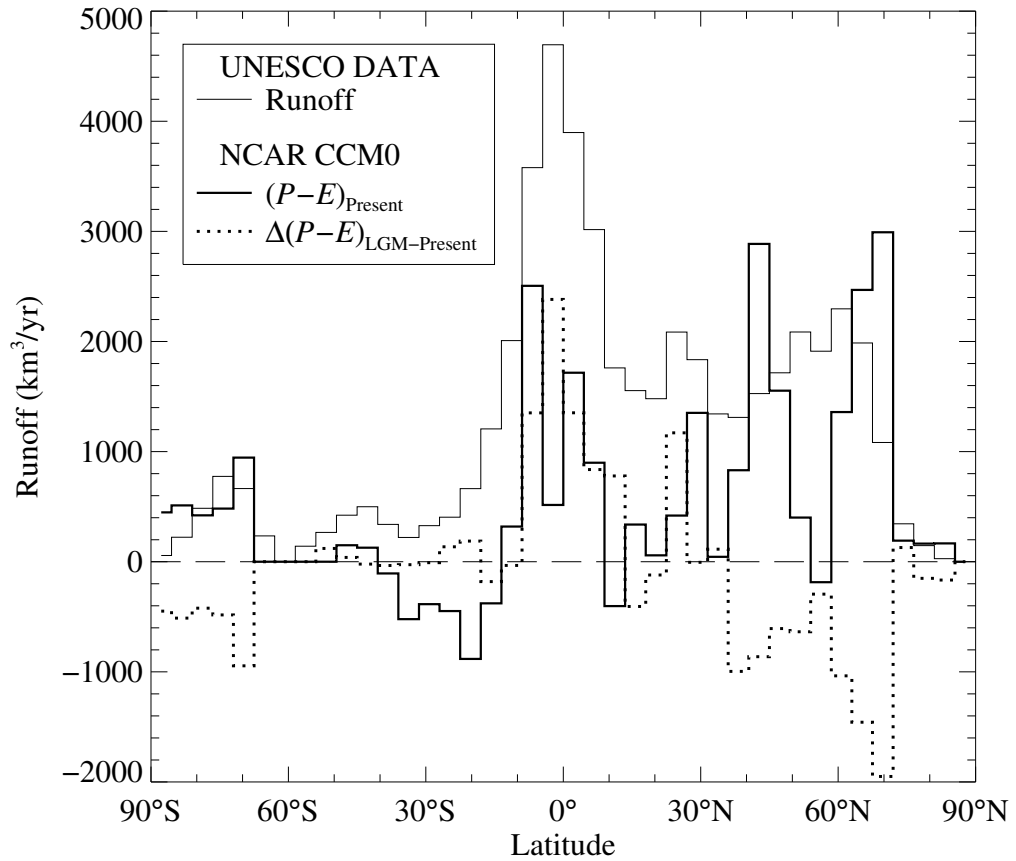Figure 7.3: Present-day distribution of continental runoff.

Figure 7.4: Latitudinal distribution of the present-day average continental $P - E$ (thick solid line) and of its variation between the LGM and Present (thick dotted line) as derived from the climate simulations with the NCAR-CCM0 Atmospheric General Circulation Model. For comparison, the runoff distribution from the UNESCO atlas, integrated over the same 4.5° wide latitudinal bands as the GCM, is also represented (thin solid line). Contributions from glaciated areas are not taken into account since the GCM data do not allow to distinguish between marine and continental ice.

over even much larger areas than the present-day control simulation. Because of these discrepancies we decided not to take the results from this model into account, not even for the calculation of glacial-interglacial anomalies.

Runoff distributions calculated by GCMs are furthermore often highly underestimated. Deviations of up to 50–75% from the observed runoff are quite common, due to excess evapotranspiration. A typical example of this shortcoming is the large Amazon river basin, for which we find that the models produce only a third of the actually observed discharge, although their precipitation distributions compares rather well to the field data.

In order to avoid the use of the GCM evapotranspiration and runoff fields, we resorted to the empirical runoff model of LUDWIG (1996). This author has shown that the annual mean distribution of continental runoff can be calculated in good approximation from the seasonal variability of precipitation and from the temperature distribution if morphological parameters such as slope are also taken into account. With this empirical method, based upon a statistical regression, temperature and precipitation are the only model outputs required to calculate runoff distributions. It has also the advantage that no extrapolation from the nearby continental points is required to obtain the runoff anomalies over continental margins that are covered by the ocean at present, but that were lying dry and were hence subject to erosion during the Last Glacial Maximum. The anomalies at such points can easily be calculated from precipitation and temperature. We have not taken the runoff fields provided by the GCMs into account for our experiments because of their very poor quality when compared to the observations. $P - E$ was only used as a runoff estimator when it made some physical sense, i.e., in case it was not negative over large areas, but we allowed for a few outliers in each case.

Table 7.4 lists the different models that we have considered, together with some basic characteristics. The results from the GISS model (HANSEN et al., 1983, 1984; RIND et al., 1986; OVERPECK et al., 1989) have been retrieved from the FTP server of the National Geophysical Data Center (NGDC) in Boulder, Colorado (data set 94-012, RIND, 1994), and those for ECHAM2 (see, e.g., LAUTENSCHLAGER and HERTERICH, 1990) from the server of the Deutsches KlimaRechenZentrum (DKRZ) in Hamburg. The LMD4bis and LMD5ter results have been provided by S. JOUSSAUME and G. RAMSTEIN of the Laboratoire de Modélisation du Climat et de l'Environnement (LMCE) in Saclay. The results from the NCAR-CCM0 model, not taken into account for our investigations for the reasons discussed earlier, have also been obtained from NGDC's FTP server (data set 94-025, KUTZBACH, 1994).

Table 7.5 summarizes the global exoreic runoff (i.e. from areas draining to the oceans) at the LGM derived from the various models using the two

Table 7.4: General Circulation Models used in this study.

GISS	NASA Goddard Institute for Space Studies, New York Resolution: $10° \times 7.83°$ (longitude $\times$ latitude), with half grid boxes ($10° \times 3.91°$) at the poles
ECHAM2	Deutsches Klimarechenzentrum, Hamburg. Resolution: $5.62° \times 5.62°$
LMD4bis	Laboratoire de Météorologie Dynamique, Paris, in the version of the Laboratoire de Modélisation du Climat et de l'Environnement, Saclay Resolution: grid with 48×36 equal-area elements, giving a resolution of $\sim 7.5° \times 3.2°$ at the equator and of $\sim 7.5° \times 4.5°$ near $45°$ of latitude
LMD5ter	Laboratoire de Météorologie Dynamique, Paris, in the version of the Laboratoire de Modélisation du Climat et de l'Environnement, Saclay. Resolution: grid with 64×50 equal-area elements, giving a resolution of $\sim 5.62° \times 2.3°$ at the equator and of $\sim 5.62° \times 3.2°$ near $45°$ of latitude

Table 7.5: Runoff from the different types of exoreic areas at LGM.

GCM	R^{GCM}	Exposed Areas		Ice-covered Areas	
		Present-day Land	Emerged Shelf	Present-day Land	Emerged Shelf
Modern	—	45,100	—	2,600	—
GISS	Empir.	34,800	9,600	12,800	7,300
ECHAM2	$P-E$	37,800	10,300	6,200	7,100
	Empir.	32,400	9,100	11,200	5,900
LMD4bis	$P-E$	37,900	10,100	11,400	6,500
	Empir.	35,900	10,900	11,100	6,600
LMD5ter	$P-E$	35,600	12,500	12,000	5,900

All fluxes are given in cubic kilometers of water per year, and have been rounded to the nearest hundred before reporting. The 'Modern' values have been derived from our $1° \times 1°$ version of the digitized UNESCO map and have been included for comparison.

runoff calculation methods outlined before. To apply equation (7.1), R^{GCM} has either been calculated from the empirical model, using the GCM's precipitation and temperature fields only (labelled 'Empir.' in the R^{GCM} column), or taken as $R^{\mathrm{GCM}} = P^{\mathrm{GCM}} - E^{\mathrm{GCM}}$ (indicated by '$P-E$'), using the P^{GCM} and E^{GCM} fields from the GCM climatology. In each case, the required GCM fields were remapped to the $1° \times 1°$ grid of GEM-CO₂ by area-weighted redistribution. The empirical model could unfortunately not be used with the LMD5ter fields because of computer limitations. The present-day runoff values as calculated from our $1° \times 1°$ version of the UNESCO map, have been included for comparison in the table.

7.4 Glacial-Interglacial Carbon Dioxide Consumption Variability

Using the continental runoff and lithology reconstructions described in the previous section, we can now calculate both the amount of atmospheric CO₂ consumed by continental weathering and the resulting riverine bicarbonate yield with the help of GEM-CO₂. As already outlined in chapter 6, the respective roles of silicate and carbonate rock weathering can easily be estimated from these two quantities. The total river bicarbonate yield,

$HCO_3^-{}_{(tot)}$, can be partitioned in two ways, either according to its sources, or else according to the kind of weathering it originates from: (1) — into a part coming from the soil/atmosphere, $HCO_3^-{}_{(atm)}$, and a part coming from the dissolving carbonate rock minerals, $HCO_3^-{}_{(cark)}$, and (2) — into a part that has gone through silicate weathering, $HCO_3^-{}_{(sili)}$, and a part having gone through carbonate rock weathering, $HCO_3^-{}_{(carb)}$. Hence,

$$HCO_3^-{}_{(tot)} = HCO_3^-{}_{(atm)} + HCO_3^-{}_{(cark)} \qquad (7.2)$$

$$HCO_3^-{}_{(tot)} = HCO_3^-{}_{(sili)} + HCO_3^-{}_{(carb)}. \qquad (7.3)$$

GEM-CO_2 provides $HCO_3^-{}_{(tot)}$ and $HCO_3^-{}_{(atm)}$. Since we do not consider the role of sulphuric acid coming from pyrite oxidation here, $HCO_3^-{}_{(cark)}$ and $HCO_3^-{}_{(carb)}$ are related by

$$HCO_3^-{}_{(carb)} = 2 \times HCO_3^-{}_{(cark)}. \qquad (7.4)$$

As a consequence,

$$HCO_3^-{}_{(carb)} = 2 \times (HCO_3^-{}_{(tot)} - HCO_3^-{}_{(atm)}) \qquad (7.5)$$

$$HCO_3^-{}_{(sili)} = 2 \times HCO_3^-{}_{(atm)} - HCO_3^-{}_{(tot)}. \qquad (7.6)$$

The values for $HCO_3^-{}_{(tot)}$ and $HCO_3^-{}_{(atm)}$, derived from GEM-CO_2 for the reconstructed LGM lithology and for the various runoff distributions obtained from the different models, are reported in table 7.6, together with the corresponding $HCO_3^-{}_{(sili)}$ and $HCO_3^-{}_{(carb)}$ fluxes. The global fluxes have been separated into a part originating from the exposed shelf, and another one coming from the continental areas still exposed at present-day.

The first observation that must be done is that the glacial-interglacial variation of the respective CO_2 consumption rates are in all cases much smaller than those obtained by the inversions of the marine Sr isotope and the Ge/Si records, reported in the previous two chapters. With regard to the CO_2 consumption rate by silicate weathering, the results presented in table 7.6 are not really in contradiction with the reconstruction derived from the Sr isotope record. First of all, our reconstruction in chapter 5 is based upon a glacial-interglacial variation of ± 12 ppm of the $^{87}Sr/^{86}Sr$ ratio. The maximum possible amplitude of ± 9 ppm (HENDERSON et al., 1994a) is only 25% smaller. Then, we have shown that either source redistribution (changing average river $^{87}Sr/^{86}Sr$ ratio) or Sr flux variations could act as single mechanisms to generate the glacial-interglacial variations of the marine $^{87}Sr/^{86}Sr$. However the results of table 7.6 are clearly in contradiction with those from

Table 7.6: Partitioning of the LGM river bicarbonate yields for the standard shelf lithology.

GCM	R^{GCM}	Present-day Land				Emerged Shelf				Total LGM Continent			
		tot	atm	sili	carb	tot	atm	sili	carb	tot	atm	sili	carb
Modern	—	29.4	21.0	12.6	16.8	—	—	—	—	29.4	21.0	12.6	16.8
GISS	Empir.	23.8	17.0	10.2	13.6	12.3	8.4	4.5	7.8	36.1	25.4	14.7	21.4
ECHAM2	$P-E$	24.6	17.4	10.2	14.4	10.1	7.8	5.5	4.6	34.7	25.2	15.7	19.0
	Empir.	20.9	15.2	9.5	11.4	10.0	7.3	4.6	5.4	30.9	22.5	14.1	16.8
LMD4bis	$P-E$	24.8	17.7	10.6	14.2	12.5	8.7	4.9	7.6	37.3	26.4	15.5	21.8
	Empir.	24.2	16.9	9.6	14.6	12.3	8.9	5.5	6.8	36.5	25.8	15.1	21.4
LMD5ter	$P-E$	24.2	17.5	10.8	13.4	14.3	10.2	6.1	8.2	38.5	27.7	16.9	21.6

All fluxes in 10^{12} mol/yr. 'Modern' values are obtained from GEM-CO$_2$, using the UNESCO runoff map.

Table 7.7: River bicarbonate flux partitioning for different shelf lithologies.

GCM	R^{GCM}	Full Shale	Standard				Full Carbonate	
		tot/atm/sili	tot	atm	sili	carb	tot/carb	atm
GISS	Empir.	6.0	12.3	8.4	4.5	7.8	30.5	15.3
ECHAM2	$P-E$	6.4	10.1	7.8	5.5	4.6	32.6	16.3
	Empir.	5.7	10.0	7.3	4.6	5.4	28.8	14.4
LMD4bis	$P-E$	6.3	12.5	8.7	4.9	7.6	32.1	16.0
	Empir.	6.9	12.3	8.9	5.5	6.8	34.7	17.3
LMD5ter	$P-E$	7.8	14.3	10.2	6.1	8.2	39.6	19.8

All fluxes in 10^{12} mol/yr. For full shale shelves, $\mathrm{HCO_3^-}_{\,(\mathrm{carb})} = 0$, and for full carbonate shelves, $\mathrm{HCO_3^-}_{\,(\mathrm{sili})} = 0$.

the Ge/Si inversion (chapter 6), where we found that glacial rates should at least be of the order of 10×10^{12} mol/yr (or 95%) higher than the present interglacial ones. Nevertheless, it would have been unreasonable to expect such large variations from the GEM-CO_2 approach. Because GEM-CO_2 relates the CO_2 consumption rates in a linear way to continental runoff, this latter would have had to change by a factor of 2–3 as well in order to reach the high consumption rates calculated from the inversion of the marine Ge/Si. There are several reasons that we may call upon to explain this discrepancy. On one hand, we must not forget that our present knowledge of the Ge cycle still needs to be better constrained by observational data. On the other hand, GEM-CO_2 does in no way take the concept of weathering intensity into account: it assumes that for a given runoff volume, CO_2 consumption rates are the same, whatever the climate condition, the weathering regime, and the physical weathering intensity. It furthermore neglects chemical weathering in glaciated areas.

Let us now have a more thorough look at the results from table 7.6. Despite its small area (13.6×10^6 km² or 14% of the total exoreic, ice-free area of 97.3×10^6 km² — see table 7.3), the exposed shelf is responsible for a large part of the global response according to our results. If only the present-day continental area had been considered, the overall consumption rate of CO_2 by continental weathering would indeed have been of the order of 20% lower at the Last Glacial Maximum than at present. Taking the exposed shelf into account nevertheless leads to an overall LGM consumption rate that exceeds the present one by about 20%. Similar differences can be observed for the total bicarbonate yield. This is due to the relatively high runoff in these regions that are close to the oceans. In the ice-free areas, the average exoreic runoff in our LGM reconstructions is about 700–950 mm/yr over the exposed continental shelf and 380–450 mm over the present-day land. The results obtained by the empirical runoff model with the GISS and the ECHAM2 climates illustrate this point. Although the runoff over the presently emerged continental area is reduced by about 20 and nearly 30% in these two cases respectively, they still lead to enhanced CO_2 consumption at the LGM. This shelf effect also explains why our general conclusion that the glacial average CO_2 consumption rates by weathering were *higher* at the Last Glacial Maximum than they are at present is apparently at odds with the findings of Ludwig (1996). This author does in fact not explicitly take the weathering of the exposed shelf into account. The contribution from the exposed shelf is merely calculated by extrapolation from the land also exposed at present, differences between climatic zones being taken into account. His results suggest that CO_2 consumption rates should have been at least 10–15% *lower* at the LGM than today (Ludwig, 1996; Ludwig et al., 1997). If we

adopt a simple surface-weighted extrapolation of our CO_2 consumption rates from the land exposed both now and at the LGM (15.2–17.7×10^{12} mol/yr for an area of 84.2×10^{12} km^3 — see 'Present-day Land' columns in table 7.6) to the whole exoreic part of the continent, we obtain a global consumption of 17.6–20.5×10^{12} mol/yr for an area of 97.3×10^{12} km^3, i.e., of the order of 5–15% lower than the present-day rate of 21.0×10^{12} mol/yr calculated from GEM-CO_2. Interestingly, the upper extreme of 15% corresponds to the empirical runoff reconstruction with the ECHAM2 climatology. This is exactly the combination adopted by LUDWIG (1996), although in a more elaborate way.

To further analyse the importance of the continental margins lying dry at the LGM, we made another two series of sensitivity calculations, where we took them as monolithologic (consisting only of carbonates or only of shales). The results of these calculations are given in table 7.7, where we compare them with the results for the standard shelf lithology, taken from 7.6 above it.

Regarding the inter-model variability, it can be seen that the empirical approach for the runoff calculation generally leads to lower global discharges, and hence to lower consumption of CO_2 and of bicarbonate production. Furthermore, we find that the two LMD models generate the largest variations.

7.5 Carbon Cycle Model Simulations and Discussion

The $HCO_{3\ (carb)}$ and $HCO_{3\ (sili)}$ calculated for the LGM and the pre-industrial periods are now used to construct simple sawtooth-shaped forcing scenarios for our carbon cycle model. Figure 7.5 shows the resulting forcing functions, varying linearly between the LGM and pre-industrial values reported in table 7.7. Forced by these input scenarios, the carbon cycle model calculates the evolution of the atmospheric CO_2 levels over time. The model nevertheless requires some important recalibration before using these scenarios. If we adopt the set of transient parameters reported in table 4.7, our simulations end up with about 310 ppm of CO_2 in the pre-industrial atmosphere, as shown in the top panel of figure 7.6. It furthermore produces much too small concentrations of total alkalinity and dissolved inorganic carbon over the whole ocean, and lysoclines are by 1,000 m too shallow. To bring the pre-industrial model ocean back close to the observed state, given in table 4.3, we had to reduce the rain ratios in the Surface Equatorial Atlantic and Indo-Pacific, r^C_{SEATL} and $r^C_{\mathrm{SEI-P}}$ from 0.35 to 0.28, and from 0.25 to 0.23 respectively. Further-
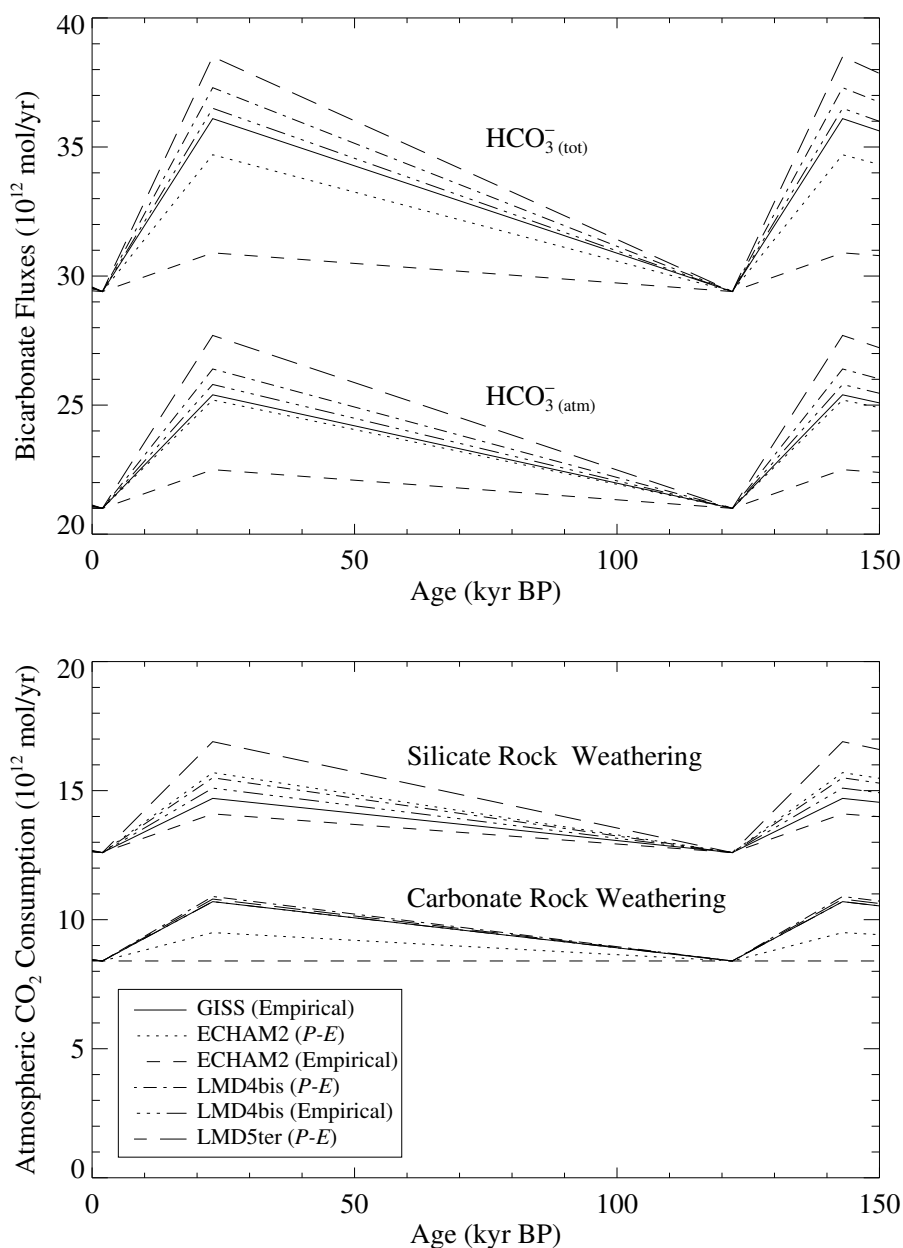
Figure 7.5: Adopted scenarios for the evolution of $HCO_3^-{}_{(tot)}$ and $HCO_3^-{}_{(atm)}$ (top), and corresponding CO_2 consumption rates by silicate and carbonate weathering (bottom) derived from the variations between the LGM and the present-day, calculated by GEM-CO_2 according to the different runoff reconstructions, as reported in table 7.6. The scales of the two panels are the same, only the ranges differ. The fluxes can thus be easily compared.
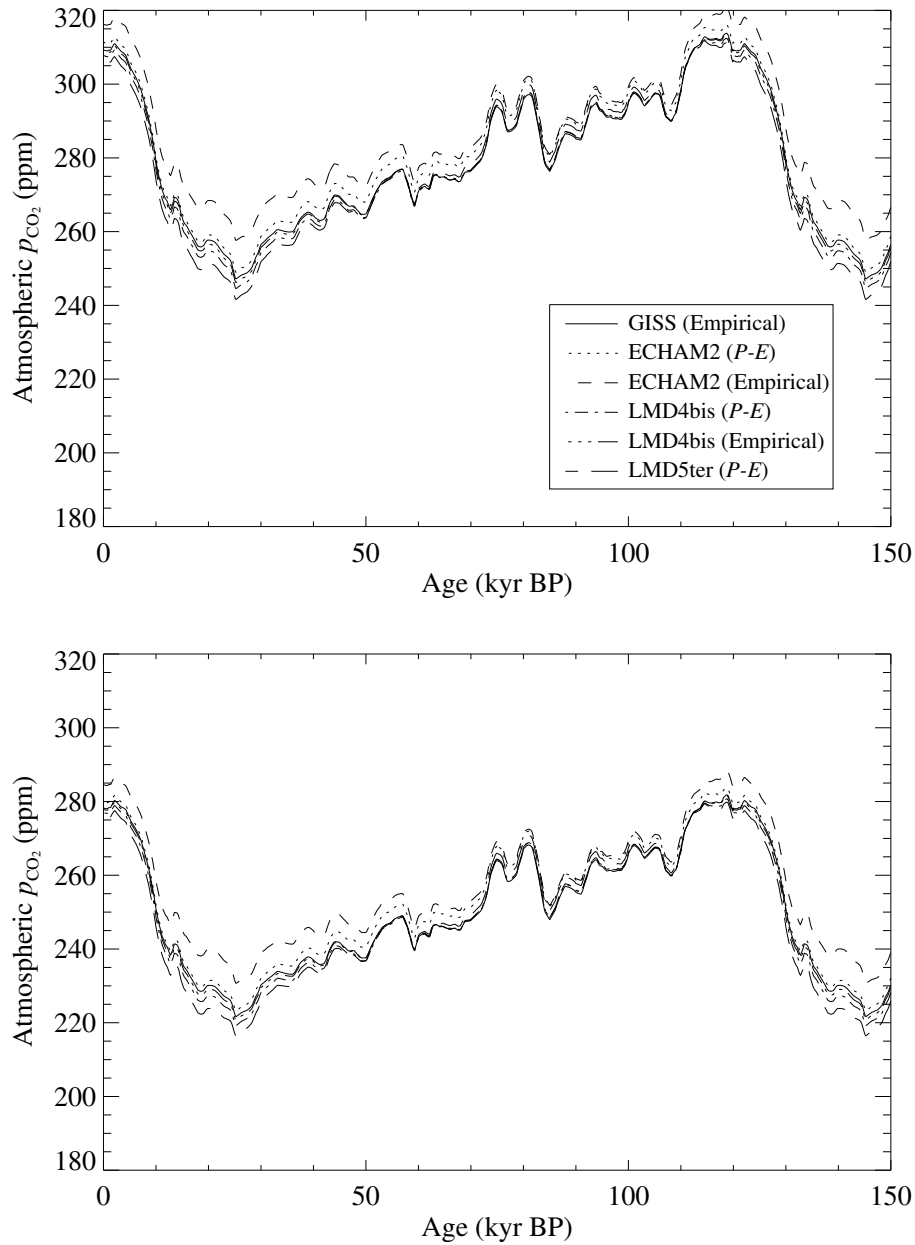
Figure 7.6: Atmospheric CO_2 variations derived from the reconstructed weathering histories, using the standard transient set of parameters given in table 4.7 (top) and after recalibration of the model, as described in the text (bottom). The general shift by about 30 ppm between the two sets of results is accompanied by profound changes in the global ocean distributions of C_T and A_T.

more, we had to increase the aragonite fraction to almost its value for the steady-state adjustment, from 0.37 to 0.65. Table 7.8 gives a summary on how these parameter changes affect the deep-sea distributions of C_T and A_T, as well as the CSDs in our model. However, the tracer distribution reached at the pre-industrial with these adapted parameter values is not as good as that from the transient adjustment: the residual R defined in chapter 4 for the calibration procedure (see page 143), is now of 5.38, compared to 5.03 for the earlier transient adjustment. From a qualitative point of view, it is thus only comparable to our steady-state adjustment, which is characterized by a residual of 5.36. As a consequence of this recalibration, the overall export of carbonate from the surface reservoirs in our model slightly decreases from 51.7×10^{12} mol/yr to 47.8×10^{12} mol/yr. The deep-sea deposition rate also decreases, from 14.9×10^{12} mol/yr to 8.7×10^{12} mol/yr, while the input due to chemical erosion of deep-sea sediments decreases from 13.5×10^{12} mol/yr to 6.7×10^{12} mol/yr. Shelf deposition rates are only marginally affected by this modification.

The computed evolutions of CO_2 in the atmosphere after this recalibration are represented in the bottom panel of figure 7.6. The model still produces rather large variations, with a peak-to-peak amplitude of about 55–60 ppm. But only a small fraction of this response, 12 ± 5 ppm, comes from the changing rates of CO_2 consumption by silicate rock weathering, as shown in figure 7.7.

To estimate the contribution from silicate weathering we have produced the same kind of control runs as for the scenarios from the inversion of the Ge/Si signal. For these control runs, the variable CO_2 consumption rates by silicate weathering were in each case held constant at their glacial-interglacial levels. The evolutions from these control runs are then subtracted from the full responses shown in figure 7.6. It appears from figure 7.7 that only a small fraction of the response, 12 ± 5 ppm, comes from the changing rates of CO_2 consumption by silicate rock weathering. Most of the response must therefore be attributed to the changing carbonate weathering, and to the changing basin-to-shelf partitioning of carbonate accumulation in the ocean.

All of the weathering scenarios defined in table 7.6 give rise to variations of about 800 m of the Calcite Saturation Depth in the deep Indo-Pacific reservoir. This amplitude is in much better agreement with the estimated variation of 600 m (FARRELL and PRELL, 1989) than that generated by the Ge/Si based scenarios, which generally led to excursions of more than 2 km. Most of these latter scenarios in turn produce pH variations in good agreement with both the surface- and the deep-water pH reconstructions of SANYAL et al. (1995). But, as mentioned in the review chapter on the global carbon cycle, there is a contradiction between the sedimentary carbonate

Table 7.8: Effect of the model recalibration

	DATL	DANT	DI-P
Dissolved Inorganic Carbon			
Before Recalibration	2.26	2.32	2.37
After Recalibration	2.31	2.36	2.42
Data Constraints	2.30	2.36	2.42
Transient Adjustment	2.30	2.36	2.42
Total Alkalinity			
Before Recalibration	2.37	2.38	2.43
After Recalibration	2.45	2.47	2.51
Data Constraints	2.44	2.46	2.52
Transient Adjustment	2.44	2.47	2.52
Calcite Saturation Depth			
Before Recalibration	3,300	2,000	1,750
After Recalibration	4,250	3,050	2,850
Data Constraints	4,300	3,400	3,000
Transient Adjustment	4,200	3,100	3,000

The distributions of C_T, A_T and the calcite saturation depths in the deep reservoirs at the pre-industrial simulation end as calculated from the 'GISS (Empir.)' scenario (solid lines in figures 7.5 and 7.6) before and after recalibration are compared here with the adopted data constraints and the best-fit distributions from the transient adjustment described in chapter 4, on pages 146 and 147.
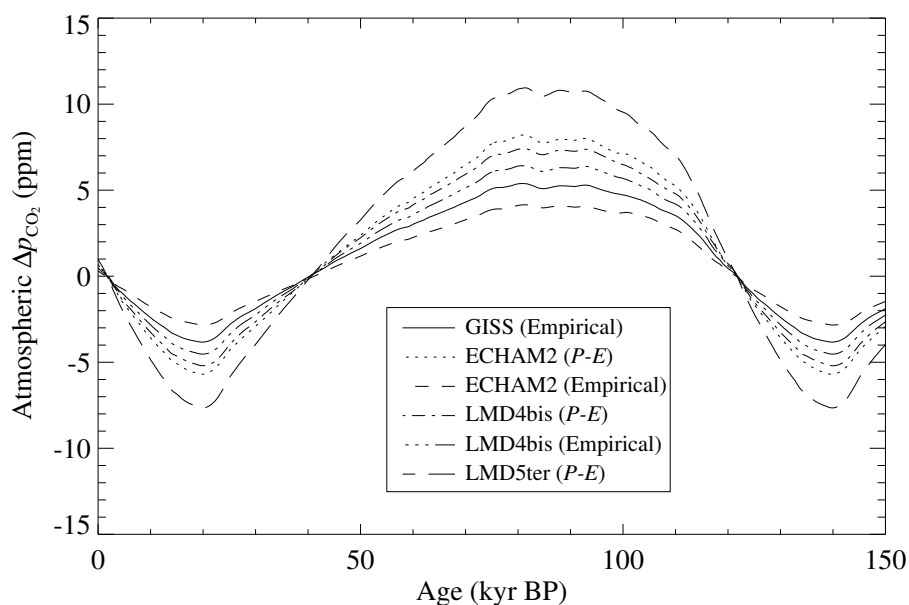
Figure 7.7: Net contribution of silicate weathering processes in the total variations of atmospheric CO_2 generated by the different weathering histories.

content record and the pH reconstructions based upon boron isotopes that still has to be explained.

In conclusion, the results presented in this chapter confirm those from the earlier study by GIBBS and KUMP (1994). They seem to contradict the conclusions of LUDWIG (1996) who finds that weathering consumed 15% less CO_2 during glacial times than at present. As shown above, this is clearly related to the simplified treatment of the emerged shelf areas in his study. However, the disagreement with our own results obtained by the inversion of the marine Ge/Si record, a completely independent method (MUNHOVEN and FRANÇOIS, 1996), is more difficult to explain, and will require further study. This problem can probably only be solved once our quantitative understanding of the germanium cycle, and especially of its relationship with weathering intensity, which remains very qualitative for the moment, has been improved. Some basic hypotheses of GEM-CO_2, such as the assumed absence of chemical weathering in ice-covered regions, should probably also be reconsidered. But the carbon cycle model recalibration that was necessary before using the calculated river bicarbonate scenarios also points out the need for a better understanding of the marine carbon cycle.

Summary and Conclusions

In this study, we have developed an 11-box model of the ocean-atmosphere subsystem of the global carbon cycle, including sedimentary processes. We have used this model to explore the impact of continental weathering processes, and especially of silicate rock weathering, on the evolution of CO_2 in the atmosphere as documented by the Vostok ice core record. Previous studies dealing with the observed glacial-interglacial CO_2 cycles have focused on oceanic processes alone, generally neglecting the CO_2 fluxes involved in rock weathering processes (with the notable exceptions of KEIR and BERGER (1983) who included a constant riverine supply of Ca^{2+} and HCO_3^-, and of OPDYKE and WALKER (1992b) and WALKER and OPDYKE (1995), who included a variable input of bicarbonate from the erosion of shelf carbonates during glacial times).

We have adopted three different approaches to derive possible histories of the evolution of the consumption rate of atmospheric CO_2 and the resulting transfer of bicarbonate by rivers to the ocean.

1. *A tracer-based approach, using the marine strontium isotopic record.* This record suggests that the flux of alkalinity delivered to the ocean from continental silicate weathering may have been substantially larger during glacial times than today. We have demonstrated that it is possible to obtain a history of silicate rock weathering, that reproduces both the strontium isotopic record and the glacial-interglacial CO_2 signal, when used in our carbon cycle model (which includes a coral reef model). According to that weathering history, the consumption of atmospheric CO_2 by silicate rock weathering was about 1.2 times higher during glacial than during interglacial time.

2. *A second tracer-based approach, using the marine Ge/Si record.* The inversion of this signal provides histories for the glacial-interglacial evolution of riverine silica fluxes. These are converted into equivalent CO_2 consumption histories. We find that glacial rates of CO_2 consumption by chemical silicate rock weathering could have been 2–3.5 times as

high as they are today. This leads to p_{CO_2} variations with amplitudes of 80–90 ppm, and in some cases of up to 125–135 ppm. Silicate weathering contributes typically for 50–60 ppm and up to 95–110 ppm to the total variation. This large atmospheric CO_2 change goes together with a deepening of the calcite saturation depth by more than 2 km in the deep ocean during glacial time. This is much larger than the observed lysocline deepening of about 600 m, observed in sediments from the equatorial deep Pacific (FARRELL and PRELL, 1989). However, the glacial-to-interglacial pH decrease of 0.24 in the deep ocean produced by the scenarios with a high amplitude falls well within the range of 0.3 ± 0.1 observed by SANYAL et al. (1995).

3. *A model-based approach, using the global erosion model GEM-CO₂.* The GEM-CO₂ model has been adapted to ice age conditions, by extending its lithological map to the shelf areas. The continental runoff at LGM is derived from four different GCM climatologies. We calculated that CO_2 consumption and river bicarbonate fluxes were about 20% higher at LGM than at present-day. The constructed weathering scenarios can produce p_{CO_2} variations of about 60 ppm between glacial and interglacial times, but the contribution from variable silicate weathering to this signal is estimated at 12 ± 5 ppm only. The largest part of the signal comes from the basin-to-shelf repartitioning of the carbonate deposition. The produced lysocline variations of the order of 800 m, are in better agreement with the observations, whereas the deep-sea pH changes are limited to 0.1.

As the $^{87}Sr/^{86}Sr$ record has been withdrawn in the meantime, we focus on the results obtained from the Ge/Si inversion and the erosion model scenarios in this final discussion.

Our model results confirm the efficiency of the coral reef buildup and erosion as driving forces of atmospheric CO_2 variations over glacial-interglacial time scales. They furthermore stress that climate-driven changes of the CO_2 consumption by chemical rock weathering — previously not taken into account — have the potential to generate atmospheric p_{CO_2} variations that are much too large to be neglected.

Just like previous hypotheses, the proposed weathering scenarios have consequences that are not in agreement with all of the available deep-sea records. The GEM-CO₂ based scenarios produce variations of the calcite saturation depth that are in better agreement with the observed evolution of the lysocline depth than those obtained from the Ge/Si scenarios. The latter are in better agreement with the deep-sea pH reconstructions. Only

when new light is shed on the contradiction between the pH and the lysocline variations can we discriminate between the two.

The p_{CO_2} evolution produced from the GEM-CO$_2$ scenarios is not large enough to reproduce the Vostok signal, but in shape, it is nevertheless very similar. With the present version of GEM-CO$_2$, we cannot expect large glacial-interglacial variations, because it calculates CO$_2$ consumption rates as a linear function of runoff, and neglects chemical weathering in glacierized areas.

The p_{CO_2} variations produced from the Ge/Si based scenarios on the other hand are even larger than the observed variation. A changing CO$_2$ consumption by silicate weathering could hence help to compensate for the p_{CO_2} variations related to the carbon transfer from the ocean to the terrestrial biosphere at the deglaciation. It also raises new problems, such as too high CO$_2$ levels during the period from 110–70 kyr BP. However, it should not be forgotten that there are many other processes at work that have not been taken into account here, such as productivity, respiration-driven dissolution of carbonate in the sea-floor sediments, ocean circulation.

The most important topics to be envisaged for future research include

- the impact of circulation changes, especially with regard to the different lysocline variations in the Atlantic and the Pacific;

- respiration-driven carbonate dissolution in the sedimentary part of the model;

- quantitative study of chemical erosion enhancement by glaciers, due to the production of fine grained, easily weatherable material;

- systematic analysis of the silica-bicarbonate relationships in rivers in order to test the proposed interpretation of the ratio of bicarbonate derived from silicate weathering alone to dissolved silica as a weathering indicator.

Addressing these problems will help to understand and to reduce the discrepancies between the results obtained from the different methods described in this study.

Appendix A

Constants and Data

Table A.1: Earth Data

Area of the Earth	509.90×10^{12} m^2
Volume of the Oceans	1.3414×10^{18} m^3
Area of the Oceans	358.46×10^{12} m^2
Continental Runoff	37.4×10^{12} m^3/yr (MEYBECK, 1979)
	45.0×10^{12} m^3/yr (KORZOUN et al., 1977)

Table A.2: Physical Constants

Avogadro number	N_A	6.0221367×10^{23} mol^{-1}
Molar gas constant	R	8.314510 J mol^{-1} K^{-1}

Table A.3: Composition of 1 kg of Average Seawater

Solute	g/Cl($^0\!/_{00}$)	g/S	g	mol
Na$^+$	0.55653	0.30806	10.78221	0.46900
Mg^{2+}	0.06626	0.03668	1.28372	0.05282
Ca^{2+}	0.02127	0.01177	0.41208	0.01028
K$^+$	0.02060	0.01140	0.39910	0.01021
Sr^{2+}	0.00041	0.00023	0.00794	0.00009
Cl$^-$	0.99891	0.55294	19.35288	0.54588
SO$_4^{2-}$	0.14000	0.07750	2.71236	0.02823
HCO$_3^-$	0.00586	0.00324	0.11353	0.00186
Br$^-$	0.00347	0.00192	0.06723	0.00084
CO$_3^{2-}$	0.00060	0.00033	0.01162	0.00019
B(OH)$_4^-$	0.00034	0.00019	0.00659	0.00008
F$^-$	0.00007	0.00004	0.00130	0.00007
B(OH)$_3$	0.00105	0.00058	0.02034	0.00033
Total	1.81537	1.00488	35.17090	—

The first two columns give the abundances of each solute in grams per unit chlorinity and salinity respectively. The last two give the total composition respectively in grams and in moles for each solute, for seawater with $S = 35$ ($Cl = 19.374$ $^0\!/_{00}$). After MILLERO (1982b) and MILLERO and SOHN (1992).

Appendix B

Technical Results

In this appendix chapter, we present some theoretical results used for this study and technical developments which would have made the main text too difficult to read.

B.1 Component Ratios in a Reservoir: General Differential Equation of Variations

Let us consider a reservoir containing amounts Q and q of two components Q and q. The respective mass balance equations for these two are

$$\frac{dq}{dt} = \sum_i (\mathcal{F}_{\mathrm{q}}^{\mathrm{in}})_i - \sum_j (\mathcal{F}_{\mathrm{q}}^{\mathrm{out}})_j \qquad (\mathrm{B.1})$$

and

$$\frac{dQ}{dt} = \sum_i (\mathcal{F}_{\mathrm{Q}}^{\mathrm{in}})_i - \sum_j (\mathcal{F}_{\mathrm{Q}}^{\mathrm{out}})_j \qquad (\mathrm{B.2})$$

where $(\mathcal{F}_{\mathrm{q}}^{\mathrm{in}})_i$ and $(\mathcal{F}_{\mathrm{q}}^{\mathrm{out}})_j$ are the in- and output fluxes of q for the reservoir (and correspondingly for Q). If we denote r the q/Q ratio of the reservoir (i. e. $r = q/Q$), $r_i^{\mathrm{in}} = (\mathcal{F}_{\mathrm{q}}^{\mathrm{in}})_i / (\mathcal{F}_{\mathrm{Q}}^{\mathrm{in}})_i$ and $r_j^{\mathrm{out}} = (\mathcal{F}_{\mathrm{q}}^{\mathrm{out}})_j / (\mathcal{F}_{\mathrm{Q}}^{\mathrm{out}})_j$ those of the in- and output fluxes respectively, equation (B.1) can be rewritten as

$$\frac{dq}{dt} = \sum_i \left((\mathcal{F}_{\mathrm{Q}}^{\mathrm{in}})_i \times r_i^{\mathrm{in}} \right) - \sum_j \left((\mathcal{F}_{\mathrm{Q}}^{\mathrm{out}})_j \times r_j^{\mathrm{out}} \right). \qquad (\mathrm{B.3})$$

On the other hand,

$$\frac{dq}{dt} = \frac{d(rQ)}{dt} = \frac{dr}{dt} Q + r \frac{dQ}{dt}. \qquad (\mathrm{B.4})$$

By eliminating dq/dt between equations (B.3) and (B.4), we find that

$$Q \frac{dr}{dt} = \sum_i \left((\mathcal{F}_Q^{\text{in}})_i \times r_i^{\text{in}} \right) - \sum_j \left((\mathcal{F}_Q^{\text{out}})_j \times r_j^{\text{out}} \right) - r \frac{dQ}{dt}. \tag{B.5}$$

If we now take (B.2) into account and regroup the corresponding terms, we finally obtain the following equation which can be used to describe the evolution of r in time, as a function of the exchange fluxes and their respective q/Q

$$Q \frac{dr}{dt} = \sum_i \left((\mathcal{F}_Q^{\text{in}})_i \times (r_i^{\text{in}} - r) \right) - \sum_j \left((\mathcal{F}_Q^{\text{out}})_j \times (r_j^{\text{out}} - r) \right) \tag{B.6}$$

Sometimes, there are exchange fluxes which can not be evaluated in terms of distinct in- and outputs, but only as net exchange fluxes $(\mathcal{N}_Q)_k$ and $(\mathcal{N}_q)_k$. In this case, the previous equation can be written in the more general form

$$Q \frac{dr}{dt} = \sum_i \left((\mathcal{F}_Q^{\text{in}})_i \times (r_i^{\text{in}} - r) \right) - \sum_j \left((\mathcal{F}_Q^{\text{out}})_j \times (r_j^{\text{out}} - r) \right)$$
$$+ \sum_k \left((\mathcal{N}_q)_k - (\mathcal{N}_Q)_k \times r \right) \tag{B.7}$$

where we have supposed that the net fluxes represent algebraic gains for the reservoir.

This equation (in its first or its second form, whichever is most appropriate) serves as a starting point to establish the equations that govern the evolution for a various q/Q ratios, such as ^{13}C/C and ^{14}C/C (section 4.2), ^{87}Sr/^{86}Sr or Ge/Si. Each time, specific adaptations may be required. In the case of ^{87}Sr/^{86}Sr for example, the two other Sr isotopes ^{84}Sr and ^{85}Sr must be taken into account in order to relate variations of the ^{87}Sr/^{86}Sr ratio to gross Sr fluxes instead of ^{86}Sr fluxes as the raw equations above would require.

The information on $r = q/Q$ is often not reported as an absolute figure, but rather as the relative deviation δ from a standard ratio $r_* = (q/Q)_{\text{std}}$, i. e.

$$\delta = \frac{r - r_*}{r_*}. \tag{B.8}$$

^{13}C/C and ^{14}C/C are probably the most important examples in this context, but others exist as well. The equation governing the evolution of δ in time is then

$$Q \frac{d\delta}{dt} = \sum_i \left((\mathcal{F}_Q^{\text{in}})_i \times (\delta_i^{\text{in}} - \delta) \right) - \sum_j \left((\mathcal{F}_Q^{\text{out}})_j \times (\delta_j^{\text{out}} - \delta) \right), \tag{B.9}$$

obtained from equation (B.6) by replacing the different ratios r by their equivalents $(\delta + 1)r_*$ taken from (B.8) and simplifying for r_*.

B.2 Linear Ordinary Differential Equation With Periodic Coefficients

Theorem. *Let f and g be two continuous real functions, periodic of the same period T. The solution R of the ordinary differential equation*

$$\frac{dR}{dt} = f(t)R + g(t), \quad R(t_0) = R_0 \tag{B.10}$$

can be written in the general form

$$R(t) = G(t) + H(t)E(t)$$

where G and H are periodic of period T, and where E is exponential in t if f has a non zero integral mean over one period of length T, and E is linear in t else.

Proof. The solution of the differential equation (B.10) is of course

$$R(t) = \exp(F(t)) \left(\int_{t_0}^{t} g(u) \exp(-F(u)) \, du + R_0 \right)$$

where

$$F(t) = \int_{t_0}^{t} f(u) \, du.$$

$$
\begin{aligned}
R(t + T) &= \exp(F(t+T)) \left(\int_{t_0}^{t+T} g(u) \exp(-F(u)) \, du + R_0 \right) \\
&= \exp(F(t+T)) \left(\int_{t_0}^{t_0+T} g(u) \exp(-F(u)) \, du \right. \\
&\qquad\qquad \left. + \int_{t_0+T}^{t+T} g(u) \exp(-F(u)) \, du + R_0 \right)
\end{aligned}
$$

Defining

$$I_{gF} = \int_{t_0}^{t_0+T} g(u) \exp(-F(u)) \, du$$

and changing the variable u to $v = u - T$, we can rewrite this previous identity as

$$R(t+T) = \exp(F(t+T)) \left(I_{gF} + \int_{t_0}^{t} g(v) \exp(-F(v+T)) \, dv + R_0 \right) \tag{B.11}$$

Defining

$$I_f = \int_{t_0}^{t_0+T} f(u)\, du$$

we find that

$$
\begin{aligned}
F(t+T) &= \int_{t_0}^{t+T} f(u)\, du \\
&= I_f + \int_{t_0+T}^{t+T} f(u)\, du \\
&= I_f + \int_{t_0}^{t} f(v)\, dv, \quad \text{where } v = u - T.
\end{aligned}
$$

Thus

$$F(t+T) = I_f + F(t). \tag{B.12}$$

It follows that

$$
\begin{aligned}
R(t+T) &= (I_{gF} + R_0)\exp(F(t+T)) + \exp(F(t))\int_{t_0}^{t} g(v)\,\exp(-F(v))\, dv \\
&= (I_{gF} + R_0)\exp(F(t+T)) + (R(t) - R_0\exp(F(t)))
\end{aligned}
$$

and, equivalently

$$R(t+T) - R_0\exp(F(t+T)) = I_{gF}\exp(F(t+T)) + R(t) - R_0\exp(F(t)). \tag{B.13}$$

To conclude, it would now be sufficient to split up the term $I_{gF}\exp(F(t+T))$ in equation (B.13) into two antisymmetric parts, respectively function of t and of $t+T$. To achieve this, we try to find a function a, verifying

$$\exp(F(t+T)) = a(t)\exp(F(t)) - a(t+T)\exp(F(t+T)).$$

Taking advantage of (B.12) above, and dividing by $\exp(F(t)) \neq 0$, we find that such an a must satisfy

$$a(t) - a(t+T)\exp(I_f) - \exp(I_f) = 0 \tag{B.14}$$

at any t.

If $I_f \neq 0$, this can be easily fulfilled by

$$a(t) \equiv \frac{\exp(I_f)}{1 - \exp(I_f)}. \tag{B.15}$$

In this case, equation (B.13) can be rewritten as

$$R(t+T) - R_0 \exp(F(t+T)) + \frac{I_{gF}\exp(I_f)}{1-\exp(I_f)}\exp(F(t+T))$$

$$= R(t) - R_0 \exp(F(t))\frac{I_{gF}\exp(I_f)}{1-\exp(I_f)}\exp(F(t)).$$

As a consequence, the function G, defined by

$$G(t) = R(t) - R_0 \exp(F(t)) + \frac{I_{gF}\exp(I_f)}{1-\exp(I_f)}\exp(F(t))$$

is periodic of period T. Thus

$$R(t) = G(t) + \left(R_0 - \frac{I_{gF}\exp(I_f)}{1-\exp(I_f)}\right)\exp(F(t)).$$

Using

$$F'(t) = F(t) - I_f\frac{t-t_0}{T},$$

the linearily detrended F, which is periodic of period T since

$$
\begin{aligned}
F'(t+T) &= F(t+T) - I_f\frac{t+T-t_0}{T} \\
&= F(t) + I_f - I_f\frac{t-t_0}{T} - I_f \\
&= F'(t),
\end{aligned}
$$

for any t, we obtain

$$R(t) = G(t) + \left(\left(R_0 - \frac{I_{gF}\exp(I_f)}{1-\exp(I_f)}\right)\exp(F'(t))\right)\exp\left(\frac{I_f}{T}(t-t_0)\right).$$

With

$$H(t) = \left(R_0 - \frac{I_{gF}\exp(I_f)}{1-\exp(I_f)}\right)\exp(F'(t))$$

and

$$E(t) = \exp\left(\frac{I_f}{T}(t-t_0)\right),$$

the proof of the assertion is complete for $I_f \neq 0$. If $I_f < 0$, the exponential term decreases to 0 with increasing t and $R(t)$ tends asymptotically to the periodic function G. The multiplying factor is indeed bound because it is periodic and continuous (it is even continuously differentiable).

If $I_f = 0$, on the other hand, then F is periodic (of period T) and, hence also $\exp(F)$. (B.14) above simplifies to

$$a(t) - a(t+T) - 1 = 0 \tag{B.16}$$

which should again hold for any t. Noticing that

$$1 = \frac{(t+T) - t}{T} = \frac{t+T}{T} - \frac{t}{T},$$

condition (B.16) becomes

$$a(t) + \frac{t}{T} = a(t+T) + \frac{t+T}{T}. \tag{B.17}$$

We may thus chose

$$a(t) = -\frac{t}{T} + b(t)$$

where b is any periodic function of period T. Equation (B.13) can then be rewritten as

$$R(t+T) + I_{gF}\left(-\frac{t+T}{T} + b(t+T)\right)\exp(F(t+T))$$

$$= R(t) + I_{gF}\left(-\frac{t}{T} + b(t)\right)\exp(F(t)).$$

G', defined as

$$G'(t) = R(t) + I_{gF}\left(-\frac{t}{T} + b(t)\right)\exp(F(t))$$

is therefore periodic (of period T) just like

$$G(t) = G'(t) - I_{gF}b(t)\exp(F(t))$$

since both b and $\exp(F)$ are. We have thus shown that

$$R(t) = G(t) + I_{gF}\frac{t}{T}\exp(F(t))$$

if $I_f = 0$. In this case, it is obvious that

$$H(t) = I_{gF}\exp(F(t))$$

and

$$E(t) = \frac{t}{T}$$

fulfil the requirements to complete the demonstration.

Bibliography

J. G. ACKER, R. H. BYRNE, S. BEN-YAAKOV, R. A. FEELY, & P. R. BETZER. The effect of pressure on aragonite dissolution rates in seawater. *Geochim. Cosmochim. Acta*, 51:2171–2175, 1987.

J. M. ADAMS, H. FAURE, L. FAURE-DENARD, J. M. MCGLADE, & F. I. WOODWARD. Increases in the terrestrial carbon storage from the Last Glacial Maximum to the present. *Nature*, 348:711–714, 1990.

P. AMIOTTE SUCHET. Cycle du carbone, érosion chimique des continents et transferts vers les océans. Sci. Géol. Mém. 97, Institut de Géologie, Université Louis Pasteur, Strasbourg, 1995. (In French.).

P. AMIOTTE SUCHET & J.-L. PROBST. Flux de CO_2 consommé par altération chimique continentale : Influences du drainage et de la lithologie. *C. R. Acad. Sci. Paris Ser. II*, 317:615–622, 1993a. (In French, with English Abstract.).

P. AMIOTTE SUCHET & J.-L. PROBST. Modelling of atmospheric CO_2 consumption by chemical weathering of rocks : Application to the Garonne, Congo and Amazon basins. *Chem. Geol.*, 107(3/4):205–210, 1993b.

P. AMIOTTE SUCHET & J.-L. PROBST. A global model for present-day atmospheric/soil CO_2 consumption by chemical erosion of continental rocks (GEM-CO_2). *Tellus*, 47B(1/2):273–280, 1995.

L. A. ANDERSON & J. L. SARMIENTO. Redfield ratios of remineralization determined by nutrient data analysis. *Global Biogeochem. Cycles*, 8(1):65–80, 1994.

D. ANTOINE, J.-M. ANDRÉ, & A. MOREL. Oceanic primary production. 2. Estimation at global scale from satellite (coastal zone color scanner) chlorophyll. *Global Biogeochem. Cycles*, 10(1), 1996.

D. ARCHER. A data-driven model of the global calcite lysocline. *Global Biogeochem. Cycles*, 10(3):511–526, 1996.

D. ARCHER, S. EMERSON, & C. REIMERS. Dissolution of calcite in deep-sea sediments : pH and O_2 microelectrode results. *Geochim. Cosmochim. Acta*, 53:2831–2845, 1989.

D. ARCHER & E. MAIER-REIMER. Effect of deep-sea sedimentary calcite preservation on atmospheric CO_2 concentration. *Nature*, 367:260–263, 1994.

D. E. ARCHER. Modeling the calcite lysocline. *J. Geophys. Res.*, 96(C9):17037–17050, 1991.

G. ARRHENIUS. Rate of production, dissolution and accumulation of biogenic solids in the ocean. *Palaeogeogr., Palaeoclimatol., Palaeoecol.*, 67:119–146, 1988.

W. L. BALSAM. Carbonate dissolution on the Muir Seamount (Western North Atlantic) : Interglacial/glacial changes. *J. Sedim. Petrol.*, 53(3):719–731, 1983.

J.-M. BARNOLA, M. ANKLIN, J. PORCHERON, D. RAYNAUD, J. SCHWANDER, & B. STAUFFER. CO_2 evolution during the last millenium as recorded by Antarctic and Greenland ice. *Tellus*, 47B(1/2):264–272, 1995.

J.-M. BARNOLA, D. RAYNAUD, Y. S. KOROTKEVICH, & C. LORIUS. Vostok ice core

provides 160,000-year record of atmospheric CO_2. *Nature*, 329:408–414, 1987.

A. Baumgartner & E. Reichel. *The World Water Balance*. Elsevier, New York, NY, 1975.

S. Ben-Yaakov & I. R. Kaplan. Deep-sea in situ calcium carbonate saturometry. *J. Geophys. Res.*, 76(3):722–731, 1971.

W. H. Berger. Increase of carbon dioxide in the atmosphere during deglaciation : The coral reef hypothesis. *Naturwissenschaften*, 69:87–88, 1982.

W. H. Berger. On the time-scale of deglaciation : Atlantic deep-sea sediments and Gulf of Mexico. *Palaeogeogr., Palaeoclimatol., Palaeoecol.*, 50:167–184, 1985.

W. H. Berger & R. S. Keir. Glacial-Holocene changes in atmospheric CO_2 and the deep-sea record. In J. E. Hansen & T. Takahashi, editors, *Climate Processes and Climate Sensitivity*, volume 29 of *Geophys. Monogr. Ser.*, pages 337–351. AGU, Washington, DC, 1984.

W. H. Berger & J. S. Killingley. The Worthington effect and the origin of the Younger Dryas. *J. Mar. Res.*, 40:27–38, 1982.

W. H. Berger & G. Wefer. Export production : seasonality and intermittency, and paleoceanographic implications. *Palaeogeogr., Palaeoclimatol., Palaeoecol. (Glob. Planet. Change Sect.)*, 89:245–254, 1990.

E. K. Berner & R. A. Berner. *The Global Water Cycle*. Prentice Hall, Englewood Cliffs, NJ, 1987.

R. A. Berner. Sedimentation and dissolution of pteropods in the ocean. In N. R. Andersen & A. Malahoff, editors, *The Fate of Fossil Fuel CO_2 in the Oceans*, pages 243–260. Plenum Press, New York, NY, 1977.

R. A. Berner. *Early Diagenesis. A Theoretical Approach*. Princeton Series in Geochemistry. Princeton University Press, Princeton, NJ, 1980.

R. A. Berner. Burial of organic carbon and pyrite sulfur in the modern ocean : Its geochemical and environmental significance. *Am. J. Sci.*, 282:451–473, 1982.

R. A. Berner. Atmospheric carbon dioxide levels over Phanerozoic time. *Science*, 249:1382–1386, 1990.

R. A. Berner. A model for atmospheric CO_2 over Phanerozoic time. *Am. J. Sci.*, 291:339–376, 1991.

R. A. Berner & S. Honjo. Pelagic sedimentation of aragonite : Its geochemical significance. *Science*, 211:940–942, 1981.

R. A. Berner, A. C. Lasaga, & R. M. Garrels. The carbonate-silicate geochemical cycle and its effect on atmospheric carbon dioxide over the past 100 million years. *Am. J. Sci.*, 283:641–683, 1983.

R. A. Berner & D. M. Rye. Calculation of the Phanerozoic strontium isotope record of the oceans from a carbon cycle model. *Am. J. Sci.*, 292:136–148, 1992.

P. R. Betzer, R. H. Byrne, J. G. Acker, C. S. Lewis, R. R. Jolley, & R. A. Feely. The oceanic carbonate system : A reassessment of biogenic controls. *Science*, 226:1074–1077, 1984.

G. J. S. Bluth & L. R. Kump. Phanerozoic paleogeology. *Am. J. Sci.*, 291:284–308, 1991.

G. J. S. Bluth & L. R. Kump. Lithologic and climatologic controls of river chemistry. *Geochim. Cosmochim. Acta*, 58(10): 2341–2359, 1994.

B. Bolin, A. Björkström, K. Holmén, & B. Moore. The simultaneous use of tracers for ocean circulation studies. *Tellus*, 35B (3):206–236, 1983.

B. Bolin, A. Björkström, C. D. Keeling, R. Bacastow, & U. Siegenthaler. Carbon cycle modeling. In B. Bolin, editor, *Carbon Cycle Modelling*, volume 16 of *SCOPE*, chapter 1, pages 1–28. John Wiley & Sons, Chichester, NY, 1981.

E. A. Boyle. The role of vertical chemical fractionation in controlling Late Quaternary atmospheric carbon dioxide. *J. Geophys. Res.*, 93(C12):15701–15714, 1988a.

E. A. Boyle. Vertical oceanic nutrient fractionation and glacial/interglacial CO_2 cycles. *Nature*, 331:55–56, 1988b.

E. A. Boyle & L. D. Keigwin. Deep circulation of the North Atlantic over the last 200,000 years : Geochemical evidence. *Science*, 218:784–787, 1982.

G. W. Brass. The variation of the marine $^{87}Sr/^{86}Sr$ ratio during Phanerozoic time : Interpretation using a flux model. *Geochim. Cosmochim. Acta*, 40:721–730, 1976.

P. G. Brewer. Direct observation of the oceanic CO_2 increase. *Geophys. Res. Lett.*, 5(12):997–1000, 1978.

W. S. Broecker. A revised estimate for the radiocarbon age of North Atlantic Deep Water. *J. Geophys. Res.*, 84(C6):3218–3226, 1979.

W. S. Broecker. Ocean chemistry during glacial times. *Geochim. Cosmochim. Acta*, 46:1689–1705, 1982.

W. S. Broecker. The great ocean conveyor. *Oceanography*, 4(2):79–89, 1991.

W. S. Broecker. *The Glacial World according to Wally*. Lamont-Doherty Geological Observatory of Columbia University, Palisades, NY 10964, draft edition, 1992.

W. S. Broecker, S. Blanton, W. M. Smethie, Jr., & G. Ostlund. Radiocarbon decay and oxygen utilization in the deep Atlantic Ocean. *Global Biogeochem. Cycles*, 5(1):87–117, 1991a.

W. S. Broecker, M. Klas, E. Clark, G. Bonani, S. Ivy, & W. Wolfli. The influence of $CaCO_3$ dissolution on core top radiocarbon ages for deep-sea sediments. *Paleoceanography*, 6(5):593–608, 1991b.

W. S. Broecker & T.-H. Peng. *Tracers in the Sea.* Lamont-Doherty Geological Observatory of Columbia University, Palisades, NY 10964, 1982.

W. S. Broecker & T.-H. Peng. The role of $CaCO_3$ compensation in the glacial to interglacial atmosphere CO_2 change. *Global Biogeochem. Cycles*, 1(1):15–29, 1987.

W. S. Broecker & T.-H. Peng. The cause of the glacial to interglacial atmospheric CO_2 change : A polar alkalinity hypothesis. *Global Biogeochem. Cycles*, 3(3): 215–239, 1989.

W. S. Broecker & T.-H. Peng. What caused glacial to interglacial CO_2 change ? In M. Heimann, editor, *The Global Carbon Cycle*, volume 15 of *NATO ASI Series I : Global Environmental Change*, pages 95–115. Springer-Verlag, Berlin, 1993.

W. S. Broecker & T. Takahashi. The relationship between lysocline depth and *in situ* carbonate ion concentration. *Deep-Sea Res.*, 25:65–95, 1978.

W. H. Burke, R. E. Denison, E. A. Hetherington, R. B. Koepnick, H. F. Nelson, & J. B. Otto. Variation of seawater $^{87}Sr/^{86}Sr$ throughout Phanerozoic time. *Geology*, 10:516–519, 1982.

R. C. Capo & D. J. DePaolo. Seawater strontium isotopic variations from 2.5 million years ago to the present. *Science*, 249: 51–55, 1990.

H. Chamley. *Clay Sedimentology.* Springer-Verlag, Berlin, 1989. 623 p.

J. Chappell & N. J. Shackleton. Oxygen isotopes and sea level. *Nature*, 324:137–140, 1986.

J. Chappellaz, J.-M. Barnola, D. Raynaud, Y. S. Korotkevich, & C. Lorius. Ice-core record of atmospheric methane over the past 160,000 years. *Nature*, 345:127–131, 1990.

G.-T. Chen & F. J. Millero. Gradual increase of oceanic CO_2. *Nature*, 277:205–206, 1979.

P. Ciais, P. P. Tans, J. W. C. White, M. Trolier, R. J. Francey, J. A. Berry, D. R. Randall, P. J. Sellers, J. G. Collatz, & D. S. Schimel. Partitioning of ocean and land uptake of CO_2

as inferred by δ^{13}C measurements from the NOAA Climate Monitoring and Diagnostics Laboratory Global Air Sampling Network. *J. Geophys. Res.*, 100(D3):5051–5070, 1995.

P. U. CLARK, J. M. LICCIARDI, D. R. MACAYEAL, & J. W. JENSON. Numerical reconstruction of a soft-bedded Laurentide Ice Sheet during the last glacial maximum. *Geology*, 24(8):679–682, 1996.

S. C. CLEMENS, J. F. FARRELL, & P. GROMET. Syncronous changes in seawater strontium isotope composition and global climate. *Nature*, 363:607–610, 1993.

S. C. CLEMENS, P. GROMET, & J. F. FARRELL. The 100,000 year cyclicity in seawater ^{87}Sr/^{86}Sr : An enviro-analytical artefact ? *Mineral. Magaz.*, 58A:179–180, 1994.

S. C. CLEMENS, P. GROMET, & J. F. FARRELL. Artefacts in Sr isotope records. *Nature*, 373:201, 1995.

CLIMAP PROJECT MEMBERS. Seasonal reconstruction of the earth's surface at the last glacial maximum. *Geol. Soc. America Map Chart Ser.*, MC-36, 1981.

T. CROWLEY. Late Quaternary carbonate changes in the North Atlantic and Atlantic/Pacific comparisons. In E. T. SUNDQUIST & W. S. BROECKER, editors, *The Carbon Cycle and Atmospheric CO_2 : Natural Variations Archean to Present*, volume 32 of *Geophys. Monogr. Ser.*, pages 271–284. AGU, Washington, DC, 1985.

T. J. CROWLEY. Calcium-carbonate preservation patterns in the Central North Atlantic during the last 150,000 years. *Mar. Geol.*, 51:1–14, 1983.

T. J. CROWLEY. Ice age carbon. *Nature*, 352:575–576, 1991.

T. J. CROWLEY. Ice age terrestrial carbon changes revisited. *Global Biogeochem. Cycles*, 9(3):377–389, 1995.

T. J. CROWLEY & G. S. NORTH. *Paleoclimatology*, volume 18 of *Oxford Monographs on Geology and Geophysics*. Oxford University Press, New York, NY, 1991.

C. H. CULBERSON & R. M. PYTKOWICZ. Ionization of water in seawater. *Mar. Chem.*, 1:309–316, 1973.

F. CULKIN. The major constituents of sea water. In J. P. RILEY & G. SKIRROW, editors, *Chemical Oceanography*, volume 1, chapter 4, pages 121–161. Academic Press, London, 1965.

W. B. CURRY, J.-C. DUPLESSY, L. D. LABEYRIE, & N. J. SHACKLETON. Changes in the distribution of δ^{13}C of deep water ΣCO_2 between the last glaciation and the Holocene. *Paleoceanography*, 3(3):317–341, 1988.

R. J. DELMAS. A natural artefact in Greenland ice-core CO_2 measurements. *Tellus*, 45B(4):391–396, 1993.

R. J. DELMAS, J.-M. ASCENCIO, & M. LEGRAND. Polar ice evidence that atmospheric CO_2 20,000 yr BP was 50% of present. *Nature*, 284:155–157, 1980.

D. J. DEMASTER. The supply and accumulation of silica in the marine environment. *Geochim. Cosmochim. Acta*, 45:1715–1732, 1981.

L. A. DERRY & C. FRANCE-LANORD. Neogene growth of the sedimentary organic carbon reservoir. *Paleoceanography*, 11(3):267–275, 1996.

D. J. DES MARAIS. Carbon exchange between the mantle and the crust, and its effect upon the atmosphere : Today compared to Archean time. In E. T. SUNDQUIST & W. S. BROECKER, editors, *The Carbon Cycle and Atmospheric CO_2 : Natural Variations Archean to Present*, volume 32 of *Geophys. Monogr. Ser.*, pages 602–611. AGU, Washington, DC, 1985.

A. N. DIA, A. S. COHEN, R. K. O'NIONS, & N. J. SHACKLETON. Seawater Sr isotope variation over the past 300 kyr and influence of global climate cycles. *Nature*, 356:786–788, 1992.

A. G. DICKSON. An exact definition of total alkalinity and a procedure for the estimation of alkalinity and total inorganic carbon

from titration data. *Deep-Sea Res.*, 28A(6): 609–623, 1981.

A. G. DICKSON. pH scales and proton-transfer reactions in saline media such as sea water. *Geochim. Cosmochim. Acta*, 48: 2299–2308, 1984.

A. G. DICKSON. Standard potential of the reaction : $AgCl(s) + \frac{1}{2}H_2(g) = Ag(s) + HCl(aq)$, and the standard acidity constant of the ion HSO_4^- in synthetic sea water from 273.15 to 318.15 K. *J. Chem. Thermodynamics*, 22:113–127, 1990a.

A. G. DICKSON. Thermodynamics of the dissociation of boric acid in synthetic seawater from 273.15 K to 318.15 K. *Deep-Sea Res.*, 37(5):755–766, 1990b.

A. G. DICKSON & J. P. RILEY. The estimation of acid dissolution constants in seawater media from potentiometric titrations with strong base. I. The ionic product of water – K_w. *Mar. Chem.*, 7:89–99, 1979.

J.-C. DUPLESSY & P. MOREL. *Gros temps sur la planète.* Éditions Odile Jacob, Paris, 1990.

J.-C. DUPLESSY, N. J. SHACKLETON, R. G. FAIRBANKS, L. LABEYRIE, D. OPPO, & N. KALLEL. Deepwater source variations during the last climatic cycle and their impact on the global deepwater circulation. *Paleoceanography*, 3(3):343–360, 1988.

J. DYMOND & M. LYLE. Flux comparisons between sediments and sediment traps in the eastern tropical Pacific : Implications for atmospheric CO_2 variations during the Pleistocene. *Limnol. Oceanogr.*, 30(4):699–712, 1985.

J. M. EDMOND. Himalayan tectonics, weathering processes, and the strontium isotopic record in marine limestones. *Science*, 258:1594–1597, 1992.

H. ELDERFIELD & J. M. GIESKES. Sr isotopes in interstitial waters of marine sediments from Deep Sea Drilling Project cores. *Nature*, 300:493–497, 1982.

C. EMILIANI. Pleistocene temperatures. *J. Geol.*, 63, 1955.

R. W. EPPLEY & B. J. PETERSON. Particulate organic matter flux and planktonic new production in the deep ocean. *Nature*, 282:677–680, 1979.

V. J. FABRY. Aragonite production by pteropod molluscs in the subarctic Pacific. *Deep-Sea Res.*, 36(11):1735–1751, 1989.

R. G. FAIRBANKS. A 17,000-year glacio-eustatic sea level record : Influence of glacial melting rates on the Younger Dryas event and the deep-ocean circulation. *Nature*, 342: 637–642, 1989.

J. W. FARRELL & W. L. PRELL. Climatic change and $CaCO_3$ preservation : An 800,000 year bathymetric reconstruction from the Central Equatorial Pacific Ocean. *Paleoceanography*, 4(4):447–466, 1989.

G. FAURE. *Principles of Isotope Geology.* John Wiley & Sons, New York, NY, 2nd edition, 1986.

G. FAURE. *Principles and Applications of Inorganic Geochemistry.* Macmillan Publishing Company, New York, NY, 1st edition, 1991.

G. FAURE, P. M. HURLEY, & J. L. POWELL. The isotopic composition of strontium in surface water from the North Atlantic Ocean. *Geochim. Cosmochim. Acta*, 29:209–220, 1965.

L. M. FRANÇOIS, J.-C. GÉRARD, B. NEMRY, P. WARNANT, C. DELIRE, & G. MUNHOVEN. A global model of the biosphere : Validation and applications to present and past climatic conditions. *Sci. Géol. Bull.*, 50(1-4):89–107, 1997.

L. M. FRANÇOIS & Y. GODDÉRIS. Isotopic constraints on the Cenozoic evolution of the carbon cycle. *Chem. Geol.*, 1997. In press.

L. M. FRANÇOIS & J. C. G. WALKER. Modelling the Phanerozoic carbon cycle and climate : Constraints from the $^{87}Sr/^{86}Sr$ isotopic ratio of seawater. *Am. J. Sci.*, 292: 81–135, 1992.

L. M. François, J. C. G. Walker, & B. N. Opdyke. The history of global weathering and the chemical evolution of the ocean-atmosphere system. In E. Takahashi & R. Jeanloz, editors, *Evolution of the Earth and Planets*, volume 74 of *Geophys. Monogr. Ser.*, pages 143–159. AGU, Washington, DC, 1993. IUGG Volume 14.

M. Frankignoulle. A complete set of buffer factors for acid/base CO_2 system in seawater. *J. Mar. Syst.*, 5:111–118, 1994.

H. Friedli, H. Loetscher, H. Oeschger, U. Siegenthaler, & B. Stauffer. Ice core record of the $^{13}C/^{12}C$ ratio of atmospheric CO_2 in the past two centuries. *Nature*, 324, 1986.

P. Friedlingstein, C. Delire, J.-F. Müller, & J.-C. Gérard. The climate-induced variation of the continental biosphere : A model simulation of the Last Glacial Maximum. *Geophys. Res. Lett.*, 19 (9):897–900, 1992.

P. N. Froelich. Paleogeochemical cycling of germanium and silica : The present is key to the past (& vice versa). *EOS Trans. AGU*, 76(46):F304, 1995. Fall Meet. Suppl.

P. N. Froelich, V. Blanc, R. A. Mortlock, S. N. Chillrud, W. Dunstan, A. Udomkit, & T.-H. Peng. River fluxes of dissolved silica to the ocean were higher during glacials : Ge/Si in diatoms, rivers, and oceans. *Paleoceanography*, 7(6):739–767, 1992.

P. N. Froelich, R. A. Mortlock, & A. Shemesh. Inorganic germanium and silica in the Indian Ocean : Biological fractionation during $(Ge/Si)_{opal}$ formation. *Global Biogeochem. Cycles*, 3(1):79–88, 1989.

R. M. Garrels. Genesis of some ground waters from igneous rocks. In P. H. Abelson, editor, *Researches in Geochemistry*, volume 2, pages 405–420. John Wiley & Sons, New York, NY, 1967.

R. M. Garrels & F. T. Mackenzie. *Evolution of Sedimentary Rocks*. W. W. Norton and Company, Inc., New York, NY, 1971.

W. L. Gates & A. B. Nelson. A new (revised) tabulation of the Scripps topography on a 1 degree global grid. Part I : Terrain heights. Technical Report R-1276-1-ARPA, The Rand Corporation, 1975a.

W. L. Gates & A. B. Nelson. A new (revised) tabulation of the Scripps topography on a 1 degree global grid. Part II : Ocean depths. Technical Report R-1277-1-ARPA, The Rand Corporation, 1975b.

M. T. Gibbs & L. R. Kump. Global chemical erosion during the last glacial maximum and the present : Sensitivity to changes in lithology and hydrology. *Paleoceanography*, 9(4):529–543, 1994.

J. M. Gieskes. The alkalinity-total carbon dioxide system in seawater. In E. A. Goldberg, editor, *The Sea*, volume 5, chapter 3, pages 123–151. John Wiley & Sons, New York, NY, 1974.

Y. Goddéris & L. M. François. The Cenozoic evolution of the strontium and carbon cycles : Relative importance of continental erosion and mantle exchanges. *Chem. Geol.*, 126(2):169–190, 1995.

Y. Goddéris & L. M. François. Balancing the Cenozoic carbon and alkalinity cycles : Constraints from isotopic records. *Geophys. Res. Lett.*, 23(25):3743–3746, 1996.

Yves Goddéris. *Modélisation de l'évolution cénozoïque des cycles biogéochimiques : Impact de l'orogenèse himalayenne*. PhD thesis, Université de Liège, Liège, 1997. (In French.).

Godwin. Half-life of radiocarbon. *Nature*, 195, 1962.

S. J. Goldstein & S. B. Jacobsen. The Nd and Sr isotopic systematics of river-water dissolved material : Implications for the sources of Nd and Sr in seawater. *Chem. Geol. (Isot. Geosc. Sect.)*, 66:245–272, 1987.

C. Goyet & A. Poisson. New determination of carbonic acid dissociation constants in seawater as a function of temperature and

salinity. *Deep-Sea Res.*, 36(11):1635–1654, 1989.

M. G. Gross. *Oceanography. A view of the Earth.* Prentice-Hall, Englewood Cliffs, NJ, 3rd edition, 1982.

N. L. Guinasso, Jr. & D. R. Schink. Quantitative estimates of biological mixing rates in abyssal sediments. *J. Geophys. Res.*, 80(21):3032–3043, 1975.

B. Hallet, L. Hunter, & J. Bogen. Rates of erosion and sediment evacuation by glaciers : A review of field data and their implications. *Global Planet. Change*, 12(1-4): 213–235, 1996.

J. Hansen, A. Lacis, D. Rind, G. Russell, P. Stone, I. Fung, R. Ruedy, & J. Lerner. Climate sensitivity: Analysis of feedback mechanisms. In J. E. Hansen & T. Takahashi, editors, *Climate Processes and Climate Sensitivity*, volume 29 of *Geophys. Monogr. Ser.*, pages 130–163. AGU, Washington, DC, 1984.

J. Hansen, G. Russell, D. Rind, P. Stone, A. Lacis, S. Lebedeff, R. Ruedy, & L. Travis. Efficient three-dimensional global models for climate studies. *Mon. Wea. Rev.*, 111:609–662, 1983.

I. Hansson. A new set of acidity constants for carbonic acid and boric acid in sea water. *Deep-Sea Res.*, 20:461–478, 1973a.

I. Hansson. A new set of pH-scales and standard buffers for sea water. *Deep-Sea Res.*, 20:479–491, 1973b.

W. W. Hay & J. R. Southam. Modulation of marine sedimentation by the continental shelves. In N. R. Andersen & A. Malahoff, editors, *The Fate of Fossil Fuel CO$_2$ in the Oceans*, volume 6 of *Marine Science*, pages 569–604. Plenum Press, New York, NY, 1977.

J. I. Hedges & R. G. Keil. Sedimentary organic matter preservation : an assessment and speculative synthesis. *Mar. Chem.*, 49: 81–115, 1995.

N. G. Hemming & G. N. Hanson. Boron isotopic composition and concentration in modern marine carbonates. *Geochim. Cosmochim. Acta*, 56:537–543, 1992.

G. M. Henderson, D. J. Martel, R. K. O'Nions, & N. J. Shackleton. Evolution of seawater ^{87}Sr/^{86}Sr over the last 400 ka : The absence of glacial/interglacial cycles. *Earth Planet. Sci. Lett.*, 128:643–651, 1994a.

G. M. Henderson, D. J. Martel, R. K. O'Nions, & N. J. Shackleton. High precision ^{87}Sr/^{86}Sr measurements on foraminifera from the equatorial Pacific and Indian oceans : The search for climate related seawater ^{87}Sr/^{86}Sr cycles. *Mineral. Magaz.*, 58A:404–405, 1994b.

J. Hess, M. L. Bender, & J.-G. Schilling. Evolution of the ratio of strontium-87 to strontium-86 in seawater from Cretaceous to present. *Science*, 231: 979–984, 1986.

D. A. Hodell, G. A. Mead, & P. A. Mueller. Variation in the strontium isotopic composition of seawater (8 Ma to present) : Implications for chemical weathering rates and dissolved fluxes to the oceans. *Chem. Geol. (Isot. Geosc. Sect.)*, 80:291–307, 1990.

H. D. Holland. *The Chemistry of the Atmosphere and the Oceans.* Wiley-Interscience, New York, NY, 1978.

H. D. Holland. *The Chemical Evolution of the Atmosphere and Oceans.* Princeton Series in Geochemistry. Princeton University Press, Princeton, NJ, 1984.

K. Holmén. The global carbon cycle. In S. S. Butcher, R. J. Charlson, G. H. Orians, & G. V. Wolfe, editors, *Global Biogeochemical Cycles*, volume 50 of *International Geophysics Series*, chapter 11, pages 239–262. Academic Press, London, 1992.

R. A. Houghton, W. H. Schlesinger, S. Brown, & J. F. Richards. Carbon dioxide exchange between the atmosphere

and terrestrial ecosystems. In J. R. TRA-BALKA, editor, *Atmospheric Carbon Dioxide and the Global Carbon Cycle*, chapter 6, pages 113–140. U. S. Department of Energy, Washington DC, 1985.

J. IMBRIE, J. D. HAYS, D. G. MARTINSON, A. MCINTYRE, A. C. MIX, J. J. MORLEY, N. G. PISIAS, W. L. PRELL, & N. J. SHACKLETON. The orbital theory of Pleistocene climate : Support from a revised chronology of the marine $\delta^{18}O$ record. In A. BERGER, J. IMBRIE, J. D. HAYS, G. KUKLA, & B. SALTZMAN, editors, *Milankowitch and Climate (Part I)*, pages 269–305. Reidel, Dordrecht, 1984.

RICHARD A. JAHNKE. The global ocean flux of particulate organic carbon : Areal distribution and magnitude. *Global Biogeochem. Cycles*, 10(1):71–88, 1996.

M. JAVOY, F. PINEAU, & C. J. ALLÈGRE. Carbon geodynamic cycle. *Nature*, 300:171–173, 1982.

C. E. JONES, H. C. JENKYNS, A. L. COE, & S. P. HESSELBO. Strontium isotopic variations in Jurassic and Cretaceous seawater. *Geochim. Cosmochim. Acta*, 58(14):3061–3074, 1994.

P. D. JONES, T. M. L. WIGLEY, & P. B. WRIGHT. Global temperature variations between 1861 and 1984. *Nature*, 322:430–434, 1986.

B. B. JØRGENSEN. Processes at the sediment-water interface. In B. BOLIN & R. B. COOK, editors, *The Major Biogeochemical Cycles and Their Interactions*, volume 21 of *SCOPE*, chapter 18, pages 477–509. John Wiley & Sons, Chichester, NY, 1983.

J. JOUZEL, N. I. BARKOV, J. M. BARNOLA, M. BENDER, J. CHAPPELLAZ, C. GENTHON, V. M. KOTLYAKOV, V. LIPENKOV, C. LORIUS, J.-R. PETIT, D. RAYNAUD, G. RAISBECK, C. RITZ, T. SOWERS, M. STIEVENARD, F. YIOU, & P. YIOU. Extending the Vostok ice-core record of palaeoclimate to the penultimate glacial period. *Nature*, 364:407–412, 1993.

J. JOUZEL, C. LORIUS, J.-R. PETIT, C. GENTHON, N. I. BARKOV, V. M. KOTLYAKOV, & V. N. PETROV. Vostok ice core : A continuous isotope temperature record over the last climatic cycle (160,000 years). *Nature*, 329:403–408, 1987.

W. J. SCHMITZ JR. On the interbasin-scale thermohaline circulation. *Rev. Geophys.*, 33 (2):151–173, 1995.

H. KAKIHANA, M. KOTAKA, S. SATOH, M. NOMURA, & M. OKAMOTO. Fundamental studies on the ion-exchange separation of boron isotopes. *Bull. Chem. Soc. Japan*, 50 (1):158–163, 1977.

C. D. KEELING. Lecture 1 : Global observations of atmospheric CO_2. In M. HEIMANN, editor, *The Global Carbon Cycle*, volume 15 of *NATO ASI Series I : Global Environmental Change*, pages 1–29. Springer-Verlag, Berlin, 1993.

C. D. KEELING, S. C. PIPER, & M. HEIMANN. A three-dimensional model of atmospheric CO_2 transport based on observed winds : 4. Mean annual gradients and interannual variations. In D. H. PETERSON, editor, *Aspects of Climate Variability in the Pacific and the Western Americas*, volume 55 of *Geophys. Monogr. Ser.*, pages 305–363. AGU, Washington, DC, 1989.

C. D. KEELING & T. P. WHORF. Atmospheric CO_2 records from sites in the SIO air sampling network. In *Trends : A Compendium of Global Change*, Oak Ridge, Tenn., U.S.A., 1996. Carbon Dioxide Information Analysis Center, ORNL. Available under URL http://cdiac.esd.ornl.gov/trends_html/trends/co2/trends.html.

C. D. KEELING, T. P. WHORF, M. WAHLEN, & J. VAN DER PLICHT. Interannual extremes in the rate of rise of atmospheric carbon dioxide since 1980. *Nature*, 375:666–670, 1995.

R. S. KEIR. The dissolution kinetics of biogenic calcium carbonates in seawater. *Geochim. Cosmochim. Acta*, 44:241–252, 1980.

R. S. KEIR. Recent increase in Pacific $CaCO_3$ dissolution : A mechanism for generating old ^{14}C ages. *Mar. Geol.*, 59:227–250, 1984.

R. S. KEIR. On the Late Pleistocene ocean geochemistry and circulation. *Paleoceanography*, 3(4):413–445, 1988.

R. S. KEIR & W. H. BERGER. Atmospheric CO_2 content in the last 120,000 years : The phosphate-extraction model. *J. Geophys. Res.*, 88(C10):6027–6038, 1983.

R. S. KEIR & W. H. BERGER. Late Holocene carbonate dissolution in the Equatorial Pacific : Reef growth or dissolution ? In E. T. SUNDQUIST & W. S. BROECKER, editors, *The Carbon Cycle and Atmospheric CO_2 : Natural Variations Archean to Present*, volume 32 of *Geophys. Monogr. Ser.*, pages 208–219. AGU, Washington, DC, 1985.

D. W. KINSEY & D. HOPLEY. The significance of coral reefs as global carbon sinks — Response to Greenhouse. *Palaeogeogr., Palaeoclimatol., Palaeoecol. (Glob. Planet. Change Sect.)*, 89:363–377, 1991.

F. KNOX & M. B. MCELROY. Changes in atmospheric CO_2 : Influence of the marine biota at high latitude. *J. Geophys. Res.*, 89 (D3):4629–4637, 1984.

F. KNOX-ENNEVER & M. B. MCELROY. Changes in atmospheric CO_2 : Factors regulating the glacial to interglacial transition. In E. T. SUNDQUIST & W. S. BROECKER, editors, *The Carbon Cycle and Atmospheric CO_2 : Natural Variations Archean to Present*, volume 32 of *Geophys. Monogr. Ser.*, pages 154–162. AGU, Washington, DC, 1985.

R. B. KOEPNICK, R. E. DENISON, & D. A. DAHL. The Cenozoic seawater $^{87}Sr/^{86}Sr$: Data review and implications for correlation of marine strata. *Paleoceanography*, 3(6): 743–756, 1988.

V. I. KORZOUN, A. A. SOKOLOV, M. I. BUDYKO, K. P. VOSKRESENSKY, G. P. KALININ, A. A. KONOPLYANTSEV, E. S. KOROTKEVICH, & M. I. LVOVICH. *Atlas of World Water Balance.* The UNESCO Press, Paris, 1977.

P. M. KROOPNICK. The distribution of ^{13}C of ΣCO_2 in the world oceans. *Deep-Sea Res.*, 32(1):57–84, 1985.

L. R. KUMP & R. B. ALLEY. Global chemical weathering on glacial time scales. In NATIONAL RESEARCH COUNCIL, PANEL ON GLOBAL SURFICIAL GEOFLUXES, editor, *Material Fluxes on the Surface of the Earth*, chapter 3, pages 46–60. National Academy Press, Washington DC, 1994.

J. KUTZBACH. CCM0 general circulation model output data set. Technical Report 94-025, NOAA/NGDC Paleoclimatology Program, Boulder, CO, 1994.

J. E. KUTZBACH & P. J. GUETTER. The influence of changing orbital parameters and surface boundary conditions on climate simulations for the past 18 000 years. *J. Atmos. Sci.*, 43(16):1726–1759, 1986.

L. D. LABEYRIE, J.-C. DUPLESSY, & P. L. BLANC. Variations in mode of formation and temperature of oceanic deep waters over the past 125,000 years. *Nature*, 327:477–482, 1987.

A. C. LASAGA, R. A. BERNER, & R. M. GARRELS. An improved geochemical model of atmospheric CO_2 fluctuations over the past 100 million years. In E. T. SUNDQUIST & W. S. BROECKER, editors, *The Carbon Cycle and Atmospheric CO_2 : Natural Variations Archean to Present*, volume 32 of *Geophys. Monogr. Ser.*, pages 397–411. AGU, Washington, DC, 1985.

M. LAUTENSCHLAGER & K. HERTERICH. Atmospheric response to ice age conditions : Climatology near the Earth's surface. *J. Geophys. Res.*, 95(D13):22547–22557, 1990.

A. LERMAN. Chemical exchange across the sediment-water interface. *Annu. Rev. Earth Planet. Sci.*, 6:281–303, 1978.

Y.-H. LI & S. GREGORY. Diffusion of ions in sea water and in deep-sea sedi-

ments. *Geochim. Cosmochim. Acta*, 38:703–714, 1974.

A. P. LISITZIN. The silica cycle during the last ice age. *Palaeogeogr., Palaeoclimatol., Palaeoecol.*, 50:241–270, 1985.

W. LUDWIG, P. AMIOTTE SUCHET, G. MUNHOVEN, & J.-L. PROBST. Atmospheric CO_2 consumption by continental erosion : Present-day controls and implications for the last glacial maximum. *Global Planet. Change*, 1997. In press.

WOLFGANG LUDWIG. *Continental Erosion and River Transport of Organic Carbon in the World's Oceans*. PhD thesis, Université Louis Pasteur, Strasbourg, 1996.

F. T. MACKENZIE, L. MAY VER, C. SABINE, M. LANE, & A. LERMAN. C, N, P, S global biogeochemical cycles and modeling of global change. In R. WOLLAST, F. T. MACKENZIE, & L. CHOU, editors, *Interactions of C, N, P and S Biogeochemical Cycles and Global Change*, volume 4 of *NATO ASI Series I : Global Environmental Change*, pages 1–61. Springer-Verlag, Berlin, 1993.

E. MAIER-REIMER. Geochemical cycles in an ocean general circulation model. preindustrial tracer distributions. *Global Biogeochem. Cycles*, 7(3):645–677, 1993.

E. MAIER-REIMER & R. BACASTOW. Modelling of geochemical tracers in the ocean. In M. E. SCHLESINGER, editor, *Climate-Ocean Interaction*, pages 233–267. Kluwer Academic Publishers, Dordrecht, 1990.

E. MAIER-REIMER & U. MIKOLAJEW-ICZ. The Hamburg Large Scale Geostrophic Ocean General Circulation Model (Cycle 1). Technical Report 2, Deutsches KlimaRechenZentrum, Hamburg, 1991.

E. MAIER-REIMER, U. MIKOLAJEWICZ, & K. HASSELMANN. On the sensitivity of the global ocean circulation to changes in the surface heat flux forcing. MPI Report 68, Max-Planck-Institut für Meteorologie, Hamburg, 1991.

E. MAIER-REIMER, U. MIKOLAJEWICZ, & K. HASSELMANN. Mean circulation of the Hamburg LSG OGCM and its sensitivity to the thermohaline surface forcing. *J. Phys. Oceanog.*, 23:731–757, 1993.

D. H. MALING. *Coordinate Systems and Map Projections*. Pergamon Press, Oxford, 2nd edition, 1992. 2nd printing.

J. H. MARTIN. Glacial-interglacial CO_2 change: The iron hypothesis. *Paleoceanography*, 5(1):1–13, 1990.

M. MEYBECK. Concentrations des eaux fluviales en éléments majeurs et apports en solution aux océans. *Rev. Géol. Dyn. Géogr. Phys.*, 21(3):215–246, 1979. (In French, with English Abstract.).

M. MEYBECK. Carbon, nitrogen, and phosphorus transport by world rivers. *Am. J. Sci.*, 282:401–450, 1982.

M. MEYBECK. Composition chimique des ruisseaux non pollués de France. *Sci. Géol. Bull.*, 39(1):3–77, 1986. (In French, with English Abstract.).

M. MEYBECK. Global chemical weathering of surficial rocks estimated from river dissolved loads. *Am. J. Sci.*, 287:401–428, 1987.

M. MEYBECK. C, N, P and S in rivers : From sources to global inputs. In R. WOLLAST, F. T. MACKENZIE, & L. CHOU, editors, *Interactions of C, N, P and S Biogeochemical Cycles and Global Change*, volume 4 of *NATO ASI Series I : Global Environmental Change*, pages 163–193. Springer-Verlag, Berlin, 1993.

F. J. MILLERO. The thermodynamics of the carbonate system in seawater. *Geochim. Cosmochim. Acta*, 43:1651–1661, 1979.

F. J. MILLERO. The effect of pressure on the solubility of minerals in water and seawater. *Geochim. Cosmochim. Acta*, 46:11–22, 1982a.

F. J. MILLERO. The thermodynamics of seawater. Part I. The PVT properties. *Ocean Sci. Eng.*, 7(4):403–460, 1982b.

F. J. Millero. Thermodynamics of the carbon dioxide system in the oceans. *Geochim. Cosmochim. Acta*, 59(4):661–677, 1995.

F. J. Millero & M. L. Sohn. *Chemical Oceanography*. CRC Press, Boca Raton, Florida, 1992. 531 p.

J. D. Milliman. Production and accumulation of calcium carbonate in the ocean : Budget of a nonsteady state. *Global Biogeochem. Cycles*, 7(4):927–957, 1993.

J. D. Milliman & A. W. Droxler. Neritic and pelagic carbonate sedimentation in the marine environment : ignorance is not bliss. *Geol. Rundsch.*, 85(3):496–504, 1996.

J. W. Morse & F. T. Mackenzie. *Geochemistry of Sedimentary Carbonates*, volume 48 of *Developments in Sedimentology*. Elsevier, Amsterdam, 1990.

R. A. Mortlock, C. D. Charles, P. N. Froelich, M. A. Zibello, J. Saltzman, J. D. Hays, & L. H. Burkle. Evidence for lower productivity in the Antarctic Ocean during the last glaciation. *Nature*, 351:220–223, 1991.

R. A. Mortlock & P. N. Froelich. Continental weathering of germanium : Ge/Si in the global river discharge. *Geochim. Cosmochim. Acta*, 51:2075–2082, 1987.

R. A. Mortlock, P. N. Froelich, R. A. Feely, G. J. Massoth, D. A. Butterfield, & J. E. Lupton. Silica and germanium in Pacific Ocean hydrothermal vents and plumes. *Earth Planet. Sci. Lett.*, 119:365–378, 1993.

A. Mucci. The solubility of calcite and aragonite in seawater at various salinities, and one atmosphere total pressure. *Am. J. Sci.*, 283:780–799, 1983.

G. Munhoven. Modélisation du cycle du carbone. Rôle des océans dans l'évolution passée et future du CO_2 atmosphérique. Master's thesis, Université de Liège, Faculté des Sciences, 1990. 109 p.

G. Munhoven & L. M. François. Glacial-interglacial changes in continental weathering : Possible implications for atmospheric CO_2. In R. Zahn, T. F. Pedersen, M. A. Kaminski, & L. Labeyrie, editors, *Carbon Cycling in the Glacial Ocean : Constraints on the Ocean's Role in Global Change*, volume 17 of *NATO ASI Series I : Global Environmental Change*, pages 39–58. Springer-Verlag, Berlin, 1994.

G. Munhoven & L. M. François. Glacial-interglacial variability of atmospheric CO_2 due to changing continental silicate rock weathering : A model study. *J. Geophys. Res.*, 101(D16):21423–21437, 1996.

G. Munhoven & J.-L. Probst. Influence of continental erosion processes on the glacial-interglacial evolution of atmospheric carbon dioxide. Final report for CEC "Human Capital and Mobility" fellowship contract ERBCHBI-CT94-1053, 16 p., 1995.

R. J. Murnane & R. F. Stallard. Germanium/silicon fractionation during biogenic opal formation. *Paleoceanography*, 3 (4):461–469, 1988.

R. J. Murnane & R. F. Stallard. Germanium and silicon in rivers of the Orinoco drainage basin. *Nature*, 344:749–752, 1990.

A. Neftel, E. Moor, H. Oeschger, & B. Stauffer. Evidence from polar ice cores for an increase in atmospheric CO_2 in the past two centuries. *Nature*, 315:45–47, 1985.

A. Neftel, H. Oeschger, J. Schwander, B. Stauffer, & R. Zumbrunn. Ice core samplements give atmospheric CO_2 content during the past 40,000 yr. *Nature*, 295:220–223, 1982.

D. M. Nelson, P. Tréguer, M. A. Brzezinski, A. Leynaert, & B. Quéguiner. Production and dissolution of biogenic silica in the ocean : Revised global estimates, comparison with regional data and relationship to biogenic sedimentation. *Global Biogeochem. Cycles*, 9(3):359–372, 1995.

J. S. Olson, R. M. Garrels, R. A. Berner, T. V. Armentano, M. I. Dyer, & D. H. Yaalon. Carbon dioxide exchange between the atmosphere and terrestrial ecosystems. In J. R. Trabalka, editor, *Atmospheric Carbon Dioxide and the Global Carbon Cycle*, chapter 8, pages 175–213. U. S. Department of Energy, Washington DC, 1985.

B. N. Opdyke & J. C. G. Walker. Glacial to interglacial, basin to shelf partitioning of $CaCO_3$ and its effect on atmospheric CO_2. In M. Sarnthein, J. Thiede, & R. Zahn, editors, *Fourth International Conference on Paleoceanography (ICP IV). Short- and Long-term Globals Change : Records and Modelling*, page 221, Kiel, 1992a. GEOMAR Report 15.

B. N. Opdyke & J. C. G. Walker. Return of the coral reef hypothesis : Basin to shelf partitioning of $CaCO_3$ and its effect on atmospheric CO_2. *Geology*, 20:733–736, 1992b.

B. N. Opdyke & B. H. Wilkinson. Surface area control of shallow cratonic to deep marine carbonate accumulation. *Paleoceanography*, 3(6):685–703, 1988.

J. T. Overpeck, L. C. Peterson, N. Kipp, J. Imbrie, & D. Rind. Climate change in the circum-North Atlantic region during the last deglaciation. *Nature*, 338: 553–557, 1989.

M. R. Palmer & J. M. Edmond. The strontium isotope budget of the modern ocean. *Earth Planet. Sci. Lett.*, 92:11–26, 1989.

M. R. Palmer & H. Elderfield. Sr isotope composition of sea water over the past 75 Myr. *Nature*, 314:526–528, 1985.

G. Pedro. Distribution des principaux types d'altération chimique à la surface du globe. *Rev. Géogr. Phys. Géol. Dyn. (2)*, 10 (5):457–470, 1968.

W. R. Peltier. Ice age paleotopography. *Science*, 265:195–201, 1994.

T.-H. Peng. Atmospheric CO_2 variations based on the tree-ring ^{13}C record. In E. T. Sundquist & W. S. Broecker, editors, *The Carbon Cycle and Atmospheric CO_2 : Natural Variations Archean to Present*, volume 32 of *Geophys. Monogr. Ser.*, pages 123–131. AGU, Washington, DC, 1985.

Z. E. Peterman, C. E. Hedge, & H. A. Tourtelot. Isotopic composition of strontium in sea water throughout Phanerozoic time. *Geochim. Cosmochim. Acta*, 34:105–120, 1970.

K. C. Prentice & I. Y. Fung. The sensitivity of terrestrial carbon storage to climate change. *Nature*, 346:48–51, 1990.

William H. Press, Brian P. Flannery, Saul A. Teukolsky, & William T. Vetterling. *Numerical Recipes (FORTRAN Version.* Cambridge University Press, Cambridge, 1989.

J.-L. Probst. *Géochimie et hydrologie des l'érosion continentale. Mécanismes, bilan global actuel et fluctuations au cours des 500 derniers millions d'années*, volume 94 of *Sci. Géol. Mém.* 1992. (In French.).

J.-L. Probst, J. Mortatti, & Y. Tardy. Carbon river fluxes and weathering CO_2 consumption in the Congo and the Amazon river basins. *Appl. Geochem.*, 9:1–13, 1994.

J.-L. Probst, R.-R. NKounkou, G. Krempp, J.-P. Bricquet, J.-P. Thiébaux, & J.-C. Olivry. Dissolved major elements exported by the Congo and the Ubangi rivers during the period 1987–1989. *J. Hydrol.*, 135:237–257, 1992.

M. E. Raymo. Geochemical evidence supporting T. C. Chamberlin's theory of glaciation. *Geology*, 19:344–347, 1991.

M. E. Raymo, W. F. Ruddiman, & P. N. Froelich. Influence of Late Cenozoic mountain building on ocean geochemical cycles. *Geology*, 16:649–653, 1988.

A. C. Redfield, B. H. Ketchum, & F. A. Richards. The influence of organisms on the composition of sea water. In

M. N. Hill, editor, *The Sea*, volume 2, pages 26–77. Wiley-Interscience, New York, 1963.

F. M. Richter, D. B. Rowley, & D. J. DePaolo. Sr isotope evolution of seawater : The role of tectonics. *Earth Planet. Sci. Lett.*, 109:11–23, 1992.

D. Rind. General circulation model output data set. Technical Report 94-012, NOAA/NGDC Paleoclimatology Program, Boulder, CO, 1994.

D. Rind, D. Peteet, W. Broecker, A. McIntyre, & W. Ruddiman. The impact of cold North Atlantic sea surface temperatures on climate: implications for the Younger Dryas cooling (11–10k). *Climate Dynamics*, 1, 1986.

R. N. Roy, L. N. Roy, K. M. Vogel, C. Porter-Moore, T. Pearson, C. E. Good, F. J. Millero, & D. M. Campbell. The dissociation constants of carbonic acid in seawater at salinities 5 to 45 and temperatures 0 to 45 °C. *Mar. Chem.*, 44:249–267, 1993.

A. Sanyal, N. G. Hemming, G. H. Hanson, & W. S. Broecker. Evidence for a higher pH in the glacial ocean from boron isotopes in foraminifera. *Nature*, 373:234–236, 1995.

J. L. Sarmiento. Modeling oceanic transport of dissolved constituents. In P. Buat-Ménard, editor, *The Role of Air-Sea Exchange in Geochemical Cycling*, volume 185 of *NATO ASI Series C : Mathematical and Physical Sciences*, pages 65–82. Reidel, Dordrecht, 1986.

J. L. Sarmiento. Biogeochemical ocean models. In K. E. Trenberth, editor, *Climate System Modeling*, chapter 16, pages 519–551. Cambridge University Press, Cambridge, 1992.

J. L. Sarmiento & M. Bender. Carbon biochemistry and climate change. *Photosynthesis Res.*, 39:209–234, 1994.

J. L. Sarmiento, J. C. Orr, & U. Siegenthaler. A perturbation simulation of CO_2 uptake in an ocean general circulation model. *J. Geophys. Res.*, 97(C3): 3621–3645, 1992.

J. L. Sarmiento & U. Siegenthaler. New production and the global carbon cycle. In P. G. Falkowski & A. D. Woodhead, editors, *Primary Productivity and Biogeochemical Cycles in the Sea*, volume 43 of *Environmental Science Research*, pages 317–332. Plenum Press, New York, 1992.

J. L. Sarmiento & J. R. Toggweiler. A new model for the role of the oceans in determining atmospheric p_{CO_2}. *Nature*, 308: 621–624, 1984.

D. Schimel, D. Alves, I. Enting, M. Heimann, F. Joos, D. Raynaud, T. Wigley, M. Prather, R. Derwent, D. Ehalt, P. Fraser, E. Sanhueza, X. Zhou, P. Jonas, R. Charlson, H. Rodhe, S. Sasdasivan, K. P. Shine, Y. Fouquart, V. Ramaswamy, S. Solomon, J. Srinivasan, D. Albritton, R. Derwent, I. Isaksen, M. Lal, & D. Wuebbles. Radiative forcing of climate change. In J. T. Houghton, L. G. Meira Filho, B. A. Callander, N. Harris, A. Kattenberg, & K. Maskell, editors, *Climate Change 1995. The Science of Climate Change*, chapter 2, pages 65–131. Cambridge University Press, Cambridge, 1996.

D. Schimel, I. G. Enting, M. Heimann, T. M. L. Wigley, D. Raynaud, D. Alves, & U. Siegenthaler. CO_2 and the carbon cycle. In J. T. Houghton, L. G. Meira Filho, J. Bruce, Hoesung Lee, B. A. Chandler, E. Haites, N. Harris, & K. Maskell, editors, *Climate Change 1994. Radiative Forcing of Climate Change and an Evaluation of the IPCC IS92 Emission Scenarios*, chapter 1, pages 35–71. Cambridge University Press, Cambridge, 1995.

D. R. Schink & N. L. Guinasso, Jr. Modelling the influence of bioturbation and other processes on calcium carbonate dissolution at the sea floor. In N. R. Andersen

& A. Malahoff, editors, *The Fate of Fossil Fuel CO_2 in the Oceans*, pages 375–399. Plenum Press, New York, NY, 1977.

G. Shaffer. Effects of marine biota on global carbon cycling. In M. Heimann, editor, *The Global Carbon Cycle*, volume 15 of *NATO ASI Series I : Global Environmental Change*, pages 431–455. Springer-Verlag, Berlin, 1993.

G. Shaffer. Biogeochemical cycling in the global ocean : 2. New production, Redfield ratios, and remineralization in the organic pump. *J. Geophys. Res.*, 101(C2):3723–3745, 1996.

M. Sharp, M. Tranter, G. H. Brown, & M. Skidmore. Rates of chemical denudation and CO_2 drawdown in a glacier-covered alpine catchment. *Geology*, 23(1): 61–64, 1995.

U. Siegenthaler. Modelling the present-day carbon cycle. In M. Heimann, editor, *The Global Carbon Cycle*, volume 15 of *NATO ASI Series I : Global Environmental Change*, pages 367–395. Springer-Verlag, Berlin, 1993.

U. Siegenthaler, H. Friedli, H. Loetscher, E. Moor, A. Neftel, H. Oeschger, & B. Stauffer. Stable-isotope ratios and concentration of CO_2 in air from polar ice cores. *Ann. Glaciol.*, 10, 1988.

U. Siegenthaler & K. O. Münnich. $^{13}C/^{12}C$ fractionation during CO_2 transfer from air to sea. In B. Bolin, editor, *Carbon Cycle Modelling*, volume 16 of *SCOPE*, pages 249–257. John Wiley & Sons, Chichester, NY, 1981.

U. Siegenthaler & J. L. Sarmiento. Atmospheric carbon dioxide and the ocean. *Nature*, 365:119–125, 1993.

U. Siegenthaler & T. Wenk. Rapid atmospheric CO_2 variations and ocean circulation. *Nature*, 308:624–626, 1984.

S. V. Smith & J. T. Hollibaugh. Coastal metabolism and the oceanic organic carbon balance. *Rev. Geophys.*, 31(1):75–89, 1993.

S. V. Smith & P. Kroopnick. Carbon-13 isotopic fractionation as a measure of aquatic metabolism. *Nature*, 294:252–253, 1981.

A. M. Solomon, J. R. Trabalka, D. E. Reichle, & L. D. Vorhees. The global cycle of carbon. In J. R. Trabalka, editor, *Atmospheric Carbon Dioxide and the Global Carbon Cycle*, pages 1–13. U. S. Department of Energy, Washington DC, 1985.

R. A. Souchez & M. M. Lemmens. Solutes. In A. M. Gurnell & M. J. Clark, editors, *Glacio-fluvial Sediment Transfer*, chapter 11, pages 285–303. John Wiley & Sons, Chichester, 1987.

R. F. Stallard. *Major element geochemistry of the Amazon River system*. PhD thesis, Massachusetts Institute of Technology – Woods Hole Oceanographic Institution Joint Program in Oceanography, Woods Hole, MA, 1980.

R. F. Stallard & J. M. Edmond. Geochemistry of the Amazon. 3. Weathering chemistry and limits to dissolved inputs. *J. Geophys. Res.*, 92(C8):8293–8302, 1987.

M. Stuiver & H. A. Polach. Discussion. Reporting of ^{14}C data. *Radiocarbon*, 19(3): 355–363, 1977.

M. Stuiver, P. Quay, & H. G. Ostlund. Abyssal water carbon-14 distribution and the age of the World oceans. *Science*, 219: 849–851, 1983.

W. Stumm & J. J. Morgan. *Aquatic Chemistry*. John Wiley & Sons, New York, NY, 2nd edition, 1981.

E. Suess. Particulate organic carbon flux in the oceans — surface productivity and oxygen utilization. *Nature*, 288:260–265, 1980.

H. E. Suess. Radiocarbon concentration in modern wood. *Science*, 122, 1955.

M. A. Summerfield. *Global Geomorphology*. Longman Scientific and Technical, London, 1991.

E. T. Sundquist. Geological perspectives on carbon dioxide and the carbon

cycle. In E. T. SUNDQUIST & W. S. BROECKER, editors, *The Carbon Cycle and Atmospheric CO$_2$: Natural Variations Archean to Present*, volume 32 of *Geophys. Monogr. Ser.*, pages 5–59. AGU, Washington, DC, 1985.

T. TAKAHASHI & W. S. BROECKER. Mechanisms for calcite dissolution on the sea floor. In N. R. ANDERSEN & A. MALAHOFF, editors, *The Fate of Fossil Fuel CO$_2$ in the Oceans*, volume 6 of *Marine Science*, pages 455–477. Plenum Press, New York, NY, 1977.

T. TAKAHASHI, W. S. BROECKER, & A. E. BAINBRIDGE. The alkalinity and total carbon dioxide concentration in the world oceans. In B. BOLIN, editor, *Carbon Cycle Modelling*, volume 16 of *SCOPE*, pages 271–286. John Wiley & Sons, Chichester, NY, 1981a.

T. TAKAHASHI, W. S. BROECKER, & A. E. BAINBRIDGE. Supplement to the alkalinity and total carbon dioxide concentration in the world oceans. In B. BOLIN, editor, *Carbon Cycle Modelling*, volume 16 of *SCOPE*, pages 159–199. John Wiley & Sons, Chichester, NY, 1981b.

T. TAKAHASHI, W. S. BROECKER, & S. LANGER. Redfield ratio based on chemical data from isopycnal surfaces. *J. Geophys. Res.*, 90(C4):6907–6924, 1985.

P. TANS. ^{13}C/^{12}C of industrial CO$_2$. In B. BOLIN, editor, *Carbon Cycle Modelling*, volume 16 of *SCOPE*, pages 127–129. John Wiley & Sons, Chichester, NY, 1981.

P. P. TANS, J. A. BERRY, & R. F. KEELING. Oceanic ^{13}C/^{12}C observations : A new window on ocean CO$_2$ uptake. *Global Biogeochem. Cycles*, 7(2):353–368, 1993.

P. P. TANS, I. Y. FUNG, & T. TAKAHASHI. Observational constraints on the global atmospheric CO$_2$ budget. *Science*, 247:1431–1438, 1990.

J. R. TOGGWEILER & J. L. SARMIENTO. Glacial to interglacial changes in atmospheric carbone dioxide : The critical role of ocean surface water in high latitudes. In E. T. SUNDQUIST & W. S. BROECKER, editors, *The Carbon Cycle and Atmospheric CO$_2$: Natural Variations Archean to Present*, volume 32 of *Geophys. Monogr. Ser.*, pages 163–184. AGU, Washington, DC, 1985.

P. TRÉGUER, D. M. NELSON, A. J. VAN BENNEKOM, D. J. DEMASTER, A. LEYNAERT, & B. QUÉGUINER. The silica balance in the world ocean. *Science*, 268:375–379, 1995.

UNESCO. Background papers and supporting data on the International Equation of State of Seawater. Unesco technical papers in marine science 38, UNESCO, Paris, 1981.

UNESCO. Algorithms for computation of fundamental properties of seawater. Unesco technical papers in marine science 44, UNESCO, Paris, 1983.

UNESCO. Reference materials for oceanic carbon dioxide measurements. Unesco technical papers in marine science 60, UNESCO, Paris, 1991.

E. VAN CAMPO, J. GUIOT, & C. PENG. A data-based re-appraisal of the terrestrial carbon budget at the last glacial maximum. *Global Planet. Change*, 8:189–201, 1993.

J. VEIZER & W. COMPSTON. ^{87}Sr/^{86}Sr composition of seawater during the Phanerozoic. *Geochim. Cosmochim. Acta*, 38:1461–1484, 1974.

J.-L. VOLAT, L. PASTOURET, & C. VERGNAUD-GRAZZINI. Dissolution and carbonate fluctuations in Pleistocene deep-sea cores : A review. *Mar. Geol.*, 34:1–28, 1980.

T. VOLK & M. I. HOFFERT. Ocean carbon pumps : Analysis of relative strengths and efficiencies in ocean-driven atmospheric CO$_2$ changes. In E. T. SUNDQUIST & W. S. BROECKER, editors, *The Carbon Cycle and Atmospheric CO$_2$: Natural Variations Archean to Present*, volume 32 of

Geophys. Monogr. Ser., pages 99–110. AGU, Washington, DC, 1985.

M. A. WADLEIGH, J. VEIZER, & C. BROOKS. Controls over the strontium isotope composition of river water. *Geochim. Cosmochim. Acta*, 49:1727–1736, 1985.

J. C. G. WALKER. *Evolution of the Atmosphere.* Macmillan, New York, NY, 1977.

J. C. G. WALKER, P. B. HAYS, & J. F. KASTING. A negative feedback mechanism for the long-term stabilization of Earth's surface temperature. *J. Geophys. Res.*, 86 (C10):9776–9782, 1981.

J. C. G. WALKER & B. N. OPDYKE. Influence of variable rates of neritic carbonate deposition on atmospheric carbon dioxide and pelagic sediments. *Paleoceanography*, 10(3):415–427, 1995.

P. WARNANT, L. M. FRANÇOIS, D. STRIVAY, & J.-C. GÉRARD. CARAIB : A global model of terrestrial biological productivity. *Global Biogeochem. Cycles*, 8 (3):255–270, 1994.

A. WATSON. Air-sea gas exchange and carbon dioxide. In M. HEIMANN, editor, *The Global Carbon Cycle*, volume 15 of *NATO ASI Series I : Global Environmental Change*, pages 397–411. Springer-Verlag, Berlin, 1993.

R. T. WATSON, H. ROHDE, H. OESCHGER, & U. SIEGENTHALER. Greenhouse gases and aerosols. In J. T. HOUGHTON, G. J. JENKINS, & J. J. EPHRAUMS, editors, *Climate Change. The IPCC Scientific Assessment*, chapter 1, pages 1–40. Cambridge University Press, Cambridge, 1990.

R. F. WEISS. Carbon dioxide in water and seawater : The solubility of a non-ideal gas. *Mar. Chem.*, 2:203–215, 1974.

T. WENK & U. SIEGENTHALER. The high-latitude ocean as a control of atmospheric CO_2. In E. T. SUNDQUIST & W. S. BROECKER, editors, *The Carbon Cycle and Atmospheric CO_2 : Natural Varia-*

tions Archean to Present, volume 32 of *Geophys. Monogr. Ser.*, pages 185–194. AGU, Washington, DC, 1985.

L. WESTERNHAUSEN, M. SARNTHEIN, U. STRUCK, H. ERLENKEUSER, & J. POYNTER. pCO_2 variations of equatorial surface water over the last 330,000 years : The $\delta^{13}C$ record of organic carbon. In R. ZAHN, T. F. PEDERSEN, M. A. KAMINSKI, & L. LABEYRIE, editors, *Carbon Cycling in the Glacial Ocean : Constraints on the Ocean's Role in Global Change*, volume 17 of *NATO ASI Series I : Global Environmental Change*, pages 367–382. Springer-Verlag, Berlin, 1994.

T. M. L. WIGLEY & L. N. PLUMMER. Mixing of carbonate waters. *Geochim. Cosmochim. Acta*, 40:989–995, 1976.

S. N. WILLIAMS, S. J. SCHAEFER, M. L. CALVACHE V., & D. LOPEZ. Global carbon dioxide emission to the atmosphere by volcanoes. *Geochim. Cosmochim. Acta*, 56: 1765–1770, 1992.

C. J. WILLMOTT, C. M. ROWE, & Y. MINTZ. Climatology of the terrestrial seasonal water cycle. *J. Climatol.*, 5:589–606, 1985.

T. J. WOLERY & N. H. SLEEP. Interaction of geochemical cycles with the mantle. In C. B. GREGOR, R. M. GARRELS, F. T. MACKENZIE, & J. B. MAYNARD, editors, *Chemical Cycles in the Evolution of the Earth*, chapter 3, pages 77–103. John Wiley & Sons, New York, NY, 1988.

R. WOLLAST. The relative importance of biomineralization and dissolution of $CaCO_3$ in the global carbon cycle. In F. DOUMENGE, editor, *Past and Present Biomineralization Processes. Considerations about the Carbonate Cycle*, Bulletin de l'Institut Océanographique, Numéro spécial 13, pages 13–35, Monaco, 1994. Musée Océanographique.

R. WOLLAST & F. T. MACKENZIE. The global cycle of silica. In S. R. ASTON, editor, *Silicon Geochemistry and Biogeochem-*

istry, pages 39–76. Academic Press, London, 1983.

H. E. WRIGHT, J. E. KUTZBACH, T. WEBB III, W. F. RUDDIMAN, F.A. STREET-PERROTT, & P. J. BARTLEIN. *Global Climates Since the Last Glacial Maximum.* University of Minnesota Press, Minneapolis, MN, 1993. 569 pp.

List of Figures

List of Tables

273